METHOD DEVELOPMENT FOR THE INVESTIGATION OF FREEZE/THAW STRESS–INDUCED PROTEIN INSTABILITY

zur Erlangung des akademischen Grades eines
DOKTORS DER INGENIEURWISSENSCHAFTEN (Dr.-Ing.)

von der KIT-Fakultät für Chemieingenieurwesen und Verfahrenstechnik des
Karlsruher Instituts für Technologie (KIT)
genehmigte

DISSERTATION

von
M.Sc. Anna Katharina Wöll
aus Heidelberg

Referent: Prof. Dr. Jürgen Hubbuch
Korreferent: Prof. Dr.-Ing. Michael Türk

Tag der mündlichen Prüfung: 06.03.2020

Danksagung

Diese Arbeit ist mit tatkräftiger, fachlicher und emotionaler Unterstützung von verschiedenen Personen angefertigt worden, welche im Folgenden erwähnt werden:

Zunächst möchte ich meinem Doktorvater Prof. Dr. Jürgen Hubbuch danken, die Möglichkeit bekommen zu haben meine Dissertation in seiner Arbeitsgruppe und Laboren anfertigen zu dürfen. Vielen Dank für die spannenden fachlichen Diskussionen, den Freiraum den du mir gegeben hast und dein Vertrauen.
Für die freundliche Übernahme des Korreferats und das Interesse an meiner Arbeit möchte ich Prof. Dr.-Ing. Michael Türk danken.

Vielen Dank auch an alle meine Kollegen für die tolle Zeit am Institut, die spannenden und hilfreichen Diskussionen, die zahlreichen Partys und Freizeitaktivitäten.
Ganz besonderen Dank an Juliane Schütz, die mich mit der Bachelorarbeit ans Institut geholt hat und in den ganzen Jahren unterstützend zur Seite stand und den Einstieg in die Promotion erleichtert hat.
Herzlichen Dank auch an meine Studenten Angela Valentic, Jana Zabel, Monika Desombre, Lena Enghauser und Rafaela Meutelet für die fleißige Unterstützung im Labor, den interessanten Diskussionen und den unterhaltsamen Pausen.
Danke auch an meine Bürokollegen Marieke Klijn, Juliane Schütz, Nils Hillebrandt, Dennis Weber und Angela Valentic für die angenehme Arbeitsatmosphäre, die unterhaltsame Unterbrechungen und das Ertragen des niedrigen Sauerstoffsgehaltes dank meiner Kälteempfindlichkeit.
Susanna Suhm vielen Dank für die sehr unterhaltsame gemeinsame Zeit im Labor und die zahlreichen lustigen Pausen.
Lukas Wenger danke für das Aufmuntern und gut zureden, wenn etwas schief gelaufen ist, das Weiterhelfen und Erklären.

Danke auch an meine Freunde, ganz besonders meiner Studiums Clique mit Eva, Lukas, Christian, Ursula und Marina sowie der ganzen CIWler Clique für viele unvergesslichen Unternehmungen, Kochabende, Spielabende, Partys und gemeinsame Urlaube. Ohne euch wäre das Studium und die Promotion mindestens doppelt so herausfordernd und anstrengend und nicht mal annähernd so lustig gewesen.
Ganz besonders hervorheben möchte ich dabei Eva Conraths. Danke für die stundenlangen Telefonate und die motivierenden Worte. Du warst und bist eine sehr große Unterstützung

für mich!

Danke an meine Familie für die Unterstützung und den Rückhalt, ganz besonders meiner Mutter die immer wieder aufbauenden Worte gefunden hat. Auch meiner Bremer Familie möchte ich vom Herzen für den Zuspruch und die Ablenkung danken.

Zuletzt möchte ich meinem Freund Leonard Westkamp für den bedingungslosen Rückhalt, stundenlanges Zuhören und Motivieren, von ganzem Herzen danken. Du hast mehr an mich geglaubt, als ich es selber getan habe und mich oft daran erinnert, dass es wichtigere Dinge als die Doktorarbeit im Leben gibt. Ich bin sehr dankbar dich an meiner Seite zu haben und freue mich sehr auf unseren neuen Lebensabschnitt.

"Mögen sich alle deine Wünsche erfüllen...,außer einem, sodass du immer etwas hast, wofür du ringen, wonach du streben kannst."

Irischer Segenswunsch

Zusammenfassung

Das allgemeine Ziel dieser Arbeit ist die Entwicklung einer einfachen, zeitsparenden Hochdurchsatz (*high-throughput*, HT) Methode zur Untersuchung des Einflusses von Einfrier-/Auftau- (*freeze/thaw*, FT) Stress auf die Langzeitstabilität von rekombinanten Proteinen. Rekombinante Proteine sind biologische Makromoleküle, die über eine hochspezialisierte Funktionalität verfügen und deren Langzeitstabilität eine entscheidende Rolle bei der biotechnologischen Produkt- und Prozessentwicklung spielt. Während des Produktionsprozesses (USP and DSP) von rekombinanten Proteinen sind ein oder mehrere FT–Schritte zur Lagerung, beim Transport oder zur Zwischenlagerung aufgrund von Engpässen bei der Aufreinigung notwenig. Innerhalb des FT–Schrittes sollen die Proteinstabilität garantiert, sowie die Haltbarkeit der Proteine erhöht werden. Im Allgemeinen muss die Proteinstabilität sowohl bei der Produktion und Aufreinigung, als auch beim Einfrieren/Auftauen, gewährleistet werden. Die Proteinstabilität, einschließlich Konformation– und Kolloidstabilität, ist sehr empfindlich gegenüber Umweltveränderungen wie Temperatur, Art und Konzentration von gelösten Stoffen, sowie der pH–Wert. Geht die Proteinstabilität verloren, führt dies auch zum Verlust der Funktionalität. Das ist problematisch im Bezug auf die Wirkung aber auch der Sicherheit. Die Empfindlichkeit der Proteinstabilität gegenüber Umgebungsbedingungen ist besonders am Ende der Aufreinigung problematisch, wenn die rekombinanten Proteine formuliert werden. Dabei muss eine Langzeitstabilität des Proteins von mindestens 18–24 Monaten gewährleistet sein. Im Rahmen der Formulierungsentwicklung muss die Proteinstabilität im Laufe der Zeit als Funktion verschiedener umweltbedingter Faktoren untersucht werden. Dies ist sehr komplex, da alle Faktoren sich untereinander beeinflussen. Insbesondere beim Einfrieren und Auftauen haben neben Formulierungsparametern (pH–Wert, Additive und Puffersysteme), auch Prozessparameter (FT–Rampe, Probenvolumen, Lagerzeit und Temperatur) einen Einfluss auf die Proteinstabilität. Darüber hinaus werden Systemparameter wie die Glasübergangstemperatur (*glass transition point*, T_g) oder der Trübungspunkt (*cloud point*, T_{cloud}) durch die Formulierungs– und Prozessparameter beeinflusst und haben wiederum auch einen Einfluss auf die Proteinstabilität. Daher ist es wichtig, ein Gesamtverständnis über die Beziehung all dieser Parameter und ihren Einfluss auf die langfristige Proteinstabilität zu generieren, um ein hohes Maß an Proteinstabilität nach einem oder mehreren FT–Schritten zu gewährleisten. Zur Charakterisierung der Proteinstabilität können verschiedene Analytikmethoden verwendet werden. Beispielsweise werden Größenmessungen mittels Größenausslusschromatographie (*size exclusion chromatography*, SEC), Strukturmessungen mittels Fourier–Transform–Infrarotspektrometer (*Fourier–transform infrared spectroscopy*, FTIR) oder Aktivitätsmessungen mit Hilfe von

Aktivitätsassays durchgeführt. Diese Methoden sind zeitaufwändig, teuer und die Korrelation der Daten ist komplex und nicht immer offensichtlich. Um den Einfluss der Formulierungsparameter auf die Langzeitstabilität von Proteinen zu untersuchen werden zum Beispiel Phasendiagramme verwendet. Ein großer Vorteil dabei ist die hohe Flexibilität und Freiheit bei der Erstellung der Phasendiagramme. Vor diesem Hintergrund wurde im ersten Schritt dieser Arbeit die Entwicklung einer phasendiagrammbasierten Methode angestrebt, um die Möglichkeit eines einfachen, zeitsparenden HT–Screenings verschiedener Formulierungs- und Prozessparameter, sowie die Erkennung von Systemparametern zu ermöglichen. Bei der Erstellung der Phasendiagramme mittels eines Pipettierroboters wurden die Protein- und Salzkonzentration variiert und der Einfluss des Phasenverhaltens in Abhängigkeit von verschiedenen Formulierungsparametern (Puffersysteme, Pufferkapazitäten, pH–Wert, Ionenstärke) untersucht. Es wurden Phasendiagramme mit dem Modellprotein Lysozym aus Hühnereiweiß und dem Fällungsmittel Natriumchlorid erstellt. Um die FT Stress–induzierten Instabilitäten zu bewerten, wurden nach 40-tägiger Lagerung bei 20 °C in einer Inkubationskammer Veränderungen im Phasenverhalten, in der Kristallmorphologie und in der Proteinlöslichkeit als sensitive Parameter identifiziert. Das Phasenverhalten und die Kristallmorphologie wurden visuell bewertet und die Proteinlöslichkeit anhand der Proteinkonzentration, gemessen mittels UV-Vis-Spektroskopie, im Überstand berechnet. Im ersten Schritt konzentriert sich diese Studie zunächst auf den Einfluss verschiedener Formulierungsparameter als Funktion der FT Zyklenanzahl. Dabei wurden die Platten in einem Gefrierschrank auf -80 °C gefroren und bei 20 °C aufgetaut. Die Ergebnisse zeigten einen Einfluss von FT Stress auf alle Parameter (Phasenverhalten, Kristallmorphologie und Proteinlöslichkeit), während dieser Einfluss durch die Erhöhung der Zyklenanzahl, unabhängig vom verwendeten pH–Wert oder Puffersystem, zunahm. Die Erhöhung der Zyklenanzahl führte zu kleineren Bereichen in denen das Protein stabil/löslich blieb, zu kleineren und komplexer strukturierten Kristallen und zu niedrigeren Proteinlöslichkeiten, was ingesamt eine erhöhte Instabilität repräsentierte. Diese Trends wurden immer so bewertet, dass sie mehr Instabilitäten repräsentieren. Die Wirkung von FT Stress wurde in Abhängigkeit der Pufferkomponente und dem pH–Wert ermittelt. Wurden die Proteine bereits durch den pH–Wert destabilisiert (z.B. pH 3), so wurde eine geringerer Einfluss vom FT Stress beobachtet, als bei den Proteinen bei denen eine Destabilisierung durch den pH–Wert selbst nicht angenommen wurde (z.B. pH 5). Formulierungen mit Pufferkomponenten, von denen bekannt ist, dass sie mit dem Protein interagieren, zeigten ein höheres Maß an FT Stress–induzierten Instabilitäten.

Die beobachteten Möglichkeiten den Einfluss verschiedener Formulierungsparameter beim Einfrieren und Auftauen zu bewerten konnte durch die Anwendung der entwickelten Methode mittels Variation der Prozessparameter bestätigt werden. Dafür wurden verschiedene Einfrier- und Auftaurampen getestet, wobei jeweils eine Rampe konstant gehalten wurde um die Einfrier– und Auftaueinflüsse voneinander zu trennen. Zudem wurde der Einfluss des Systemparameters T_g, durch Änderung der Geschwindigkeit beim Einfrieren bei verschiedenen Temperaturen, untersucht. Dabei wurde nach der Erstellung der Phasendiagramme das entsprechende FT Protokoll durchgeführt. Hierfür wurden die Platten auf eine Kühlapparatur gelegt und das jeweilige FT Protokoll angepasst. Anschließend wurden die Platten in einer Inkubationskammer für 40 Tage bei 20 °C gelagert. Die für

vi

die Proteinstabilität relevanten Parameter, Phasenverhalten, Kristallmorphologie und Proteinlöslichkeit, wurden anschließend verwendet um den Einfluss der verschiedenen getesteten Rampen zu bewerten. Der Einfluss von Einfrierrampen auf die Proteinstabilität war ausgeprägter als von Auftaurampen, wobei schnellere Rampen weniger stressbedingte Instabilitäten hervorriefen. Dementsprechend wurde davon ausgegangen, dass die Gefrierkonzentration, und nicht die Bildung der Wasser-Eis-Grenzfläche, das Hauptproblem beim Einfrieren von Lysozyme ist. Darüber hinaus war die Gesamtzeit, in der das Protein kalten Temperaturen ausgesetzt war, bzw. die Lösung nicht T_g überschritten hatte, kritisch. Je später die Temperatur der Einfriergeschwindigkeit von schnell auf langsam geändert wurde, desto weniger Proteininstabilitäten wurden durch das Einfrieren/Auftauen verursacht.

Um noch mehr Erkenntnisse über den Einfrier- und Auftauprozess bei Verwendung der entwickelten Methode zu erhalten, wurde der Aufbau durch eine Kamera erweitert. Die Platten wurden beim Einfrieren und Auftauen gefilmt um den Prozessparameter T_{cloud} zu bestimmen. Ausgenutzt wurde dabei der Effekt, dass bei T_{cloud} die Lösung durch die Bildung von wässrigen Zweiphasensystemen (*liquid–liquid phase separation*, LLPS) trüb wird. Darüber hinaus wurde T_{cloud} als Funktion der Lysozymkonzentration, des Ionentyps, der Ionenstärke und des FT Stresses bestimmt. Dabei wurde die Korrelation des Kurzzeitparameters T_{cloud} und der Langzeitstabilität von Proteinen durch die Erstellung von Phasendiagrammen in einer Fallstudie untersucht. Die Reproduzierbarkeit der Methode und eine Korrelation der ermittelten T_{cloud} Werte mit Literaturdaten wurden ebenfalls überprüft. Bezüglich der Reproduzierbarkeit konnte eine geringe absolute Abweichung vom Median (*median absolute deviation*, MAD) von 0,2 °C innerhalb von 60 Proben erreicht werden. Darüber hinaus wurde eine hohe Korrelation zu Literaturdaten mit einem Pearson Korrelationskoeffizienten (*Pearson correlation coefficient*, PCC) von 0,996 gezeigt werden. Die anschließende Fallstudie wies eine partielle Korrelation zwischen dem gemessenen scheinbaren T_{cloud}–Wert und der langfristigen Proteininstabilität als Funktion der Lysozymkonzentration, des Ionentyps, der Ionenstärke und des FT Stresses auf. Die getesteten Lysozym– und/oder Salzkonzentrationen waren jedoch zu niedrig, um bei Zugabe von den Additiven Natriumsulfat und Ammoniumsulfat eine Aggregation zu erzeugen. Demnach konnten auch keine T_{cloud} vor dem Einfrieren der Lösung detektiert werden. Mit Natriumchlorid und Ammoniumchlorid fand eine Aggregation statt. Zudem konnte T_{cloud} bei den Formulierungen mit Natriumchlorid bestimmt werden. Für diese Formulierungen konnte das Auftreten von T_{cloud} bei Temperaturen um die -10 °C mit langfristigen Instabilitäten korreliert werden.

Um Stabilisierungsparameter aber auch die Reversibilität von FT Stress–induzierten Instabilitäten zu untersuchen, wurde im letzten Abschnitt der Arbeit die Reversibilität als Funktion verschiedener Gefrierschutzstoffe (Saccharose, Glycerin, PEG200, Tween20) beurteilt. Dabei wurde der Einfluss der verschiedenen Gefrierschutzstoffe auf das Phasenverhalten von Lysozym und dem Fällungsmittel Natriumchlorid ohne FT Stress und mit bis zu drei FT Zyklen untersucht. Um die Reversibilität der induzierten Instabilitäten zu untersuchen, wurde ein Wärmeschritt hinzugefügt, bei dem das Phasendiagramm auf 40 °C für 30 Minuten erwärmt wurde. Darüber hinaus wurden die Proteingröße und die Proteinstruktur ausgewählter löslicher Proben unmittelbar nach der Verarbeitung des

Stressprotokolls durch Dynamische Lichtstreuung (*dynamic light scattering*, DLS) bzw. FTIR bestimmt. Diese Kurzzeit–Parameter wurden dann mit der Langzeitstabilität der Proteine nach 40 Tagen und dem angewandten FT Stress korreliert. Um die Stabilisierung durch Gefrierschutzstoffe und die Reversibilität durch Wärme zu bewerten, wurden, wie zuvor beschrieben, Änderungen des Phasenverhaltens, der Kristallmorphologie und der Proteinlöslichkeit berücksichtigt. Um die Stabilisierungseffekte zu beurteilen, wurden die Formulierungen mit Gefrierschutzstoffen mit denene die nur Natriumchlorid enthielten, verglichen. Mit dem Vergleich der gestressten und nicht gestressten Systeme konnte die Reversibilität beurteilt werden. Bezüglich der Stabilisierung von Lysozyme hinsichtlich FT Stress, zeigten die Osmolyten Saccharose und Glycerol verglichen zu den anderen getesteten Formulierungen die wenigsten Instabilitäten. Außerdem zeigten sie eine gute Reversibilität. Die Formulierungen mit dem getesteten Polymer PEG200 zeigten keine Stabilisierung/Destabilisierung, wenn die Proben gestresst wurden. Die Reversibilität war ohne den Zusatz von PEG200 höher, was vermutlich auf die Bildung von Proteinaggregaten mit stärkeren Protein–Protein–Wechselwirkungen, bei Anwesenheit von PEG200, zurückzuführen ist, die durch Hitze nicht gelöst werden konnten. Das Tensid Tween20, von dem bekannt ist, dass es sich an Wasser-Eis-Grenzflächen anlagert um das Protein vor Denaturierung zu schützen, zeigte eine destabilisierende Wirkung, wenn die Formulierungen durch Einfrieren und Auftauen gestresst wurden. Darüber hinaus konnte durch das Erwärmen der Platten auf 40 °C nahezu keine Reversibilität erreicht werden. Hier wurde angenommen, dass die Wasser-Eis-Oberfläche die Proteinstabilität nicht beeinflusst sondern die Interaktion zwischen Protein und Tween20 zu den Instabilitäten führt. Für alle Formulierungen konnte ein destabilisierender Effekt durch Erhöhung der Zyklenzahl beobachtet werden, während bei Tween20 der Unterschied zwischen einem und drei Zyklen geringer war. Hier wurde angenommen, dass der Grad der Destabilisierung nach einem Zyklus so groß war, dass keine zusätzliche Destabilisierung durch weitere Zyklen stattfinden konnte. Bezüglich der Korrelation der Kurzzeit–Parameter Größe und Struktur zur Langzeitstabilität der Proteine konnte keine Abhängigkeit festgestellt werden. Weder die Größe, noch die Struktur wurden durch die Zugabe von Gefrierschutzstoffen, der Anwendung von FT Stress oder der Wärmebehandlung beeinflusst.

Zusammenfassend lässt sich sagen, dass eine phasendiagrammbasierte Methode zur Untersuchung von FT Stress–induzierten Proteininstabilitäten entwickelt wurde. Mit dieser Methode ist eine parallele Erforschung und Entwicklung von Formulierungs- und Prozessparametern und deren Einfluss auf die Protein–Langzeitstabilität möglich. Darüber hinaus wurde die Bestimmung eines Systemparameters, dem Trübungspunkt T_{cloud}, beim Einfrieren und Auftauen entwickelt um noch mehr Informationen über den FT–Prozess zu generieren. Zum Schluss wurde die Stabilisierung durch Gefrierschutzstoffe hinsichtlich der FT Stress–induzierten Instabilitäten und deren Reversibilität durch Wärme mit Hilfe der entwickelten Methode untersucht.

Abstract

The general purpose of this thesis is the development of a simple, time–saving high–throughput screening (HTS) method to investigate the impact of freeze/thaw (FT) stress on the long–term stability of recombinant proteins. Recombinant proteins are biological macromolecules, which have a highly specialized functionality, and their long–term stability plays a crucial role in the biotechnology product and process development. During the upstream process (USP) and downstream process (DSP) of recombinant proteins, one or more FT steps are necessary, for storage, transportation, or for intermediate storage due to bottlenecks during purification. Within the FT step, the protein stability should be guaranteed as well as the shelf life of the proteins should be increased. In general, the protein stability has to be guaranteed, during USP, DSP, and freezing/thawing. The protein stability, including conformational and colloidal stability, is very sensitive to environmental changes, such as temperature, solute type and concentration, and pH value. A loss of the protein stability results in the loss of the protein functionality. This is problematic both in terms of effect and safety. The sensitivity of the protein stability to environmental conditions is challenging especially at the end of purification when recombinant proteins are formulated. By the formulation, a protein long-term stability shall be ensured for at least 18-24 months. Within the formulation development, the protein stability over time as a function of different environmental conditions has to be studied. This is very complex due to the fact that all factors influence each other. Especially during freezing and thawing, both formulation parameters (pH value, additive and buffer system) and process parameters (FT ramp, sample volume, storage time and temperature) have an influence on the protein stability. In addition, system parameters, such as the glass transition temperature (T_g) or the cloud point (T_{cloud}), are influenced by the formulation and process parameters and have, in turn, also an influence on protein stability. Therefore, it is important to generate an overall understanding of the relationship of all these parameters and their influence on long–term stability to ensure a high level of protein stability after one or more FT steps. Different analytical methods can be used to characterize the protein stability during pharmaceutical formulation development. For example, size measurements using size exclusion chromatography (SEC), structure measurements using Fourier–transform infrared spectroscopy (FTIR), or activity measurements using activity assays, are performed. These methods are time-consuming, expensive, and the correlation of the data is complex and not always obvious. To investigate the effects of formulation parameters on the protein long–term stability, protein phase diagrams are used exemplarily. Here, the high flexibility and freedom by creating the phase diagrams is a huge benefit. With this background, in

a first step of this work the development of a phase diagram–based method was aimed to create the possibility of a simple, time–saving high–throughput (HT) screening of different formulation and process parameters, and the detection of system parameters. When creating the phase diagrams using a liquid handling station, the protein and salt concentrations were varied, and the influence on the phase behavior was investigated as function of different formulation parameters (buffer systems, buffer capacities, pH value, ionic strength). Here, the phase diagrams were created using the model protein lysozyme from chicken egg white and the precipitant sodium chloride. The evaluation of the FT stress–induced instabilities showed, that changes in phase behavior, crystal morphology, and protein solubility after 40–day storage at 20 °C in an incubation chamber, are sensitive parameters. The phase behavior and the crystal morphology were rated visually, and the protein solubility was calculated using the protein concentration in the supernatant, measured by UV-vis spectroscopy. This study in a first view focused on the influence of different formulation parameters as a function of the number of FT cycles. Thereby, the plates were frozen in a freezer to -80 °C and thawed at 20 °C. The results showed an influence of FT stress on all parameters (phase behavior, crystal morphology, and protein solubility), whereas this influence increased by the increase in the number of FT cycles, no matter which pH or buffer system was used. Increasing the number of cycles resulted in smaller regions in which the protein stayed stable/soluble, in smaller and more complex structured crystals, and in lower protein solubilities, which overall represented an increased degree of instabilities. These trends were always rated to represent more instabilities. The effect of FT stress was found to be dependent on the buffer component and pH value. If the proteins were already destabilized by the pH value (e.g. pH 3), a smaller influence of FT stress was observed than in the case of proteins which were not assumed to be destabilized by the pH value itself (e.g. pH 5). Formulations with buffer components, which are known to interact with the protein itself, showed a higher degree of FT stress–induced instabilities. Considering the observed possibilities to rate the influence of different formulation parameters during freezing and thawing, the applicability of the developed method was verified by varying the process parameters. Here, different freezing and thawing ramps were tested while one ramp was kept constant to separate the freeze and thaw influences from each other. In addition, the influence of the system parameter T_g by changing the speed during freezing at different temperatures was investigated. The respective FT protocol was performed after the phase diagrams were created. Here, the plates were placed on a cryogenic device and the respective FT protocol was adjusted. Afterwards, the plates were stored in an incubation chamber at 20 °C for 40 days. Parameters relevant for protein stability, phase behavior, crystal morphology, and protein solubility, were used to evaluate the influence of the different tested ramps. The influence on the protein stability of freezing ramps was found to be more pronounced than on thawing ramps, where faster freezing ramps showed less FT stress–induced instabilities. According to this, it was assumed that freeze concentration and not the creation of the water–ice interface is the main issue when lysozyme is frozen. Furthermore, the overall time where the protein is exposed to cold temperature or the solution did not cross T_g, was critical. Consequently, the later the temperature of the freezing speed was changed from fast to slow, the less protein instabilities were induced by freezing/thawing.

To generate even more knowledge about the freezing and thawing process while using the developed method, the setup was extended by a camera. The plates were recorded during freezing and thawing to determine the process parameter T_{cloud}. The effect was exploited that the solution at T_{cloud} becomes turbid through the formation of liquid–liquid phase separation (LLPS). In addition, T_{cloud} was determined as a function of lysozyme concentration, ion type, ionic strength, and FT stress. Here, the correlation of the short–term parameter T_{cloud} and the long–term protein stability, by creating phase diagrams, was investigated in a case study. Reproducibility of the method and a correlation of the determined T_{cloud} values to literature data were checked as well. Regarding the reproducibility, a small median absolute deviation (MAD) of 0.2 °C within 60 samples was shown. In addition, a high correlation to literature data with a Pearson correlation coefficient (PCC) of 0.996 was demonstrated. The subsequent case study demonstrated a partial correlation between the obtained apparent T_{cloud} parameter and long–term protein stability as a function of lysozyme concentration, ion type, ionic strength, and FT stress. However, the tested lysozyme and/or salt concentrations were too low to create aggregation when the additives sodium sulfate, and ammonium sulfate were added. Subsequently, T_{cloud} did not appear either before the solution froze. With sodium chloride and ammonium chloride, aggregation took place. In addition, T_{cloud} could be determined for formulations containing sodium chloride. For these formulations, the appearance of T_{cloud} at temperatures around -10 °C could be correlated with long–term instabilities.

In order to determine stabilization parameters as well as the reversibility of FT stress–induced instabilities, the reversibility as a function of different antifreeze substances was investigated in the last section. The influence of the different cryoprotectants on the phase behavior of lysozyme and the precipitant sodium chloride without FT stress and with up to three FT cycles was researched. To investigate the reversibility of the induced instabilities, a heat step where the phase diagram was heated to 40 °C for 30 minutes, was added. In addition, the protein size and the protein structure of selected soluble samples were determined right after the stress protocol was processed by dynamic light scattering (DLS) and FTIR, respectively. These short–term parameters were then correlated to the long–term protein stability after 40 days and to the applied FT stress. To evaluate the stabilization by cryoprotectants and the reversibility by heat, changes in phase behavior, crystal morphology, and protein solubility were considered, as described before. Here, the formulations containing cryoprotectants were compared to the formulations containing only sodium chloride when investigating the stabilization effect. To evaluate the reversibility, the stressed systems were compared to the non–stressed systems. The osmolytes, sucrose and glycerol, were found to stabilize lysozyme regarding FT stress compared to the other tested formulations. Moreover, they showed a good reversibility. The formulations containing the tested polymer PEG200 showed no stabilization/destabilization effect when stressed. Reversibility was higher without the addition of PEG200, presumably due to the formation of protein aggregates with stronger protein–protein interactions in the presence of PEG200, which could not be resolved by heat. The surfactant Tween20, known to stabilize against denaturation on water–ice interfaces, showed a destabilizing effect when the formulations were stressed by freezing and thawing. In addition, nearly no reversibility could be induced by heating the plates to 40 °C. Here, it was assumed that the water–ice interface does not

influence the protein stability, but that the interaction between protein and Tween20 leads to instabilities. For all formulations, a destabilizing effect by increasing the number of cycles could be reported, whereas with Tween20, the difference between one and three cycles was less. Here, it was assumed that the degree of destabilization was too significant after one cycle and no additional destabilization could take place through further cycles. Regarding the correlation of the short–term parameters, size and structure to the long–term protein stability, no correlation could determined. Neither the size nor the structure were influenced by the addition of cryoprotectants, the application of FT stress, or heat treatment.

In summary, a phase diagram–based method to investigate FT stress–induced protein instabilities was developed. Using this method, a parallel research and development of formulation and process parameters and their influence on protein long–term stability is possible. In addition, the determination of a system parameter T_{cloud} during freezing and thawing was developed to gain even more information on the FT process. At the end, the stabilization by cryoprotectants regarding the FT stress–induced instabilities and their reversibility by heat were investigated by using the developed method.

Contents

1. Introduction

Proteins are complex biomolecules which fulfill essential tasks in living organisms. The unique three–dimensional structure defines the functional property of acting as antibody, enzyme, hormone or structural cell component. One of the main groups of the biopharmaceutical industry is the production of recombinant proteins [1]. Recombinant proteins are expressed by organisms modified with recombinant DNA. For example, as expression system for human insulin, bacterial cells are used [2]. Several criteria have to be fulfilled to obtain a successfully developed recombinant protein. The safety and efficacy for the patient have to be guaranteed, and a long–term stability of at least 18–24 months has to be proven. Furthermore, the production process has to be scalable and economical [3, 4]. Due to the complex structure and the specific functionality, the protein stability is very sensitive to environmental changes. These changes might result in unfolding of the protein or aggregation, both of which might result in a loss of the protein functionality [5]. Therefore, it is necessary to investigate the environmental changes during production (USP), purification (DSP), and final formulation [6]. When this is not guaranteed, an insufficient, excessive, or defective recombinant protein production can lead to serious diseases, such as diabetes [7], Alzheimer's disease or Parkinson [8, 9].

To avoid these issues, an understanding of the impact of environmental changes on the protein stability as well as the long–term stability is required. In the following sections, a theoretical background of protein structure, protein stability, and their influencing factors is presented. The focus is laid on the impact of freeze/thaw stress. Furthermore, an overview is given of the used analytical techniques to monitor protein stability.

1.1. Protein conformation and interactions

The unique three–dimensional conformation of proteins is based on an amino acid sequence. The amino acids are linked by peptide bonds, thus forming an individual polypeptide chain. This chain is called the primary structure; is is built up of combinations of 20 different proteinogenic amino acids, see Figure 1.1 a. The number of amino acids defines the molecular weight and varies between the biopharmaceutical proteins. The molecular weight range is between 5 kDa (insulin) and 150 kDa (mAbs). The amino acids have different characteristics and are either basic, acid, hydrophobic (non-polar), or hydrophilic (polar) [10]. This results

in electrostatic, hydrophobic, van der Waals interactions or hydrogen bonds and disulfide bonds between the amino acids. These intermolecular interactions create the secondary structure of proteins, where α–helix, β–sheet, or β–sheet anti parallel conformations are created by hydrogen bonds between carbonyl and amino groups, see Figure 1.1 b. Through intermolecular interactions, like hydrophobic and hydrophilic interactions as well as disulfide bonds, the protein is folded even more in a specific three–dimensional conformation, called tertiary structure, see Figure 1.1 c. There, hydrophobic interactions are the most dominant ones. To stabilize the folded native state, most of the peptide groups and non–polar side chains ($\sim 80\%$) are covered in the inside of the molecule to avoid contact with water. The polar side chains are present on the protein surface, and by building stable hydrogen bonds, the protein conformation is stabilized. Larger and more complex proteins are built of more than one polypeptide chain; the subunits aggregate and create a protein molecule. This structure is called quaternary structure, see Figure 1.1 d [11–16]. The protein stability is
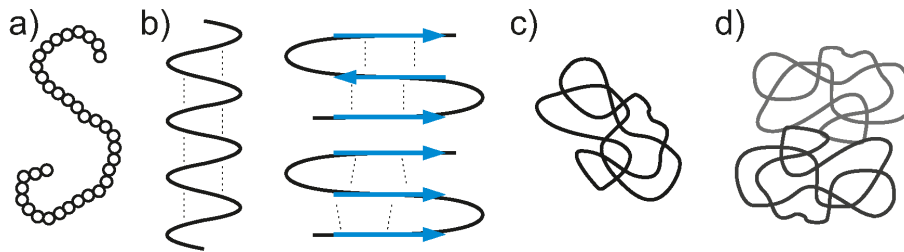
Figure 1.1.: The different protein structures are shown. The primary structure is shown in a), whereas the amino acid are represented by the circles. The secondary structure possibilities, α–helix (left), β–sheet anti parallel (right up), and β–sheet (right down) are displayed in b), whereas interactions between the chains are presented schematically by dotted lines. The tertiary structure is shown in c), and the quaternary structure with two subunits (grey and black) in d).

directly related to the protein conformation (conformational stability). Environmental changes influence the intermolecular interactions, which might cause conformational changes and results in the loss of protein stability and activity. These factors are explained in more detail in Section 1.3.

By folding the polypeptide chain into a tertiary (or quaternary) structure, a protein surface is created. As described before, mainly charged side chains are present at the surface and due to electrostatic interactions with water molecules the protein is stabilized in solution [17]. These interactions influence the intermolecular protein–protein interactions. Long–range repulsive interactions take place when both molecules are similarly charged [18]. Besides, attractive short-range protein–protein interactions might also occur. Next to the electrostatic interactions, additionally van der Waal, hydrophobic, and steric (excluded–volume) interactions influence the aggregation tendency (colloidal stability) of the protein [14, 19, 20]. Depending on the environmental conditions the protein surface charge as well as the aggregation tendency are affected; both are described in more detail in Section 1.3.

1.2. Lysozyme from chicken egg white

In this study, the model protein lysozyme from chicken egg white is used. Lysozyme has a molecular weight of 14.6 kDa and the polypeptide chain exist of 129 amino acids [21, 22]. The isoelectric point (pI) of lysozyme is at ~11.35 [23]. The native conformation is displayed in Figure 1.2.
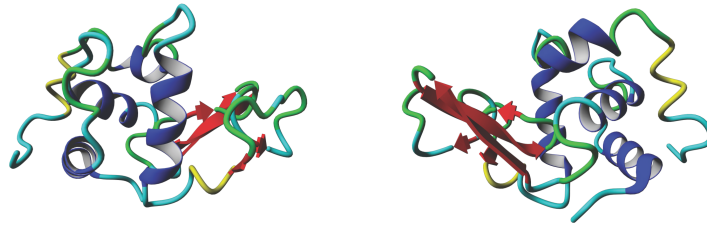
Figure 1.2.: The native protein conformation of lysozyme from chicken egg white from two perspectives. The alpa–helix structures are presented in blue and the beta–sheet structures are displayed in red.

1.3. Protein aggregation

Protein aggregates occur due to the loss of colloidal stability, which might be induced by the loss of conformational stability. The protein aggregates are classified into different categories [24, 25]: a) The type of bond: non–covalent aggregates are bound by electrostatic interactions, whereas covalent aggregates are bond by disulfide bridges. b) Depending on the type of bond, the reversibilities differ: non–covalent aggregates are reversible, and covalent bond aggregates are irreversible. c) The aggregate size: there are small soluble oligomers (dimers, trimers, etc.), large oligomers ($\geq$ 10-mer oligomers), aggregates from 20 nm to 1 μm, insoluble aggregates up to 25 μm, and visible aggregates ($>$ 100 μm). d) The protein conformation: native aggregates and non–native aggregates, where the proteins lost their activity.

There are different aggregation mechanisms, depending on the initial protein state (native/-non–native), and the reason for aggregation (environmental changes or applied stress) [24, 26]. A classification of the five most common mechanisms are published by Philo and Arakawa [26], and is schematically shown in Figure 1.3. Mechanism 1, describes the aggregation of native monomers, here the oligomerization is reversible and the creation of higher oligomers might be irreversible. Mechanisms 2 and 3 show aggregation of non–native (2) or chemically modified (3) proteins. The chemical modification is irreversible, like the higher oligomers which are created for both mechanisms. The mechanism 4 shows the attachment of native proteins to critical nuclei, created out of protein aggregates or
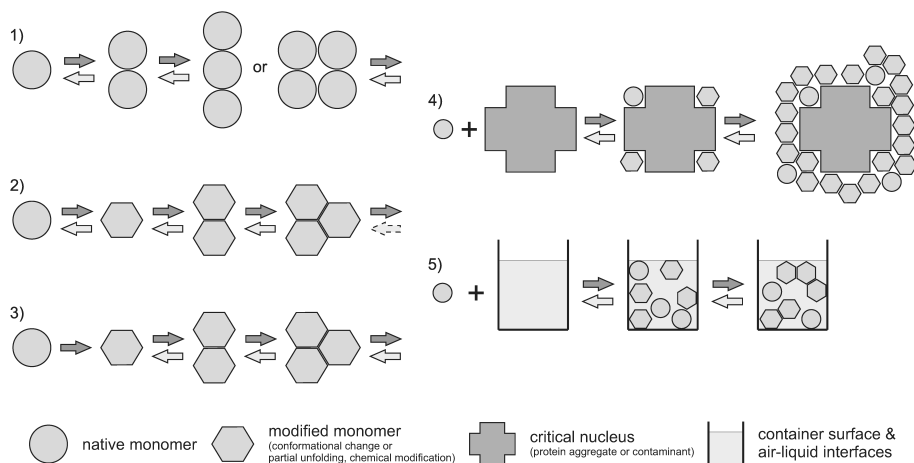
Figure 1.3.: Schematic illustration of five common aggregation mechanism, adapted from [26].

contaminants. While attaching of the proteins to the nuclei surface, partial unfolding of the protein might take place. As a consequence, visible particles or precipitate are created, which are irreversible. Mechanism 5 describes the process of adsorption of native monomers to the container or air–water surfaces which promotes partial unfolding, resulting in protein aggregation.

1.3.1. Aggregation process and morphologies

The assembly of protein monomers to form multimers because of attractive protein interactions result in the appearance of different crystal shapes, precipitate types, or gel formation. The aggregation process is thereby split into two main steps: nucleation and crystal growth. First, an energetic barrier (ΔG^*) has to be overcome to create critical nuclei. Therefore, the attractive interactions have to be significantly high, see Figure 1.4 [27]. The theoretical background of ΔG^* is explained in the following. The nucleation of protein crystals is based on the classical nucleation theory developed in 1926 for the condensation of a drop from its vapor [29]. The applicability for protein crystallization was then forwarded by Feher and Kam [30]. The formation of a spherical nucleus with the radius r is described by the Gibbs free energy $\Delta G(r)$, and the calculation is shown in Equation 1.1. The first summand describes a volume term and a surface term is described in the second summand, see Figure 1.4 (left) [27, 28].

$$\Delta G = -\frac{4}{3}\pi r^3 \frac{k_b T}{\nu} ln S_{sat} + 4\pi r^2 \gamma \tag{1.1}$$

The interfacial free energy between the crystal nucleus and the bulk solution is described by γ. The radius r describes the size of the nucleus. $k_b T/\nu \; ln S_{sat}$ describes the free energy difference between a protein molecule in solution and attached to the crystal, ν represents
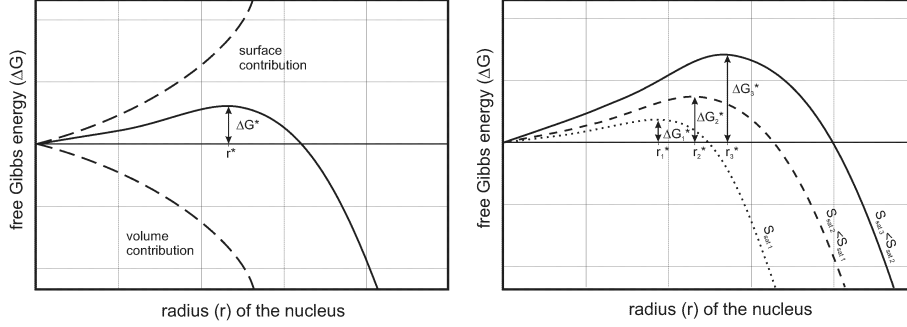
Figure 1.4.: Gibbs free energetics (ΔG) of nucleus formation as a function of the nucleus radius (r)(left) and the variation of the energetic barrier as a function of supersaturation (S_{sat}) (right), adapted from [28]

the occupied molar volume of one protein molecule, S_{sat} the supersaturation in the solution, k_b the Boltzmann constant, and T the absolute temperature. The maximal ΔG value calculated with Equation 1.1, describes the nucleation barrier ΔG^* with the radius r^* of the critical nucleus. This is defined by

$$\left(\frac{\delta \Delta G(r)}{\delta r}\right)_{S_{sat},T} = 0 \tag{1.2}$$

resulting in

$$r^* = \frac{2\nu\gamma}{k_b T ln S_{sat}} \tag{1.3}$$

To calculate the nucleation barrier ΔG^*, r^* (Equation 1.3) has to be inserted into Equation 1.1. Both parameters, r^* and ΔG^*, are strongly dependent on the supersaturation S_{sat}. As illustrated in Figure 1.4 (right), the higher the supersaturation S_{sat}, the lower r^* and ΔG^*, consequently the easier the nucleation barrier is overcome [27, 28].

Using the supersaturation S_{sat}, the metastable and the labile zones, which are created in a phase diagram (Figure 1.8), can be differentiated. In the metastable zone, ΔG^* is not reached, due to the low supersaturation, e.g. the contribution of the surface term (second summand in Eq. 1.1) is too high and therefore is not exceeded by the volume term (first summand in Eq. 1.1). Consequently, nucleation does not take place, but existing crystals continue growing. Increasing the supersaturation, the volume and surface term counterbalance each other at the borderline between metastable and labile zone before the supersaturation is so high that nucleation starts. Once a critical nucleus of size r^* is created, the crystal continues growing [27]. The nucleation rate is dependent on the kinetics of monomers attaching to the nucleus and hence dependent on the solution viscosity and density [28, 31].

The nucleation process controls the aggregation type. The differences between crystallization and precipitation are dependent on the level of the nucleation barrier. Precipitation occurs only for very high supersaturation. Accordingly, the critical nucleus size r^* becomes smaller than the smallest structural unit (e.g. size of a protein monomer), and the nucleation barrier disappears [27, 28]. Besides, the nucleation structure controls the structure of

the crystalline phase and subsequently the size of the crystals [30, 32].

Depending on several parameters (e.g. solution condition, supersaturation degree, temperature, additive, etc.), protein aggregation may lead to different morphologies, such as the creation of precipitate, crystals or gelation [24, 33, 34]. Precipitation is known to be spontaneous and fast. Two types of precipitate are acknowledged: amorphous precipitate and cloudy precipitate. According to [34, 35], amorphous precipitate corresponds to incomplete gelation. Gelation is the formation of network–like and associated spacious structures with increased viscosity [36–38]. Cloudy precipitate appears when LLPS takes place [35, 39]. Precipitate, in general, is associated with the loss of conformational stability of the protein monomer [36]. This results in the loss of the protein native state, and non–native aggregation occurs [14]. However, native precipitation has been observed as well [40]. Crystallization describes well–structured protein aggregation [41], and is assumed to be native aggregation [26, 42]. The nucleation steps control also the structure of the crystalline phase and the number and subsequently the size of the crystals [30, 32]. Due to the influence of solution conditions as well as environmental parameters (e.g. temperature, pressure) on the nucleation process [35, 43, 44], changes in morphology could be used as an indicator for changes in the system [45, 46]. For example, increasing supersaturation increases the nucleation rate, resulting in smaller crystals [47]. Consequently, the morphology can be used to generate a better understanding of complex processes in the solution while it is, for example, frozen.

1.3.2. Parameters affecting stability

During the production and storage of biopharmaceutical proteins, protein aggregation may occur. Changing the solution conditions during purification, like pH value, ionic strength, buffer system, and/or addition of additives, might destabilize the colloidal and conformational stability. In addition agitation stress due to pumping, stirring, or shaking influences the protein stability as well [6, 14, 24, 33, 48]. Subsequent to purification, during the formulation process the protein is concentrated. The protein concentration itself is known to influence the protein stability [24]. During storage, the long–term protein stability has to be ensured, and therefore, most of the time the protein solutions are frozen [49, 50]. These stability–affecting parameters are explained in more detail in the following.

pH value

Varying the pH value of the formulation, the protein interactions change the type and the distribution of charges on the protein surface. This affects the colloidal and the conformational protein stability [24, 33]. At pH values with a high distance to the pI, the protein is strongly charged. When the pH value is higher than the pI, the protein is charged negatively, hence in formulations with pH values below the pI the protein is charged positively, see Figure 1.5. These differences in charge influences the electrostatic interactions inside of

and between protein molecules. When the protein surface is charged similarly, protein
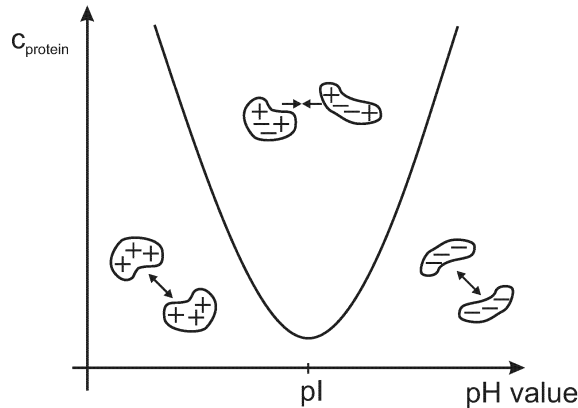
Figure 1.5.: The influence of the pH value on the surface charge of proteins (adapted from [51]).

aggregation from an energetic perspective is not preferred, and repulsive interactions take place. When the charge density is high, inter– and intra–molecular interactions increase, which results in a partial unfolding of the protein. Hence, the hydrophobicity arise at the protein surface, which increases the aggregation tendency. At the pI, the surface net charge is zero i.e., the same amount of positive and negative charges are present. This results in attractive dipole interactions. Consequently, the solubility decreases while the aggregation tendency increases [14, 33, 52].

Ionic strength

Besides the pH value, the ionic strength influences the protein stability as well. This influence is protein–dependent and differs according to the buffer systems and concentrations used in the formulation [33, 53–55]. Protein aggregation is inhibited due to the shielding of electrostatic interactions. However, a decrease in these interactions might cause protein destabilization. Subsequently, hydrophobic groups expose and lead to attractive protein interactions [14, 56].

Protein concentration

The protein stability is also dependent on the protein concentration. The distance between the protein molecules influences the strength and occurrence of protein interactions [24, 53]. Huge intermolecular molecule distances appear in diluted protein solutions. Long–range interactions are present and the protein is stabilized in the solution [57, 58]. The distance between the molecules decreases, when the protein concentration increases. Consequently, attractive short–range, van der Waals and hydrophobic interactions become significant [58, 59].

Buffer components

Buffer components are used to control the pH value of the solution, including e.g. citrate, acetate, phosphate, glycine, and Tris to adjust pH values between 2–10 [60]. Different buffer components might have an impact on the protein stability, stabilizing or destabilizing, as explained in more detail in Section 1.3.2 (Additives). This might limit the choice of the buffer system. In addition, some buffer components, e.g. Tris or phosphate are known to change the solution pH value with temperature or upon freezing, respectively [60]. The effect of freezing is explained in more detail in Section 1.3.4 (Stress types). To avoid these problems, buffer component which do not influence the protein stability and do not show temperature dependencies are preferred. In previous studies, synthetic buffer components, such as AMPSO or MES, were shown to have no impact on protein stability [61].

Additives

Additives or excipients are substances added to the formulation, next to proteins or buffer components. They are used in the biopharmaceutical industry to stabilize/destabilize the conformational as well as the colloidal protein stability [62, 63]. The common used additive classes are salts, polyols, sugars, surfactants, polymers and amino acids [14, 62–65].

The influence of these excipients is based on two theories: preferential interaction/binding and preferential exclusion/hydration [66]. When preferential interaction/binding takes place, the excipient prefers to bind to the protein surface, which results in a destabilizing effect [14, 63]. In contrast, when preferential exclusion/hydration takes place, the protein is stabilized. Here, the excipients are excluded from the proximity environment of the protein. Consequently, the protein surface is hydrated, which stabilizes the protein conformation [67–69]. Depending on the size, concentration and functional group of the excipient, preferential interaction/binding or preferential exclusion/hydration are the mechanisms of choice.

Salts influence the colloidal and conformational protein stability. The salt concentration as well as the salt type have an impact on the protein stability [14, 70]. The colloidal stability is destabilized at low salt concentrations due to the shielding of protein surface charges and covering repulsive electrostatic forces [71]. At higher salt concentrations the conformational stability might be influenced due to preferential binding of the salt ions to the molecule. This results in a decrease in the thermodynamic stability of the native conformation [14]. Depending on the salt type, the salt ion is preferentially excluded or preferentially bound to the protein molecule. Preferentially excluded salt ions stabilize the protein conformation whereas preferentially bound salt ions destabilize the protein conformation [70]. The influence of the different salt ion types is summarized in the Hofmeister series [72], and is ordered according to their ability to aggregate proteins. The Hofmeister series is split into anions and cations and is ordered according to their salting–out (increasing precipitation) or salting–in (stabilizing) effects. The order of the Hofmeister series (direct or inverse)

is dependent on different factors, like the protein charge, the salt concentration, as well as the pH value. The solution pH value influences the impact of anions on the colloidal protein stability. This is presented in the direct Hofmeister series [72]. Furthermore, the pI of the protein has an impact on the order of the series. Above the pI a direct order and below the pI an inverse order of the Hofmeister series was found [73]. It was also reported that the salt concentration has an impact on the Hofmeister series order. For example, positive macromolecules show direct Hofmeister behavior at low salt concentrations, but revert to an inverse Hofmeister series when salt concentration increases [74].

Sugars, polyols, and amino acids are known to stabilize native protein state and reduce aggregation propensity [75, 76]. Sugars and polyols are known to be preferentially excluded, which promotes conformational stability [33, 43, 69]. While stabilizing the conformational stability, the energy gap between the native and non–native state is increased [77]. This decreases the free energy, due to a self–association which lowers the colloidal stability [62]. Whereas amino acids stabilize proteins with a variety of mechanisms, either preferential interaction or exclusion, and their buffering capacity or chemical degradation prevention, like oxidation, increase the protein stability [65, 78, 79].

Surfactants (non–ionic) prevent protein aggregation due to their ability to compete with protein molecules for hydrophobic surfaces, like air–water interfaces [80]. They interact not only with hydrophobic surfaces but also with hydrophobic regions on the protein surface [81, 82]. The two frequently used surfactants are polysorbate 20 and polysorbate 80 [83].

Polymers, like polyethylen glycol (PEG) do also influence protein stability, whereas it is strongly dependent on polymer molecular weight [84] and concentration [85]. Steric shielding of attractive protein–protein interactions might induce protein stabilization, when only low PEG molecule weights and concentrations are added to the formulation. Higher molecular weight and concentrations, however, induce protein destabilization. The reason is steric exclusion of the protein molecules from the solvent occupied by PEG molecules. Consequently, the proteins are concentrated and precipitate as soon as the solubility limit is exceeded [85–87].

Additives/excipients which are used to aggregate proteins are called precipitants, e.g. sodium chloride. Some additives, called cryoprotectants, are useful to stabilize the protein against freeze/thaw stress, e.g. sucrose [88, 89] or Tween20 [90, 91].

Mechanical stress

During processing and purification, proteins are exposed to mechanical stress, including stirring, pumping or shaking. This has an influence on protein interactions and stability. Here, mainly the conformational stability is assumed to be influenced by induced shear, interfacial effects, cavitation or local thermal effects [43, 92–94].

Temperature

The surrounding temperature the protein is exposed to influences the protein conformational

and colloidal stabilities significantly. As presented in Section 1.3.1, the colloidal stability is dependent on the amount of Gibbs free energy needed to create aggregates. The conformational stability is also described by the Gibbs free energy G. The native structure of the protein is stable under physiological conditions when the Gibbs free energy is at a global minimum [95, 96]. Changing to non–physiological conditions, molecular interactions are changed, and a transition from the native to an unfolded state is favored. The Gibbs free energy is defined as a function of the enthalpy H, the entropy S, and the temperature T, see Equation 1.4.

$$G = H - T * S \tag{1.4}$$

The change of the Gibbs free energy is described by Equation 1.5:

$$\Delta G = \Delta H - T * \Delta S \tag{1.5}$$

While unfolding, the protein conformation changes. This results in a change of interactions with the surrounding water. This influences the entropy S. The entropy is low when the protein state is folded/native, since the attractive molecular interactions hold the protein atoms in a well–defined geometry. Conformational changes result in an increase in entropy due to the loss of interactions and the higher degree of freedom for each amino acid residue. While the entropy of the protein increases, the enthalpy of the solvent relatively to the folded state decreases. The reason are the compensation of the water molecules due to their ordered conformation to reduce the contact with non–polar side chains [97]. The energy due to the disruption of molecular interactions (hydrogen bonds, ionic salt bridges, and van–der–Waals interactions) and the hydration of buried groups in the native state which expose to the solvent upon unfolding, are reflected by the change of enthalpy ΔH [98].

ΔG is dependent on the temperature, according to Equation 1.4. An increase or decrease
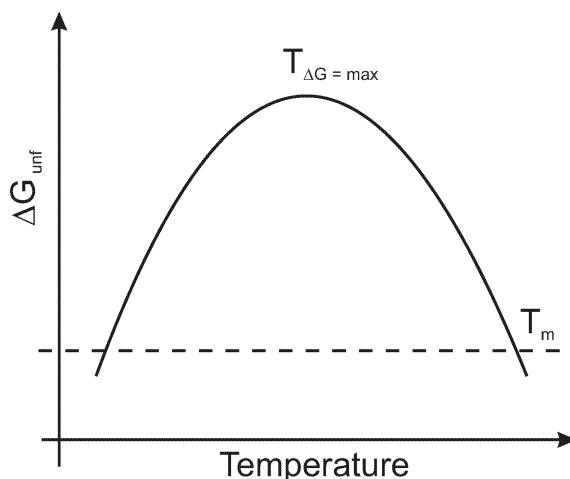
Figure 1.6.: Gibbs free energy as function of temperature (adapted from [33, 99])

in the temperature, decreases the amount of energy needed to unfold the protein (ΔG_{unf}). ΔG_{unf} describes the difference between the Gibbs free energy of the unfolded and native

state [100]. The highest value of ΔG_{unf} is reached at the temperature $T_{\Delta G=max}$ when the native state of the protein appears, see Figure 1.6 [101]. The higher the difference of the surrounding temperature to $T_{\Delta G=max}$, the lower the protein stability up to a point where the entropy term becomes greater than the enthalpy term and ΔG becomes negative, thus resulting in protein unfolding. Already small temperature changes might result in the disruption of molecular interactions [48]. It was also shown that this is pH–dependent [102]. In the two following subsections temperature increase (heating) and decrease (freezing) are presented in more detail.

1.3.3. Heating

When $T_{\Delta G=max}$ is crossed, applying heat causes protein denaturation as described in Section 1.3.2 (Temperature). However, when $T_{\Delta G=max}$ is not crossed, protein aggregates can be reversed to monomers when heat is applied [25, 33]. Only non–covalent weak protein–protein interaction can be reversed by heat [25]. To keep the proteins stable after the temperature is decreasing again, the conditions which have induced the aggregates have to be changed [5, 33] .

1.3.4. Freezing

During freezing and thawing, the protein is applied to different types of stress [103]. On the one hand, as mentioned in Section 1.3.2 (Temperature) the cold temperatures might result in cold denaturation [104]. On the other hand, freeze concentration might occur. Here, the solutes (like buffer, excipients, and buffer components) are concentrated [105–108] as a result of ice formation. Additionally, when ice crystals grow, a water–ice surface is created which might cause protein destabilization [90, 109]. To minimize the destabilizing effects, formulation, process and/or system parameters can be adjusted. In the following, the different stress types as well as different stabilizing parameters are explained in more detail.

Stress types

Cold denaturation

As mentioned in Section 1.3.2 (Temperature), low temperatures (below 0 ℃) might result in protein denaturation [104]. The cold denaturation temperature is dependent on the pH value of the solution, concentration of the protein, the presence of additives such as sugars, and pressure [102, 110–112].
While the temperature decreases Privalov and Jaenicke published that hydrophilic interactions are stabilized and hydrophobic interactions are destabilized [104, 113]. In addition, it

was assumed that only the quaternary structure of proteins is affected by cold denaturation, probably due to the ionization of essential groups which results in an unfolding of the compact structure [104]. When cryoprotectants are preferentially excluded from the protein surface, a stabilization against cold denaturation is not possible, due to preferential hydration of the protein and the creation of a "cover". The water in the "cover" starts to create even more hydrogen bonds when the temperature decreases. This supports protein unfolding [112].

Ice formation

The appearance of ice crystals causes the major change in the formulations. Due to this, other stress types are resulting e.g. the freeze concentration of solutes, which is explained in the next paragraph (Freeze concentration) in more detail. Besides, a water–ice surface is created which might lead to protein denaturation. The appearance of ice crystals is strongly dependent on the degree of supercooling and the freezing rate. Lindenmeyer *et. al* published that the ice crystal growth is proportional to the degree of supercooling [114]. When the supercooling and the freezing rate are too high, a lot of small ice crystals are created which form a huge ice surface [103]. This promotes denaturation of protein molecules on the ice surface [90, 109, 115, 116]. In addition, not only the appearance of ice crystals but also the ice structure is dependent on the degree of supercooling and the freezing rate. Fast freezing and supercooling support the growth and amount of ice dendrites, which have a high ice–surface [109, 115, 117]. However, the huge benefit of ice dendrites is the creation of interdendritic spaces. In these spaces, solutes (additives, proteins, buffer components) are trapped, and extensive freeze concentration is hindered [118]. Due to the significant influence of supercooling on the ice crystal growth, it might be beneficial to separate the cooling and freezing step from each other to simultaneously freeze the samples, show reproducibility and generate a better understanding of the cooling and freezing processes [119]. Therefore, a seeding step has to be added while cooling. Here, different seeding methods can be used. In previous studies, small ice crystals [120, 121] or chemical nucleants [122–124] were added to the supercooled sample. The addition of seeds might lead to contamination. Furthermore, the chemical nucleants are not biocompatible [119]. To avoid these problems, externally applied seeding methods are preferred. Exemplary electrofreezing, mechanical methods, shock cooling/cold spot creation, or a pressure shift can be listed here. Electrofreezing implies the application of high voltage to a metal electrode in a supercooled solution to induce ice formation [125]. Different mechanical methods, like shaking, taping, and the application of ultrasound, can be used to effectively induce ice in supercooled solutions [126].To induce ice nucleation from the outside, also a cold spot at the cryocontainer can be created from where the ice crystal growth starts. To standardize this method, commonly a step during freezing is added where the temperature is held constant below 0 ℃ for a certain time to create a nucleation plateau [119]. To create this cold spot, shock cooling can be performed. Here, the initial slow cooling ramp is changed to a rapid ramp. Thereby, a cold pot is formed at the wall of the container [127, 128]. Reducing the pressure significantly ($\sim$1 psig) also induces ice nucleation [129].

Freeze concentration

Due to ice crystal growth the solutes in solution are concentrated. This results in different effects. The concentration of the solutes, like protein, additive, buffer component, might result in aggregation of the different components. (1) Protein aggregation might take place due to the increased protein and/or additive concentration [130]. (2) Crystallization of buffer components might result in a pH shift which probably leads to a protein destabilization [103]. The appearance of buffer salt crystals is dependent on the nature and concentration of the buffer components as well as the presence of other solutes, like salt in the solution. A huge pH shift (∼3-4 pH units) was shown for sodium and potassium phosphate buffer systems [131, 132]. The temperature decrease might also cause a pH shift, but this shift is very low (<0.5 pH unit) [103]. (3) The high concentrations of proteins and additives might result in LLPS which might be created also due to decreasing temperature [35, 41, 133]. This phase separation might result in a separation of proteins and cryoprotectants which increase protein denaturation [107, 108, 134]. The appearance of LLPS is indicated by two glass transition temperatures (T_g) [105, 135–137]. And fourth due to the temperature decrease as well as the solute concentration increase the solution viscosity increases [138, 139]. Concerning the increased viscosity the protein is stabilized due to the lowered molecule moving in solutions [33].

Stabilizing parameters

The influence of the mentioned effects on the protein stability is complex and depends on formulation parameters (buffer, excipient and protein type and concentration, pH value), system parameters (freezing and thawing point, T_g, and T_{cloud} temperature), and process parameters (cycle number, freezing/thawing ramp, storage temperature and time, and volume) [41, 103, 109, 117, 133, 140]. All parameters influence each other and, therefore, all parameters have to be taken into account when a freezing/thawing step has to be included. Each parameter and the correlations to each other are explained in the following.

Formulation parameters

The formulation parameters include additives (precipitant and/or cryoprotectants), buffer system and buffer capacity, the pH value and the solute concentration. All these parameters have an influence on the degree of freeze concentration, the ice structure, and, in general, the protein stability during freezing [35, 103, 118, 130, 133].

Cryoprotectants

As mentioned in Section 1.3.2 (Additives) additives are used as cryoprotectants. They are specifically known to stabilize the protein against FT stress [33, 103, 133]. On the one hand, there are additives which stabilize the native structure of proteins, e.g. osmolytes [141–143], on the other hand, attractive protein–protein interactions are shielded, e.g. by polymers [85, 87]. Furthermore, there are excipients which prevent protein molecules from interactions with interfaces. Here, the water–air interface, the container wall as well as the water–ice interface are included. An example of these excipients are surfactants [80, 90, 91].

Buffer systems, buffer capacity and pH value

The choice of the buffer systems is even more important when an FT step is included. Because of the low temperature and freeze concentration, buffer substances might crystallize and the pH shifts during freezing, which destabilizes the protein. Phosphate buffers are known to crystallize during freezing and result in a pH shift [118, 144, 145]. The degree of the shift is dependent on the buffer capacity. The lower the buffer capacity, the lower the pH shift [103], due to the lower crystallization degree of buffer components [145]. Additives, the sample volume, and the freezing rate change the crystallization grade of buffer components and have to be taken into account when the formulation is developed for the FT step [130, 131, 145].

Solute concentrations

The initial solute concentration influences the degree of freeze concentration as well as the appearance of solute aggregation. Higher concentrations lead to a higher viscosity, a higher degree of freeze concentration, a decrease in the freezing point, and probably to a higher degree of aggregation and LLPS creation [103, 133].

System parameter

System parameters, which influence protein stability, are the freezing and the thawing point, the glass transition temperature (T_g) and the eutectic point (T_{eu}), as well as the cloud point (T_{cloud}). These points ar dependent and adjustable through formulation and process parameters.

Glass transition temperature (T_g) and eutectic point (T_{eu})

While cooling down a protein solution, depending on the temperature and solute concen-

tration different states can be reached, see Figure 1.7. The temperature, where the solution reaches a glassy state is called T_g. Here, the viscosity is so high that molecule movement is hindered, conformational changes of proteins do not take place any more [146]. Before this point is reached, the eutectic point (T_{eu}) might be crossed. Here, the components of a homogeneous mixture crystallize next to each other when the temperature is decreased. If the mixture varies from the mixture at T_{eu}, the components do not crystallize in parallel, and the component with a higher proportion than at T_{eu} crystallizes first [147]. However, the crystallization of the components is mostly hindered by the high viscosities in these systems. Due to this, T_g is concentration–dependent for concentrated solutions, while T_g is concentration–independent for dilute systems [133].
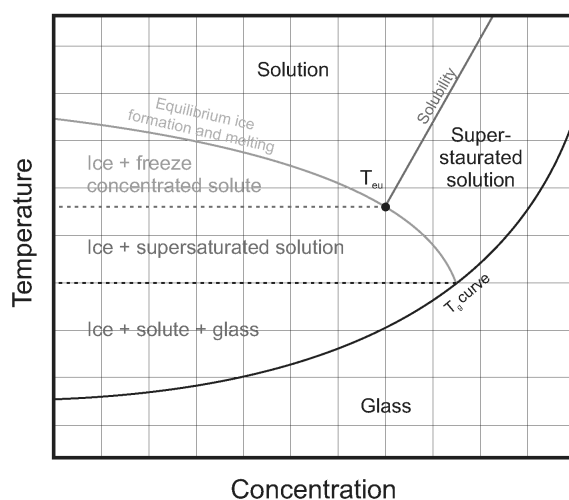
Figure 1.7.: Overview of the dependence of T_g and T_{eu} on temperature and solute concentration (adapted from [133, 148]).

Freezing and thawing points

The freezing point is defined as the point where ice crystals start to grow, and the thawing point is defined as the point where all ice crystals melt. At these points, the solution states change and next to the low temperature, a water–ice surface is created or disappears, which influences the protein stability [90, 104, 109, 115, 116]

Cloud point (T_{cloud})

The T_{cloud} temperature is defined as the temperature where LLPS takes place, as mentioned in Section 1.3.4 (Freeze concentration). LLPS formation results in a turbidity increase due to the creation of protein–rich droplets in a protein–poor liquid phase, and therefore this point is called cloud point. The formation of the LLPS is dependent on the strength of protein–protein interactions, stronger interactions lead to a shift of LLPS to higher temper-

atures [149]. Due to the dependency of T_{cloud} and protein–protein interactions, T_{cloud} was found to be a respective parameter for colloidal stability [140, 149–151]. Furthermore, this parameter might be a factor that influences protein stability during freezing and thawing due to the fact that formulations with low protein and salt concentrations show LLPS creation at sub–zero temperatures [150].

Process parameters

The process parameters, including cycle number, freezing/thawing rate, final storage temperature and time, and sample volume, influence the protein stability significantly. The optimal process is mainly formulation-, protein- and volume–dependent and must be carefully investigated. All parameters and their correlations are explained in the following.

Cycle number

Increasing the amount of FT stress applied to the sample by freezing and thawing the sample several times, e.g. during production and then for storage, the mentioned stress types described in Section 1.3.4 (Stress types) are repeated, and the protein stability might be destabilized even more [152]. Consequently, it is important to investigate which FT step is necessary and which one can be skipped.

Freezing and thawing rates

The selection of the freezing rate has a major influence on the time during which the protein is exposed to low temperatures and on the growth of the ice crystals (structure and size). Optimization of both influencing factors is not possible. To minimize the overall time, the protein is subjected to potential damage states, (receptively cross T_g) as fast as possible, the rate has to be maximized [145, 153]. This, however, that would maximize the ice crystal surface, due to the creation of many small ice crystals. Consequently, protein denaturation on the ice surface is promoted [90, 109, 115, 116]. As mentioned in Section 1.3.4 (Ice formation), the freezing speed not only influences the size of the ice crystals, but also the structure. The steeper the freezing rate, the more supercooling takes place (when there is no seeding) and the more ice dendrites are created, which maximizes the ice surface. However, the creation of ice dendrites minimizes the degree of freeze concentration [109, 115, 117].
The choice of the thawing rate is critical as well due to the period of time the protein is exposed to cold temperatures or rather in the non–glassy state (above T_g). But also, Ostwald ripening, i.e. the simultaneous ice crystal melting and growing into bigger crystals, also called recrystallization, should be avoided [118, 154].

Final storage temperature and time

The choice of the final storage temperature is important to the long–term protein stability. A storage below T_g is necessary to ensure long–term stability. Above T_g, still molecule movement is possible and consequently, long–term stability cannot be ensured [103, 133, 145, 153]. The storage of all proteins at -80 °C, no matter where T_g is, is economically ineffective due to the fact that a lot of energy is used which does not necessary ensure long–term protein stability.

Sample volume

The sample volume influences the freezing point, thawing point, degree of freeze concentration and, consequently, the crystallization grade of, e.g. buffer components. In addition, the ice crystal growth and structure, due to the creation of an ice front through the sample container, is influenced as well [130, 131, 133]. Due to the creation of this ice front, a scale–up is not trivial. The development of different FT ramps as well as the formulation might be necessary depending on the sample volume and the cryogenic device. Furthermore it is very important to take into account the shape and cooling mechanism of the cryogenic device [103, 133]. In this study, the sample volume is maximal 30 µL and, therefore, the creation of an ice front has not been taken into account.

1.4. Analytical techniques

1.4.1. Phase diagrams

For the development of the protein purification and formulation process, it is important to have information about the protein phase behavior, one the one hand, to avoid undesired phase transition during processing, and on the other hand, to apply phase transition to the purification process (e.g. precipitation). When phase transition occurs, conditions with soluble protein molecules show aggregation (or the other way around). Aggregation might result in crystallization, precipitation, gelation, LLPS, or skin formation [155]. To visualize and investigate the protein phase behavior as function of different environmental parameters (pH value, buffer system, protein concentration, additive type and concentration, and temperature), phase diagrams are created, see Figure 1.8. Usually two parameters are varied, e.g. protein concentration ($c_{protein}$) and precipitant concentration ($c_{precipitant}$), while the other parameters, like the pH value, remain constant. Further possibilities are: protein concentration as a function of temperature (see [39, 156, 157]) or protein concentration as a function of a protein interaction parameter, like the second osmotic viral coefficient (B_{22}) [155]. Consequently, phase diagrams present an option to screen the

influence of a wide range of environmental parameters to investigate the long–term protein stability. To keep the material usage and the experimental workload low, a method in a HT format with microbath experiments has been optimized by Baumgartner *et al.* and used in this study [158].

The phase diagrams used in this study are shown in Figure 1.8. The protein concentration
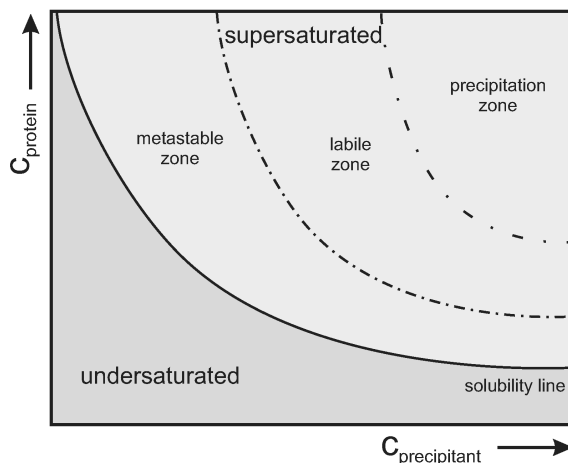
Figure 1.8.: Phase diagram with increasing protein and precipitant concentration, adapted from [41].

and precipitant concentration were varied. Thereby, two main zones are created, which are separated by the solubility line: the undersaturated and the supersaturated zone. At concentrations below the solubility line the protein stays soluble. The solubility line has to be crossed to reach phase transition and thus create protein aggregates. The solubility describes the equilibrium between aggregated and monomer proteins. Crystals appearing in the supersaturated zone are growing as along as the supersaturation in the supernatant is still high and stop when the supernatant is saturated. At this point, the crystal and supernatant composition remain constant [41, 159]. Starting with under– or supersaturated solutions, crystallization occurs when the supersaturation is high enough, and crystal growth will stop when the equilibrium between aggregated and monomer crystals is reached [160, 161](see Section 1.3.1). Then, the supernatant of crystalline solution is saturated and the protein concentration in the supernatant thus reflects the protein solubility [41, 162, 163]. Based on this, the solubility line can be determined when performing micro–bath experiments. Galm *et al.* developed a method to determine the solubility line by measuring the protein concentration in the supernatant of crystalline suspensions after 40 days [164]. This method was also used in this study, to combine HT microbatch protein diagram experiments with the determination of solubility lines.

When the solubility line is crossed, the supersaturated zone is created and protein crystal-lization, precipitation, and other phase transitions occur [41, 159]. The driving force for this phase transition is a thermodynamic imbalance, because of unfavorable interactions between the solvent and exposed side chains which are minimized by attractive protein interactions, which is also referred to as supersaturation [13, 14]. This zone is split into three zones: the metastable zone at the border to the undersaturated zone, the labile

zone, and, at very high supersaturation, the precipitation zone. In the metastable zone, no crystals are created, but existing ones will grow. In the labile zone, crystal formation and growth occur. Precipitate is created in the precipitation zone [27], see also Section 1.3.1.

1.4.2. Solubility line (SL)

The solubility line describes the equilibrium between monomer and aggregated protein molecules. The more the equilibrium is shifted towards monomer protein molecules, the higher the protein solubility in the respective formulation. To investigate the solubility line, the supernatant of crystalline solutions was determined. The supernatant of solutions where crystals grow is saturated and, therefore, the measured concentrations reflect the protein solubility [41, 162, 163]. According to the method published by Galm *et. al* [164], to calculate the solubility line (SL) the supernatant concentrations for each salt concentration are averaged, due to the fact that the initial protein concentration does not influence the supernatant concentration of conditions where crystals have grown [41]. The averaged values are fitted using Equation 1.6:

$$S_{sol} = S_0 + A \cdot e^{R_0 \cdot c_{salt}} \tag{1.6}$$

Here, S_{sol} is the protein solubility, S_0 is the theoretical protein solubility when nothing is added. A and R_0 are variable parameters, and c_{salt} describes the used salt concentration. The determined SLs can then be used to compare different phase diagrams to each other regarding their protein solubility [164]. Furthermore, the protein solubility is described in many publications to directly correlate to protein–protein interactions [165–168]. Consequently, no change in the solubility lines implies no influence on protein–protein interactions.

1.4.3. Dynamic light scattering (DLS)

To monitor the colloidal protein stability in the formulations, DLS measurements were performed. The Brownian motion of protein molecules results in scattered light fluctuation which is monitored over time using DLS [169]. These fluctuations over time correlate to the particle size. Using the decay rate (Equation 1.7, q = wave vector) and the Stokes–Einstein equation (Equation 1.8), the translational diffusion coefficient (D_t) and hydrodynamic radius (R_H) can be calculated, respectively.

$$\Gamma = q^2 D_t \tag{1.7}$$

$$D_t = \frac{k_b * T}{6\pi * \eta * R_H} \tag{1.8}$$

The decay rate Γ describes the analysis of the auto correlation of the fluctuation of the scattered light intensity, namely the similarity of the function to itself after a certain time increment. Smaller particles diffuse faster and the light fluctuation function is only shifted slightly before it does not correlate to itself any more. Consequently, the decay rate Γ is small. For bigger molecules it is the other way around. Using the Stokes–Einstein equation (Equation 1.8) to calculate the hydrodynamic radius R_H, the viscosity η, the temperature T, and the Boltzmann constant (k_b=1.281 $* 10^{-23}$[J/K]) have been taken into account [169–171]. Besides these parameters, protein–protein interactions also influence R_H [172]. Attractive interactions reduce the movement in the solution and therefore a bigger R_H is calculated. Therefore, DLS measurements calculate more an apparent R_H for non–diluted formulations [173]. For this work, the appearance of only large protein species was taken into account.

1.4.4. Fourier transform infrared spectroscopy (FTIR)

Using FTIR, the unique stretch vibrations or molecular bonds are used to identify the secondary structure, like α–helix, β–sheet, or β–sheet anti parallel (see Section 1.1) [174]. The stretch vibrations are induced by the infrared radiation absorbance, and are a result of changes in dipole moments of molecular bonds. Here, the carbonyl group (C–O) shows the most distinct stretch vibration for proteins [175, 176]. These changes are measured in a wavenumber range from $1700\,\mathrm{cm^{-1}}$ to $1600\,\mathrm{cm^{-1}}$, also called the Amide I band [177]. In accordance with the position of the carbonyl groups' differences between the different structures and, therefore, within the Amide I, band each secondary structure corresponds to a specific range: α-helix (1650 - $1685\,\mathrm{cm^{-1}}$), β-sheet (1615 - $1635\,\mathrm{cm^{-1}}$), and β-sheet anti parallel (1670 - $1685\,\mathrm{cm^{-1}}$).

2. Research Proposal

The production of recombinant proteins is complex and split into an upstream (USP) and downstream (DSP) part. Within USP the product is produced by e.g. modified bacteria or cells. In DSP and formulation the product is purified and formulated for the final application to the patient. DSP exists out of several purification steps using chromatography, virus inactivation, and buffer exchange steps. During production, purification, storage and transportation the protein stability has to be guaranteed [6]. To prolong protein stability throughout these steps the solution is frozen and when needed thawed again. Even when there is no bottleneck within the production process, for storage and transportation products are often frozen to increase the shelf life [133]. The development and optimization of the FT step is dependent on formulation parameters (pH value, buffer system and capacity, additives, solute concentration), system parameters (glass transition point T_g, freezing and thawing point, cloud point temperature T_{cloud}), and process parameters (freeze and thaw ramp, storage temperature, storage time, cycle number, volume) [103, 133]. To characterize the effect of the FT step concerning the protein stability, different analytical methods are used to investigate short– and long–term protein stability. These analytical methods include for example SEC to determine protein size, UV-vis spectroscopy to identify protein concentration, osmolality and pH value to determine the solute distribution of additives and buffer components, and activity assays to study protein activity [152, 178]. Furthermore, the appearance of T_g and T_{cloud} is identified, by differential scanning calorimetry (DSC) or refractometry, respectively [179–181]. However, these methods are expensive, complex and time consuming, due to the often missing ability of HTSs, and data handling. Furthermore, to find a correlation between induced stress and protein properties is often not obvious and straight forward. In addition, to study the long–term stability samples have to be stored over at least 18-24 months [3, 4]. To speed up the characterization of the formulation step regarding long–term protein stability, the creation of phase diagrams can be used to indicate the influence to different formulation parameters [158]. In addition, these observation can be correlated to short–term parameters like viscosity, rheological behavior, and structure changes [164, 182–185]. Missing however, is the investigation of the influence of temperature to the phase behavior.

This work focusses on the investigation of FT stress–induced instabilities using phase diagrams. Here, the flexibility of phase diagrams is used to study the influence of formulation parameters, which can be varied while the phase diagram is created, and process parameters, which can be varied while handling the phase diagram. In addition, the setup of the freezing and thawing is used to determine system parameters in parallel. By

doing so a toolbox will be generated where a simple, time–saving HT screening of different formulation and process parameters and the detection of system parameters is possible to generate a larger understanding of the influence of freezing/thawing on long–term protein stability. As a consequence, the present work concentrates on three subsections dealing with the development, verification and extension of a phase diagram–based method to enable access to a better understanding of the influence of formulation, process, and system parameters on the long–term protein stability when freezing and thawing. In addition, the fourth subsection focussed on the reversibility of the FT stress–induced instabilities as function of cryoprotectants.

The first subsection aims on the development of a phase diagram–based method to investigative the influence of FT stress. The phase behavior [41, 158], the crystal morphology [35], and the solubility line [164] are known to be sensitive to environmental changes. Hence, the evaluation of FT stress–induced instabilities focusses on these parameters. Next to the method development, the study deals with the influence of different formulation parameters, like buffer systems and pH value, on the long–term protein stability while freezing and thawing. Furthermore, the influence of the different formulation parameters will be studied as function of the process parameter cycle number. In order to verify the possibilities of the developed method, the second subsection aims on the influence of varying process parameters due to the known influence of e.g. the freezing rate on the protein stability [103, 133].

Next to the influence of the formulation and process parameters on the protein stability, the position and appearance of the above listed process parameters, like T_g or T_{cloud}, are known to affect protein stability [133]. Hence, the third section aims to extend the developed method by the possibility to detect T_{cloud} in parallel using video analysis while the plates are frozen/thawed. Here, the ability to find a correlation between short–term parameter T_{cloud} and the protein long–term stability influenced by FT stress will be investigated. Based on the correlations between short–term and long–term protein stability made before using the protein structure, solution viscosity or the rheological behavior [164, 182–185], it is also figured out whether T_{cloud} is also a suitable parameter for such correlations. In addition, the method extension will be validated by the influence of different additives.

Even when instabilities are induced by FT stress the fourth subsection aims a method to reverse these instabilities. Reversibility of protein aggregates by e.g. heat is well known, whereas the aggregate type is important (reversible/irreversible, strength of protein–protein interactions) [13, 25, 26, 33, 43]. The reversibility of aggregates in this study will be investigated as function of different cryoprotectants. In addition, again a correlation between short–term parameters (size and structure) and long–term protein stability is aimed, influenced by FT.

In summary, this work aims to develop a phase diagram–based methodology to investigate FT stress–induced protein instabilities, in which the parallel research of formulation and process parameters as well as the detection of a system parameter is possible. Furthermore, a possibility to reverse FT stress–induced protein instabilities will be presented. In any experimental method the sample volume will be minimized in order to save product consumption. Furthermore, the potential of HT methods will be used, whenever possible, to reduce time consumption. As method development and applicability are protein con-

suming, the model protein lysozyme from chicken egg white will be used. Nevertheless, the developed method can be transferred to any biopharmaceutical protein of interest, such as monoclonal antibodies.
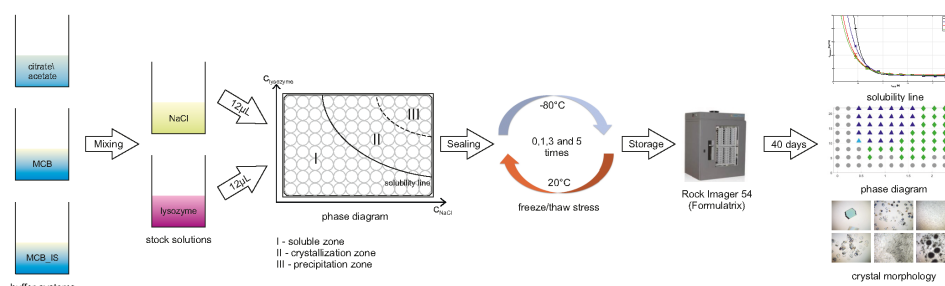
3. Comprehensive Overview of Publications

Chapter 4: Analysis of phase behavior and morphology during freeze/thaw applications of lysozyme

Anna K. Wöll, Juliane Schütz, Jana Zabel, Jürgen Hubbuch

This article present the development of a toolbox to investigate FT stress. The influence of different formulation parameter – buffer system, buffer capacity and pH value, in combination with varying the process parameter – number of FT cycles – were investigated. Therefor, to determine the long–term stability of lysozyme, phase diagrams were created by using the method published by Baumgartner *et al.* [158]. These phase diagrams were stressed up to five times with the following FT protocol: freezing for 30 minutes in a -80 °C freezer and thawing for 30 minutes at 20 °C in an incubation chamber. As reference an unstressed plate fo each formulation was prepared. Afterwards, the long–term protein stability was evaluated by determining the protein solubility, the phase behavior and the crystal morphology. The buffer systems and the pH value had an influence on the degree of FT stress–induced instabilities. The formulations were more stable at pH 5, whereas the buffer systems with acetate and citrate showed more instabilities compared to the multi–component buffer (MCB) buffers. Increasing the number of FT cycles resulted in a decrease of the soluble zone and crystal size, and the appearance of sea urchin crystals in the high concentrated region.

Chapter 5: A phase diagram–based toolbox to assess freeze/thaw ramps on the phase behavior of lysozyme from chicken egg white

Anna K. Wöll, Monika Desombre, Lena Enghauser, Jürgen Hubbuch
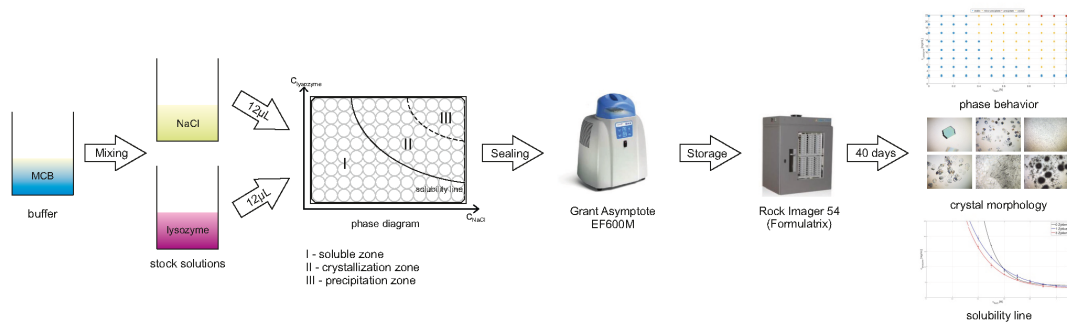
In this study, the developed method presented in Chapter 4 was extended by varying the process parameters such as freezing/thawing ramp and number of FT cycles, whereas the formulation parameters were kept constant using a MCB at pH 5. Different freezing ramps with constant thaw ramps, as well as the other way around, were tested to investigate the destabilizing freezing and thawing effects separately. Besides, combination of the best and worst ramps were investigates as well. To do so the created phase diagram were placed on a cryogenic device, where it was able to adjust the respective ramps. To evaluate the differences between the ramps, the long–term protein stability of lysozyme was determined by checking the protein solubility, the phase behavior, and the crystal morphology. Freezing ramps had a more significant impact on the long–term stability of lysozyme than thawing ramps. Whereas, fast freezing resulted in less instabilities. The influence of the cycle number seen in Chapter 4 could be verified in this study.

Chapter 6: Application of a cryogenic device for high-throughput low volume sub-zero cloud point temperature determination by means of automated video analysis

Marieke Klijn[1], Anna K. Wöll[1], Jürgen Hubbuch

[1] These authors contributed equally to this work
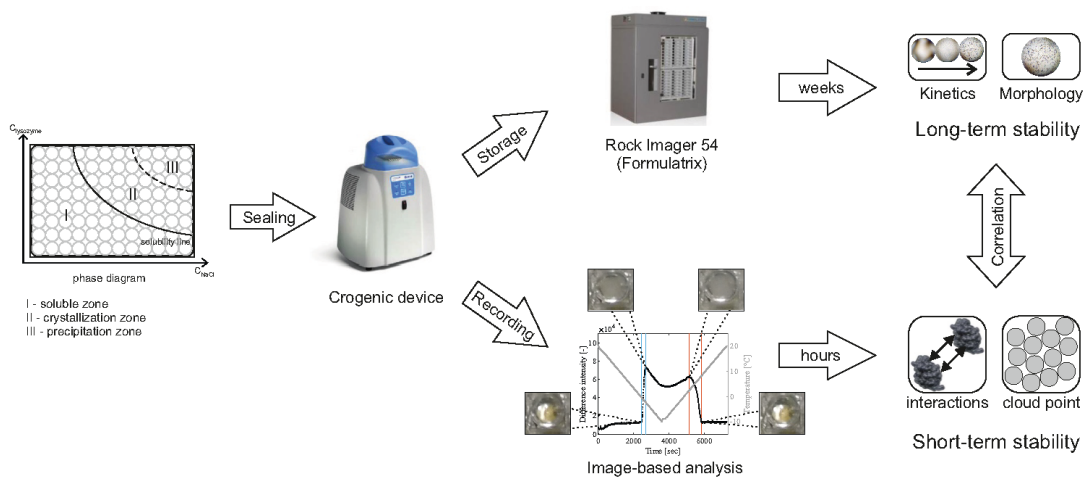
This publication presents an expansion to the developed method (see Chapter 4 and 5) to determine the system parameter – cloud point (T_{cloud}). The image-based method with an automated image acquisition system was evaluated by means of robustness, validation and a case study. The robustness study showed that the point detected (T_{CE}) with the developed method represents T_{cloud}. The applicability of this parameter was verified in the validation study where eight lysozyme concentrations were measured and compared to literature data. In the case study the correlation between T_{cloud} and the long–term stability of lysozyme was evaluated. Thereby the influence of the lysozyme concentration, the ion type, the ionic strength and FT stress were studied. A partial correlation could be established. Formulations which showed long–term instabilities showed also an increasing T_{cloud} value by increasing the supersaturation. Ammonium chloride formulations were sensitive to FT stress and showed higher T_{cloud} values compared to formulations which stayed stable over time, even when FT stress was applied.

Chapter 7: Investigation of the reversibility of freeze/thaw stress-induced instability using heat cycling as a function of different cryoprotectants

Anna K. Wöll, Jürgen Hubbuch

This manuscript aims to investigate the reversibility of FT stress–induced instabilities of lysozyme by the application of heat (40 °C) as a function of different formulation parameters – cryoprotectants (sucrose, glycerol, PEG200, and Tween20). In addition, a process parameter – number of FT cycles, was varied as well. Phase diagrams were created to investigate the long–term stability and additionally short–term stability analysis were performed. Therefor, the colloidal and conformational protein stability were studied, by performing DLS (size) and FTIR (structure) measurements. All formulations containing additionally cryoprotectants were compared to formulations including only NaCl. The phase behavior, protein solubility, aggregation kinetics, and crystal morphology differed between the formulations with and without any stress (freezing/thawing or heating). All formulations showed FT stress–induced instabilities, which increases with a higher number of FT cycles. The degree of instabilities were dependent on the cryoprotectant, as well as the degree of reproducibility. Sucrose and glycerol showed a significant stabilization effect regarding FT stress and the degree of reproducibility by heat was very high. Nearly the same behavior, solubility and crystal morphology could be reached compared to the formulations where no stress was applied.

4. Analysis of phase behavior and morphology during freeze/thaw applications of lysozyme

Anna K. Wöll, Juliane Schütz, Jana Zabel, Jürgen Hubbuch*
*Corresponding author. E-mail address: juergen.hubbuch@kit.edu

Karlsruhe Institute of Technology (KIT), Institute of Process Engineering in Life Sciences, Section IV: Biomolecular Separation Engineering, Karlsruhe, Germany

Abstract

Knowledge of protein behavior/stability during FT operations is essential for storage and production processes in the biopharmaceutical industry. FT stress involves freeze concentration, cold denaturation, and ice crystals formation which can result in protein aggregation. Therefore, it is important to understand the ongoing FT processes, and the influence of different solution parameters. In order to evaluate the ongoing processes during FT (up to -80 ℃), phase diagrams with lysozyme from chicken egg white and sodium chloride were generated. Thereby, three different buffer systems with varying buffer substances and ionic strengths at pH 3 and pH 5 were investigated. As indicators for the ongoing FT processes, the phase behavior, crystal morphology and solubility were used. An increased number of cycles led, for example, to the formation of micro crystals, sea urchin crystals – indicating LLPS and/or high supersaturation – and precipitate. Furthermore, the buffer substances had a more distinct influence on the phase behavior and morphology compared to the ionic strength differences. The solubility line itself was only shifted when distinct changes in the phase behavior could be observed. In summary, a tool was developed for using the phase behavior and especially the crystal morphology as indicator for underlying processes during FT operations.

Keywords: *phase diagrams, temperature, cycles, sodium chloride, precipitant*

30

4.1. Introduction

Stability of biopharmaceutical proteins during and after the production process is essential. Important factors of impact on protein stability are mostly chemically (pH, additives, etc.) and mechanically induced stresses (pumps, lines) [33, 48]. In order to increase stability and enable long–term storage or transportation, protein solutions are often frozen down to -20 or -80 °C and thawed again prior to use [49, 50]. During such freeze/thaw (FT) operations, both chemical and physical stress is experienced by the protein in solution. While the underlying processes leading to such stress are known, only a complex analytical toolbox allows its detection. These underlying processes occurring can be grouped into three clusters, namely cold denaturation [104], freeze concentration [105–108], and ice crystal formation [90, 109]. Cold denaturation describes the process of structural denaturation of the protein due to cold temperatures. Privalov found that this process only affects the quaternary structures of proteins [104]. During freeze concentration, water ice crystals grow and the soluble solutes become concentrated. This includes the protein itself, buffer components, and additives. A concentration of protein or additives may result in supersaturation [186]. The formation of ice crystals during freezing may also cause LLPS [35, 133], meaning the demixing of the solution due to high concentrations (concentration–induced) and/or low temperatures (temperature–induced). Thereby, LLPS might lead to a change in concentration of formulation excipients or even a shift of the pH value [187]. Finally, ice crystal formation, in particular the water–ice–interface, can have destabilizing effects on the protein due to denaturation at this interface [109].

As mentioned, the FT stress introduced might have an influence on the protein stability [178, 188]. In this context, a distinction has to be made between colloidal and conformational stability. In general, it can be differentiated between two different types of aggregation, a fast unstructured – leading to precipitate – and a slow well–structured – leading to crystals – aggregation [41]. Thus, depending on system composition or changes within the system, different types and morphologies of crystals appear. One key point is the actual concentration of protein in the liquid phase of the system. If supersaturation is low, spontaneous nucleation does not take place within a reasonable time frame, and well–ordered stable crystals grow best [45]. At higher supersaturation, spontaneous nucleation within the crystallization/labile zone occurs. With the supersaturation increasing even more, the energy barrier is easily overcome, and a precipitation zone is created [41, 186]. The whole nucleation and growth process is further depends on parameters such as solution conditions, the sample preparation, and the sample history [35, 43, 44]. Thus, alterations in morphology might be used as an indicator for changes occurring in the system investigated [45, 46]. As an example, the typical morphology of lysozyme crystals with sodium chloride (NaCl) as precipitant can be described as tetragonal [189]. An increase in protein concentration might lead to a higher nucleation rate, which in results in a decrease in the crystal size. Small tetragonal and micro crystals grow [47]. Furthermore, the creation of temperature– or concentration–induced LLPS favors the growth of micro crystals [186]. Increasing the level of stress and/or supersaturation results in the growth of the so–called flower crystals,

needle crystals, and sea urchin crystals. The needle crystals are unstable polymorphs and are slowly converted into tetragonal crystals [190]. For the growth of sea urchin crystals, additionally LLPS and a very high supersaturation are necessary for needles growing fast out of the nucleation center [35, 191]. If the growth process is too fast, because of a excessive supersaturation, unstructured precipitation takes place [41].

Solubility as a general parameter is normally determined by supernatant measurements of samples where crystals occur or co–occur, and the protein in the supernatant reflects the protein solubility [41, 162, 164]. A shift in the overall solubility zone thus marks the stability/instability of the respective system.

As mentioned above, morphology, and the parameters influencing the crystal shape, such as supersaturation and LLPS, are sensitive to a whole set of parameters. On the one hand to solution conditions, e.g. salt and protein type and concentration, and further additives as well as the pH value and ion strength (IS) [35, 43–45, 151, 192–194]. On the other hand to stress factors like FT [103]. In general, a toolbox of analytics is available to gain some insight into processes occurring during FT operations such as size exclusion chromatography, micro–flow image processes, activity assays, or dynamic light scattering [24, 178, 195, 196]. Missing however are a holistic view on systems and the use of an easily accessible signature to identify and describe the stability of given systems in potentially ongoing processes during FT applications.

In this work, a phase diagram–based tool is developed to use the analytically easily accessible phase behavior, the crystal morphology, and the solubility as indicators for system stability and ongoing processes during FT applications. The applicability of the tool is shown for the cases of changing buffer compositions, pH values, protein and precipitant concentrations as well as for the number of FT cycles.

4.2. Materials and methods

For investigation of the impact of FT cycles on the phase behavior of lysozyme from chicken egg white, phase diagrams are generated using different buffer systems at pH 3 and pH 5. Additionally, a reproducible FT method has been established. In all studies, a protein concentration of up to 21.75 mg/mL and NaCl concentrations of up to 2.5 M were used. In the following, the preparation of buffers, protein solution, and the creation of the phase diagrams are described. Furthermore, an explanation of the FT protocol can be found in this section.

4.2.1. Preparation of stock solutions

Three different buffer systems were used in this study. We employed common 100 mM *citrate/acetate* buffer solutions. The relative buffer components were citric acid (Merck
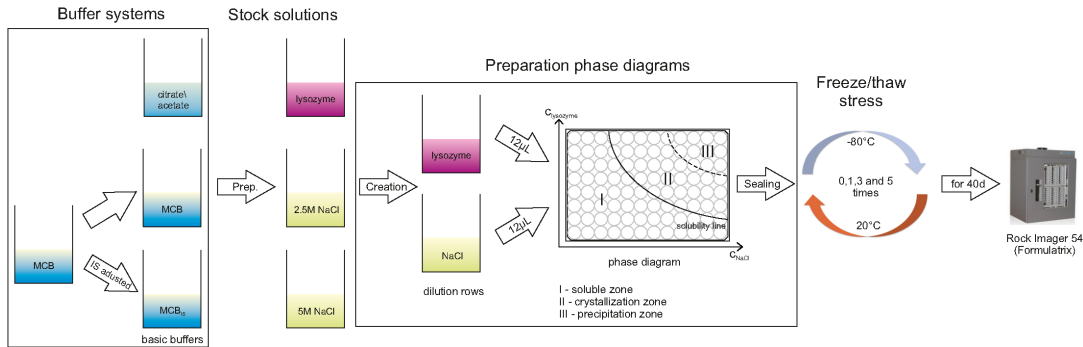
Figure 4.1.: Schematic visualization of the method used.

KGaA, Darmstadt, Germany) and trisodium citrate (Sigma–Aldrich, St.Louis, MO, USA) for pH 3, and for pH 5 acetic acid (Merck KGaA) and sodium acetate (Sigma–Aldrich). In addition, a 20 mM *multi–component buffer* (*MCB*) system was used. The preparation differs. Both *MCB* were created for a pH range from 3 to 9 using the tool published by Kröner *et al.* [197]. For both *MCB* systems, the following buffer components were used: AMPSO (Sigma–Aldrich), TAPSO (Sigma–Aldrich), MES (AppliChem GmbH, Darmstadt, Germany), formic acid (Merck KGaA), and D–(+)–malic acid (Sigma–Aldrich). An overview of the tested buffer systems is shown in Table 4.1. Besides the basic buffer without any NaCl, for all buffer systems, two salt buffers were prepared in addition, the low–salt buffer with 2.5 M NaCl (Merck KGaA) and the high–salt buffer with 5 M NaCl (Merck KGaA). An schematic overview of the buffer systems, the basic buffers, and the stock solutions is shown in Figure 4.1.

The pH was controlled and adjusted by means of a five–point calibrated pH meter

Table 4.1.: Buffer systems

buffer system	pH	buffer capacity [mM]	NaCl conc. [M]	conductivity [mS/cm] pH 3	conductivity [mS/cm] pH 5
citrate	3		0	3.3	-
			2.5	156.6	-
			5	182.5	-
		100	0	-	4.6
acetate	5		2.5	-	156.7
			5	-	208.6
MCB			0	1.541	5.144
			2.5	151.9	171.6
			5	193.9	221.9
	3; 5	20	0	10.86	10.25
MCB$_{IS}$			2.5	153.8	176
			5	193	224.4

(HI–3220, Hanna® Instruments, Woonsocket, RI, USA) equipped with a SenTix® 62 pH electrode (Xylem Inc., White Plains, NY, USA). The titration to the desired pH value was done with NaOH or HCl (Merck KGaA). On the day the preparation was made, the pH was adjusted to a value differing by up to ± 0.2 pH units from the final pH value. After one day, the buffer pH of the basic buffer was adjusted to the respective final pH value with an accuracy of ± 0.02 pH units. For the MCB_{IS} system, additionally the ionic strength (IS) was adjusted with NaCl (Merck KGaA) to 10.08 mS/cm with an accuracy of ± 1 mS/cm at 24 °C ± 1 °C by using the conductivity meter CDM 230 (Radiometer analyticals, Lyon, France) and the four-point calibrated conductivity cell E61M014 (Radiometer analyticals, Lyon, France). After filtration with a $0.2\,\mu$m membrane consisting of Supor® Polyethersulfone (PES)(Pall Corporation, Port Washington, NY, USA), the buffers were stored at room temperature and were used for up to two weeks after preparation. Additionally, a pre-test with all basic buffers at both tested pH values was performed. Therefore, the liquid universal pH indicator UNISOL 113 (VWR, Radnor, PA, USA) was added to the buffer (ratio 1/250), and the solution was frozen to -80 °C The colors of the buffers were checked before and while freezing, and after thawing.

The lyophilized protein lysozyme from chicken egg white (Hampton Research, Aliso Viejo, CA, USA) was weighted and dissolved in the basic buffer of the corresponding buffer system. The protein solution was filtered through a $0.2\,\mu$m syringe cellulose acetate filter (VWR, Radnor, PA, USA). For the removal of production–related additives, a desalting step with PD–10 (GE Healthcare, Uppsala, Sweden) columns was performed by using the spin protocol [198]. The concentration was controlled by a NanoDrop™ 2000c UV–Vis spectrophotometer (Thermo Fisher Scientific, Waltham, MA, USA). An extinction coefficient of $E^{1\%}(280\,\text{nm}) = 22.00\,\text{Lg}^{-1}\text{cm}^{-1}$ was used. To generate one phase diagram, 1 mL stock solution with a concentration of 43.5 mg/mL $\pm$ 1 mg/mL was needed. The protein stock solution was prepared freshly every time and was not used for more than one day.

4.2.2. Phase diagrams

Phase diagrams with lysozyme concentrations between 2.5 and 21.75 mg/mL and NaCl concentrations between 0 and 2.5 M at pH 3 and pH 5 were created applying the method published by Baumgartner *et al.* [158]. A Freedom EVO® 100 fully automated liquid handling station (Tecan Group Ltd., Männedorf, Switzerland) equipped with fixed tips and 250 μL dilutors was used. It was controlled by Freedom EVO® 2.4 SP3 (Tecan Group Ltd.). Both NaCl and protein concentration rows were prepared with the liquid handling station. Therefore, the stock solutions of protein with 43.5 mg/mL and NaCl buffers with a concentration of 2.5 M and 5 M NaCl were placed onto the liquid handling station platform. The dilution rows were mixed in a Deepwell PP plate (Greiner Bio–one, Frickenhausen, Germany). Afterwards, the phase diagram was generated by mixing 12 μL protein with 12 μL of the respective buffer in a MRC Under Oil 96 Well Crystallization Plate (SWISSCI AG, Neuheim, Switzerland), schematically shown in Figure 4.1. To avoid evaporation, the plate was sealed with Duck® Brand HD Clear sealing tape (ShurTech® brands, Avon, OH,

USA). Before the phase diagrams were placed in the incubation chamber RockImager54 (Formulatrix, Bedford, MA, USA) at 20 °C for 40 days, they had to pass the respective FT protocol, which is described in the next section. During the 40 days, pictures were taken from each well automatically and were scored after 40 days concerning phase states and morphology. Whereas the magnitude was the same for the whole scoring.

4.2.3. Freeze/thaw method

From each buffer system, four plates were created. One of them was directly placed in the incubation chamber, the other plates were frozen and thawed one, three or five times. For freezing, they were placed into the -80 °C freezer (Skadi by Telstar, Terassa, Spain) for 30 min. Subsequently, the thawing took place under temperature–controlled conditions at 20 °C for another 30 min in the temperature cupboard WBK200/120 (Mytron, Heilbad Heiligenstadt, Germany). If a higher cycle number was performed after the thawing, the phase diagram was directly placed in the freezer. After the respective number of cycles, the plates were placed into the incubation chamber at 20 °C and the phase behavior developing over 40 days was monitored (see Figure 4.1).

4.2.4. Solubility line

After 40 days, the supernatant of each well was measured in triplicate with the NanoDrop™ 2000c to evaluate the solubility line. Therefore, $3 \mu L$ of the supernatant were carefully pipetted on the NanoDrop™2000c. Attention was paid not to pipette visible aggregates. To evaluate the solubility line, the method described by Galm *et al.* was used [164]. The averaged values from the measurements were fitted using Eq. 4.1, where S_{sol} is the protein solubility, S_0 is the theoretical protein solubility for 0 M NaCl, A and R_0 are adaptable parameters, and c_{NaCl} describes the NaCl concentration.

$$S_{sol} = S_0 + A \cdot e^{R_0 \cdot c_{NaCl}} \tag{4.1}$$

It is known that the supernatant concentrations of conditions where crystals grew are always around the same value no matter which initial protein concentration was chosen [41]. This being said, when precipitation occurs, the initial protein concentration has an influence on the supernatant measurement [199]. Nevertheless, in this work, the supernatant concentration of conditions with crystals, and combinations of crystals and precipitates were taken into account for the solubility line.

4.3. Results

The general goal of this study is the evaluation of different systems varying in the spread and occurrence of their solubility, crystallization and precipitation zone as well as in the morphology of the underlying aggregation as a function of FT cycles. To evaluate the phase behavior and influencing factors of lysozyme after FT operations with NaCl as a precipitant, three different buffer systems at pH 3 and pH 5 and increasing numbers of FT cycles (FT cx; x = 0, 1, 3, 5) were investigated. The tested buffer systems differed in their buffer components and ionic strength (IS). All in all, 24 phase diagrams were created and in the following, the results concerning the solubility line, the phase behavior, and the aggregate morphology are presented.

4.3.1. Solubility line

The changes of the course of the solubility line and thus spread of the solubility zone were investigated and are shown in Figure 4.2 at pH 3 and pH 5. The solubility lines were calculated from supernatant measurements according to Eq. 4.1 (see Section 4.2.4). For each curve, the associated parameters are listed in the Supplementary material, Table B.1.

pH 3

Generally, highest solubility is seen for FT c0. For the *citrate* system, a slight change of the solubility line between two subsequent cycles is mainly seen between FT c0 and FT c1. The *MCB* system showed the strongest variations both between FT c0 – FT c1 and FT c1 – FT c3 – FT c5. For the $MCB_{IS,pH3}$ system, a solubility line could be only created for the initial system at FT c0.

pH 5

At pH 5 with the *acetate buffer*, a shift in the region lower than 0.91 M NaCl could be detected. The lines of FT c1 and FT c3 are shifted to lower protein concentrations, while FT c0 and FT c5 were nearly identical. Due to the difference of only one measurement point at each line, the shift is not really informative and should be handled carefully. With the MCB_{pH5} system small differences are detectable, see Figure 4.2. Only with the $MCB_{IS,pH5}$ system, a clear shift from FT c0 to FT c1 is pictured in Figure 4.2. The other cycles did not show a further shift to lower lysozyme concentrations.
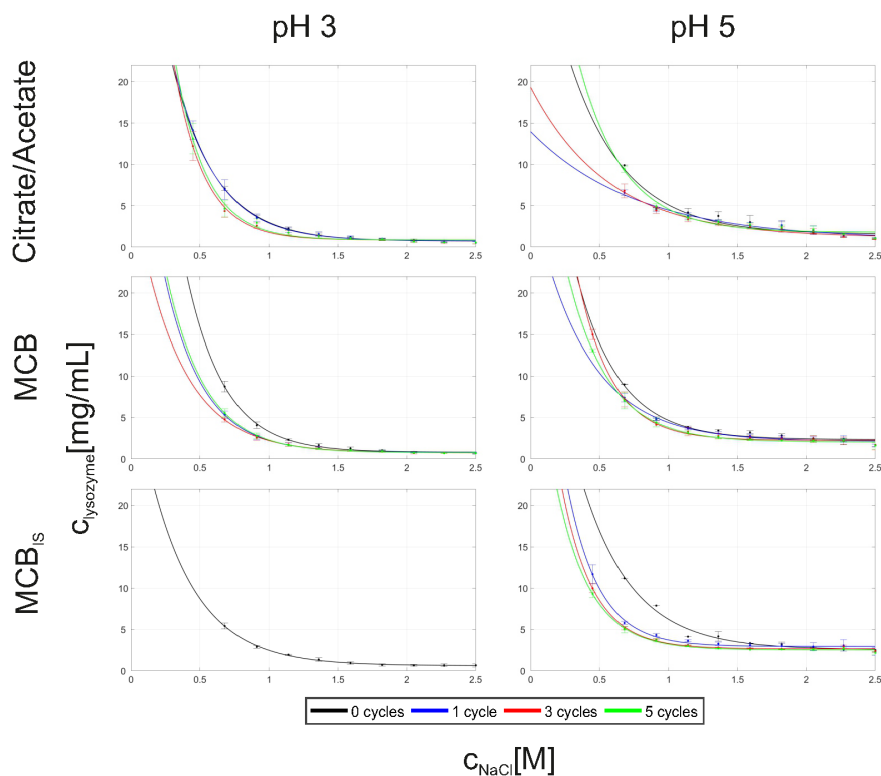
Figure 4.2.: Solubility line of all tested buffer systems at pH 3 (left) and pH 5 (right) at different cycle numbers. The solid lines are fitted as described by Galm *et al.* [164], and the fit parameters are listed in the supplementary material.

4.3.2. Phase behavior

The phase diagrams for the different buffer systems and pH values are shown in Figure 4.3 for pH 3 and Figure 4.4 for pH 5. In general, pH 3 is characterized by a variation of crystallization, co-precipitation and precipitation zones. At pH 5, most of the phase diagrams obtained are characterized by pure crystallization zones.

pH 3

At pH 3, differences between the tested buffer systems could be seen and are described in the following.

Citrate buffer

In general, at FT c0, complete lysozyme solubility was seen for NaCl concentrations at and

below 0.45 M. Following at FT c1, all NaCl concentrations at and below 0.23 M showed complete lysozyme solubility. For increasing NaCl or lysozyme concentrations, a typical transition curve of the soluble systems is obtained showing a balance between precipitant agent and protein concentration. For the lowest lysozyme concentration tested (2.5 mg/mL), complete solubility decreased as a function of FT cycle carried out, ranging from 1.59 M (FT c0) to 1.14 M (FT c1) and 0.91 M (FT c3) through to 0.68 M (FT c5) NaCl, see Figure 4.3 (A left). The aggregation zone was mainly characterized by a large crystallization zone and
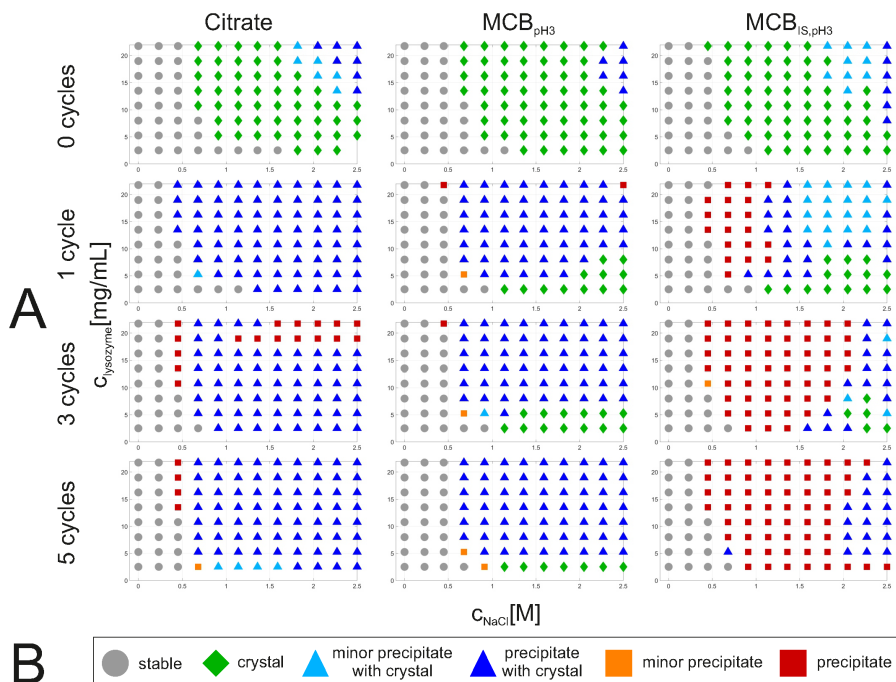
Figure 4.3.: In A, the phase diagrams of all tested buffer systems without and with FT stress at pH 3 are shown. The column on the left shows the phase diagrams of the *citrate* buffer. In the column in the middle, the phase diagrams of the MCB_{pH3} system and in the column on the right, the diagrams of the $MCB_{IS,pH3}$ system are shown. B represents the appropriate legend.

only showed an increasing co-precipitation at high lysozyme and NaCl concentrations. No pure precipitation zone could be observed. After FT c1, this picture changed so that the majority of systems are now characterized by co–precipitation for all cycles up to FT c5. Scattered systems showing only light co-precipitation at low lysozyme concentrations and a small pure precipitation zone at FT c3 and FT c5 were observed. These precipitation zones occurred either at high lysozyme concentrations (FT c3) or low NaCl concentrations (FT c3, FT c5), see Figure 4.3 (A left).

$MCB_{pH\,3}$ *system*

At FT c0 lysozyme showed a solubility zone for NaCl concentrations at and below 0,45 M. This picture does not remarkably change after applying FT operations. While, initially, still

a solubility zone is seen for 0.68 M NaCl and lysozyme concentrations below 10.75 mg/mL, only the lowest lysozyme concentration of 2.5 mg/mL showed to be soluble under these NaCl concentrations and FT operations, see Figure 4.3 (A middle). Concerning the aggregation zone initially, the aggregation zone was mainly characterized by a large crystallization zone and only showed an increasing co-precipitation at high lysozyme and NaCl concentrations. No pure precipitation zone could be observed. After FT c1 this picture changed so that the majority of systems is now characterized by co-precipitation for all cycles up to FT c5. Only for low lysozyme concentrations and the complete range of added NaCl, a crystallization region is observed, see Figure 4.3 (A middle).

$MCB_{IS,pH\,3}$ system

In general, lysozyme at FT c0, was soluble for NaCl concentrations at and below 0.45 M. After FT operations, the solubility zone was reduced to NaCl concentrations of 0.23 M to systems with a lysozyme concentration at and below 13.5 mg/mg, see Figure 4.3 (A right). As seen for all systems, the aggregation zone at FT c0 was mainly characterized by a large crystallization zone and only showed an increasing coprecipitation at high lysozyme and NaCl concentrations. No pure precipitation zone could be observed. After FT c1 the crystallization zone moved to the lowest lysozyme concentration while at counter–clockwise coprecipitation and at medium concentrations of NaCl, a pure precipitation zone developed. With every FT cycle (FT c3, FT c5), the precipitation zone increases and spreads to lower lysozyme concentrations and higher NaCl concentration. At FT c5, the crystallization zone completely disappears leaving only a zone of co–precipitation for high NaCl concentrations, see Figure 4.3 (A right).

pH 5

In general, all investigated systems (FT c0   FT c5) for all three buffer types showed a solubility zone over the whole lysozyme concentration range for NaCl concentrations of 0.45 M (*Acetate*) and 0.23 M NaCl for the *MCB* systems. Furthermore, for the lowest lysozyme concentration of 2.5 mg/mL and the whole NaCl range, all systems expressed a solubility zone. Regarding the aggregation zone, this zone was predominantly characterized by a pure crystallization zone. Significant co-precipitation only occurred for the *MCB* systems at FT c5. The co-precipitation zone developed at high lysozyme (from 13.5 mg/mL) and medium NaCl concentrations (0.45 – 1.82 M), see Figure 4.4.

4.3.3. Morphology

The above–mentioned aggregation zones only show a general picture of the solid phase appearing. To obtain a more exact picture, morphologies within the different zones were
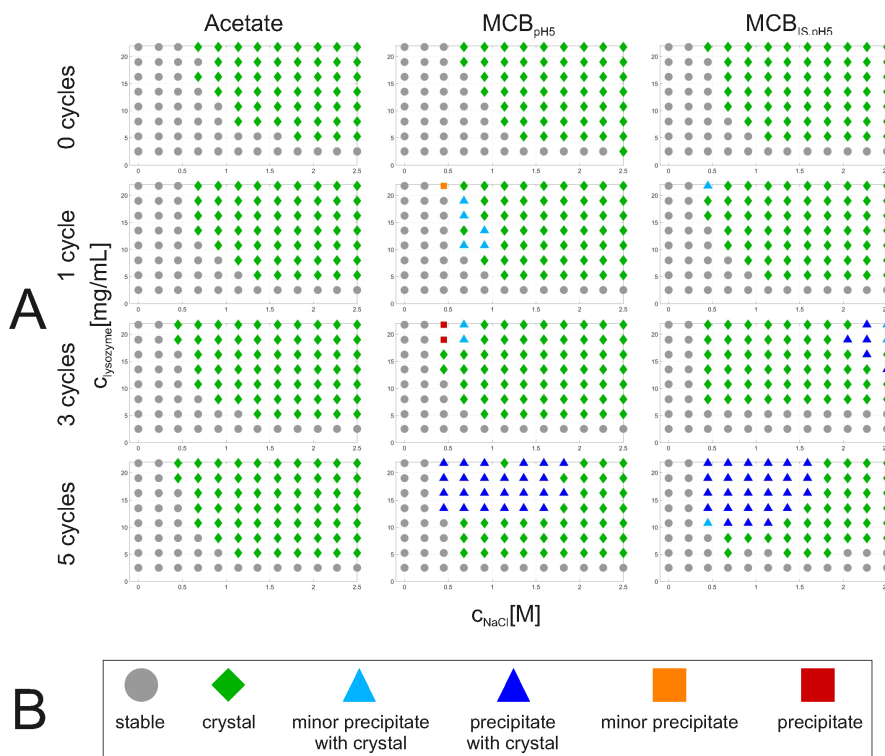
Figure 4.4.: In A, the phase diagrams of all tested buffer systems without and with FT stress at pH 5 are shown. The column on the left shows the phase diagrams of the *citrate* buffer. In the column in the middle, the phase diagrams of the MCB_{pH3} system and in the column on the right, the diagrams of the $MCB_{IS,pH3}$ system are shown. B represents the appropriate legend.

evaluated. The obtained habits are shown in Figure 4.5 (B) and Figure 4.6 (B). Mainly four different crystal shapes were observed, whereas the tetragonal crystals differ in size (micro, small, and big tetragonal crystals). In general, the higher the NaCl and lysozyme concentration and/or the FT stress, the smaller and the more complex the crystals, e.g. flower, needle and sea urchin crystals. When no structured aggregation is possible, precipitate is growing. In the following section, the pH value, buffer system and FT stress dependencies of the morphology are described.

pH 3

When looking at FT c0, a largely homogeneous picture occurs. Close to the transition zone from solubility zone to crystal zone, small tetragonal crystals grew. By increasing the lysozyme and NaCl concentration, micro crystals occurred. When entering the precipitation zone at high lysozyme and NaCl concentrations, precipitate, needle crystals (*citrate buffer*, $MCB_{IS,pH3}$), flower crystals (MCB_{pH3}) and sea urchin crystals co-existed, see Figure 4.5 (B).

Citrate buffer

With increasing FT cycles, the morphology changed. Everywhere in the aggregation region, precipitation co-occurred with crystals. Additional, the shape of crystals changed from small tetragonal crystals to micro crystals and the area of sea urchin crystals increased with the number of cycles (see Figure 4.5 (B)). For FT c1 and FT c3, small tetragonal crystals were only found for medium NaCl and high lysozyme concentrations. Next to this zone, a pure aggregation zone was found for low NaCl and high lysozyme concentrations, see Figure 4.5 (A left).

$MCB_{pH\,3}$ system

For increasing cycle numbers, the pure - relatively small - crystallization zone for low lysozyme concentrations showed micro crystals. A mixture of micro crystals and co-precipitate describes the main part of the aggregation zone. For high lysozyme and NaCl concentrations, habits found with co-precipitation change with increasing FT cycle number from flower and sea urchin crystals (FT c0), small tetragonal crystals (FT c1), micro and sea urchin crystals (FT c3) to micro crystals (FT c5), see Figure 4.5 (A middle).

$MCB_{IS,pH\,3}$ system

Again, a small zone for low lysozyme concentrations with micro crystals was found for FT c1 and FT c3. The latter disappeared for FT c5. The main part of the aggregation zone could be described by a pure precipitation zone slowly replacing a zone where crystals and precipitate were found. In this zone, at high NaCl concentration, a wide mix of habits is found, i.e. small tetragonal, micro, needle and sea urchin crystals, see Figure 4.5 (A right).

pH 5

The homogeneous picture seen in Figure 4.4 changes clearly when looking at the morphologies obtained, see Figure 6 (A).

Acetate buffer

For FT c0, the crystallization zone is characterized by tetragonal crystals followed by sea urchin crystals for higher lysozyme and NaCl concentrations. The zone showing sea urchin crystals is found in all phase diagrams reducing in size with increasing FT cycle number. For FT c1, the tetragonal crystals change into small tetragonal crystals. For
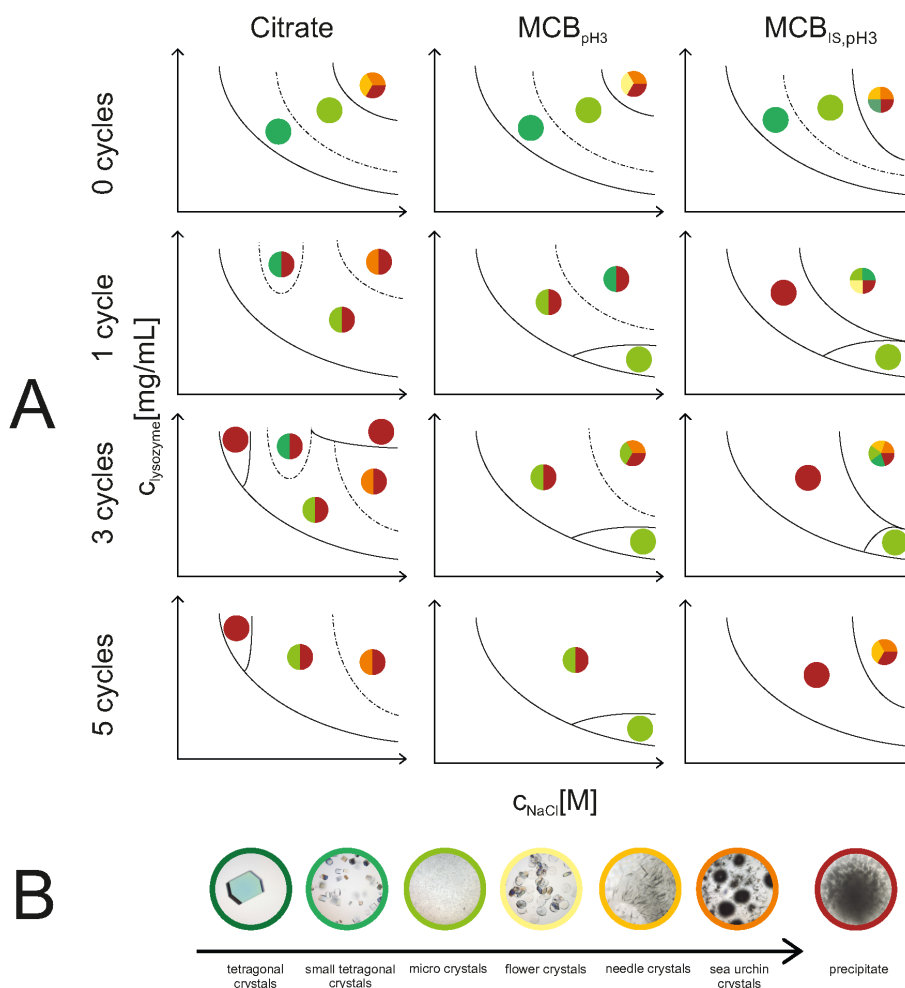
Figure 4.5.: A gives a schematic overview of the morphology with the different buffer systems and at different FT cycles at pH 3. The column on the left shows the phase diagrams of the *citrate* buffer. In the column in the middle, the phase diagrams of the MCB_{pH3} system and in the column on the right, the diagrams of the $MCB_{IS,pH3}$ system at pH 3 are shown. The legend of the figure is presented in B. From the left, crystal types are shown, which grow when the nucleation rate and the supersaturation are low, e.g. tetragonal crystals (21.75 mg/mL lysozyme, 0.91 M NaCl, *acetate* buffer pH 5, FT c0), small tetragonal crystals (19 mg/mL lysozyme, 0.91 M NaCl, MCB_{pH3}, zero cycles), micro crystals (10.75 mg/mL lysozyme, 2.05 M NaCl, MCB_{pH3}, FT c0). The further on the right, the higher the supersaturation and the nucleation rate. Hence, flower crystals (21.75 mg/mL lysozyme, 2.05 M NaCl, MCB_{pH5}, FT c3), needle crystals (13.5 mg/mL lysozyme, 1.36 M NaCl, *citrate* buffer pH 3, FT c0), and sea urchin crystals (13.5 mg/mL lysozyme, 2.05 M NaCl, *acetate* buffer pH 5, FT c5) grow. The crystal types on the right side often occur when FT stress was applied. In addition, precipitate (19 mg/mL lysozyme, 0.45 M NaCl, *citrate* buffer pH 3, FT c3) might also grow when the aggregation is not ordered any more. This is often the case when FT operations were performed.

FT c3 and FT c5 and low lysozyme and NaCl concentrations, the first zone is characterized by micro crystals. The second zone - medium NaCl and lysozyme concentrations - shows small tetragonal crystals for low and flower crystals for high lysozyme concentrations, see Figure 4.6 (A left).

$MCB_{pH\,5}$ system

At FT c0, three different crystallization zones develop. For low NaCl and high lysozyme concentrations, tetragonal crystals are found. The main part of the aggregation zone spreading over all NaCl concentrations is described by small tetragonal crystals, and the third zone for high NaCl and high lysozyme concentrations is a mixture of flower, needle and sea urchin crystals. The latter zone is seen on all cycles. For FT c1 and FT c3, two distinct zones develop. For low NaCl and low lysozyme concentrations, micro crystals and at the medium concentration range, small tetragonal crystals are found. For FT c5, high lysozyme concentrations led to a zone of micro crystals and co-precipitate while the lower lysozyme concentrations are characterized by a mixture of small tetragonal and micro crystals, see Figure 4.6 (A middle).

$MCB_{IS,pH\,5}$ system

At FT c0, three zones develop. The first zone is characterized by small tetragonal crystals, the second zone by flower crystals, and the third zone - high NaCl and high lysozyme concentrations - by sea urchin crystals. For all cycles, zone two and zone three decrease in size with the cycle number. Zone three reveals a co-appearance of needle crystals for FT c1 and higher. In zone one, the small tetragonal crystals move to higher NaCl and lower lysozyme concentrations. For lower NaCl and higher lysozyme concentrations, small tetragonal crystals develop into micro crystals. At FT c5, largely identical phase diagrams for both *MCB* systems develop, showing a co-precipitation zone at low NaCl and high lysozyme concentrations, see Figure 4.6 (A right).

4.3.4. Influence of buffer systems

A comparison of the results of the different buffer systems shows that, at both pH values, there are differences in phase behavior, and morphology could be seen for all cycle numbers. These differences were found to occur between strongly dependent buffer systems, like the *citrate/acetate* buffer and *MCB* systems, as well as between rather similar buffer systems, such as *MCB* and MCB_{IS}. While the solubility lines did not show a clear trend nor presented deeper information on buffer suitability, more information is given by changes in aggregate morphology. At pH 3, in all tested systems, tetragonal crystals in different sizes occurred in the lower concentration region, whereas first small tetragonal and then

micro crystals occurred. In the highly concentrated area, precipitate co–occurred with different types of crystals in all tested buffer systems. When FT operations took place at $pH\,3$ mainly changes in the aggregation zone and the morphology appeared. The aggregation zone increased mainly due to the increase in the precipitation zone, where crystals also co–appeared, with the *citrate* buffer to the $MCB_{,pH\,3}$ system. With the $MCB_{IS,pH\,3}$ system, in addition, a pure precipitation zone was created at middle NaCl concentrations. Furthermore, a pure crystallization zone appeared only for the two *MCB* systems at low lysozyme concentrations, see Figure 4.5. Besides the effects mentioned above, the area of sea urchin crystals grew with an increasing number of cycles in the case of the *citrate* buffer.

At $pH\,5$ and $FT\,c0$, both the solubility zone and the aggregate morphology differs. The size of the solubility zone shows a trend from the *acetate* buffer (large) to the $MCB_{pH\,5}$ trough to the $MCB_{IS,pH\,5}$ system (small). Regarding the morphology, big tetragonal crystals grew with the *acetate* buffer and the $MCB_{pH\,5}$ system, whereas in the $MCB_{IS,pH\,5}$ system, only small tetragonal crystals grew within the middle NaCl concentration region, see Figure 4.6. Moreover, the zone of sea urchin crystals was the biggest when using the *acetate* buffer.

When FT operations were performed, the phase behavior did not changed for the *acetate* buffer, with the exception of a slightly decreasing size of the solubility zone. When increasing the cycle number, a precipitation zone with co–appearance of crystals occurs at high lysozyme and middle NaCl concentrations at pH 5 next to the decrease of the solubility zone in both *MCB* systems. Regarding the morphology, all systems were found to follow the same trend of smaller and more complex crystal structures, see arrows shown in Figures 4.5 (B) and 4.6 (B).
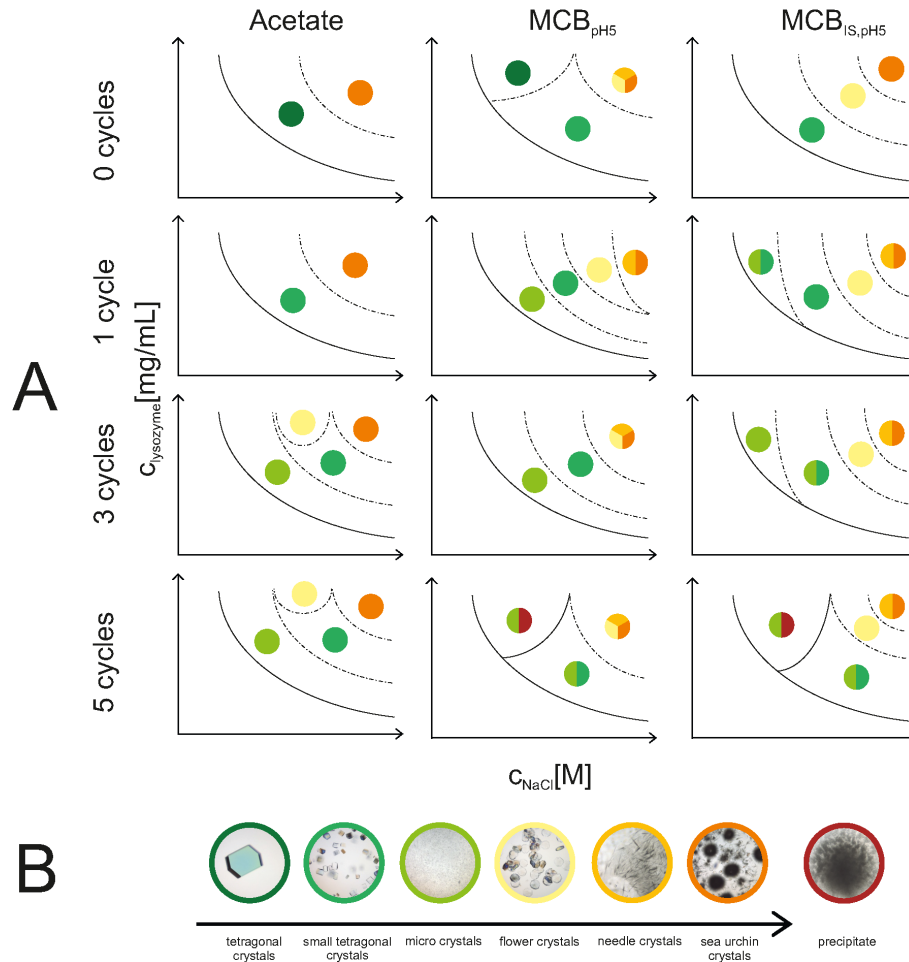
Figure 4.6.: A gives a schematic overview of the morphology with the different buffer systems and at different FT cycles at pH 5. The column on the left shows the phase diagrams of the *citrate* buffer. In the column in the middle, the phase diagrams of the MCB_{pH5} system and in the column on the right, the diagrams of the $MCB_{IS,pH5}$ system at pH 5 are shown. The legend of the figure is presented in B. From the left, crystal types are shown, which grow when the nucleation rate and the supersaturation are low, e.g. tetragonal crystals (21.75 mg/mL lysozyme, 0.91 M NaCl, *acetate* buffer pH 5, FT c0), small tetragonal crystals (19 mg/mL lysozyme, 0.91 M NaCl, MCB_{pH3}, zero cycles), micro crystals (10.75 mg/mL lysozyme, 2.05 M NaCl, MCB_{pH3}, FT c0). The further on the right, the higher the supersaturation and the nucleation rate. Hence, flower crystals (21.75 mg/mL lysozyme, 2.05 M NaCl, MCB_{pH5}, FT c3), needle crystals (13.5 mg/mL lysozyme, 1.36 M NaCl, *citrate* buffer pH 3, FT c0), and sea urchin crystals (13.5 mg/mL lysozyme, 2.05 M NaCl, *acetate* buffer pH 5, FT c5) grow. The crystal types on the right side often occur when FT stress was applied. In addition, precipitate (19 mg/mL lysozyme, 0.45 M NaCl, *citrate* buffer pH 3, FT c3) might also grow when the aggregation is not ordered any more. This is often the case when FT operations were performed.

4.4. Discussion

At first glance, the study shows that the solubility, phase behavior, and morphology of lysozyme from chicken egg white were influenced by the pH value and the NaCl concentration as well as the initial lysozyme concentration. Furthermore, the choice of the buffer system and the number of cycles had an influence on the phase behavior characteristics. While these are obvious findings, the methodology of the study reveals the importance of adding morphology as a screening parameter in order to gain a more complete and a deeper insight when evaluating stable/soluble protein systems.

4.4.1. Solubility line

The solubility curves exhibit the lowest amount of analytical information in this study. Changes in the course of the solubility line are not significant enough to derive deeper conclusions – only when comparing the different buffer systems at pH 5 among each other we see significant changes – and might mainly be used to support the trends of the other parameters. Remarkable might be that independent of FT cycles no significant changes in the soluble region occur. Finally, changes observed result mainly from a variation of single points in connection with the exponential fitting procedure.

4.4.2. Phase behavior and morphology

Phase behavior within the aggregation zone already reveals the general picture and volatility of aggregation processes occurring. However, a more distinct picture on processes occurring within the different systems is then given by the analysis of changes in morphology and the insight into when such changes occur.

FT c0 at pH 3

At pH 3 and FT c0, lysozyme showed a phase transition from soluble to crystals and further to precipitate with all used buffer systems (see Figure 4.5 A). At pH 3, the distance to the isoelectric point (pI) of lysozyme (pI is around 11.4) leads to an increase in long–range electrostatic (stabilizing) protein–protein interactions [52, 158, 200, 201]. This stabilizing repulsion leads generally to a higher solubility and a decrease in aggregation tendency [6, 202]. With increasing NaCl concentrations, the repulsive electrostatic forces between the proteins decrease due to shielding by neighbouring salt ions. Hence, short–range attractive interactions become noticeable [20, 203, 204]. These interactions can be a result of van der Waals forces, hydrophobic or osmotic forces [18, 165]. However, at pH 3, the protein

is probably partially unfolded [205] and thus the inner hydrophobic patches are exposed to the surface, which leads to even more hydrophobic interactions [51, 206, 207]. Thus at least in the high concentration regime a heterogenic picture expressing both crystals and precipitate at FT c0 results from this situation. Regarding the crystal morphology at pH 3, tetragonal crystals of different sizes grew. The crystal size was decreasing with increasing NaCl concentration, regardless of the buffer system used. Thus, the supersaturation and nucleation rate were increasing [47, 208]. Accordingly, more critical nuclei were created leading to an increase of the amount of crystals which in return resulted in a decrease in crystal size. When supersaturation is high, the energy barrier is overcome even more easily, which results in the growth of critical nuclei and micro crystals [186]. For the *citrate* buffer and both MCB_{pH3} systems at pH 3, sea urchin, needle and flower crystals co–occurred with precipitate in the high–concentration area of lysozyme and NaCl. Whereas the size of the area differs. In the high concentration region, supersaturation seems to reach a certain level that might promote the growth of unstable polymorph crystals with needle morphology. Thereby, the nucleation process as well as the growth process are influenced at these high concentrations [190]. Besides high supersaturation, temporary concentration–induced LLPS is another prerequisite for the growth of sea urchin crystals. Needle crystals grow fast outside the nucleus if the concentration around the nucleus is still very high [35, 191]. The state in the highly concentrated area is metastable, as precipitate co–appeared with all mentioned crystals. Nevertheless, both phase behavior and morphology show typical behavior with an expected sensitivity at high concentrations. This said, the morphological observations already reveal a deeper insight is the underlying processes as it is given by the phase behavior only.

FT operations at pH 3

In all tested systems, a destabilizing effect – generation of precipitate – arising from FT cycling on lysozyme phase behavior was detected. At FT c1, precipitation co–occurred in the whole aggregation area. The phenomenon of precipitation with FT cycling might be explained by an increase in concentration of solutes such as salts, buffer substances, and the protein itself [28, 90, 105–109]. At some point, the increasing concentration of solutes reaches a critical concentration where long–range repulsive electrostatic forces are shielded. This phenomenon enhances the effect of attractive interaction forces under unstressed metastable conditions, increasing the aggregation tendency. Additionally, partial unfolding on the water–ice–surface caused by the growth of ice crystals might take place [109]. Both effects, high supersaturation and partial unfolding, might be indicators of precipitation [209]. This is supported by the theory that precipitate is assigned to LLPS, whereas the latter can be caused by high concentration, or an incomplete gelation at high supersaturation [35, 39], which is an indicator for partly denaturation of the protein [210]. LLPS takes place when the cloud temperature (T_{cloud}) is crossed [140, 150, 151]. At this point, LLPS is created and highly concentrated protein drops are separated [35], which could be observed while recording the freezing process. This induces the growth of crystal types which are preferred when LLPS occurs, like micro crystals and sea urchin

crystals [35, 186, 191]. However, these two crystal types were mainly observed in the high concentration region of the obtained phase diagrams. With increasing number of FT cycles, the morphological variety was increasing. Reason are the repetition of the FT stress and the adding–up of the mentioned impacts of freeze concentration, water–ice interface denaturation, and temperature–induced LLPS. Other effects such as cold denaturation or a pH shift can be excluded here. Cold denaturation only effects the quaternary structure [104] and lysozyme from chicken egg white does not exhibit a quaternary structure [211]. Further initial testing revealed that changes in the pH value can be ruled out (data not shown). Additionally, the buffer substances are not known to crystallize during freezing [118, 130, 212]. The phase behavior and morphology in more detail are dependent on buffer system. This is explained in Section 4.4.3.

FT c0 at pH 5

At pH 5, the phase behavior shows only soluble and crystal conditions for all used buffer systems at FT c0, see Figure 4.6 A. Thus, a more detailed picture can only be obtained when looking at changes in morphology. At pH 5, hydrophobicity is reduced when compared to pH 3 and no partial unfolding of lysozyme is taking place [205] leading to structured aggregation such as crystallization. When looking at the morphology it is noticeable, that only two sizes of tetragonal crystals grew in the lower salt region, indicating a rather low nucleation rate. By increasing the lysozyme and NaCl concentrations, crystals grow following the progression of shapes (see Figures 4.5 (B) and 4.6 (B)), resulting in needle, flower and sea urchin crystals. Both are indicators of higher supersaturation and the possibility of concentration induced LLPS [35, 190, 191]. The morphology in detail is dependent on the buffer system. This is discussed in Section 4.4.3.

FT operations at pH 5

At pH 5 and FT cycles, lysozyme started to aggregated at lower NaCl concentrations. Reasons for this might be the freeze concentration of salt and protein which generates higher supersaturated regions, the temperature–induced LLPS which creates highly concentrated hot spots, and also the denaturation on the water–ice interface can take a role here [90, 105–109, 150]. Regarding the influence of the increasing number of cycles, the same trend as for pH 3 could be observed. The crystal type followed the natural morphology changes as shown in Figures 4.5 (B) and 4.6 (B). High supersaturation and appearance of concentration– and temperature–induced LLPS might be the reason for the different crystal types [47, 208]. Precipitation only co–occurred at FT c5 with both *MCB* systems. Whereas precipitate appears in the low NaCl and lysozyme concentration area. This is atypical of phase diagrams and was not observed before with lysozyme and NaCl [41, 158]. In general, at pH 5 significantly less co–appearance of crystal and precipitate was observed compared to pH 3 probably due to higher structural integrity of the molecule at this pH.

4.4.3. Influence of buffer systems

Adding morphological analysis to the evaluation of system stability complements the picture obtained during phase behavior studies. The applied buffer systems differ in buffer components, buffer capacity, and IS (see Table 4.1). The *citrate/acetate* buffers only consist of two buffer components. Citrate and acetate are both kosmotropic salts and known as water structure makers. They are strongly hydrated ions and, as a result, have a salting out effect [51, 213]. When compared to citrate, acetate is the more kosmotropic salt and possibly induces a stronger salting–out effect [213]. According to Forsythe and Pusey, acetate as buffer component affects the solubility; an increase in the acetate concentration reduces the solubility of lysozyme [214]. The *MCB* systems consist of five different synthetic buffer substances. In previous studies, it was shown that synthetic buffer components do not show any interaction with proteins [61]. Furthermore, the *MCB* systems do not change in component composition for pH 3 and 5. Moreover, the buffer capacity differs between the *citrate/acetate* buffer (100 mM) and *MCB* systems (20 mM).

pH 3

Precipitation. At pH 3 and FT c0, the smallest precipitation zone could be observed for the MCB_{pH3} system. Whereas the precipitation of the *citrate* buffer showed approximately the same size like the $MCB_{IS,pH3}$ system (see Figure 4.3). Nevertheless, the picture did not show significant differences for the different buffer systems.

Applying FT cycles however distinct differences develop. Concerning the phase behavior, precipitate co–occurred with crystals for the *citrate* buffer and MCB_{pH3} system in the main aggregation area. This can be attributed to freeze concentration and the unfolding on the water–ice interface while FT [103] and results in high supersaturation and a partly unfolded protein, which both induce precipitation [35, 39, 209]. For the $MCB_{IS,pH3}$ system the co–appearance only occur at the highest lysozyme and NaCl concentrations. Additionally, pure precipitation occurred at lower NaCl concentrations, so the zones were switched (see Figure 4.3). The level of the IS and the absence of interacting buffer substances for both MCB systems might have an influence on the aggregation propensity itself. Because of decreasing temperature, LLPS droplets are created in the highly concentrated region [140, 150, 151], which could be observed while recording the freezing process. With increasing time and decreasing temperature, LLPS droplets might also occur in the lower concentration region. During this period, freeze concentration and ice crystals formation might occur leading to precipitation. This picture proposes that several points in time play a crucial role: a) the point in time of the appearance of T_{cloud}, temperature–induced LLPS [140, 150, 151], and b) the start of ice crystal growth, point where FT stress occurs [103]. The coincidence of these points seemed to be crucial for the appearance of crystals, precipitate or, precipitate and crystals at pH 3. The growth of the pure precipitation phase starting at low NaCl concentration for the citrate and $MCB_{IS,pH3}$ system is remarkable, but follows an increasing buffer IS (see Table 4.1) for low NaCl concentrations.

Crystallization. Finally at lower lysozyme concentrations and NaCl concentrations of 1.1 M and higher a pure crystal phase exhibiting tetragonal shape is observed at FT c1 and FT c3 for both the MCB_{pH3} and $MCB_{IS,pH3}$ system. Here, specific the interactions or the absence of such interactions of buffer substances might be the reason. With the known interactions of citrate [72, 213], in the zone which otherwise seems to be stable while FT stress is applied, precipitate co–exist, while this is not the case for the synthetic (non–interacting) components used in the *MCB* systems [61]. Changes in the morphology did not show similar correlations to buffer composition. The respective degree of changes, due to the change of crystal structure, following the row of shapes (see Figures 4.5 (B) and 4.6 (B)), is dependent on the initial morphology.

pH 5

Aggregation area. At pH 5 and FT c0, the phase behavior was only influenced by the different buffer systems in the size of the respective aggregation area. The latter was slightly larger for the $MCB_{IS,pH5}$ system compared to the other two systems. This might be explained by the higher IS of this system. A higher IS leads to a higher supersaturation and subsequently the energy barrier for aggregation is overcome earlier.
Precipitation. Precipitate started to co–occur at FT c3 and FT c5 in the lower NaCl concentrated region. It can be concluded that the influence of the buffer components is predominant here, as the conductivity is approximately the same for the *acetate* buffer and the $MCB_{IS,pH5}$ system, and clearly lower than for the $MCB_{IS,pH5}$ system (see Table 4.1). The influence of acetate on lysozyme seems to stabilize the phase behavior when FT operations took place, which is a contradiction to the salting–out effect of acetate [51, 61, 213]. Compared to that the synthetic buffer components of the *MCB* systems are known to not influence the protein itself [61], following the phase behavior is changing due to the FT stress.
Crystallisation. A major difference observed in crystal morphology between the buffer systems is seen in the size of the area expressing sea urchin crystals. For the *acetate* buffer this area was largest followed by the MCB_{pH5} and $MCB_{IS,pH5}$ systems. It is known that acetate influences the solubility of lysozyme in higher salt regions [214]. This might be the reason for the larger size of the area of sea urchin crystals compared to both *MCB* systems. Furthermore the system with the *acetate* buffer only expressed tetragonal crystals and sea urchin crystals, while no intermediate crystal type, like micro or needle crystals could be detected (see Figure 4.6). This might be due to interactions of acetate with lysozyme which resulted from increasing NaCl and lysozyme concentration and thus in a direct transition from tetragonal to sea urchin crystals [214]. With both *MCB* systems, a zone of intermediate crystal types was created before the zone with sea urchin crystals occur, by increasing the concentration of NaCl and lysozyme.
Whereas, the MCB_{pH5} system showed the highest number of different crystal types and the $MCB_{IS,pH5}$ system clearly separated crystal zones. However, the only difference between the systems can be pinpointed in a slightly different IS explaining the only small differences observed. Depending on the initial IS the nucleation rate and the growing

process is influenced. Both systems the morphology follows the order of supersaturation (see Figures 4.5 (B) and 4.6 (B)) [35, 47, 191].

4.5. Conclusion

In order to gain a holistic view of the phase behavior of protein systems during FT cycling, a methodology was developed based on solubility, phase and morphological data to obtain an easily accessible signature of the underlying processes. The solubility thereby showed the lowest amount of analytical information and can not be used for any deeper conclusion. However, the phase behavior and especially the morphology are informative parameters to characterize the system stability as well as ongoing processes during FT. The applicability of the developed tool was shown with changing buffer compositions, pH value, protein and precipitant concentrations as well as the FT cycle number. With the phase behavior differences between buffer substances, *citrate/acetate* buffer systems – MCB systems, as well as different IS, $MCB - MCB_{IS}$, could be detected.

In future work, complex analytics will be performed to evaluate whether the susceptibility to changes in the aggregation state points towards changes in the liquid phase.

5. A phase diagram–based toolbox to assess freeze/thaw ramps on the phase behavior of lysozyme from chicken egg white

Anna K. Wöll, Monika Desombre, Lena Enghauser, Jürgen Hubbuch*
*Corresponding author. E-mail address: juergen.hubbuch@kit.edu

Karlsruhe Institute of Technology (KIT), Institute of Process Engineering in Life Sciences, Section IV: Biomolecular Separation Engineering, Karlsruhe, Germany

Abstract

The influence of process parameters during FT operations is essential for the preservation of protein stability/activity during production and storage processes in the biopharmaceutical industry. Process parameters, such as FT ramps, final storage time and temperature, affect the occurring FT stress onto the target protein in different ways. FT stress includes cold denaturation, freeze concentration, and ice crystal formation which can result in protein aggregation. To visualize the impact of variations in FT ramps, analytically easy accessible descriptors such as solubility, phase behavior, and crystal morphology were evaluated. The phase diagram-based toolbox in combination with an HTS–compatible cryo-device allowed the identification of suitable ramping schemes during FT operations. It could be clearly shown that rapid operations are needed above T_g to circumvent precipitation during FT cycles. Finally, a stability index is introduced which allows ranking of the systems investigated.

Keywords: *phase diagram, temperature ramps, stability index, lysozyme*

5.1. Introduction

Most biopharmaceutical proteins are stored and transported in a frozen state to improve flexibility during manufacturing and long–term stability during storage [215–217]. During manufacture, storage, and use, the proteins experience chemical–induced stress (pH value, salt type and concentrations, buffer components, and IS [43]), mechanical–induced stress (shear stress from pumping and mixing operations), and physical–induced stress (process time, temperature and cycling [103, 109, 178]) [33, 48]. The different stress types might cause protein damage, which is then mostly manifested in the formation of aggregates, structural and/or conformational changes, or loss of biological activity [103, 139, 178, 217, 218]. Possible processes occuring during FT operation are cold denaturation [104], freeze concentration [105–108], and/or ice crystal formation with concomitant protein denaturation on the ice–water interface [90, 109]. The development of these processes can be controlled by the use of cryoprotectants, adjustment of FT ramps, choice of frozen temperature and duration as well as sample volume [109, 118, 152, 219, 220]. It is thus mandatory, that the influence of these parameters is investigated prior to FT operations. In this scenario, variations of FT ramping might be the most straight forward strategy from a process engineering point of view. The choice of a freezing ramp should fulfill at least two criteria: on the one hand T_g has to be crossed and the glassy state needs to be reached rapidly to minimize the time the protein is subjected to potentially damaging states [145, 153]. On the other hand, if a freezing ramp is too steep, ice-crystal interfaces might become too large, due to the ratio between volume and surface; when a lot of small crystals are created, protein denaturation on the ice surface is promoted [90, 109, 115, 116]. The choice of the thawing ramp is a critical parameter to counteract the possible appearance of recrystallization where small ice crystals melt and simultaneously grow into bigger ones (Ostwald ripening) [118, 154]. Different critical parameters, e.g. particle size, amount of aggregates or structural changes, can be detected to be characterizing the stability of proteins [152, 178, 196, 221–223]. These parameters, however, are difficult to determine and the needed methods are not always available. Wöll *et al.* developed an easily accessible method to characterize different systems with increasing protein and precipitant concentrations by creating phase diagrams, and using the solubility, phase behavior, and the morphology as indicators for ongoing FT processes [224]. In a first study, the influence of the pH values, IS, and buffer systems on the solubility, phase behavior, and morphology were investigated [224]. So far missing, however, is a study on the applicability of such toolbox for investigating different ramping schemes during FT operations. In this work, the phase diagram–based toolbox is used to show the influences of different FT ramps and FT cycles on protein solubility, phase behavior, and crystal morphology. The influence of ramps during FT operations on system stability was evaluated independently. In addition to simple ramping schemes, we also introduced inflection points realizing different processing speeds during FT operations. Finally, a ranking of the different systems according to the processing time, and a stability index based on a classification procedure of morphological changes were established.

5.2. Materials and methods

To determine the influence of variations in FT ramps as well as different numbers of cycles on the colloidal protein stability of lysozyme from chicken egg white, phase diagrams at pH 5 were generated. In the following, the preparation of stock solutions and the creation of phase diagrams as well as the performance of the freeze/thaw protocol are described. Furthermore, the analytical methods used are explained.

5.2.1. Preparation of stock solutions

Two different stock solutions were prepared for the creation of phase diagrams. As basic buffer for protein dissolution and the sodium chloride stock solution (2.5 M NaCl), a 20 mM MCB was prepared using a tool published by Kröner *et al.* [197]. The MCB included the following buffer substances: AMPSO (Sigma-Aldrich), TAPSO (Sigma-Aldrich), MES (AppliChem GmbH, Darmstadt, Germany), formic acid (Merck KGaA), and D-(+)-malic acid (Sigma-Aldrich). In a final step, pH 5 was adjusted with a five-point calibrated pH meter (HI-3220, Hanna® Instruments, Woonsocket, RI, USA) equipped with a SenTix® 62 pH electrode (Xylem Inc., White Plains, NY, USA). For adjustment of the desired pH value, NaOH or HCl (Merck KGaA) was used. The pH was adjusted on the preparation day to a value differing by up to ±0.2 pH units from the final pH value. Prior to using the buffer, the pH was verified again and finally adjusted to a value differing by only ±0.02 pH units. The IS of all systems was adjusted to 10.1 mS/cm with an accuracy of ±1.0 mS/cm at 24 ℃ ±1 ℃ by using the conductivity meter CDM 230 (Radiometer Analyticals, Lyon, France) and the four-point calibrated conductivity cell E61M014 (Radiometer Analyticals, Lyon, France) using NaCl (Merck KGaA). Finally, all buffers were filtered through a 0.2 µm Supor® Polyethersulfone (Pall Corporation, Port Washington, NY, USA) filter. The prepared buffers were stored at room temperature and not used for longer than 2 weeks after preparation. For protein stock solution, lyophilized lysozyme from chicken egg white (Hampton Research, Aliso Viejo, CA, USA) was used. Following dissolution of the protein, the solution was filtered through a 0.2 µm syringe cellulose acetate filter (VWR, Radnor, PA, USA) and a desalting step with PD-10 (GE Healthcare, Uppsala, Sweden) columns was performed by using the spin protocol [198] to remove aggregates and production-related additives. Finally the protein concentration was adjusted to 43.5 mg/mL ± 1 mg/mL. To do so, a NanoDrop™2000c UV-Vis spectrophotometer (Thermo Fisher Scientific, Waltham, MA, USA) and an extinction coefficient of $E^{1\%}(280\,nm) = 22.00\,Lg^{-1}cm^{-1}$ was used. The protein stock solution was prepared freshly for every experimental cycle and was not used for more than 1 day.

5.2.2. Phase diagrams

Phase diagrams with lysozyme concentrations between 2.5 mg/mL and 21.75 mg/mL and NaCl concentrations between 0 M and 1.1 M at pH 5 were created, applying the method published by Baumgartner *et al.* [158]. The protein and salt stock solutions were placed onto a Freedom EVO® 100 fully automated liquid handling station (Tecan Group Ltd., Männedorf, Switzerland) platform. The liquid handling station (Tecan Group Ltd., Männedorf, Switzerland), equipped with fixed tips and 250 µL dilutors and controlled by Freedom EVO® 2.4 SP3 (Tecan Group Ltd.). The needed protein and salt concentrations were prepared in a Deepwell PP plate (Greiner Bio-one, Frickenhausen, Germany). Following this, the phase diagram was created in a MRC Under Oil 96 Well Crystallization Plate (SWISSCI AG, Neuheim, Switzerland), and 12 µL of the protein solution and 12 µL of the salt solution were mixed. The plates were centrifuged in an Eppendorf centrifuge 5810 R (Eppendorf AG, Hamburg, Germany) at 1000 rpm for 1 min to remove all air bubbles. To avoid evaporation, the plate was sealed with Duck® Brand HD Clear sealing tape (ShurTech® brands, Avon, OH, USA). Before the phase diagrams were placed in the incubation chamber RockImager54 (Formulatrix, Bedford, MA, USA) at 20 °C for 40 days, they were subjected to the respective freeze/thaw protocols, which are described in the next section.

5.2.3. Freeze/thaw ramps

Different FT ramps as well as a number of cycles (FT cx; x=0, 1, 3) were tested. Initially, a control plate (without FT stress) was directly placed in the incubation chamber. All other plates were placed onto the cryo–device EF600M 105 (Grant Instruments, Cambridgeshire, UK) after preparation. The cryo–device is controlled with the software iTools Engineering Studio (Eurotherm, Worthing, UK) and equipped with a 96-well adapter. To facilitate optimal heat transfer on the adapter, thermal conductivity grease was used. To prevent direct contact of the thermal conductivity grease (Apiezon® N, Merk KGaA) with the crystallization plate, a layer of plastic wrap was placed in between plate and grease. Additionally, the plate was clamped on the adapter to ensure a contact of each well with the adapter. The needed motor parameters for each ramp were calibrated using an optimization run with a dummy prior to the actual experimental run. The ramps applied are listed in Table 5.1. A detailed description of FT procedures is given in [224]. Using the thermal grease, the clamps, and a very small sample volume of 24 µL, it is supposed that the temperature profile of the adjusted ramp is the same as the actual temperature profile experienced by the sample solution. The temperature profile of R 3 is shown in Figure B.1 in the Supplementary Material.

Table 5.1.: Overview of the system applied. The FT parameters for each ramp as well as the overall process time of FT operations and the stability index (SI) are listed. Yellow marked systems have a stability index above -100, grey marked between -100 and -200 and blue marked between -200 and -340.

| Sys-tem | Freezing | | | Thaw-ing | | | Pro-cess time | SI_{cycle} |
	temp. Range [°C]	ramp [°C/min.]	time [min]	temp. Range [°C]	ramp [°C/min]	time [min]	time [min]	MK_{FTc1} - MK_{FTc3}
R1	20 / -80	0.5	200	-80 / 20	2.5	40	240	-399
R2	20 / -80	5	20	-80 / 20	2.5	40	60	-63
R3	20 / -80	10	10	-80 / 20	2.5	40	50	-79
R4	20 / -35 / -80	0.5 / 10	114.5	-80 / 20	2.5	40	154.5	-427
R5	20 / -35 / -80	10 / 0.5	95.5	-80 / 20	2.5	40	135.5	-141
R6	20 / -20 / -80	0.5 / 10	86	-80 / 20	2.5	40	126	-309
R7	20 / -20 / -80	10 / 0.5	124	-80 / 20	2.5	40	164	-347
R8	20 / -80	5	20	-80 / 20	0,5	200	220	-387
R2	20 / -80	5	20	-80 / 20	2.5	40	60	-63
R9	20 / -80	5	20	-80 / 20	5	20	40	-39
R10	20 / -80	5	20	-80 / -20 / 20	0.5 / 5	128	148	-175
R11	20 / -80	5	20	-80 / -20 / 20	5 / 0.5	92	112	-313
R12	20 / -80	5	20	-80 / -35 / 20	0.5 / 5	101	121	-71
R13	20 / -80	5	20	-80 / -35 / 20	5 / 0.5	119	139	-335
R14	20 / -80	10	10	-80 / 20	5	20	30	-75
R15	20 / -80	0.5	200	-80 / 20	0.5	200	400	-429

5.2.4. Analytics

In this study, three different analytical methods were performed to score the phase states and crystal morphology, and calculate the solubility line of each system.

Phase behavior and crystal morphology

After 40 days, pictures taken from the RockImager54 (Formulatrix, Bedford, MA, USA) were scored visually concerning phase states and morphology. During this procedure we differentiated between soluble, crystals and precipitate and for the crystals between micro, small tetragonal, and tetragonal crystals, see Table 5.2 and Figure 5.5 C. Additionally, some conditions were characterized by combinations of the mentioned phase states.

Solubility line

Supernatant measurements were performed in triplicate with a NanoDrop™ 2000c UV/Vis spectrophotometer. For each measurement $3\,\mu L$ of the supernatant was carefully pipetted on the NanoDrop™2000c taking care not to pipette any visible aggregates. Then, the method published by Galm *et al.* was used to calculate the solubility line [164]. In this work, the supernatant concentration of conditions with crystals, and combinations of crystals and precipitates were taken into account for the solubility line.
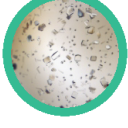
5.2.5. Stability index

To reach an empirical ranking or SI of the FT ramps investigated, a morphology–based weighting was performed. The hypothesis behind this procedure is that stable systems (in this study, favorable FT ramp combinations) show a lower susceptibility towards variations in morphology over different FT cycles than unstable ones. The morphological composition in each well of the different systems was determined and rated by an arbitrary weight (1: soluble; 2 - 5: pure crystals of different habit; 10 - 13: occurrence of precipitation) given to each of these compositions (see Table 5.2). Summing up the classification values of all 96 wells resulted in a morphology–based classificat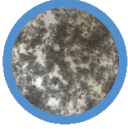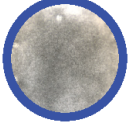ion of the respective systems (R 1 – R 15). To differentiate between the process of an initial FT step and repeated cycling we introduced two independent stability indices. For initial FT operations the $SI_{FT\,c0}$ is defined according to Equation 5.1 ($MR_{FT\,cx}$) stands for the morphology rating according to Table 5.2 for a given cycle x):

$$SI_{FT\,c0} = MR_{FT\,c0} - MR_{FT\,c1} \qquad (5.1)$$

To quantify potential changes in the morphological composition over cycle numbers of FT ramps performed (repeated cycling), the value obtained for FT c3 is subtracted from the

Table 5.2.: Rating system based on morphology. The pictures of the morphologies are shown: soluble (8 mg/mL lysozyme, 0.4 M NaCl, FT c0), micro crystals (19 mg/mL lysozyme, 0.5 M NaCl, R 9, FT c1), small tetragonal crystals (21.75 mg/mL lysozyme, 0.9 M NaCl, R 2, FT c1), big tetragonal crystals (19 mg/mL lysozyme, 0.8 M NaCl, FT c0), small tetragonal and micro crystals (10.75 mg/mL lysozyme, 0.9 M NaCl, R 1, FT c1), micro crystals and precipitate (16.25 mg/mL lysozyme, 0.4 M NaCl, R 4, FT c3), small tetragonal crystals and precipitate (10.75 mg/mL lysozyme, 0.9 M NaCl, R 1, FT c3), light precipitate (16.25 mg/mL lysozyme, 0.4 M NaCl, R 2, FT c3) and precipitate (21.75 mg/mL lysozyme, 0.4 M NaCl, R 4, FT c3).

Rating no.		Morphology
1		soluble
2		normal tetragonal crystals
3		small tetragonal crystals
4		small tetragonal and microcrystals
5		micro crystals
10		small tetragonal crystals and precipitate
11		micro crystals and precipitate
12		light precipitate
13		precipitate

value obtained for FT c1 (see Equation 5.2).

$$SI_{cycle} = MR_{FT\,c1} - MR_{FT\,c3} \qquad (5.2)$$

The systems investigated were then sorted according to the lowest changes occurring in the morphological composition (the highest value obtained after substation). Values obtained and the respective rankings are listed in Table 5.1 and Table 5.3.

Table 5.3.: System ranking. Both stability indicies (SI_{cycle}, SI_{FTc0}) as well as the process time of FT operations are listed, according to a descending SI_{cycle} and ascending process time. Yellow–marked systems have a SI_{cycle} above -100, gray–marked ones between -100 and -200, and blue–marked ones between -200 and -340.

System	$SI_{cycle} = MR_{FT\,c1} - MR_{FT\,c3}$	System	Process time [min]	System	$SI_{FT\,c0} = MR_{FT\,c0} - MR_{FT\,c1}$
R9	-39	R14	30	R10	-35
R2	-63	R9	40	R3	-47
R12	-71	R3	50	R12	-48
R14	-75	R2	60	R4	-56
R3	-79	R11	112	R14	-57
R5	-141	R12	121	R5	-57
R10	-175	R6	126	R1	-57
R6	-309	R5	135.5	R7	-61
R11	-313	R13	139	R9	-80
R13	-335	R10	148	R6	-82
R7	-347	R4	154.5	R2	-84
R8	-387	R7	164	R13	-90
R1	-399	R8	220	R15	-96
R4	-427	R1	240	R8	-109
R15	-429	R15	400	R11	-122

5.3. Results

The aim of this study was to evaluate if a toolbox developed previously for investigating the influence of fluid phase parameters on protein phase behavior during FT operations [224] allows analysis or suitability of different FT ramps. The model system used to perform this investigation consisted of lysozyme from chicken egg white, applying different protein concentrations and different concentrations of NaCl as a precipitant at pH 5. A systematic investigation into the use of different ramping schemes was performed by varying the ramping applied to freezing (R 1-7), thawing (R 2,8-13), and combinations thereof

(R 14-15); see Table 5.1 and Figure 5.1. Additionally, the influence of the cycle number (FT cx; x = 0, 1, 3) was added as a variable parameter. In total 31 phase diagrams were created. The results obtained describing solubility line, phase behavior, and morphology are presented in the following. Prior to a detailed description of the data generated, the overall trend obtained for varying cycle numbers is presented.

5.3.1. Influence of cycle number

In this section, an overall view of the influence of the number of cycles is given, and the detailed changes for each ramping combination are described below in Sections 5.3.2, 5.3.3, and 5.3.4.

An overall shift of the solubility line to lower NaCl and lysozyme concentrations is seen when the number of cycles increases. Regarding the phase behavior at FT c0, a solubility zone and a crystallization zone, starting at 0.5 M NaCl and at 21.75 mg/mL lysozyme, were observed. At lower lysozyme concentrations, the aggregation onset took place at increasing NaCl concentrations. While increasing the number of cycles, four main effects were seen concerning the overall phase behavior. First, a decrease in the solubility zone and an increase in the aggregation zone were detected, see Figure 5.2. Second, a zone with co-appearance of crystals and precipitate occurs. Third, the creation of a pure precipitation zone was observed, mainly at FT c3 (see Figures 5.4 B and C and Figure 5.3). Fourth, changes in the solubility line with increasing cycle number were mainly seen for high protein concentrations and/or to low NaCl concentrations (see Figure 5.2). In the crystallization zone at FT c0, mainly tetragonal crystals were observed for all systems. With increase in the number of cycles, the crystal size decreased and zones with small tetragonal and micro crystals grew. Additionally, co-appearance of crystals (mainly micro crystals) and precipitate were observed. Finally, in some systems, a pure precipitation zone was observed, see Figure 5.5.
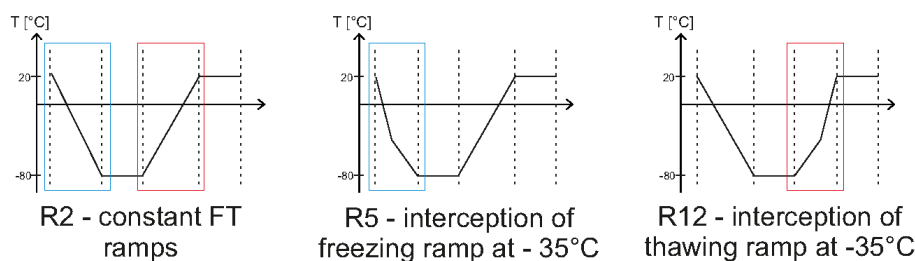
Figure 5.1.: Ramping methodology. The performed process is shown for R 2, R 5, and R 15 to visualize the listed parameters in Table 5.1. The blue rectangle highlight changes while freezing and the red one while thawing.
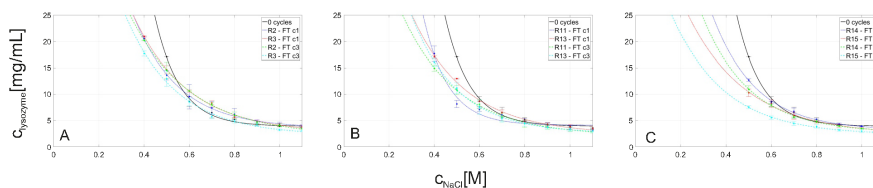
Figure 5.2.: The solubility lines for systems exhibiting high stability (a), medium stability (b), and extreme combinations (c) (see Table 5.1 and Table 5.3). The solid line represents 0 cycles, the dotted lines FT c1, and the dashed line FT c3.
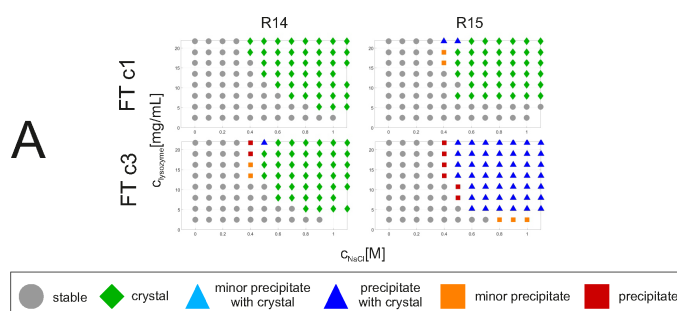
Figure 5.3.: Phase diagrams for systems R 14 R 15 representing a combination of steep and flat ramps for FT c1 and FT c3. Detailed information for each ramp is listed in Table 5.1.

5.3.2. Variation of ramps during freezing

In this section, it was examined if the toolbox applied could distinguish the influence of different freezing ramps (R 1-7) with a constant thawing ramp (Table 5.1 and Figure 5.1) on the solubility line, phase behavior, and morphology. When increasing the slope of the freezing ramp (R 1 to R 3) no significant differences for all three descriptors at FT c1, namely solubility line (Figure 5.2 and Figure B.2 A in the Supplementary Material), solubility zone (Figure 5.4 B), and aggregate morphology Figure 5.5 A, could be seen. For FT c3, the only main difference among the systems appeared for the aggregation morphology – a lower slope of the freezing ramp (R 1) led to a larger zone of co-appearance of precipitate and crystals, see Figure 5.4 B. In contrast, R 2 and R 3 representing faster freezing and thus steeper ramps exhibited mainly small tetragonal and small micro crystals (Figure 5.4 B). When comparing R 2 and R 3, a slight difference was observed for the amount of micro crystals formed. Here, slightly more micro crystals in R 2 than in R 3 are visible, see Figure 5.5 B. Finally, for both systems a small amount of precipitate is seen mainly in the upper left region of the aggregation area, representing high protein and low salt concentrations. To investigate the necessity for rapid freezing for the whole range from 20 to -80 °C the systems R 4–R 7 show varying speeds for two inflection points, namely -20 and -35 °C (Table 5.1 and Figure 5.4 C). Again, for FT c1, no significant trend could be seen in terms of solubility line, solubility zone (Figure 5.4 C and Figure B.2) or aggregate morphology (Figure 5.4 C
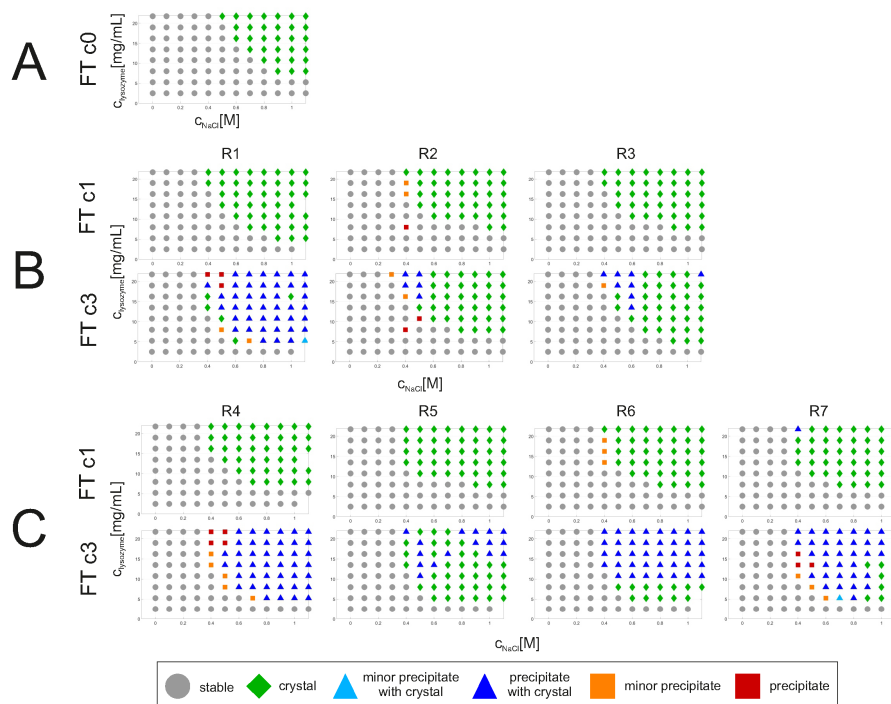
Figure 5.4.: a Phase diagram obtained for 0 cycles. b Phase diagrams for systems R 1-R 3 representing flat, mid and steep freezing ramps for FT c1 and FT c3. c Phase diagrams for systems R 4-R 7 representing flat and steep ramps with inflection points at -35 and -20 °C for FT c1 and FT c3. A detailed information of each ramp is listed in Table 5.1

and Figure 5.5 A). This picture changed at FT c3, where co–appearance of precipitate and crystals was detected for all ramps (Figure 5.4 C). R 5 also showed a larger amount of conditions with small tetragonal and micro crystals, the number of crystalline conditions decreased at R 6 and R 7; they were mainly seen for low protein concentrations over the span of salt concentration applied (R 6) and in the lower right corner of the aggregation zone representing low protein and high salt concentrations (R 7). At R 4, only co–appearance and precipitation took place, see Figure 5.5 B. As seen for R 1, precipitation occurred for the systems R 4 and R 7 at the border between solubility and aggregation zone.

5.3.3. Variation of ramps during thawing

In this section, the influence of different thawing ramps (R 2, R 8-13) was investigated, whereas the freezing ramp was kept constant at 5 °C/min (Table 5.1 and Figure 5.1). In analogy to the systems R 1 - R 3 presented above, the influence of different thawing ramps was evaluated in the set comprising R 8 (flat), R 2 (mid), and R 9 (steep). When comparing the solubility lines at FT c1 and FT c3 to each other, a small shift to lower lysozyme and NaCl concentration could be observed for R 8 at FT c1, whereas a mostly identical set of
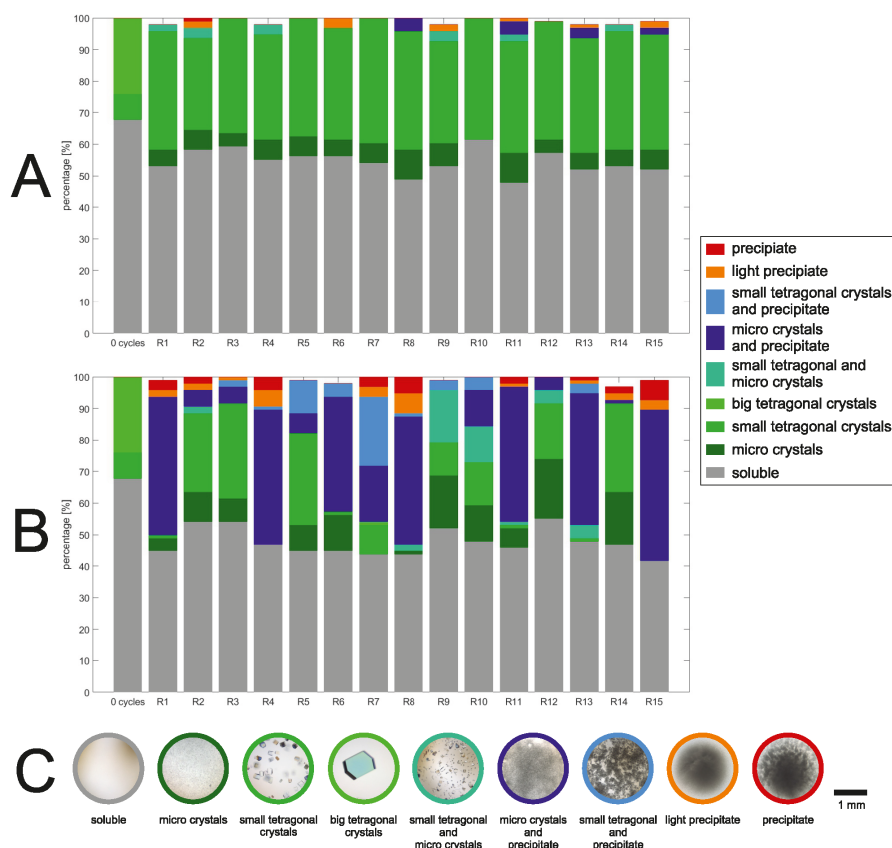
Figure 5.5.: An overview (percentage of appearance for a given system) of the morphology portions is shown for FT c0 and all tested ramps for cycles FT c1 (a) and FT c3 (b). Gray represents the portion of soluble states, the different shades of green represent the crystal habits detected, and the shades of blue show the co–appearance of crystals and precipitate. Orange illustrates light precipitate and red precipitate. c Example pictures of these morphologies are shown: soluble (8 mg/mL lysozyme, 0.4 M NaCl, FT c0), micro crystals (19 mg/mL lysozyme, 0.5 M NaCl, R 9, FT c1), small tetragonal crystals (21.75 mg/mL lysozyme, 0.9 M NaCl, R 2, FT c1), big tetragonal crystals (19 mg/mL lysozyme, 0.8 M NaCl, FT c0), small tetragonal and micro crystals (10.75 mg/mL lysozyme, 0.9 M NaCl, R 1, FT c1), micro crystals and precipitate (16.25 mg/mL lysozyme, 0.4 M NaCl, R 4, FT c3), small tetragonal crystals and precipitate (10.75 mg/mL lysozyme, 0.9 M NaCl, R 1, FT c3), light precipitate (16.25 mg/mL lysozyme, 0.4 M NaCl, R 2, FT c3) and precipitate (21.75 mg/mL lysozyme, 0.4 M NaCl, R 4, FT c3).

solubility lines was obtained at FT c3 for all systems investigated (see Figures B.2 and B.3). This is also reflected in the dimensions of the solubility zone (see Figure 5.6 A). Regarding the morphology for FT c1 at all ramps mainly micro crystals and small tetragonal crystals grew in the aggregation zone (see Figures 5.6 A and Figure 5.5 A), whereas the micro crystals covered mainly the border of the solubility zone (data not shown). The amount of micro crystals expressed was the highest at R 8 followed by R 2 and R 9 (Figure 5.5 A). The morphologies encountered in the aggregation zone at FT c3 differed among the three
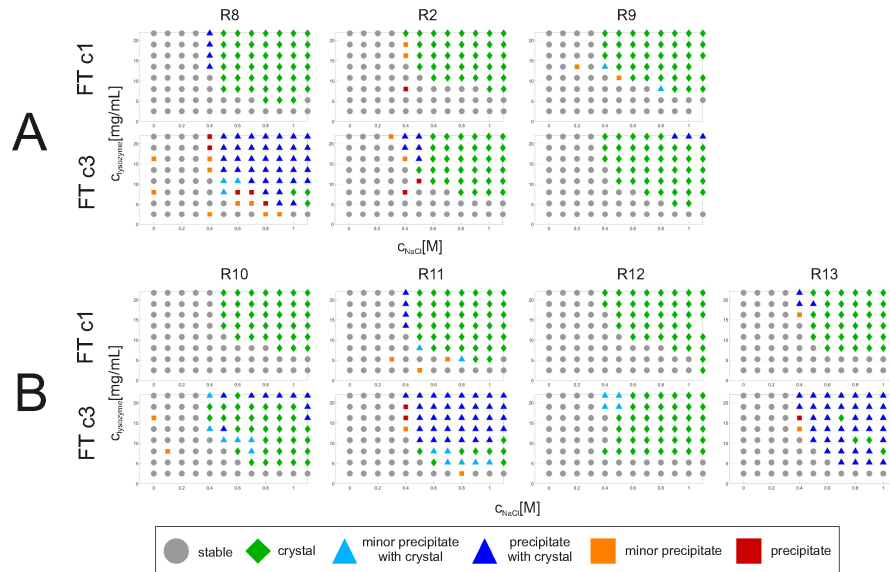
Figure 5.6.: (A) Phase diagrams for systems R 8, R 2 and R 9 representing flat, mid and steep thawing ramps for FT c1 and FT c3. (B) Phase diagrams for systems R 10 - R 13 representing flat and steep ramps with inflection points at -35 and -20 °C for FT c1 and FT c3. A detailed information of each ramp is listed in Table 5.1

systems. At R 8, the morphological composition found in the aggregation zone consisted mainly of a co-appearance of precipitate and crystals, as well as pure precipitate, see Figure 5.6 A. In the systems where co–appearance took place, micro crystals always grew next to precipitate. At R 2 and R 9, mainly crystals were observed (see Figure 5.6 A), whereas the amount of micro crystals was higher at R 9 than at R 2 (Figure 5.5 B). To investigate the necessity for rapid thawing for the whole range from 20 to -80 °C the systems R 10 to R 13 were created. These ramps show varying thawing speeds with two different inflection points, namely -20 and -35 °C (Table 5.1 and Figure 5.1). For FT c1, a difference in the solubility line between R 13 and R 10-12 is seen in a shift towards lower NaCl and protein concentrations for R 13. This deviation, however, disappeared for FT c3 (see Figure 5.2, Figures B.2 and B.3). Concerning the aggregation zone for the two systems, where a rapid thawing after the respective inflection point was set (R 10 and R 12), crystallization dominated the aggregation zone while the morphological composition of the two other systems (R 11 and R 13) could be characterized by a co-appearance of crystals and precipitate nearly quantitatively covering the respective aggregation zone (Figure 5.6 B). Additionally, R 11 and R 13 showed higher amounts of micro crystals (see Figure 5.5 A). Again, micro crystals were mainly seen at the border between the aggregation and solubility zone.

5.3.4. Combinations

In the following section, the two systems R 14 (fast) and R 15 (slow) are compared representing extreme cases (Table 5.1). Comparing these two extreme ramps to each other, differences could be seen for all descriptors, mainly the solubility line, phase behavior, and morphology. The solubility line of R 15 is shifted to lower lysozyme and NaCl concentrations at FT c1 and FT c3 (see Figure 5.2 C). Regarding the phase behavior in the aggregation zone, mainly crystals were created at FT c1. At FT c3 the aggregation zone of R 15 consists of the co-appearance of precipitate and crystals as well as pure precipitate, whereas R 14 mainly shows crystals (see Figure 5.3). Regarding the morphology at FT c1, micro crystals and small tetragonal crystals grew for R 14 and R 15 (see Figure 5.5 A). This was still observed for R 14 at FT c3, whereas the amount of micro crystals increased. Micro crystals also grew at R 15 but only in combination with precipitate (see Figure 5.5 B).

5.3.5. Stability index vs. process time

Next to the solubility line, phase behavior, and morphology, a stability index was established trying to assess the variability of the morphological composition obtained over an increasing number of cycles for a given system. Thus a measure for the stability of a given system was created. Qualitatively, we attributed a certain value to each of the system morphologies obtained (see Table 5.2).
Looking at the data obtained, it became clear that initial freezing and repeated cycling provide different pictures in terms of underlying processes and initial system state. We thus introduced two stability indices, one for initial freezing ($\text{SI}_{FT\,c0}$) and one for repeated cycling (SI_{cycle}), see Equations 5.1 and 5.2.

SI$_{cycle}$

Systems with a value above -100 in this stability index (marked yellow in Table 5.1 and Table 5.3) represent the systems where crystallization dominated over all FT cycles. Blue marked systems with a value between -100 and -200 (marked blue in Table 5.1 and Table 5.3) represent systems with dominating crystallization but also show a clear onset of precipitation over FT cycles. Unstable systems mostly characterized by a dominating shift to precipitation exhibit a morphology variation value between -200 and -340 and are gray–colored (see Table 5.1 and Table 5.3). The remaining systems with values lower than -340 were left uncolored (see Table 5.1). According to this stability index, the systems are ranked in Table 5.3. The ranking underlines the trends seen with the solubility line, the phase behavior, and the morphology presented above. A similar ranking is seen when the overall process time, without holding time, is used as classification (Table 5.3). While a strong agreement between the four systems with a low stability index and a fast processing

time was found, the systems R 11, R 6, and R 13 ranked less stable in the stability index were ranked higher when using processing time as classification (see Table 5.3).

SI$_{FT\,c0}$

The shift in morphology seen for the first FT cycle can be seen in Table 5.3. The order deviates significantly from the order obtained for repeated cycling (SI$_{cycle}$) and process duration. The color scheme developed for SI$_{cycle}$ was applied to underline this finding.

5.4. Discussion

This study aimed to show the applicability of a phase diagram–based tool [224] to use the analytically easily accessible phase behavior, crystal morphology, and solubility as indicators for system stability and ongoing processes during FT applications. In this context, different FT ramps were tested and data were obtained throughout the study analyzed.

The ramps for freezing and thawing used in this study were halted at -80 °C for 30 min. We based our study on the prerequisite that no significant changes in solubility, phase behavior, and morphology occurred during that period. Miller *et al.* claiming that there are no destabilizing processes occurring when the protein is stored at -80 °C underline this assumption [219]. The reason for this is that the chosen storage temperature is well below T_g. At these temperatures, the protein mobility is not existent, following no destabilizing processes taking place [146]. For lysozyme, T_g is in a region between -30 and -70 °C depending on the solution conditions [146, 225].

5.4.1. Influence of cycle number and morphology changes

In this study, the applied toolbox detected changes in the solubility lines as a function of the number of cycles (see Figure 5.2). In general, the creation of ice crystals, and the subsequent exposure of the protein to the ice–water interface, freeze concentration of solutes (buffer components, NaCl, lysozyme), and low temperatures, which can result in cold denaturation and LLPS [35, 103, 133], influence the protein stability. NaCl is known to be concentrate up to 22 wt% (~ 3.74 M) and precipitates along with ice when the eutectic point of 21.2 °C is reached in a binary system [226]. Salt concentration might shift the equilibrium, between aggregated and soluble protein, toward aggregation. This effect is probably mostly pronounced at low to medium salt concentrations where an interplay between salt concentration, protein concentration and ramping scheme applied might lead to different equilibrium states [96, 178, 227, 228]. This is detected by the shift of the

solubility line to lower concentration and the decrease in the size of the solubility zone when the number of cycles was increased. The morphology itself was affected. The greater the number of FT operations performed, the smaller were the crystals, higher portions of micro crystals, and precipitation co–appeared, and a zone with pure precipitation developed. Changes in morphology mainly occur when protein–protein interaction becomes favorable due to operations carried out. In this context, Chi *et al.* published that an increase in the salt concentration due to freezing can reduce intermolecular repulsion between protein molecules, which leads to more favorable attractive intermolecular interactions, resulting in the formation of protein aggregates [14]. It is further assumed that this change of intermolecular interactions might affect the aggregation mechanism or aggregation pathway resulting in a change of aggregate morphology. In general, the aggregation rate is a function of the protein and salt concentration. An increase in the aggregation rate leads to a more unstructured aggregation, which results at a certain point in the appearance of protein precipitates [41]. In addition, the amount of critical nuclei has an influence on the size of the crystals. Freezing–induced LLPS leads to highly concentrated droplets where the energetic barrier to create critical nuclei is easier to overcome and subsequently smaller crystals grow [133, 186, 194]. Following this, a decrease in crystal size might be an indicator for an increase in protein or salt concentration and/or decrease in solubility [41]. Finally, Muschol *et al.* published, that solutions which are left in a two–phase liquid region form micro crystalline precipitate [35]. With the above in mind, it is assumed that the co–appearance, of different crystal sizes, morphologies, and precipitate, is a result of various factors appearing during the FT cycles [109, 117, 219]. This is in accordance with the observation, that the co–appearance is mainly detected at FT c3. Finally, the system stability proved to be more susceptible to high protein concentrations than high salt concentrations and the transition from solubility to aggregation zone was found to led to changes in morphology mainly at this transition zone and high protein content.

5.4.2. FT ramping

In this section, the suitability of the toolbox applied to detect changes in system stability arising from different FT ramps is investigated. During the freezing process, the protein undergoes a state of freeze concentration, where protein degradation might take place. After passing T_g and entering the glassy state, protein degradation/aggregation stops [146, 219]. Before crossing T_g and entering the glassy state the eutectic point is crossed. The position of the eutectic point and the way the solution behaves are dependent on the solutes in the solution and describe how and when crystallization of the solutes and the ice takes place. The different possibilities are described in the state systems of the solutions [133]. This helps to get detailed information of the degree of concentration of the solutes while freezing.

Considering the thawing process it is the other way around and by choosing a steep initial ramp, the time, in which the protein is in the non-glassy, destructive state decreases [145, 153]. The influence of this in combination with the processing time during FT operations

might thus be a focus point when evaluating FT operations.

Freezing ramps

Three different freezing ramps were tested, a flat (R 1), mid (R 2) and steep ramp (R 3) (see Table 5.1). The phase behavior and the morphology showed clear differences, while changes in solubility line were not significant among the three systems. The two rapid systems R 2 and R 3 proved to be stable over the applied FT operations. This might be explained by several underlying processes: a) The lower the freezing speed, the more the conditions showed aggregation as seen for R 1. In general, the ratio of micro crystals to small tetragonal crystals changed towards micro crystals by lowering the slope of the freezing ramp. These trends are scored as more unstable (see Table 5.2). The trend to smaller crystals might be explained by several processes occurring during FT operations. One reason could be freeze concentration, leading to a situation where the energetic barrier is more easily overcome and critical nuclei are created for conditions otherwise not susceptible to creation of nuclei [28, 42, 45, 46], leading to an appearance of micro crystals. In addition, more critical nuclei might be created [47, 208]. Both, a decrease in size of the solubility zone, and the appearance of a lot small crystals have a negative impact on the solubility line. b) It is assumed that lysozyme is not affected by the water–ice–surface; otherwise, the steepest ramp would be the most damaging and the trend would be the other way around. With fast freezing, ice dendrites with high ice–surfaces are created, and protein species which denaturate on the ice surface are more damaged [109, 115]. In our case, however, the formation of ice dendrites would be highly desirable for improving the protein stability as well as its influence on the degree of freeze concentration [109, 229–233]. The faster the freezing ramp, the more dendrites are created [117]. In these interdendritic spaces, lysozyme and NaCl as well as all other solutes are trapped [117, 219] and extensive freeze concentration is hindered [118]. This is in agreement with the order of crystal morphologies stated above. Furthermore, when micro crystals they preferably grew in the low NaCl region. This might be due to the influence of the salt concentration on the ice front velocity and the degree of supercooling, which is higher for higher salt concentrations. Moreover, the route the solution takes trough the state diagram to reach T_g, respectively crossing the eutectic point, seems to be different for low NaCl concentrations compared to higher NaCl concentrations. The concentration of NaCl could be higher at low NaCl concentrations due to the pure crystallization of ice and no crystallization of NaCl, which leads to micro crystals. c) Finally, the overall time the protein is exposed to cold temperatures (lower than 0 °C) diminishes when steep ramps are applied and reduces the glassy state [145, 153], leading to an increase in the stability of a given system. This behavior could be observed in our study as well. R 3 and R 2 did show similar results for the solubility line, phase behavior and morphology and also have a very short process time compared to the other ramps (see Table 5.3).

Thawing ramps

The influence of the thawing ramp was investigated – in analogy to the freezing set up – applying three different ramps, a flat (R 8), mid (R 2) and steep ramp (R 9) (see Table 5.1). In general, the aggregation tendency increases when slow thawing is applied [118, 145]. This fits to a decreasing solubility zone observed. In addition flat thawing ramps show a higher degree of recrystallization compared to steep ramps [118]. Finally, applying flat thawing ramps the protein under investigation is exposed longer to the cold temperatures [145, 153]. The degree of recrystallization and/or the time at cold temperatures might be the reasons for the differences seen in phase behavior and morphology. The flat ramp (R 8) consequently showed the smallest solubility zone and co–appearance of precipitate and crystals at 0.4 M NaCl. It might further happen that with flat thawing ramps unfolding of protein increases [228], which in most cases results in protein precipitation [209].

5.4.3. Combinations

In addition to the above, two combinations with the potentially steepest (R 14) and flattest (R 15) ramp of the single steps were tested. The outcome of this comparison clearly highlights the above discussed dependencies on the processing speed (see Table 5.3).

5.4.4. Inflection points

The influence of different inflection points for ramps used in our study was tested during freezing as well as during thawing. The order of the system when applying our stability index (Table 5.3) showed that slow freezing or thawing in the higher temperature range (above or close to T_g) results in more unstable systems (R 4 and R 13). This is due to a high mobility of proteins above and a low mobility below this temperature [145, 153]. This might also have an influence on the morphology. The longer the protein is placed in the glassy state the more critical nuclei are created and lead to micro crystals, unsorted aggregation, and precipitation. The latter explains why these systems show an increasing number of micro crystals, co–appearance of crystals and precipitate (even more at FT c3). According to the literature, T_g of lysozyme is an a region between -30 and -70 °C depending on the solution conditions [146, 225]. Initial pre–tests with our system located T_g to be between -50 and -60 °C.

5.4.5. Stability index

The importance of the inflection point or T_g is further highlighted by the introduced stability index. By analyzing Table 5.3, it became clear that the processing time gives a

good first estimate on the suitability of a chosen ramp. However, a ranking according to the process time alone could not take into account, that proteins undergo different states trough trough the FT process. The introduced stability index SI_{cycles} clearly confirmed our hypothesis that suitable and stable systems show a low variability in morphology over several FT cycles. Furthermore, using morphology as a classification parameter allowed us to identify the significant influence the glass transition temperature has on the choice of suitable FT operations.

In contrast the order of SI_{FTc0} showed no correlation to the order obtained for repeated cycling or to process time. It can thus be derived that different processes dominate the two unit operations, namely initial FT operation and repeated FT cycling. This said, it becomes clear that the systems R 3, R 12, and R 14 were suitable for both initial FT operations and repeated cycling and thus might be the systems of choice for further investigations.

5.5. Conclusion

The applied phase diagram–based toolbox allowed the detection of the influence of different FT ramps on the protein solubility, phase behavior, and crystal morphology. It could be clearly shown that the glass transition temperature is a highly important parameter when designing suitable FT operations. Looking at the different process descriptors in more detail, the solubility could only support the statements made regarding the phase behavior and the morphology, with the morphology and morphological changes being the most important parameters. The data obtained when applying the toolbox allowed several assumptions to be made: (1) the ice surface does not have an influence on the stability of lysozyme, (2) recrystallization seems not to be a problem for the stability, (3) the main parameter influencing the FT operations seems to be the overall time of exposure to cold temperatures while being in the glassy state of the protein. Finally, two ranking schemes were applied based on the process time and variability of the system morphology. With the help of the overall process time, a presorting of the systems could be made regarding FT stability. Nevertheless, biochemical issues such as the glass transition temperature are not captured by this procedure. For a more detailed sorting the variation in morphology obtained between different cycles (FT c1 to FT c3) has to be taken into account. The introduced stability index could clearly capture the glass transition temperature and was found to be a good measure for system stability during FT operations.

In future work, the correlation of the underlying physical/biochemical processes with system stability will be further investigated.

6. Apparent cloud point temperature determination using a low volume high–throughput cryogenic device in combination with automated imaging

Marieke E. Klijn[1], Anna K. Wöll[1], Jürgen Hubbuch*

*Corresponding author. E-mail address: juergen.hubbuch@kit.edu

[1] These authors contributed equally to this work

Karlsruhe Institute of Technology (KIT), Institute of Process Engineering in Life Sciences, Section IV: Biomolecular Separation Engineering, Karlsruhe, Germany

Abstract

Short–term parameters correlating to long–term protein stability, such as the protein cloud point temperature T_{cloud}, are of interest to improve efficiency during protein product development. Such efficiency is reached if short–term parameters are obtained in a low volume and HT manner. This study presents a low volume HT detection method for (sub–zero) T_{cloud} determination of lysozyme, as such an experimental method is not available yet. The setup consists of a cryogenic device with an automated imaging system. Measurement reproducibility (median absolute deviation of 0.2 ℃) and literature–based parameter validation (Pearson correlation coefficient of 0.996) were shown by a robustness and validation study. The subsequent case study demonstrated a partial correlation between the obtained apparent T_{cloud} parameter and long–term protein stability as a function of lysozyme concentration, ion type, ionic strength, and freeze/thaw stress. The presented experimental setup demonstrates its ability to advance short–term strategies for efficient protein formulation development.

Keywords: *freeze/thaw, long–term protein stability, phase diagrams, lysozyme, liquid–liquid phase separation*

6.1. Introduction

Long–term protein stability is an important parameter to assess during the development of biopharmaceutical products, as it determines safety, efficacy, and manufacturability of the protein product concerned [6, 24, 26, 43, 234]. Long–term protein stability is governed by protein characteristics, such as structural flexibility, surface charge, and surface hydrophobicity, which in turn are influenced by environmental conditions, such as pH, excipients, temperature, and pressure [14, 24, 33]. Due to the intertwined influence of protein characteristics and its environmental conditions, long–term protein stability needs to be evaluated for each protein product separately. Currently, biopharmaceutical products need to be stored for at least 18–24 months to demonstrate long–term stability [4]. A wide range of environmental conditions is usually tested during the required storage time to obtain a broader product understanding. This knowledge supports the development of stable products, as well as the development of predictive approaches, which in turn leads to quicker formulation development of future products.

A common approach to evaluate long–term protein stability is to establish protein phase diagrams, where long–term protein stability is optically detected as a function of different environmental conditions [41]. In this study, protein phase diagrams were generated with microbatch experiments. These miniaturized experiments have been optimized for HT screening [158], to limit material usage and reduce the experimental workload. The microbatch experiments allow for screening a wide range of solution conditions, but these experiments still require a long–term storage period. To eliminate this prolonged storage period, and thereby reducing developmental resources, it is desired to move towards short–term protein evaluation parameters which correlate to long–term protein stability [233]. This can only be achieved when short–term evaluation parameters represent dominant factors that govern protein stability over time. In general, conformational stability (structural stability) and colloidal stability (protein–protein interactions) need to be represented, as modifications in these properties leads to protein aggregation [235]. Due to the complexity of long–term protein stability, and the underlying interplay of colloidal and conformational stability, various short–term parameters representing colloidal stability [182, 236], conformational stability [164, 237, 238], and a combination of both [53, 183, 184, 239, 240], have been evaluated. However, a set of short–term parameters that is applicable for most cases has not been established. A continued exploration of short–term parameters, to either represent colloidal or conformational stability, will advance the development of an analytical toolbox to determine environmental effects on long–term stability in a shorter time frame.

This work focusses on the protein T_{cloud} as short–term protein parameter, which is defined as the temperature at which LLPS occurs. T_{cloud} is dependent on the protein–protein interaction strength, where strong attractive interactions lead to LLPS at higher temperatures [149]. The dependency of T_{cloud} on protein–protein interactions makes it a known representative parameter of colloidal stability [140, 149–151, 241–243]. Formulations at low protein and salt concentration may need to reach sub–zero temperatures to induce

LLPS [150], as relatively weak attractive protein–protein interactions are found under such conditions [165]. When LLPS is induced by sub–zero temperatures, it occurs before the aqueous solution starts to freeze. LLPS results in the formation of protein–rich droplets in a protein–poor liquid phase, which causes an increase in solution turbidity [140]. The subsequent change in solution turbidity is often used to determine T_{cloud}. Experimental methods to determine T_{cloud} by means of solution turbidity include light scattering methods [35, 41, 140, 150, 244], UV–Vis absorbance [243], thermo–optical analysis (TOA) [242], microscopy [245, 246], and image analysis [247, 248].

T_{cloud} is a known representative of colloidal stability, but the incorporation of T_{cloud} as a short–term parameter in HT formulation screenings is dependent on its screening methodology as well. HT screening efficiency is desired to maintain an advantage over HT phase diagram construction. To achieve such screening efficiency in a T_{cloud} measurement, the following criteria have to be met: (a) an HT setup, to keep workload to a minimum, (b) low sample volume, to limit material use, and (c) the ability to measure at sub–zero Celsius temperatures, which is required to reach T_{cloud} for low protein concentrations. These three criteria are met separately by studies reported in the literature [242, 247]. However, to the best of our knowledge, an experimental method that combines all these criteria has not yet been reported. Therefore, this study seeks to combine all three criteria in a single experimental setup. In previous studies concerning the effect of FT cycles on protein formulations, an HT cryogenic device was employed [224, 249]. The HT cryogenic device meets criteria (a) and (b), as it is compatible with low volume microtiter plates. Criterion (c) is met as different FT rate combinations can be set within the operating temperature range of 20.0 °C to -100.0 °C allowing controlled sub–zero Celsius measurements. As all above–mentioned criteria are met with the HT cryogenic device, it was investigated whether the cryogenic device could be adjusted for T_{cloud} detection. To achieve this, an image–based analysis approach to detect the solution turbidity changes as a function of the temperature was employed. This was realized by adding an image acquisition system and light source onto the cryogenic device. The combination of the HT cryogenic device and the automated imaging system results in a low volume, HT, and sub–zero experimental setup for the detection of T_{cloud}.

The proposed experimental setup was subjected to a robustness and validation study to evaluate its performance. The robustness study was performed to select a representative T_{cloud} parameter and determine its reproducibility. The robustness was evaluated by T_{cloud} determination of 60 replicates at three different temperature rate combinations. The validation study was performed to compare the results obtained with the presented experimental setup to literature data. In addition to the robustness and validation study, the experimental setup was employed to perform a case study. In this case study, the effect of four different salts (sodium chloride (NaCl), sodium sulfate (Na_2SO_4), ammonium chloride (NH_4Cl), and ammonium sulfate (($NH_4)_2SO_4$) at ten different ionic strengths ($0-2025$ mM) on T_{cloud} of chicken egg–white lysozyme at six different concentrations ($3-18$ g/L) was investigated. These conditions were selected to cover a narrow range of low protein concentrations and a relatively wide range of ionic strength to further evaluate the performance of the proposed experimental setup. Subsequently, the correlation between T_{cloud} and long–term protein phase behavior was assessed. All formulations were also subjected to FT stress, in order

to investigate the correlation between T_{cloud} and FT stress–induced long–term protein instability. The correlation between T_{cloud} and the different environmental conditions was investigated to determine the applicability of the proposed experimental method as part of an analytical toolbox to correlate the long–term storage stability of protein formulations with short–term measurements. The robustness, validation, and case study were performed to demonstrate the reproducibility, reliability, and applicability of the presented low volume and HT protein T_{cloud} determination method in the field of long–term protein stability research.

6.2. Materials and methods

6.2.1. Buffer preparation

A 0.1 M acetate buffer at pH 4.5 was used for the robustness study. The respective buffer components were acetic acid (Merck KGaA, Darmstadt, DE) and sodium acetate (Sigma-Aldrich, St. Louis, MO, USA). For the validation study, a 0.6 M sodium phosphate buffer consisting of di–hydrogen phosphate (Merck KGaA) and di-sodium hydrogen phosphate (Merck KGaA), at eight different pH values (pH 5.8, 6.0, 6.3, 6.5, 6.8, 7.2, 7.4, and 7.8), was used. For the case study, a 20 mM MCB system [197] at pH 5.0 was prepared. The MCB consisted of AMPSO (33.01 mM; Sigma–Aldrich, St. Louis, MO, USA), TAPSO (28.92 mM; Sigma–Aldrich, St. Louis, MO, USA), MES (24.35 mM; AppliChem GmbH, Darmstadt, DE), formic acid (9.58 mM Merck KGaA), and D (+) malic acid (26.06 mM; Sigma–Aldrich, St. Louis, MO, USA). The pH value of each buffer was adjusted to ± 0.2 pH unit accuracy with 4 M sodium hydroxide (Merck KGaA) or 32% hydrochloric acid (Carl Roth GmbH + Co. KG, Karlsruhe, DE) as titrant, employing a five–point calibrated pH meter (HI-3220, Hanna® Instruments, Woonsocket, RI, USA) equipped with a SenTix® 62 pH electrode (Xylem Inc., White Plains, NY, USA). With the exception of the validation study buffer, for which the pH value was adjusted by mixing 0.6 M sodium di-hydrogen phosphate and 0.6 M di–sodium hydrogen phosphate in the appropriate ratios. After preparation, buffer solutions were filtered using a 0.2 μm Supor® polyethersulfone (PES) (Pall Corporation, Port Washington, NY, USA) filter. The pH value was verified and adjusted to an accuracy of ± 0.02 pH unit prior to use. The buffers were stored at room temperature for a maximum of 2 weeks after preparation.

6.2.2. Salt stock solution preparation

Salt stock solutions were prepared with sodium chloride (NaCl; Merck KGaA), ammonium chloride (NH$_4$Cl; Merck KGaA), sodium sulfate (Na$_2$SO$_4$; Merck KGaA), and ammonium

sulfate ($(NH_4)_2SO_4$; VWR, Radnor, PA, USA). For the robustness study, a sodium chloride stock solution of 2200 mM was prepared. For the case study, a stock solution with an ionic strength of 2025 mM was prepared for each of the four salts. This corresponds to a molar concentration of 2025 mM for NaCl and NH_4Cl, and 675 mM for Na_2SO_4 and $(NH_4)_2SO_4$. After stock preparation, the pH value was verified and adjusted when necessary. The salt stock solutions were filtered as described for the buffers. The salt stock solutions were stored at room temperature for a maximum of two weeks after preparation.

6.2.3. Protein stock solution preparation

A protein stock solution was prepared by dissolving lyophilized lysozyme from chicken egg white (Hampton Research, Aliso Viejo, CA, USA) in a 0.1 M acetate, 0.6 M sodium phosphate, or MCB buffer without salt for the robustness, validation, and case study, respectively. The protein stock solution was filtered over a 0.2 μm syringe cellulose acetate filter (VWR, Radnor, PA, USA). Desalting was performed with PD columns (G-25 MiniTrap or PD-10 Desalting, GE Healthcare, Uppsala, SE), employing the manufacturers spin protocol [250]. The protein concentration was determined with a NanoDrop 2000c UVVis spectrophotometer (Thermo Fisher Scientific, Waltham, MA, USA), using an extinction coefficient $E^{1\%}(280\,nm)$ of $22.00\,Lg^{-1}cm^{-1}$. The concentration of the protein stock solution was adjusted to 70.0 g/L, 90.0 g/L, and 54.0 g/L, with a standard deviation of ± 2.0 g/L, for the robustness, validation, and case study, respectively. Due to the detection range $(0-50$ g/L for lysozyme) of the employed UVVis spectrophotometer, 1:10 dilutions were prepared for all performed studies to determine the exact protein concentration. Protein stock solutions were prepared on the same day as the experiment.

6.2.4. Cloud point measurement

The experimental setup to determine T_{cloud} is composed of a cryogenic device (EF600M 105, Grant Instruments, Cambridgeshire, UK) and an image acquisition system. The complete setup is schematically depicted in Figure 6.1, where red lines indicate data transfer and blue lines indicate control connections. The image acquisition system includes a light source (USB Port 20 LED Ring, Ledmondo GmbH, Warngau, DE)(Figure 6.1 c), and a GoPro Hero4 camera (GoPro Inc., San Mateo, US)(Figure 6.1 d), which is controlled by a tablet (Samsung Galaxy NotePro 12.2, Samsung, Seoul, KR)(Figure 6.1 b). Images were obtained every 0.5 s for the robustness and the case study, and every 2.0 s for the validation study. The photo time lapse mode and the 7 megapixel medium mode were employed for all studies. Image–based data was saved on the camera (Figure 6.1 c) and transferred to the computer (Figure 6.1 a) after the measurement. Data on the measured temperatures during the experiment was transferred from the cryogenic device (Figure 6.1 g) to the computer (Figure 6.1 a). Employed settings of the cryogenic device are described

in previous work [224, 249]. All samples were prepared and measured in crystallization plates (MRC Under Oil 96 Well, SWISSCI AG, Neuheim, CH), sealed with Duck® Brand HD Clear sealing tape (ShurTech® brands, Avon, OH, USA), with a sample volume of $24\,\mu$L.
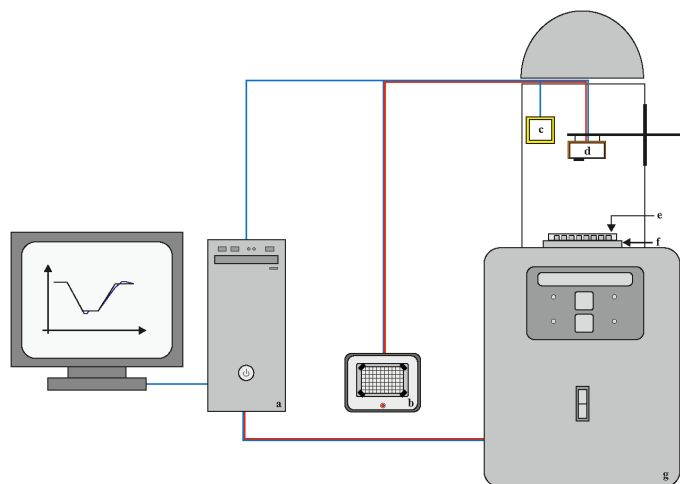
Figure 6.1.: Schematic drawing of the experimental setup. The setup is composed of a desktop computer (a), a tablet (b), a light (c), a camera (d), and a cryogenic device (g). The camera (d) is connected to a tablet (b) and a light (c). A microtiter plate (e) is clamped onto temperature-controlled adapter (f) in the cryogenic device (g). The tablet (b) displays the top view of the microtiter plate. The blue line represents control connections and the red line represents data transfer.

Robustness study

For the robustness study, 60 replicates of $54\,$g/L lysozyme in a $0.1\,$M acetate buffer at pH 4.5 with $550\,$mM NaCl were used to determine the reproducibility of the presented experimental method and the effects of FT rate combinations on T_{cloud} determination. The robustness study was also employed to evaluate the information content of the obtained data, where different distinct points were extracted and assessed. Samples were prepared using a mixing ratio of 2:1, which corresponds to $16\,\mu$L of $70\,$g/L lysozyme stock solution to $8\,\mu$L $2200\,$mM sodium chloride stock solution. To determine the effect of the selected FT rate combinations on the T_{cloud} measurement, three FT rate combinations were evaluated: (1) $0.5\,$°C/min freezing and $0.5\,$°C/min thawing, (2) $2.5\,$°C/min freezing and $2.5\,$°C/min thawing, and (3) $10.0\,$°C/min freezing and $2.5\,$°C/min thawing. All combinations were used to perform an FT run between $20.0\,$°C and -$10.0\,$°C, with a holding time of $1\,$min at -$10.0\,$°C, except for the first FT combination ($0.5\,$°C/min), where the holding time was omitted. For each rate combination, the deviation between the set temperature and the actual measured temperature in the cryogenic device can be found in the Supplementary Material, Figure B.5.

Validation study

The validation study was used to validate the presented experimental setup by comparing literature data to experimental T_{cloud} data obtained under similar conditions. The validation dataset consisted of six replicates of 90 g/L of lysozyme at eight different pH values (pH 5.8, 6.0, 6.3, 6.5, 6.8, 7.2, 7.4, and 7.8) in a 0.6 M sodium phosphate buffer. Samples (400 µL) were prepared in Eppendorf tubes (Eppendorf AG, Hamburg, DE) by dissolving the lysozyme directly into the respective buffer. Further details of the protein stock solution preparation are described in Section 6.2.3. The validation data was obtained by performing an FT run between 10.0 °C and -20.0 °C, employing a 0.1 °C/min FT rate and a holding time of 5 min at -20.0 °C. Comparative literature T_{cloud} data was obtained from Taratuta *et al.* [151].

Case study

The case study was performed to evaluate the change in lysozymes long–term stability and the correlation to T_{cloud} as an effect of four different salts (NaCl, NH_4Cl, Na_2SO_4, $(NH_4)_2SO_4$) at ten different ionic strengths (0, 225, 450, 675, 900, 1125, 1350, 1575, 1800, and 2025 mM) in combination with six lysozyme concentrations (3, 6, 9, 12, 15, and 18 g/L). This resulted in 60 samples per salt type. The samples per salt type were prepared manually in a single 96–well plate. T_{cloud} was determined with an FT rate combination of 2.5 °C/min freezing and thawing to perform an FT run between 20.0 °C and -80.0 °C, with a holding time of 30 min at -80.0 °C. All plates were prepared and measured in duplicate. These settings were chosen to match an FT cycle that was used to investigate the effect of FT stress on long–term protein stability [249]. This allowed for the evaluation of the correlation between the influence of FT stress on long–term stability and T_{cloud}, in addition to the effects of protein concentration, salt type, and ionic strength on long–term stability.

6.2.5. Long–term storage

To evaluate the correlation between T_{cloud} and long–term protein phase behavior of lysozyme, all case study samples were monitored at 20.0 °C for 40 days in the incubation chamber RockImager54 (Formulatrix, Bedford, MA, USA). Monitoring long–term protein phase behavior consisted of two experiments. The first experiment included the preparation, storage, and monitoring of lysozyme under the case study conditions that were not subjected to the FT cycle needed to determine T_{cloud}. The second experiment included the storage of lysozyme under the case study conditions that were used to determine T_{cloud}. These two experiments were performed as lysozyme aggregation during long–term storage is influenced by the required FT run to determine T_{cloud} [249]. The employed approach allowed for the evaluation of long–term phase behavior of lysozyme as a function of T_{cloud} with and without FT stress effects. Preparation and handling of the long–term phase

behavior experiments were performed as published by Baumgartner et al. [158]. Storage was monitored via imaging with visible light at 0 h, 1 h, 2 h, every 2 h until day 1, every 4 h on day 2, every 6 h until day 8, and every 24 h from day 9 until day 40. In addition to visible light imaging, cross–polarized light and ultraviolet (UV) light images were captured on day 0, 1, 5, 10, 20, 30, and 40. All plates were prepared and monitored in duplicate.

6.2.6. Data processing

Unless stated otherwise, all images obtained during T_{cloud} measurements and long–term storage experiments were imported for data processing, and all data processing and visualization was conducted with MATLAB (version 2018b, MathWorks, Natick, MA, USA) and R (version 1.0.136).

Cloud point detection

Images obtained during the T_{cloud} measurement capture the entire plate. The images were converted to grayscale and cropped to evaluate each well separately. The total intensity difference between the first image of a well and every other time point was calculated for each of the 60 wells. The intensity difference between the first well image and each well image in time was obtained by subtracting the respective images, using MATLAB function *imsubtract*. The total intensity difference was subsequently calculated by summing up the intensity of the subtraction image. This resulted in a total intensity difference value for each time point. An example of the cropped well images and a schematic overview of the described processing can be found in Supplementary Figure B.4. From the total intensity difference data over time, four temperatures of interest were extracted: (1) clouding onset temperature (T_{CO}), (2) clouding end temperature (T_{CE}), (3) declouding onset temperature (T_{DO}), and (4) declouding end temperature (T_{DE}). All extracted temperature values were based on the temperatures measured by the cryogenic device. Figure 6.2 a shows an exemplary total intensity over time graph including these temperatures of interest. An increase in total intensity difference can be observed as the temperature decrease, for which the descriptive term clouding is used, and a decrease in total intensity difference is depicted upon increasing the temperature, for which the descriptive term declouding is used.

To extract T_{CO} and T_{CE}, the maximum gradient in total intensity increase was determined during cooling. The maximum gradient was extracted from the first derivative of the total intensity difference data over time. A schematic of the first derivative is shown in Figure 6.2 b. The first derivate was calculated from a smoothing spline fit of the total intensity different data over time, employing MATLAB functions *fit* and *differentiate*. A smoothing parameter of 0.03 was used. The maximum gradient was defined as the maximum value of the first derivative within the search space during freezing. With the identification of the maximum gradient, T_{CE} and T_{CO} were extracted. The point at which the first derivative becomes negative before the maximum gradient was used to define T_{CO},
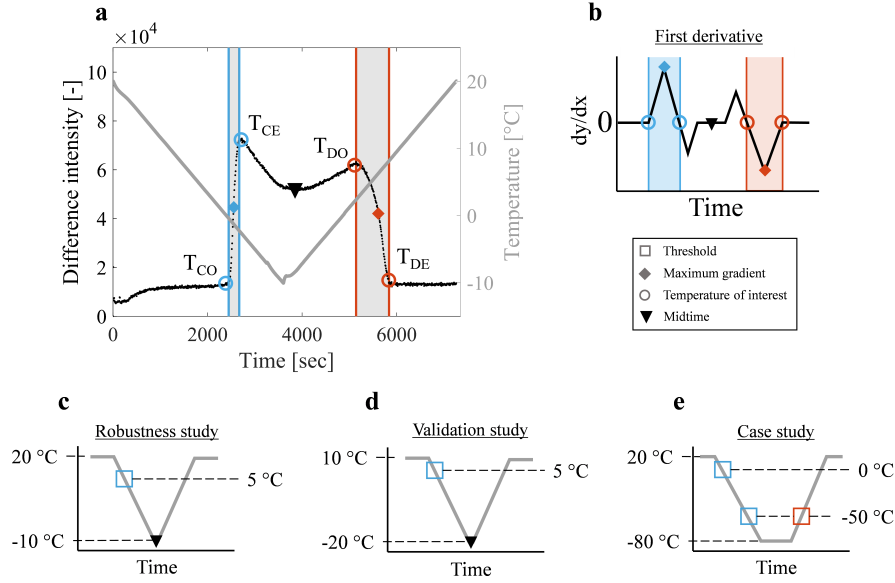
Figure 6.2.: Schematic visualization of the employed data extraction protocol. (a) An exemplary plot of a resulting intensity difference over time graph, with an indication of the start of the temperatures of interest (circles), maximum gradient (diamond), and midtime (triangle). The difference intensity (left y-axis; black) is plotted against the time (x-axis; seconds). The measured temperature is shown as well (right y-axis; gray; řC). Four points are highlighted, which are named (1) clouding onset temperature (T_{CO}), (2) clouding end temperature (T_{CE}), (3) declouding onset temperature (T_{DO}), and (4) declouding end temperature (T_{DE}). (b) Schematic of the first derivative of the data in (a). (c) Graph indicating the starting temperature of the freezing search space (blue square) of the robustness study. (d) Graph indicating the starting temperature of the freezing search space (blue square) of the validation study. (e) Graph indicating the starting and end temperature of the freezing search space (blue square), as well as the starting temperature of the thawing search space (orange square) of the case study.

while the first negative point after the maximum gradient was used to define T_{CE}. T_{CO} and T_{DE} were determined with the use of the maximum gradient of total intensity difference decrease during thawing. The maximum gradient was defined as the minimum value in the first derivative within the search space during thawing. T_{DO} was defined as the maximum total intensity value in the thawing search space before the maximum gradient. T_{DE} was defined as the point where the derivative becomes positive after the maximum gradient of total intensity decrease.

Figure 6.2 c-e depict the temperature thresholds that were employed during data extraction for each study. For the robustness and validation study, the freezing search space start was set at 5.0 °C and the freezing search space end was set at middle time point of the overall measurement (midtime). The freezing search space start was set to 5.0 °C, as camera movement was observed before this temperature was reached. The thawing search space was set between midtime and the end of the measurement for both studies. For the case study, the freezing search space was set between 0.0 °C and -50.0 °C and the thawing search

space was set between -50.0 °C and the end of the measurement. A freezing search space starting point of 0.0 °C was chosen to eliminate initial camera movement effects and a freezing search space endpoint of 50.0 °C was chosen as solutions were assumed to be frozen below -50.0 °C.

For the validation study and case study, one image every 10.0 and 2.5 s was processed, respectively, due to a large number of images generated (one every 2.0 and 0.5 s, respectively) during the ∼10.0 h (validation study) and ∼2.5 h (case study) measurements. Data obtained for the validation study was smoothed using a moving mean window of 100 data points before fitting, employing the *movmean* MATLAB function. A similar smoothing procedure was applied for the case study data, employing a moving mean window of 25 data points. An example of smoothed data can be found in the Supplementary Material, Figure B.10.

Validation study

In the validation study, six replicates of eight samples were measured. T_{CE} was determined for each replicate separately. The median T_{CE} of all six replicates was calculated to represent the central tendency of each sample, and the MAD of the T_{CE} was calculated to represent the deviation between the replicate samples. To compare experimental data with literature data, both datasets were scaled to the respective minimum and maximum value using Equation 6.1.

$$y' = \frac{y - y_{min}}{y_{max} - y_{min}} \tag{6.1}$$

In Equation 6.1, y represents the scaled value, y represents the raw value, y_{min} represents minimum value in the respective dataset, and y_{max} represents the maximum value in the respective dataset.

The PCC and mean squared error (MSE) were used as evaluation parameters to determine the correlation and error between literature and experimental data, respectively. The PCC was calculated with MATLAB function *corrcoef* and the MSE was calculated with Equation 6.2.

$$MSE = \frac{1}{n} * \sum_{i=1}^{n} i * (y_i - \hat{y}_i)^2 \tag{6.2}$$

In Equation 6.2, y_i represents the experimental data point, $\hat{y}_i$ represents the literature data point, and n the total number of data points.

MPPD

Long–term stability of lysozyme formulations was evaluated employing a MPPD [251]. In an MPPD, morphologic and kinetic aggregation data obtained from images taken during storage is compiled in one figure by data dimension reduction and subsequent clustering. The following data was extracted from images obtained during storage: (1) length of a

maximum of four crystals in m, (2) width of a maximum of four crystals in m, (3) percentage of aggregation well coverage (n_{Agg}), (4) aggregation growth onset time (t_0) in hours, and (5) aggregation cessation time (t_E) in hours. The length and width of a maximum of four crystals were used to calculate the mean crystal length (L_C) and width (W_C), as well as the interquartile range of the crystal lengths ($\triangle L_C$) and widths ($\triangle W_C$). This data was used to represent the average crystal dimensions and its distribution, respectively. For the extraction of the aggregation growth onset and cessation time, it was decided to employ UV light images. This was done as preliminary data extraction of aggregation growth onset and cessation time based on UV light images showed a good correlation to initial visual inspection (data not shown). The total intensity difference of UV images over time was obtained and fitted as described in Section 6.2.6. The first derivative of the fitted total intensity difference obtained from UV images over time was used to determine t_0 and t_E. The time point at which 90% of the maximum value in the first derivative was reached was defined as t_0. The time point at which 20% of the maximum value in the first derivative was reached after t_0 was used to define t_E. The difference between t_0 and t_E was used to define aggregation growth time (t_G).

The MPPDs were constructed using L_C, W_C, $\triangle L_C$, $\triangle W_C$, n_{Agg}, t_0, and t_G. All data was extracted for each duplicate plate and averaged. An MPPD for each plate was also constructed separately to determine reproducibility. This data can be found in the Supplementary Material, Figure B.14. The results of the long–term storage experiment were shown to be reproducible for all conditions, except for the two plates containing lysozyme in combination with $(NH_4)_2SO_4$ stored without being subjected to an FT run. One of these duplicate plates showed dried up wells after storage, which influenced the observed aggregation morphology. Based on this observation, only the data obtained from the plate without dried up wells was used. All settings for the MPPD construction have been described in previous work [251], where the clustering algorithm selected an optimal cluster number between 1 and 8 clusters.

6.3. Results and discussion

6.3.1. Robustness study

The robustness study was performed to evaluate the experimental performance and reproducibility of the proposed experimental setup. The experimental performance was assessed using three different FT rate combinations in three separate measurements. Reproducibility was evaluated by measuring 60 replicate samples for each FT rate combination. The robustness study was also used to evaluate four temperature points (T_{CO}, T_{CE}, T_{DO}, T_{DE}) that were extracted from the resulting data as potential representation of T_{cloud}. Table 6.1 lists the median $\pm$ MAD of the four temperature points obtained with three rate combinations based on 60 replicate samples.

Table 6.1.: Overview of T_{CO}, T_{CE}, T_{DO}, and T_{DE} for three different FT rate combinations (℃/min) obtained for the robustness study. The values are given as median ± MAD, obtained with a sample size of n = 60.

Freezing rate [℃/min]	Thawing rate [℃/min]	T_{CO} [℃]	T_{CE} [℃]	T_{DO} [℃]	T_{DE} [℃]
0.5	0.5	-0.4 ± 0.2	-2.3 ± 0.1	1.6 ± 0.9	7.9 ± 0.4
2.5	2.5	-4.4 ± 1.2	-7.0 ± 0.3	4.9 ± 0.0	7.1 ± 0.5
10.0	2.5	-14.1 ± 0.4	-13.3 ± 0.3	4.0 ± 0.3	6.1 ± 0.3

The applied FT rate combinations were set to operate in a range between 20.0 ℃ and -10.0 ℃. Temperature points measured outside the set boundaries, such as the T_{CO} (-14.1 ± 0.4 ℃) and T_{CE} (-13.3 ± 0.3 ℃) for a freezing rate of 10.0 ℃/min, indicated a hardware complication. It was observed that the set temperature differed from the actual measured temperature inside the cryogenic device, as shown in the Supplementary Material, Figure B.5. The evaluation of different FT rates showed a larger deviation for faster rates, where an MSE of 0.01 ℃^{2} was found for an FT rate of 0.5 ℃/min, and an MSE of 14.85 ℃^{2} for 10 ℃/min freezing in combination with 2.5 ℃/min thawing. This indicates that temperature control in the presented experimental setup is less reliable for faster FT rates compared to slower rates.

The applied FT rates affected the absolute temperature point (T_{CO}, T_{CE}, T_{DO}, T_{DE}) values as well. Both clouding temperature points, T_{CO} and T_{CE}, were highest when a freezing rate of 0.5 ℃/min was applied. Increasing the freezing rate to 2.5 ℃/min and 10.0 ℃/min showed a decrease of T_{CO} (from -0.4 ± 0.2 ℃ to -4.4 ± 1.2 ℃ and -14.1 ± 0.4 ℃, respectively) and T_{CE} (from -2.3 ± 0.1 ℃ to -7.0 ± 0.3 ℃ and -13.3 ± 0.3 ℃, respectively). This observation could be explained by two effects. The first effect considers a relatively low detection sensitivity. It was assumed that it takes a certain amount of time for the formulation to reach a level of cloudiness that is detectable by the presented experimental setup. The temperature continues to decrease during this time, and faster freezing rates resulted in a lower absolute temperature than slower freezing rates. Thus, upon reaching the detectable level of cloudiness, a lower absolute temperature was found for T_{CO} and T_{CE} for faster freezing rates. The second effect considers the inconsistency between the measured temperature in the cryogenic device and the actual (unmeasured) temperature of the sample. It has been reported for three different temperature decreasing steps (0.3 ℃, 1.0 ℃, and 3.0 ℃) that an increased amount of time (∼6, ∼20, and >30 min, respectively) was required to obtain the desired sample temperature for larger temperature steps [247]. This would result in the detection of T_{CO} and T_{CE} at lower temperatures for faster freezing rates, as the sample temperature adjusts slower than the measured temperature in the cryogenic device. Both these effects could also explain the difference in T_{DO} for different thawing rates, where the 0.5 ℃/min thawing rate shows the lowest T_{DO}.

Table 6.1 shows a difference between the range of the clouding temperature points (∼0.0 ℃ to ∼ -14.0 ℃) and the declouding temperature points (∼1.0 ℃ to ∼8.0 ℃). The occurrence of formulation clouding at a lower temperature compared to the formulation declouding

temperature has been reported in literature and was attributed to required nucleation energy for the formation of a new phase [140]. The obtained differences between the clouding temperature and the declouding temperature in the presented robustness study ($\sim$6 °C) are larger than that reported in the literature ($\sim$1.0 °C). This could be due to the employed combination of freezing and thawing instead of cycling through the clouding or the employed freezing rate, where the freezing rate in literature was 0.2 °C/min [140] instead of 0.5-10.0 °C/min. The freezing rate may have caused an increased distance between the clouding and declouding temperature, as this effect was also observed for the different FT rate combination results listed in Table 6.1.

The robustness study was also used to evaluate each temperature point individually, in order to determine which temperature point could be used to represent T_{cloud}. An absolute T_{DO} value of 4.9 $\pm$ 0.0 °C and 4.0 $\pm$ 0.3 °C was obtained with a freezing rate of 2.5 °C/min and 10.0 °C/min, respectively, while a similar 2.5 °C/min thawing rate was used. The difference between the T_{DO} values indicates that the absolute value was influenced by the freezing rate. This was attributed to the lack of temperature control for faster freezing rates. The influence of the temperature control sensitivity on the freezing rate, and indirectly on the absolute values of declouding temperature points, makes declouding temperature points less reliable as a comparative evaluation parameter. Terefore, the declouding points were not considered to represent the protein T_{cloud}. Between the two clouding points, T_{CO} and T_{CE}, T_{CE} showed a lower average MAD value (0.6 °C and 0.2 °C for T_{CO} and T_{CE}, respectively) and was, therefore, chosen as T_{cloud} representation.

Compared to the literature, the T_{CE} MAD of 0.20 °C is only slightly higher than the standard deviation of 0.13 °C reported for another image–based T_{cloud} detection setup [247]. A light scattering–based approach to determine T_{cloud} reported a reproducibility of a few tenths of a degree [35], which is comparable for the MAD shown in Table 6.1. Thus, an average MAD of 0.20 °C reflects a low deviation between 60 replicates and shows that the determination of T_{CE} is precise and reproducible. The corresponding intensity difference value for T_{CE} and T_{DO} as well as the absolute T_{CE} value was inspected per well to investigate the potential detection bias towards certain well positions as an effect of the employed light and camera setup. Upon inspection of the intensity difference values at T_{CE} and T_{DO}, a slight well position bias as a result of the experimental light and camera location could be observed, as shown in the Supplementary Material, Figure B.6. Despite this observation, the data extraction protocol has shown to be robust towards such intensity deviations, as a high precision and reproducibility of T_{CE} was found. A plate format visualization of the absolute T_{CE} values per well, for each FT rate combination, is shown in the Supplementary Material, Figure B.7.

The robustness study showed that temperature point detection by means of image analysis is precise and reproducible. However, the evaluation of three different FT rate combinations showed a hardware complication regarding set temperature values, where a decrease in temperature control was seen for faster FT rates. It was also observed that the applied FT rate combinations influenced the absolute value of the observed temperature points. This means that the results obtained with the proposed experimental setup are applicable for comparative screening purposes when similar cryogenic device settings are employed. Based on the robustness study results, T_{CE} was selected as a representation of T_{cloud}.

6.3.2. Validation study

The validation of the proposed experimental setup to yield a representative parameter of T_{cloud} was conducted based on a comparison between experimental and literature data. Eight samples were reproduced from the literature [151] and the corresponding T_{CE} was determined. The experimental and literature results are shown in Figure 6.3.

Figure 6.3 shows experimental and literature data, where normalized and absolute values
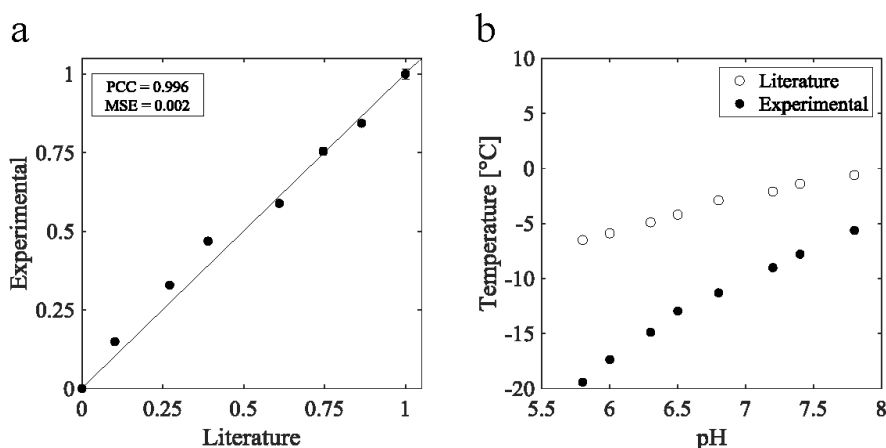
Figure 6.3.: (a) Comparison between normalized literature [151] (x–axis) and experimental data obtained for the validation study (y–axis). Two evaluation parameters are shown, (1) the Pearson correlation coefficient (PCC) and (2) the mean squared error (MSE). (b) Absolute literature cloud point temperature values as open circle and experimental clouding end temperature values as filled circles (y–axis; ℃) per pH value (x–axis).

are displayed in 6.3 a and 6.3 b, respectively. Both figures include MAD error bars for the experimental data, which were calculated based on six replicates. The relatively small size of the error bars indicates a precise measurement. This was confirmed by the inspection of the experimental T_{CE} per well (Supplementary Material Figure B.9) and the absolute T_{CE} values (Supplementary Material Table B.2). The normalized validation study results displayed in Figure 6.3 a show a strong linear dependency between T_{cloud} reported in the literature and T_{CE} obtained with the proposed experimental setup. This is represented by a PCC of 0.996, where a PCC of above 0.900 indicates a strong linear dependency between evaluated datasets [252]. In addition, an MSE of 0.002 indicates a small error between normalized experimental and literature data. The PCC and MSE reflect that T_{CE} is applicable as a representation of T_{cloud}. Despite the strong correlation between normalized experimental and literature data, the absolute values shown in Figure 6.3 b are not comparable. The strong correlation of normalized data in combination with the absolute value differences indicates that T_{CE} is an apparent T_{cloud}.

The detection of deviating absolute temperatures was attributed to the employed experimental setup, where three differences were identified compared to the literature setup. The first difference is the employed FT rate. An FT rate of 0.1 ℃/min was employed for the presented validation study. This rate was selected based on the mentioned temperature control

accuracy of 0.1 °C in the literature study used for comparison, but an exact FT rate was not documented. The applied FT rate has a large influence on the absolute temperature, as discussed in the robustness study (Section 6.3.1). The experimental data consistently shows lower absolute temperatures, which means that the employed freezing rate in the validation study was faster than the actual rate employed in the literature. A difference between set and measured temperature during the validation study measurements was not considered as a reason for the absolute temperature deviation, as the set and measured temperature were identical. This data can be found in the Supplementary Material, Figure B.8. The second difference between literature and experimental data is the T_{cloud} detection approach. With the proposed experimental setup, it was aimed to detect a T_{cloud} during an FT cycle, which is the standard application of the employed HT cryogenic device. In the literature study, the temperature was decreased until a light scattering beam disappeared ($T_{disappear}$). This was followed by a temperature increase to determine the temperature at which the scattered light beam reappeared (T_{appear}). T_{cloud} was defined as the average of $T_{disappear}$ and T_{appear}. Due to the different approaches, the literature study setup may have had a relatively high detection sensitivity (light scattering versus visible light images) and a higher control over sample temperature (cycling through T_{cloud} versus passing T_{cloud}). Both effects are mentioned in the robustness study as factors that could lead to the detection of a lower absolute temperature when the proposed experimental setup is employed. The third difference is the sample volume. Although it remains speculative, the undocumented sample volume used in the literature study was assumed to be larger compared to the sample volume of $24 \mu L$ used in this work. This was speculated as a sample volume of $20 \mu L$ was considered small in other work [242]. However, the influence of sample volume on the absolute temperature values can be refuted based on the comparison of other absolute temperature values reported on in literature. The comparable absolute T_{cloud} of ~14.0 °C [150] and 12.1 °C [242] were obtained for similar formulations (87 g/L lysozyme at pH 7.0 in a 20 mM Tris buffer with 0.5 M NaCl [150, 242]), while the sample volume was assumed to differ at least one order of magnitude ($20 \mu L$ [242] and 2 mL (undocumented) [150]). Based on the identification of these experimental differences, it is speculated that the observed absolute temperature deviation in the validation study is a result of the employed freezing rate, the detection method, the detection approach, or a combination of these factors.

Absolute temperatures obtained with the proposed experimental setup are considered apparent T_{cloud} values. Variations in temperature rates during the measurement and cycling through T_{cloud} may allow for the detection of a true T_{cloud} while employing a cryogenic device and image–based data evaluation. However, the exploration of these system settings is not within the scope of this work. The objective was to obtain a comparative evaluation parameter with the presented experimental setup that correlates to T_{cloud}. This objective was reached as the validation study showed a strong correlation between literature and experimental data.
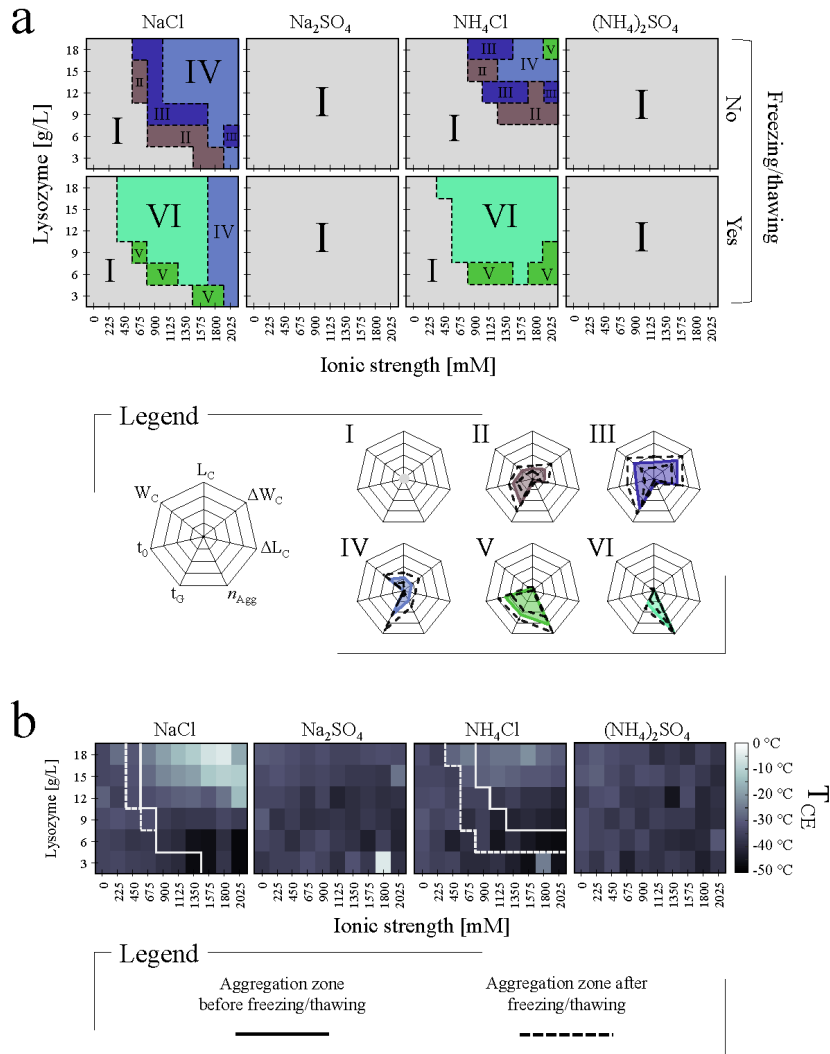
Figure 6.4.: (a) Average MPPD for four different salts (grid columns) and with or without freezing/thawing (grid rows), as well as varying lysozyme concentrations (y–axis; g/L) and ionic strength (x–axis; mM). Applied salts are sodium chloride (NaCl), sodium sulfate (NaSO$_4$), ammonium chloride (NH$_4$Cl), and ammonium sulfate ((NH$_4$)$_2$SO$_4$). Six clusters were identified and visualized in the MPPD using the mean cluster color and cluster number similar to the radar charts. The cluster regions are highlighted in the MPPD with a dashed line to guide the eye. The normalized median values of each image feature are represented with a color surface in the radar charts below the MPPD. The following image–based features are displayed per cluster: median crystal length (L_C), interquartile range (IQR) of the crystal width ($\triangle W_C$), IQR of the crystal length ($\triangle L_C$), aggregation well coverage (n_{Agg}), aggregation growth time (t_G), aggregation onset time (t_0), and median crystal width (W_C). The dotted line in the radar chart represents the median absolute deviation within each cluster for each image feature. Absolute cluster values can be found in Supplementary Table B.3. (b) Average cloud end temperature (T_{CE}; °C for the same four salts shown for the MPPD (major grid columns), as well as varying lysozyme concentrations (y–axis; g/L) and ionic strength (x–axis; mM). Aggregation zones observed in the MPPD are represented with a solid line (aggregation zone before freezing/thawing) and a dashed line (aggregation zone after freezing/thawing).

6.3.3. Case study

A case study was performed to evaluate the correlation between T_{CE} and long–term protein stability. In particular, morphologic and kinetic changes observed in long–term instable formulations as a result of different environmental conditions (lysozyme concentration, ionic strength, salt type, and FT stress) were considered. Long–term protein stability was assessed after a 40–day storage period at 20 °C with the use of MPPDs.

Long–term protein stability

Averaged results of the long–term storage experiment are depicted in the MPPDs in Figure 6.4 a, where lysozyme was monitored for 40 days at 20 °C under 240 different formulations. The top row presents formulations with NaCl, Na_2SO_4, NH_4Cl, and $(NH_4)_2SO_4$ that were not subjected to FT stress. The bottom row presents 240 similar formulations, but these formulations were subjected to FT stress. For each MPPD, the lysozyme concentration is plotted on the y–axis, ranging from 3 to 18 g/L with a step size of 3 g/L. The x–axis indicates the ionic strength of each corresponding salt, ranging from 0 to 2025 mM with a step size of 225 mM. The reproducibility of the long–term stability study was confirmed based on the separate results for each measured duplicate, which are shown in the Supplementary Material, Figure B.14.
MPPD construction includes a data dimension reduction step in order to visualize all morphologic and kinetic data in a single figure. The data reduction step resulted in an energy value of 93.6%, which indicates a 6.4% information loss. This percentage of information loss falls within the accepted range of 10% information loss upon data dimension reduction [253]. Clustering of the reduced dataset yielded an optimal number of six clusters, which are shown as radar charts (I-VI) in the legend of Figure 6.4 a. Each radar chart represents a different combination of image–based features, where the normalized median values are visualized as a colored surface and the corresponding MAD is shown as a dashed line. The image features used to construct the MPPD describe the crystal length (L_C), variation in crystal width ($\triangle W_C$), variation in crystal length ($\triangle L_C$), aggregation abundancy (n_{Agg}), aggregation growth time (t_G), aggregation onset time (t_0), and crystal width (W_C). Absolute values for each image feature per cluster can be found in the Supplementary Material, Table B.3. An exemplary image for each MPPD cluster is presented in the Supplementary Material, Figure B.12. MPPDs obtained for the case study were employed to visualize the effects of environmental conditions on aggregation morphology and kinetics detected during the long–term stability experiment. The applicability of MPPDs for this purpose was already shown in previous work [251]. In the following three subsections, the effects of anions, cations, and FT stress on long–term protein stability are presented. In the fourth section, the correlation between T_{CE} and the results obtained with the long–term stability experiment will be discussed.

Anions

Cluster I in Figure 6.4 a represents formulations that remained stable during the 40–day storage period. All image features for the formulations part of cluster I are equal to zero, as aggregation was not observed. Cluster I was identified for all formulations containing sulfate ($SO_4{}^{2-}$) anions, as well as formulations containing chloride (Cl^-) anions, but only at low lysozyme concentrations and low ionic strength. This trend remained similar upon freezing/thawing the formulations, as can be observed when comparing the top and bottom row of Figure 6.4 a. The maintained stability of lysozyme formulations containing $SO_4{}^{2-}$ can be attributed to the difference in molar concentration and the ability of the anions to promote salting–out effects. Formulations with monovalent Cl^- anions have a three–fold higher molar concentration compared to divalent $SO_4{}^{2-}$ anions, while a similar ionic strength is reached [254]. The maintained stability may be due to the relatively small absolute number of $SO_4{}^{2-}$ anions, which would be higher if similar molar concentrations were used instead of similar ionic strength. The other explanation involves the ability of anions to promote protein aggregation, which usually follows the order of the Hofmeister series [72]. However, the direction of the Hofmeister series is determined by ion-specific characteristics, such as polarizability, and protein-specific characteristics, such as surface charge and surface hydrophobicity [255]. In turn, protein-specific characteristics are dependent on environmental conditions, which results in a changing the Hofmeister series direction as a function of, for example, the solution pH [73] or the ionic strength [74]. According to the direct order of the Hofmeister series, $SO_4{}^{2-}$ is considered a protein structure stabilizer (kosmotropic), which induces salting-out behavior. Cl^- is considered a weak protein structure destabilizer (weakly choatropic), which is prone to induce salting-in behavior [255]. For a reversed Hofmeister series the opposite salting–in and salting-out effects are expected. In this case study, lysozyme was formulated at pH 5.0. It was assumed that lysozyme carries a positive charge at this pH value, as the theoretical pI of lysozyme lies at 11.35 [23]. It has been reported that a reversed Hofmeister series was observed for a positively charged lysozyme at low salt concentrations (<300 mM), while a direct Hofmeister series was observed for higher concentrations [74]. However, the mentioned Hofmeister series reversal was seen for formulations at pH 9.4 and was not confirmed for similar formulations at pH 4.1 (Supplementary data of [74]). The observations of this case study are in line with the literature results at pH 4.1, as a reversal in aggregation propensity as a function of molar salt concentrations was not seen between 0 and 2025 mM. In other works, it has been reported that lysozyme crystallizes readily at pH 5.0 in the presence of weakly hydrated anions such as Cl^-, but not with $SO_4{}^{2-}$ anions, which confirms the reversed Hofmeister series observed in the presented MPPD [163, 256]. This behavior was attributed the direct binding of Cl^-, which results in a neural lysozyme protein and subsequent attractive protein-protein interactions, while the indirect interfacial effects of strongly hydrated anion, such as $SO_4{}^{2-}$ anions, were assumed less dominant [257]. The observed long–term stability of lysozyme formulations containing $SO_4{}^{2-}$ anions is, therefore, attributed to the lack of anion binding, which was achieved by the weakly hydrated Cl^- anions.

Cations

The dominance of anions on long–term protein stability is recognized by the observed aggregation for formulations containing Cl^- anions, and the lack thereof for formulations containing $SO_4{}^{2-}$ anions. Therefore, the results obtained for formulations containing Cl^- anions will be used to discuss the influence of cations on long–term stability. MPPDs representing formulations containing sodium (Na^+), with and without FT stress, show a larger aggregation zone compared to formulations containing ammonium ($NH_4{}^+$). This translates to a lower solubility limit for the evaluated formulations containing Na^+ (3 g/L) compared to formulations containing $NH_4{}^+$ (7 g/L). Solubility data was obtained by measuring the protein concentration in the supernatant of the aggregated formulations after the 40 days of storage. The corresponding data is shown in the Supplementary Material, Figure B.11. The solubility data also shows that the solubility limit was reached at lower ionic strength for formulations containing Na^+ cations (1125 mM) compared to formulations containing $NH_4{}^+$ cations (1575 mM). The ionic strength and molar concentration of NaCl and NH_4Cl are similar, and thus observed differences are a result of the employed cation. This is in accordance with previously published work [194, 256] and was attributed to the larger hydration force of Na^+ compared to $NH_4{}^+$ [194].

The identified MPPD clusters are comparable between the cation types, where a cluster transformation from cluster II to cluster III and cluster IV can be observed for increasing ionic strength and lysozyme concentration. Cluster II is identified at the aggregation zone border. The aggregation zone border is often referred to as the labile or crystallization zone, where the energy barrier to create nuclei is overcome and crystal growth can occur [41]. The observed morphology and kinetics in cluster II correspond to this phase. Cluster II represents a few ($n_{Agg} = 5 \pm 4\%$) relatively large crystals ($L_C = 271 \pm 67\,\mu m$ and $W_C = 157 \pm 67\,\mu m$) that have a relative late onset time ($t_0 = 301 \pm 61\,h$) and grow for $553 \pm 173\,h$. The mentioned values are median $\pm$ MAD, which are calculated based on all formulation within the mentioned cluster. Upon supersaturation increase (increasing lysozyme concentration or ionic strength), cluster III is identified. An increase in supersaturation from the labile zone is expected to result in larger crystals, due to the increased ability to support crystal growth [258]. This corresponds to the changes in image features observed for cluster III compared to cluster II. For cluster III, an increase in crystal amount ($n_{Agg} = 8 \pm 4\%$), size ($L_C = 424 \pm 138\,\mu m$ and $W_C = 295 \pm 99\,\mu m$), and growth time ($t_G = 660 \pm 116\,h$) was observed compared to cluster II. A further increase in supersaturation should result in increased crystal abundance while the crystal size decreases [258, 259]. This corresponds to the features represented by cluster IV, where a higher abundance ($n_{Agg} = 23 \pm 15\%$) of smaller crystals ($L_C = 340 \pm 124\,\mu m$ and $W_C = 219 \pm 84\,\mu m$) with a more uniform size distribution ($\triangle L_C = 98 \pm 84\,\mu m$ and $\triangle W_C = 84 \pm 81\,\mu m$) was found compared to cluster III.

Freezing/thawing

The adverse effect of freezing/thawing protein formulations with respect to long–term protein stability was observed for NaCl and NH_4Cl formulations. This was reflected by

a decrease in solubility, and thus an increase in aggregation zone, as well as by MPPD cluster transformations. For formulations containing NaCl, 675 mM was the lowest ionic strength for which aggregation occurred before applying FT stress. After subjecting NaCl formulations to FT stress, the lowest ionic strength that induced protein aggregation was 450 mM. The influence of FT stress was more pronounced for NH_4Cl formulations, where a minimal ionic strength of 900 mM and 450 mM were found, respectively. The solubility limit of lysozyme for the evaluated NH_4Cl formulations after freezing/thawing decreased from 7 to 6 g/L compared to formulations when no FT stress was applied (Supplementary Material, Figure B.11). These solubility limits were reached at 1125 mM and 1575 mM ionic strength, respectively. The decrease in solubility indicates that supersaturation of the metastable zone formulations was increased upon subjection to FT stress. This suggests that formulations which only showed long–term instability upon FT stress application were part of the metastable zone before FT stress application. In the metastable zone, the required energy to support crystal growth is present, but the energy barrier that needs to be overcome to create critical nuclei is too high [28, 208]. Presumably, the applied FT stress allowed for crossing the required energy barrier, as a result of a supersaturation increase by freeze concentration effects. Freeze concentration effects are defined as the increase of dissolved substance concentrations, such as buffer components, excipients, and proteins, caused by the formation of ice crystals [35, 133]. Such environmental changes during freezing can cause a higher level of supersaturation, and thereby induce protein aggregation [224, 249].

Most of the NaCl and NH_4Cl formulations showed an MPPD cluster transformation from cluster II, III, and IV to cluster V or VI when FT stress was applied. The identification of cluster V and VI confirmed the increase in supersaturation as a result of FT stress. As mentioned in Section 6.3.3 (Cations), supersaturation is expressed by increased nucleation, which results in small and uniformly-sized crystals. This morphology is embodied by cluster VI, which represents formulations with a large amount ($n_{Agg} = 95 \pm 4\%$) of fast growing ($t_G = 296 \pm 101$ h), small ($L_C = 35 \pm 25\,\mu$m and $W_C = 26 \pm 18\,\mu$m) uniform ($\triangle L_C = 6 \pm 6\,\mu$m and $\triangle W_C = 4 \pm 3\,\mu$m) crystals. The identification of cluster V formulations at the aggregation zone border after FT stress was applied, indicates the existence of a small labile zone. Cluster V represents a high abundance ($n_{Agg} = 79 \pm 19\%$) of relatively small crystal ($L_C = 44 \pm 53\,\mu$m, $W_C = 36 \pm 32\,\mu$m). Compared to cluster II, III, and IV, the crystals in cluster V showed a more uniform size ($\triangle L_C = 16 \pm 20\,\mu$m and $\triangle W_C = 8 \pm 9\,\mu$m). However, the relatively late appearance of the crystals ($t_0 = 424 \pm 104$ h) and crystal growth for the remaining storage period ($t_G = 536 \pm 104$ h) indicates that slower kinetics were involved compared to cluster VI.

NaCl formulations at 1800 mM and 2050 mM ionic strength do not show an MPPD cluster transformation after application of FT stress. These formulations consistently showed a lower abundance of relatively big crystals that grow over a long period of time, as was described for formulations without FT stress. This means that the nucleation rate did not increase as a result of FT stress, as was seen for previously discussed formulations. It was stated in the literature that the nucleation rate is dependent on supersaturation, temperature, and interfacial tension [260]. In addition, it was reported that for the same value of initial supersaturation, an increasing precipitant concentration results in

a crystal number decrease [259]. The observation made in this study may be a result of the combination of relatively low temperatures and increased ionic strength due to FT stress and freeze concentration, as this combination results in a viscosity increase. For example, the dynamic viscosity of water already shows a temperature–induced increase of 145% in (from $1002.0\,\mu$Pas*s at 20 °C to $2456.6\,\mu$Pas*s at -8.28 °C) [138]. A similar trend in dynamic viscosity is also seen for aqueous NaCl solutions, as well as a 1.1 times higher dynamic viscosity for a 2000 mM NaCl concentration compared to 1000 mM NaCl at 0 °C ($1884\,\mu$Pas*s for 1000 mM and $2052\,\mu$Pas*s for 2000 mM at 0 °C) [261]. It has also been shown that such a viscosity effect is different for each salt, where the viscosity of NaCl solution increases for increasing salt concentration, whereas NH_4Cl solutions in a similar concentration range show a slight minimum [262]. This demonstrates that a higher NaCl content causes an increased viscosity at similar temperatures. In turn, higher viscosities are known to lead to lower nucleation rates, due to a slower diffusion rate of the protein material in solution [263, 264]. It was assumed that a substantially high viscosity was reached for formulations containing 1800 mM or more NaCl, which did not allow for additional nuclei formation. Subsequently, more protein material remained available for crystal growth over time, which corresponds to the features of cluster IV formulations. This was not the case for NH_4Cl solutions due to the lower viscosity increase compared to NaCl, which was reflected by a cluster transformation to cluster VI upon FT stress application.

6.3.4. Correlation of long–term protein stability to T_{CE}

Figure 6.4 b presents the obtained T_{CE} values, where a similar visualization format as in Figure 6.4 a was used. Two lines were added to the T_{CE} results of NaCl and NH_4Cl to indicate the observed aggregation zone before (solid line) and after (dashed line) FT stress was applied. The results for each of the duplicate plates indicated the reproducibility of the obtained T_{CE} data and can be found in the Supplementary Material, Figure B.13. Formulations containing $SO_4{}^{2-}$ anions showed little T_{CE} variation compared to the T_{CE} values obtained for formulations containing Cl^- anions. This was quantified by a variance of 26 °C^2 and 12 °C^2 for Na_2SO_4 and $(NH_4)_2SO_4$, respectively, compared to a variance of 107 °C^2 and 37 °C^2 for NaCl and NH4Cl, respectively. The lack of influence of the ionic strength on T_{CE} for formulations which contain $SO_4{}^{2-}$ anions does not correspond to data reported in literature, where an influence of Na_2SO_4 and $(NH_4)_2SO_4$ above 1000 mM ionic strength was reported for 87 g/L lysozyme formulations [150]. The lack of influence in the current study was attributed to the use of a lower lysozyme concentration (3 - 18 g/L instead of 87 g/L), as it has been shown that a lower protein concentration results in a lower LLPS temperature for similar ionic strength [35]. This led to the assumption that tested lysozyme concentrations were too low to induce LLPS before freezing occurs. The observed mean plate T_{CE} values of -35.4 ± 5.5 °C and -36.2 ± 3.4 °C for Na_2SO_4 and $(NH_4)_2SO_4$, respectively, are therefore thought to represent formulation freezing instead of LLPS. The small fluctuations within each plate were attributed to data analytical fluctuations, as the data analytical workflow was not optimized towards intensity changes that occur during

freezing of formulations. An interesting opportunity for future work might be the inclusion of more advanced data analytical techniques to distinguish between formulation freezing and LLPS. Upon realization of such a data analytical workflow, the obtained data should be validated by means of an orthogonal method that is able to distinguish between LLPS and freezing points, such as differential scanning calorimetry [265, 266]. Low temperatures of approximately -35.0 °C were not only found for formulations containing $SO_4{}^{2-}$ anions, but also for lysozyme formulations containing Cl^- anions at low ionic strength and low lysozyme concentration. Moreover, all formulations part of MPPD cluster I show a T_{CE} value below approximately -35.0 °C, as shown in Figure 6.4 a and Figure 6.4 b. This translates to a correlation between long–term stability and the absence of LLPS detection under tested conditions and settings.

In contrast to formulations containing $SO_4{}^{2-}$ anions, formulations containing Cl^- anions showed a change in T_{CE} upon increasing protein concentration and ionic strength. An exemplary influence of NaCl on the T_{CE} can be observed in Figure 6.4 b, where the T_{CE} increased from -34.1 ± 0.9 °C to -5.4 ± 1.4 °C (mean ± standard deviation of duplicates) for an ionic strength from 0 mM to 1800 mM at a lysozyme concentration of 15 g/L. The increasing T_{CE} values correlate to the previously discussed supersaturation increase (Section 6.3.3 (Cations)). A change in T_{CE} was observed for formulations containing NaCl, starting at 18 g/L lysozyme with 900 mM NaCl (T_{CE} = -19.4 ± 0.4 °C) and 12 g/L lysozyme with 2025 mM NaCl (T_{CE} = -14.8 ± 3.3 °C). Formulations with equal or higher NaCl ionic strength and lysozyme concentration showed an increase in T_{CE} as well. Any T_{CE} variation seen below these ionic strengths and lysozyme concentrations were considered data analytical fluctuations, as it was assumed that LLPS did not occur due to sample freezing. Most of the NaCl formulations that showed an increasing T_{CE} values were part of MPPD cluster IV. This indicates that a certain level of supersaturation had to be reached to induce LLPS under the tested circumstances. However, not all cluster IV NaCl formulations showed an increase in T_{CE}. This demonstrates a limitation of the short–term representation of long–term stability, where LLPS was not induced for relatively low protein concentrations while protein aggregation can still occur over time. The correlation between specific supersaturation levels and T_{CE} changes as a function of ionic strength and lysozyme concentration remains speculative, and should be confirmed by screening formulations with a wider lysozyme concentration range.

A relatively small increase in T_{CE} was seen for formulations containing NH_4Cl, starting at 18 g/L lysozyme and 450 mM NH_4Cl (T_{CE} = -28.7 ± 0.9 °C) and 15 g/L lysozyme and 675 mM NH_4Cl (T_{CE} = -30.0 ± 1.6 °C). As mentioned for NaCl, formulations with equal or higher NH_4Cl ionic strength and lysozyme concentration showed an increase in T_{CE} as well, while changes below these conditions were attributed to sample freezing. Interestingly, the mentioned conditions for NH_4Cl formulations where the first increase of T_{CE} was observed coincide with the upper border of the aggregation zone that was found after FT stress was applied. This hints at the possibility of using T_{CE} as a short–term parameter for FT stress–induced long–term protein instability. However, it should be noted that formulations at lower lysozyme concentrations do not show a T_{CE} value effect despite the observed instability after FT stress application.

A partial correlation between long–term protein stability and measured T_{CE} values was

observed. The applied experimental method did not detect LLPS for stable formulations under the applied settings. A tentative correlation between increasing T_{CE} values and increasing supersaturation was established. In addition, NH_4Cl formulations indicated a correlation between T_{CE} increase and long–term instability induced by FT stress. Solely a partial correlation was established due to the chosen lysozyme concentration range of 3 - 18 g/L, and the described observations should therefore be confirmed for a wider protein concentration range in future work. Nevertheless, the proposed experimental setup allows for a high–throughput determination of a short–term representative parameter of colloidal stability which can easily be added to the analytical toolbox to investigate long–term protein stability in a shorter time frame.

6.4. Conclusion

This study presented a low volume ($24\,\mu L$) HT (60 samples) experimental setup for the determination of an apparent T_{cloud} parameter, consisting of a cryogenic device combined with an automated image acquisition system. The performance of the presented experimental setup was evaluated by means of a robustness, validation, and case study. The robustness study identified the T_{CE} as parameter to represent T_{cloud}. The applicability of this parameter to represent T_{cloud} was confirmed by the validation study, where a PCC of 0.996 was found for normalized literature T_{cloud} data and T_{CE} data for eight similar lysozyme formulations. An average MAD of 0.2 ℃, obtained during the robustness study for 60 replicates measured with three different FT rate combinations, demonstrated the precision and reproducibility of the measurement. The robustness and validation study also reflected that T_{CE} is solely applicable for comparative formulation screening purposes when similar device settings are employed. The case study evaluated the correlation between T_{CE} and the influence of lysozyme concentration, ion type, ionic strength, and FT stress on long–term lysozyme stability. A partial correlation between T_{CE} and long–term protein stability was established. Long–term instable lysozyme formulations showed an increasing T_{CE} value for increasing supersaturation. Formulations containing NH_4Cl indicated that formulations sensitive to FT stress have higher T_{CE} values compared to formulations that did not show instability over time due to FT stress. However, evaluation of the case study results demonstrated that the obtained correlations were limited by the investigated lysozyme concentration range. Observed correlations should be confirmed in future work, where a wider lysozyme concentration range is employed. Future work might also include a more advanced data acquisition and analysis approach, which may allow for the distinction between formulation clouding and freezing. The combined results of the current work demonstrated that the developed experimental method can be incorporated into a short–term analytical screening toolbox that optimizes the development of long–term stable protein formulations.

Acknowledgement

7. Investigation of the reversibility of freeze/thaw stress-induced instability using heat cycling as a function of different cryoprotectants

Anna K. Wöll, Jürgen Hubbuch*
*Corresponding author. E-mail address: juergen.hubbuch@kit.edu

Karlsruhe Institute of Technology (KIT), Institute of Process Engineering in Life Sciences, Section IV: Biomolecular Separation Engineering, Karlsruhe, Germany

Abstract

Formulation conditions have a significant influence on the degree of FT stress–induced protein instabilities. Adding cryoprotectants might stabilize the induced FT stress instabilities. However, a simple preservation of protein stability might be insufficient and further methods are necessary. This study aims to evaluate the addition of a heat cycle up to 40 °C after FT stress application as a function of different cryoprotectants with lysozyme as exemplary protein. Sucrose and glycerol were shown to be the most effective cryoprotectants and reached the best reversibility as compared to PEG200 and Tween20. Here, aggregation was partly reversible and the solubility of non-stressed systems could be reached after the heat cycle. Next to long–term protein stability, short–term stability was investigated by determining the size and structure of lysozyme. However, the short–term stability was not influenced by any stress type (FT/ heat cycle), amount of stress (up to three FT cycles), or cryoprotectant tested.

Keywords: *aggregation, lysozyme, phase diagram, heat–induced reversibility, morphology*

7.1. Introduction

Freezing and thawing enable a higher degree of flexibility during manufacturing and improve long–term stability during storage [215–217]. To guarantee protein stability, chemically, mechanically, and physically induced stresses, including cold temperatures, have to be taken into account [50, 103, 109, 178]. The influence of freezing and thawing on the protein stability is complex and depends on formulation parameters (buffer, excipient, and protein type and concentration, pH value), system parameters (freezing and thawing point, glass transition and clouding point), and process parameters (cycle number, freezing/thawing ramp, storage temperature and time) [41, 103, 109, 117, 133, 140, 224, 249, 267]. Besides, the characteristics of induced FT stress are dependent on these parameters. Besides, the characteristics of induced FT stress are dependent on these parameters. These induced FT stress types might cause protein damage, which implies colloidal instabilities (aggregate formation), conformational instabilities (structural changes), and biological activity loss [103, 139, 178, 217, 218]. The different FT stress types include several processes. Freeze concentration of all solutes (e.g. buffer components, excipients, protein) [35, 133] due to ice crystal formation. Furthermore, LLPS might take place, which can be due to the increasing concentrations [35], and/or the decreasing temperature, also called cloud point (T_{cloud}) [140, 150]. The decreasing temperature might result in cold denaturation, which is the structural loss of proteins with quaternary structure [104]. An additional issue is the growing ice surface, due to the possible denaturation of the protein molecules on this surface [90, 109]. Consequently, protein aggregates, native or non–native, might occur because of the mentioned effects. Protein aggregates can appear through different mechanisms [26], depending on the protein surface charge, conformational changes, and excipients in the solutions. These parameters influence intermolecular and intramolecular interactions of proteins and/or excipients. On the one hand, when covalent binding (e.g disulfide bonds) arises, aggregates are irreversibly bonded to each other. On the other hand, when non–covalent binding (e.g. electrostatic, hydrophobic, van der Waals [18, 165]) occurs, aggregates might be reversible [13, 25, 26, 33, 43]. Normally, in order to stabilize proteins in solution and to prevent aggregation, the formulation is adjusted using different excipients. To inhibit FT–induced instabilities, cryoprotectants are used [33, 103, 268]. The excipients, including cryoprotectants, show different mechanisms to stabilize or destabilize proteins in solution. The excipients are either preferentially included or excluded from the proximity environment. Whereas preferential exclusion, or hydration, results in hydration of the protein surface which induces a stabilizing effect [63, 75]. As a function of the type and strength of the resulting interactions, protein aggregates form and can be classified irreversible or reversible. Of special interest are reversible native aggregates. Among these, one has to differentiate between two kinds of reversible aggregates: a) aggregates are in equilibrium with monomers, and b) induced aggregation by perturbation of the solution conditions (pH, temperature, etc.). The first type of aggregates a) is reversible by diluting the solution, whereas for the second type of aggregates, b) original solution conditions need to be re–established. Additionally, it has shown to be possible to dissociate

reversible protein aggregates by special treatments, for example through the application of heat [25]. This said, heat might cause protein denaturation and/or induce irreversible aggregation [26]. Taken all together, an investigation of the reversibility/dissociability of FT stress–induced protein aggregates as a function of different excipients using heat cycling is currently missing and promises new insights when dealing with reversible aggregation during bioprocessing.

In this study the influence of different excipients, known to be cryoprotectants, on FT stress–induced colloidal instability on the long–term stability of lysozyme is investigated. Whereas, colloidal instability is defined as a change in the phase behavior and/or crystal morphology. The excipients chosen belong to different groups, namely two osmolytes (the sugar sucrose and the polyol glycerol), a polymer (polyethylene glycol 200 (PEG200)), and a surfactant (Polysorbate 20 (Tween20)). Subsequently, the reversibility of these induced instabilities by including a heat cycle to the respective FT protocol is investigated. In order to visualize the occurrences, phase diagrams were chosen and systems clustered using a MPPD approach. The descriptors for clustering chosen consisted out of morphological and rate values. Additionally, solubility and protein structure of the different systems was measured.

7.2. Materials and methods

In this study, phase behavior, aggregation kinetics, and morphology of aggregates were investigated by creating a MPPD. In addition, the SL was calculated and the colloidal stability (size) as well as the conformational stability (protein structure) was studied. In the following, the preparation of the stock solutions, the creation of the MPPD, the performance of the FT-cycling with and without an additional heat step, as well as the analytical methods used (DLS and FTIR) are explained.

7.2.1. Preparation of stock solutions

For each experiment, a three buffers (base buffer, salt buffer, excipient buffers) and a protein stock solution had to be prepared. As base buffer, a 20 mM MCB was used. It was created using of a tool described by Kröner *et al.* [197] and consisted of the buffer substances AMPSO (Sigma–Aldrich), TAPSO (Sigma–Aldrich), MES (AppliChem GmbH, Darmstadt, Germany), formic acid (Merck KGaA), and D-(+)-malic acid (Sigma–Aldrich). Furthermore, the pH value was adjusted, using NaOH or HCl (Merck KGaA), with a five–point calibrated pH meter (HI-3220, Hanna® Instruments, Woonsocket, RI, USA) equipped with a SenTix® 62 pH electrode (Xylem Inc., White Plains, NY, USA). The pH value was adjusted to a value differing by up to ± 0.1 pH units from the final pH value. Prior to the use of the buffer, the pH value was verified again and finally adjusted to a

value differing by only ± 0.02 pH units. In addition, the IS was adjusted to 10.08 mS/cm with an accuracy of ± 1 mS/cm at 24 ℃ ± 1 ℃ by using the conductivity meter CDM 230 (Radiometer Analyticals, Lyon, France) and the four–point calibrated conductivity cell E61M014 (Radiometer Analyticals, Lyon, France) using NaCl (Merck KGaA). A salt buffer with different concentrations, 2.0 M, 3.75 M, and 4.29 M, was prepared. The respective amount of NaCl (Merck KGaA) was dissolved in the base buffer. The same procedure was performed on the excipient buffer. Stock excipient buffer with 1.8 M sucrose (Sigma-Aldrich), 3 M glycerol (VWR, Radnor, PA, USA), 84 mM polyethylene glycol 200 (PEG200)(Sigma-Aldrich), and 0.72 mM polysorbate 20 (Tween20) (AppliChem GmbH) were prepared. The pH values of all additives (salt, and excipient) were adjusted on the day of preparation and prior to use as described above. All buffers were filtered through a $0.2\,\mu$m Supor® Polyethersulfone (Pall Corporation, Port Washington, NY, USA) filter and stored at room temperature. The buffers were not used for longer than two weeks after preparation.

The protein stock solution was prepared with lyophilized lysozyme from chicken egg white (Hampton Research, Aliso Viejo, CA, USA). The protein was dissolved in the base buffer and filtered through a $0.2\,\mu$m syringe cellulose acetate filter (VWR). A desalting step was attached to remove aggregates and production–related additives, using PD-10 (GE Healthcare, Uppsala, Sweden) columns and the respective spin protocol [198]. To adjust the final protein concentration of 87 mg/mL, a 1:10 dilution was prepared and measured using the NanoDrop™2000c UV-Vis spectrophotometer (Thermo Fisher Scientific, Waltham, MA, USA). Thereby, an extinction coefficient of $\text{E}^{1\%}(280\,\text{nm}) = 22.00\,\text{Lg}^{-1}\text{cm}^{-1}$ was used for the measurement. The protein stock solution was prepared freshly and was not used for more than one day.

7.2.2. Phase diagrams

To create the phase diagrams, a method described by Baumgartner *et al.* was used [158]. The final lysozyme concentrations varied between 2.5 mg/mL and 25 mg/mL, and the final NaCl concentrations between 0 M and 2.5 M. The excipient concentration was kept constant at 300 mM sucrose, 1000 mM glycerol, 6.81 mM PEG200 or 0.03 mM Tween20. The protein and salt stock solutions were placed onto a Freedom EVO® 100 fully automated liquid handling station (Tecan Group Ltd., Männedorf, Switzerland) platform. The liquid handling station is equipped with fixed tips and 250 μL dilutors and controlled by Freedom EVO® 2.4 SP3 (Tecan Group Ltd.). The protein and salt concentration dilution rows were prepared in a Deepwell PP plate (Greiner Bio-one, Frickenhausen, Germany). After the salt dilution row was prepared, either 57.2 μL of sucrose or glycerol or 25 μL of PEG200 or Tween20 were added and mixed manually. Then, the phase diagram was created automatically in a MRC Under Oil 96–well Crystallization Plate (SWISSCI AG, Neuheim, Switzerland), whereas 18 μL of the salt/additive solution was mixed with 6 μL protein solution. Before the plates were sealed with Duck® Brand HD Clear sealing tape (ShurTech® brands, Avon, OH, USA), to avoid evaporation, plates were centrifuged in an Eppendorf

centrifuge 5810 R (Eppendorf AG, Hamburg, Germany) at 1000 rpm for 1 min to remove all air bubbles. After performing the FT protocols with and without heat cycling (Section 7.2.3), the plates were placed in the incubation chamber RockImager 54 (Formulatrix, Bedford, MA, USA) at 20 °C for 40 days.

7.2.3. Cycling

FT cycling: FT protocol with different cycles numbers (FT cx; $x = 0, 1, 3$) were carried out. A plate at FT c0, not subjected to any FT stress application, was used as a reference plate. This plate was directly placed into the incubation chamber after preparation. The other plates were placed onto the cryogenic device EF600M 105 (Grant Instruments, Cambridgeshire, UK) after preparation. The plate handling and the adjustments on the cryogenic device are described in the publication by Wöll et al. [249]. In this study, all plates were frozen at 0.5 °C/min and thawed at 2.5 °C/min.

Heat cycling: Heat cycling following FT cycling was performed (FT cy h; $y = 1, 3$) as follows. The respective plates were heated to 40 °C for 30 minutes using an HLC Cooling-ThermoMixer MKR 13 (Ditabis AG, Pforzheim, Germany). Upon completion, the plates were directly placed in the incubation chamber at 20 °C.

7.2.4. Multidimensional protein phase diagram (MPPD)

To evaluate phase transition, long–term stability and reversibility of aggregates of the used lysozyme formulation, an MPPD was employed [251]. An MPPD combines data on morphology, kinetic and aggregation obtained from images taken during storage, in one figure by data reduction and subsequent clustering. In this study, the following data was extracted manually from the images: (1,2) length and width of a maximum of eight crystals in μm, (3) percentage aggregation amount per well (n_{Agg}), (4) aggregation onset time (t_{onset}) in hours, and (5) aggregation growth time (t_G) in hours. The mean crystal length (L_C) and width (W_C) as well as the IQR of the crystal lengths ($\triangle L_C$) and widths ($\triangle W_C$) were calculated. In addition, the ratio of the length and width ($L_C : W_C$) and the interquartile range of this ratio ($\triangle(L_C : W_C)$) were calculated. By using all of these mentioned parameters, the MPPDs were constructed. The used settings for the MPPD construction have been described in a previous work [251], where the clustering algorithm selected an optimal cluster number between three and ten clusters.

In addition, to evaluate the occurrence of each cluster, the total amount of each cluster per phase diagram was determined and the occurrence in percentage per plate was calculated.

7.2.5. Analytics

In order to evaluate if structural parameter alter due to a) initial stress and b) heat reversibility, FTIR and DLS measurements were applied. Stable conditions were chosen at 18 mg/mL and 22 mg/mL at the four lowest salt concentrations (0.00, 0.23, 0.45, and 0.68 M). A condition was only analyzed when no visible aggregation appeared prior to the actual measurement ($t_{onset} > t_0$). This resulted in a total amount of 151 samples (non–stressed (FT c0), stressed (FT c1 and FT c3), stressed and heated (FT c1 h and FT c3 h)). In addition, supernatant measurements of all phase diagrams were performed to calculate SLs.

The protein stock solution for the analytics was prepared as described in Section 7.2.1. The pipetting was performed manually, whereas the protein, salt, and excipient solutions were mixed in the same ratio as was done for the phase diagrams, see Section 4.2.2. A maximum of 180 μL of the samples was prepared in 0.5 mL Eppendorf tubes (Eppendorf AG). For the stressed samples (FT cx; x = 1, 3 and FT–heating FT cy h; y = 1, 3), the samples were split into up to six 30 μL proportions and pipetted in the crystallization plate, after preparation in 0.5 mL Eppendorf tubes (Eppendorf AG). Afterwards, plate handling was done as described in Sections 4.2.2 and 7.2.3. After the respective stress protocol was performed the samples were pipetted back into Eppendorf tubes and mixed. Before the analytical method could be performed, the samples were filtered, using an Eppendorf centrifuge 5810 R (Eppendorf AG) at 2000 g for 5 min, through a 0.2 μm AcroPrep™ 96 filter plate (350 μL)(Pall Corporation, New York, New York, USA) into a 96–well PP-Microplate (U-shape)(Greiner Bio-one). After filtration, the samples were split to be used with the different analytical methods which are described below.

Dynamic light scattering (DLS)

The hydrodynamic radius of the protein in the respective solution was measured with DLS using the Wyatt DynaPro Plate Reader I (Wyatt,Santa Barbara, California, USA) and a polystyrene 384–well assay plate (Corning Inc., Corning, New York, USA). Therefore, 25 μL of the filtered sample was pipetted into the wells in triplicate and was covered with 10 μL Xiameter™ PMX-200 Silicon fluid 20cs (Dow Corning Inc. Midland, Michigan, USA) to avoid evaporation. The plate was centrifuged in an Eppendorf centrifuge 5810 R (Eppendorf AG) at 400 g for 1 min to remove all air bubbles. Next, the plate was placed in the plate reader and each sample was measured twice at 20 °C with an acquisition time of 5 seconds and an acquisition number of 10 as well as automatic attenuation.

Fourier–transform infrared spectroscopy (FTIR)

To investigate changes in the secondary protein structure FTIR spectroscopy, a Tensor 27 (Bruker Optics, Ettlingen, Germany) was used. The FTIR was equipped with a

cryo–cooled mercury cadium telluride (CC-MTC) narrow detector (Bruker Optics) and a BioATR II crystal (Bruker Optics) and controlled by OPUS 7.2 (Bruker Optics). For the measurement, 25 μL of background or sample were pipetted onto the crystals, covered with a lid, and then measured for 5 minutes (mirror speed of 160 KHz) with a resolution of 2 cm^{-1} in a range from 3500 cm^{-1} to 900 cm^{-1}. The background subtraction, as well as automatic compensation, was automatically performed by the software. Additionally, data pre–processing was performed. After atmospheric compensation and vector normalization, the data was smoothed using a Savitzky–Golay filter with a second–order polynomial and a frame length of 17 in a wavenumber region from 1750 to 1550 cm^{-1}. This data was then used to calculate the average of the samples measured in duplicate. The area within the amid I range (1700-1600 cm^{-1}) for the α–helix, β–sheet, and β–sheet antiparallel was extracted using the *trapz* function available in MATLAB (Version 2019b). Therefore, the peak minimum for α–helix (1650 - 1685 cm^{-1}), β–sheet antiparallel (1670 - 1685 cm^{-1}), and the peak maximum for β–sheet (1615 - 1635 cm^{-1}) were detected, using the function *peakdet* available in MATLAB (Version 2019b). The area was then calculated at the interval of the min/max peak $\pm$ 2 cm^{-1}.

Solubility line (SL)

For determining the SLs, the supernatant of the phase diagrams was measured. For this purpose, 3 μL of the supernatant of each condition was carefully (no air bubbles, no visible aggregates) pipetted on the NanoDrop™ 2000c, and the concentration was measured in triplicate. Afterwards, the solubility lines were calculated using a method published by Galm *et al.* [164]. For this study, the conditions with crystals were taken into account. Furthermore, the curves were integrated, using the function *integral* available in MATLAB (Version 2019a), and the areas from 0 M to 2.5 M salt and from 0 mg/mL to 25 mg/mL protein were calculated.

7.3. Results

This study aimed to evaluate twofold: a) whether the influence of different excipients on the long–term protein stability of FT–stressed formulations can be followed by the creation of MPPDs and b) whether the induced instabilities are reversible by a simple heat treatment. The model system used to perform this investigation consisted of chicken egg white lysozyme, different amounts of NaCl and cryoprotectants. The protein concentrations ranged from 2.5 mg/mL to 25 mg/mL at pH 5. The NaCl concentration as precipitant was increased up to 2.5 M. Four different cryoprotectants a) 300 mM sucrose, b) 1000 mM glycerol, c) 6.81 mM PEG200, and d) 0.03 mM Tween20 in a solution containing NaCl were added to

this model system separately. Different FT cycle numbers (FT c x; x = 0, 1, 3), as well as a heat cycle (FT c y h; y = 1, 3), were performed for each of the formulations during the study.

7.3.1. Multidimensional protein phase diagram (MPPD)

Overall, 2400 different formulations were studied and resulted in different phase states, soluble and crystalline (exemplary pictures see Figure 7.1). To visualize all morphologies and kinetic data in one figure, the MPPD construction includes a data reduction step. This reduction step results in an energy value of 95.5%, which indicates an information loss of 4.5%. An optimal number of seven clusters were obtained when the reduced dataset was clustered; they are shown as radar charts (I-VII) in Figure 7.2 A. Each radar chart represents a specific combination of image–based features: the crystal length (L_C) and widths (W_C), variation in crystal length ($\triangle L_C$) and width ($\triangle W_C$), the aggregation amount (n_{agg}), the aggregation onset time (t_{onset}), and aggregation growth time (t_G), as well as the ratio of crystal length and width ($L_C : W_C$), and the variation of this ratio ($\triangle(L_C : W_C)$). The normalized median values are visualized as a colored surface, and the corresponding MAD is shown as a dashed line in Figure 7.1. An overview of the absolute values, representing the median ± MAD, which is calculated based on all formulations within the mentioned cluster, and their ranges of each cluster is given in Table 7.1.

Table 7.1.: Overview of median ± MAD image–based feature values. The values are listed per cluster identified in the separate multidimensional protein phase diagram.

	I	II	III	IV	V	VI	VII
L_C [μm]	0 ± 0	202 ± 186	192 ± 209	34 ± 14	34 ± 11	105 ± 92	915 ± 380
W_C [μm]	0 ± 0	141 ± 124	139 ± 150	24 ± 10	25 ± 8	16 ± 9	13 ± 4
$L_C : W_C$ [-]	0 ± 0	1.4 ± 0.2	1.3 ± 0.2	1.3 ± 0.1	1.4 ± 0.1	7.8 ± 9.3	76.4 ± 37.9
t_onset [hours]	0 ± 0	6 ± 9	1 ± 1	0 ± 0	0 ± 0	0 ± 0	0 ± 0
t_G [hours]	0 ± 0	892 ± 95	456 ± 142	12 ± 15	16 ± 19	620 ± 208	783 ± 195
n_{Agg} [%]	0 ± 0	10 ± 7	15 ± 7	25 ± 7	77 ± 11	60 ± 22	75 ± 22
$\triangle L_C$ [μm]	0 ± 0	51 ± 52	52 ± 56	11 ± 7	11 ± 6	37 ± 35	1032 ± 529
$\triangle W_C$ [μm]	0 ± 0	46 ± 49	78 ± 58	9 ± 6	8 ± 4	7 ± 5	6 ± 4
$\triangle(L_C : W_C)$ [-]	0 ± 0	0.3 ± 0.3	0.4 ± 0.3	0.3 ± 0.2	0.4 ± 0.2	3.3 ± 4.2	93.2 ± 43.4

Cluster I (Cl I) represents soluble conditions, all values of the image features are equal to zero, as no aggregation took place. However, for some conditions which were clustered to Cl I aggregates were observed. These conditions were analyzed manually and are bordered by dashed lines in Figure 7.2. Cl II represents a few ($n_{agg} = 10 \pm 7\%$) relatively large ($L_C = 202 \pm 186\,\mu$m and $W_C = 141 \pm 124\,\mu$m) crystals which have an onset time after a few hours ($t_{onset} = 6 \pm 9$ hours) but a very long growth time ($t_G = 892 \pm 95$ hours). An exemplary picture of such a crystal is shown in Figure 7.1. Cl III represents crystals which show a slightly higher amount ($n_{agg} = 15 \pm 7\%$) and an earlier crystal growth onset time
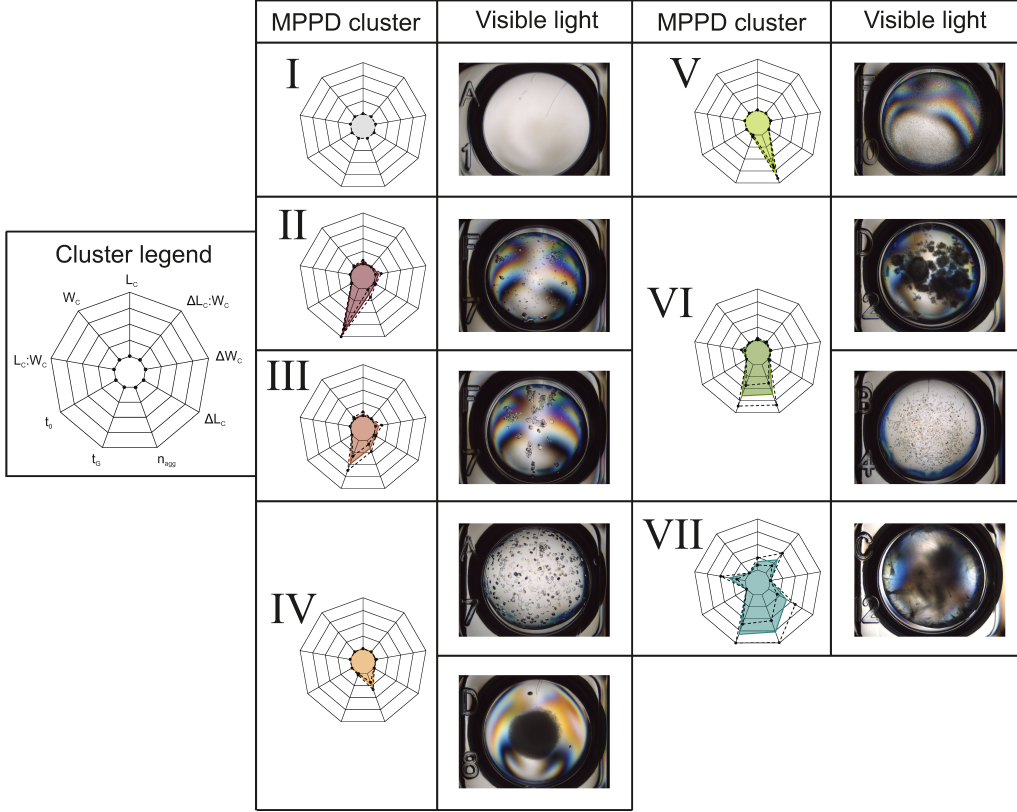
Figure 7.1.: The clusters detected for the data set are shown with the respective example pictures of exemplary crystals. The color surface in the radar charts represents the normalized median values of each image feature. The following image–based features were used for the clusters: the crystal length (L_C) and widths (W_C), the IQR of the crystal length ($\triangle L_C$) and width ($\triangle W_C$), the aggregation abundance (n_{Agg}), the aggregation onset time (t_{onset}), and aggregation growth time (t_G), as well as the ratio of crystal length and width ($L_C : W_C$), and the IQR of this ratio ($\triangle(L_C : W_C)$). The median absolute deviation within each cluster for each image–based feature is shown by a dashed line in the radar charts. The absolute cluster values can be found in Table 7.1. The exemplary crystal pictures are made with visible light. Soluble conditions were presented by Cl I, tetragonal crystals are presented by Cl II, complex structured crystals by Cl III, either tetragonal crystals at FT c0 (top) or dense grown micro crystals with FT stress (bottom) by Cl IV, micro crystals by Cl V, sea urchin (top) and small tetragonal crystal (bottom) by cluster VI, and sea urchin crystals by Cl VII.

($t_{onset} = 1 \pm 1$ hours) as well as a shorter growth time ($t_G = 456 \pm 142$ hours). Within Cl IV and Cl V the amount of crystals increased to $n_{agg} = 25 \pm 7\%$ / $77 \pm 11\%$, and the crystal size decreased significantly to $L_C = 32 \pm 14\,\mu$m / $34 \pm 11\,\mu$m and $W_C = 24 \pm 10\,\mu$m / $25 \pm 8\,\mu$m, receptively (see Table 7.1 and Figure 7.1). Whereas Cl IV indicated two different morphologies: tetragonal crystals and densely grown micro crystals, see Figure 7.1. The tetragonal crystals grew preferably when no stress was applied, whereas the micro crystals grew after FT stress was applied. Cl VI showed a significant higher crystal growth time ($t_G = 620 \pm 208$ hours) and a significant increased rati between crystal width and length

(L_C:W_C = 7.8 ± 9.3). This cluster also represented two types of crystal morphologies: sea urchin crystals and small tetragonal crystals. The sea urchins are dominant in the supersaturated region, and the small tetragonal crystals grow at lower salt and protein concentrations. Cl VII showed the highest values for the crystal length and the ratio between crystal length and width, as well as crystal growth time ($L_C = 915 \pm 380\,\mu$m, L_C:W_C = 76.4 ± 37.9, t_G = 783 ± 195 hours).
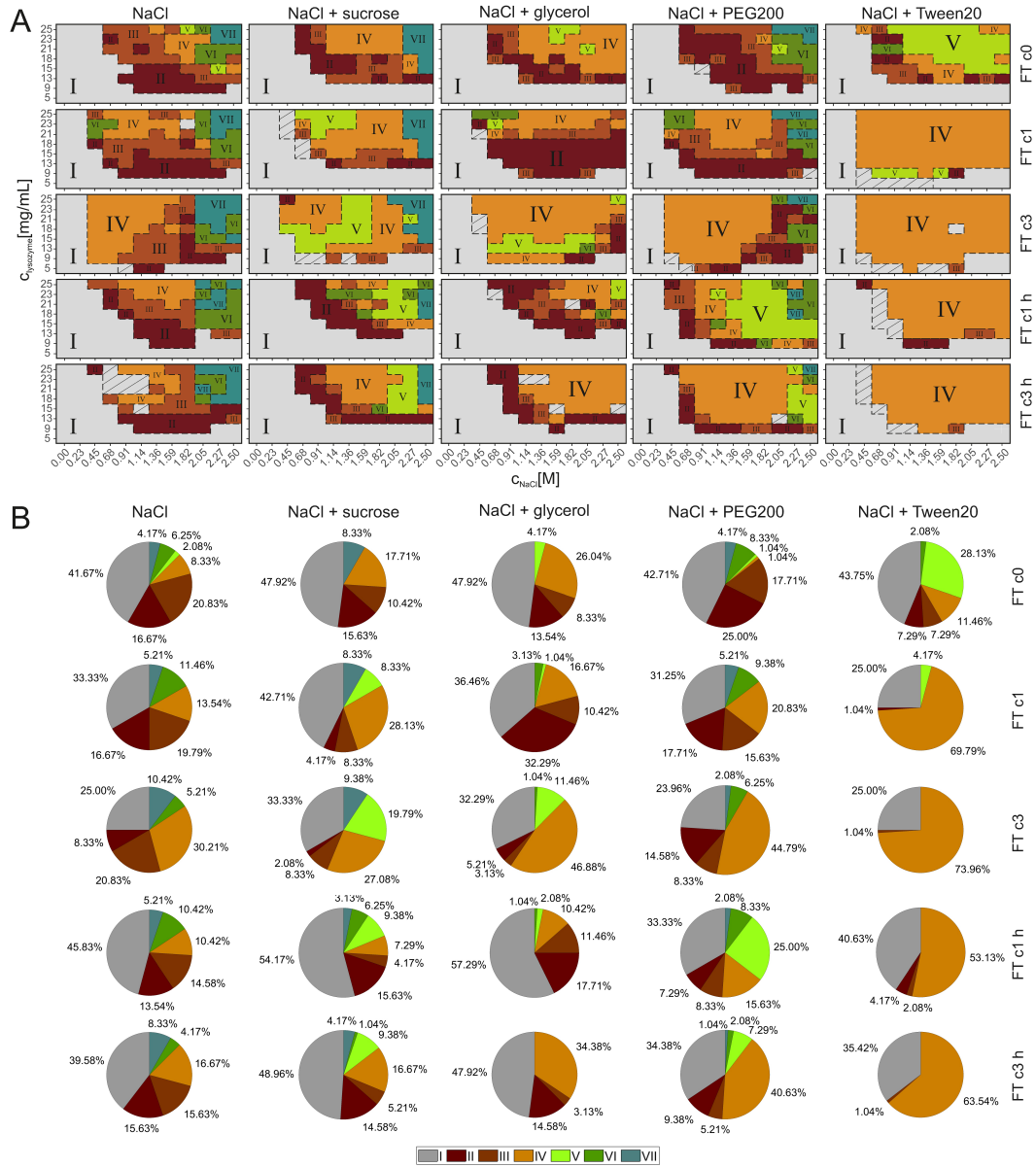
7.3.2. Formulations

The results of the long-term storage experiment are presented in the MPPD in Figure 7.2, where lysozyme was monitored for 40 days at 20 °C using 2400 different formulations. The different columns (C 1-5) in Figure 7.2 A represent the different formulations with NaCl (C 1), NaCl + 300 mM sucrose (C 2), NaCl + 1000 mM glycerol (C 3), NaCl + 6.81 mM PEG200 (C 4), and NaCl + 0.03 mM Tween20 (C 5), whereas the different rows (R 1-5) represent the different cycles performed (FT c0, FT c1, and FT c3 (R 1-3)) and the combination of FT stress followed by a heat cycle (FT c1 h and FT c3 h (R 4-5)). Figure 7.2 B summarizes the percentages occupied by the different clusters for each system.

Initial state - FT c0 *NaCl*: All clusters were present at FT c0, whereas Cl II and Cl III were dominant in the transition zone from the soluble (Cl I) to the aggregation zone, see Figure 7.2 A, R 1. Increasing the NaCl and lysozyme concentration resulted in Cl IV, Cl V, and Cl VI. At the highest lysozyme concentrations (23 mg/mL and 25 mg/mL) and NaCl concentrations (2.27 M and 2.5 M), Cl VII appeared. The overall contribution of the different clusters were for Cl I 47.92%, Cl II 15.63%, Cl III 20.83%, Cl IV 8.33%, Cl V 2.08%, Cl VI 6.25%, and Cl VII 4.17%, see Figure 7.2 B, R 1 and C 1.
Sucrose: Adding sucrose to the formulations, the aggregation zone slightly decreases for FT c0, and Cl V and VI disappeared, see Figure 7.2 A, C 2. Cl IV was present at lysozyme concentrations above 18 mg/mL and NaCl concentrations between 1.14 M and 2.05 M. The transition zone from the soluble zone (Cl I) to the aggregation zone consisted of Cl II and Cl III. Cl VII was present at the highest lysozyme and NaCl concentrations. The overall contribution of the different clusters were for Cl I 41.67%, Cl II 16.67%, Cl III 20.83%, Cl IV 8.33%, Cl V 2.08%, Cl VI 6.25%, and Cl VII 4.17%, see Figure 7.2 B, R 1 and C 2.
Glycerol: Replacing sucrose by glycerol in the formulation, resulted in a smaller aggregation zone/larger soluble zone (Cl I) compared to pure NaCl formulations for FT c0. In the transition zone to Cl I was still created out of Cl II and Cl III, whereas it was smaller compared to NaCl formulations. In the remaining aggregation zone, Cl IV was dominant, see Figure 7.2 A, C 3. The overall contribution of the different clusters were for Cl I 47.92%, Cl II 13.54%, Cl III 8.33%, Cl IV 26.04%, and Cl V 4.17%, see Figure 7.2 B, R 1 and C 3.
PEG200: PEG200 formulations showed phase behaviors very similar to those of NaCl formulations, see Figure 7.2 A, C 4. In the transition zone from the soluble zone (Cl I) to the aggregation zone, Cl II, and at increasing protein and salt concentrations, Cl III were

Figure 7.2.: In A the MPPDs for five different lysozyme formulations (NaCl, NaCl + sucrose, NaCl + glycerol, NaCl + PEG200, NaCl + Tween20 (C 1-5)) and different stress protocols (R 1-5). The lysozyme concentration [mg/mL] was varied over the NaCl concentration [M]. Seven clusters were identified and used for the MPPD using the mean cluster color and cluster number similar to the radar charts, shown in Figure 7.1. In B the calculated occurrence in [%] of each cluster per phase diagram is shown with the respective values.

dominant up to a NaCl concentration of 1.82 M. In the high concentration region, mainly Cl VI and VII were created. The overall contribution of the different clusters were for Cl I 42.71%, Cl II 25.00%, Cl III 17.71%,Cl IV 1.04%, Cl V 1.04%, Cl VI 8.33%, and Cl VII 4.17%, see Figure 7.2 B, R 1 and C 4.

Tween20: For Tween20 formulations Cl V was most dominant at FT c0, see Figure 7.2 A, C 5. The occurrence of Cl I was slightly lower compared to that of the NaCl formulations. The overall contribution of the different clusters were for Cl I 43.75%, Cl II 7.29%, Cl III 7.29%,Cl IV 11.46%, Cl V 28.13%,and %,Cl VI 2.08%, see Figure 7.2 B, R 1 and C 5.

FT cycles - FT c1 and FT c3 In general increasing the number of FT cycles resulted in a decrease in the Cl I region (soluble region) for all formulations tested, see Figure 7.2 B, R 1-3. The more FT cycles were applied, the higher the amount of Cl IV was observed.

NaCl: NaCl formulations showed an increase of condition belonging to Cl IV when increasing the cycle number, 8.33% to 13.54% to 30.21%, see Figure 7.2 B, C 1. Cl IV at FT 1 was created at lysozyme concentrations higher than 21 mg/mL up to 1.59 M NaCl. At FT c3 the region expanded and Cl IV was dominant at all lysozyme concentrations up to 1.59 M NaCl, see Figure 7.2 A, R 3. Considering that, the higher the lysozyme concentration, the more salt had to be added to create Cl IV. At high supersaturations still Cl VI and Cl VII were dominant for FT c1 and FT c3.

Sucrose: Sucrose formulations do also show a cluster transformation to Cl IV and Cl V by increasing the cycle number, see Figure 7.2 A, C 2. The occurrence of these clusters increased from 17.71% to 28.13% to 27.08% for Cl IV and from 0% to 8.33% to 19.97% for Cl V while increasing the number of cycles, see Figure 7.2 B, R 1-3 C 2. Regarding the positions of the clusters, the Cl IV region is spilt by Cl V, see Figure 7.2 A, C 2. The occurrence of Cl VII stayed the same (8.5%) whereas the region with Cl II and Cl III decreased significantly. For Cl II the occurrence decreased from 15.63% to 4.17% to 2.08% and for Cl II from 10.42% to 8.33% for FT c1 and FT 3, see Figure 7.2 B, C 2. The Cl I zone, however, was not significantly decreased at FT c1, compared to NaCl formulations, only slightly decreased at FT c3 (47.92% to 42,71% to 33.33%).

Glycerol: Formulations containing glycerol showed a signification increase of Cl II from FT c0 to FT c1, 13.54% to 32.29%, respectively, see Figure 7.2 A, C 3 and Figure 7.2 B, C 3. At FT c3 a cluster transformation to mainly Cl IV (46.88%) took place. The Cl I region was slightly decreased when the number of cycles was increased (47.92% to 36,46% to 32.29%).

PEG200: PEG200 formulations showed the same cluster transition as NaCl formulations, see Figure 7.2 A, C 4. Concerning the occurrence of the clusters small differences were seen. When the formulations were stressed the occurrence of Cl IV was dominant whereas Cl II and Cl III were less present compared to NaCl formulations. At FT c3 44.79% of the conditions belong to Cl IV whereas only 30.21% belong to this cluster when only NaCl was in the formulation, see Figure 7.2 A, C 4 and Figure 7.2 B, C 4.

Tween20: Tween20 formulation did show a cluster transformation to Cl IV from FT c0 with an occurrence of 11.46% to FT c1 with an occurrence of 69.79%. To FT c3 the occurrence of Cl IV slightly increased to maximum of 73.96%, see Figure 7.2 A, C 5 and Figure 7.2 B, C 5. The occurrence of the soluble zone (Cl I) decreased significantly from 43.75% at FT c0

to 25.00% at FT c1 and FT c3.

Heat cycle - FT c1 h and FT c3 h The reversibility regarding the phase state (soluble/aggregate) and the occurrence of Cl II and Cl III were analyzed. In general, the additional heat cycle increases the Cl I region compared to the corresponding FT cycles, see Figure 7.2 A, R 4-5.

NaCl: For NaCl formulations similar positions of the cluster at FT c1 h and FT c3 h compared to FT c0 could have been observed. Regarding the reversibility of the phase states, the occurrence of Cl I reached values similar to those at FT c0 (41.67%) at FT c1 h with 45.83% and at FT c3 h with 39.58%, see Figure 7.2 A, C 1 and Figure 7.2 B, C 1. The occurrence of Cl II and Cl III did not significantly change between all the cycles applied. The Cl II and Cl III appeared again adjacent to Cl I as it was the case for FT c0, when a heat cycle was performed.

Sucrose: When sucrose was added to the formulations and heat cycling was performed after the formulations were FT–stressed, a significant zone of Cl II were created in zone adjacent to Cl I which was not the case at FT c1 and FT c3, see Figure 7.2 A, C 2. The occurrence of these clusters was very low at FT c1 and FT c3, but Cl II reached a similar occurrence compared to FT c0 (16.67%), when a heat cycle was performed (FT c1 h 13.54%, FT c3 h 15.63%), see Figure 7.2 B, R 4-5 and C 2. The occurrence of Cl I increased significantly for FT c1 h and FT c3 h (45.83% and 39.58%) compared to the respective systems at FT c1 and FT c3 (33.33% and 25.00%), whereas nearly the same occurrence as at FT c0 (41.67%) with sucrose were reached, see Figure 7.2 A, C 2 and Figure 7.2 B, C 2.

Glycerol: Applying a heat cycle to glycerol formulations after they were stressed with freezing/thawing resulted in an appearance of the same clusters as occurred at FT c0, as well as the position of these clusters are similar, see Figure 7.2, C 3. Concerning the occurrence of Cl I, the same occurrence as at FT c0 (47.92%) could be reached at FT c3 h (47.92%), and was even increased at FT c1 h (54%). In addition the occurrence of Cl II and Cl III (FT c1 h 17.71%/11.46%, FT c3 h 14.58%/3.13%) reached values close to those at FT c0 (Cl II 13.54%, Cl III 8.33%), with the exception of Cl III at FT c3 h (3.31%), see Figure 7.2 B R 4-5 and C 3.

PEG200: The addition of a heat cycle to PEG200 formulations resulted in a similar positioning of the Cl II and Cl III region compared to FT c0, which was adjacent to Cl I. Nevertheless, these region was significant at FT c1 h (Cl II 7.29%, Cl III 8.33%) and FT c3 h (Cl II 9.38%, Cl III 5.21%) smaller than at FT c0 (Cl II 25.00%, Cl III 17.71%), see Figure 7.2 A, C 4 and Figure 7.2 B. The occurrence of Cl I for FT c1 h (33.33%) and FT c3 h (34.38%) only reached values of FT c1 (31.25%) and not the one of FT c0 (42.71%).

Tween20: The heat cycle influenced only the occurrence of Cl I for Tween20 formulations and not the cluster formation itself. Still mainly Cl IV was observed like at FT c1 and FT c3. At FT c1 h a similar occurrence of 40.63% of Cl I compared to FT c0 with 43.75% could be observed. FT c3 h showed a slightly smaller occurrence of Cl I with 35.42% compared to FT c0, see Figure 7.2 A, C 5 and Figure 7.2 B, C 5.

Formulation comparison Adding different excipients to a NaCl phase diagram resulted in a different phase behavior for each excipient, see Figure 7.2 A, R 1/C 1-5. In the following

a comparison with a focus of the effects arising from the different excipients is laid for the initial state and the different cycles studied. In general the influence of FT cycles and the reversibility by heat is strongly dependent on the cryoprotectant.

Initial state - FT c0: In the transition zone to Cl I for all formulations, Cl II and Cl III are present, whereas for Tween20 formulations, the region is very small. Regarding the size of the Cl I region, NaCl and PEG200 formulations showed a slightly smaller region than formulations containing sucrose, glycerol or Tween20, see Figure 7.2 B, R 1. Cl VII was only created in the highly concentrated region for NaCl, sucrose and PEG200 formulations.

FT cycle - FT c1 and FT c3: The influence of the FT cycles, as well as the phase behavior at FT c0, were very similar for NaCl and PEG200 formulations. The position of the clusters changed similar when FT stress was applied, see Figure 7.2 A, R1-3, C 1 and C 4. The occurrence of Cl I was highest with sucrose and glycerol formulations compared to the other formulations tested, see Figure 7.2 B. Furthermore, the FT stress did not have such a significant impact on the occurrence of Cl II for sucrose and glycerol formulations. In general, the higher the cycle number, the lower the occurrence of Cl I. For Tween20 formulations there was no difference between FT c1 and FT c3 regarding the Cl I occurrence visible, see Figure 7.2 B, R 1-3.

Heat cycle - FT c1 h and FT c3 h: When a heat cycle was performed the increase of the Cl I region when a heat cycle was added, was less pronounced for PEG200 and Tween20 formulations compared to the other formulations tested. All formulations showed cluster transformation back to the clusters seen at FT c0, with the exception of PEG200 and Tween20 formulations, see Figure 7.2 A, R 4-5 and Figure 7.2 B, R 4-5. With a heat cycle Cl V occurred for PEG200 formulations, which was not seen at any other system with PEG200 formulations. With Tween20 the heat cycle only influenced the occurrence of Cl I and did not result in a cluster transformation at all.

7.3.3. Analytics

Information of three different analytic methods: (1) protein solubility (SL), (2) protein size (DLS), and (3) protein structure (FTIR) was added to the MPPDs. These measurements were performed for two reasons: a) to evaluate if initial stress leads to changes in structural parameter or size of the proteins under investigation and b) to evaluate if the process exploiting heat reversibility leads of structural (FTIR) or size (DLS) based alterations.

Solubility line (SL)

To investigate the protein solubility, supernatant measurements of each phase diagram were performed and SLs were calculated, as described in Section 7.2.5 and presented in Figure 7.3 A. To identify more easily differences of the SLs, the area was calculated underneath the curves as described in Section 7.2.5. Bar graphs of these values are shown in Figure 7.3 B. The trend regarding the influence of FT stress and the heat reversibility

are similar for all lysozyme formulations tested. For the formulations with NaCl and the formulations where PEG200 was added, the area was the largest without any FT stress, see Figure 7.3 B. The smaller the calculated SL area, the more the SL is shifted to lower protein and salt concentrations. A large SL area indicates high protein solubility and a small aggregation zone in the respective phase diagram. In formulations where sucrose or Tween20 were added, the area of FT c0 was similar to that of FT c1 h. With glycerol, the area with the formulations which performed FT c1 h was even larger than for FT c0. An overall trend could be observed when the influence of FT cycles was taken into account. The more FT cycles were applied to the formulations, the smaller the SL area became. In addition, the heat cycle results in a significant increase in the SL area for FT c1 and FT c3. The only exception was shown with Tween20 formulations. Here, the heat cycle did not increase the SL area for FT c1, see Figure 7.3 B.

Comparing the different excipients to each other, the formulations with sucrose addition showed the highest SL area values, followed by glycerol formulations, see Figure 7.3 B. These formulations are followed by NaCl, NaCl + PEG200, and NaCl + Tween20 formulations in the order from high to low SL area values.

**Dynamic light scattering (DLS)**

The protein size of the formulations investigated was measured performing DLS measurements in triplicate, see Figure 7.4. No significant changes could be observed. The stress type (FT and the heat) and amount (cycle number) did not influences the protein size. Comparing the results of the different formulations to each other, small differences were observed: Formulations with NaCl, PEG200, and Tween20 show radii in a lower range (app. 2.0 nm to 2.5 nm), whereas formulations with sucrose or glycerol show radii with approximately 2.3 nm to 3.3 nm. Finally, heat reversibility did not show significant alteration in the size of the protein when compared to the initial dimensions.

**Fourier–transform infrared spectroscopy (FTIR)**

Protein structure information were investigated using FTIR. All samples measured with DLS were also analyzed using FTIR. After data pre-processing (see Section 7.2.5), the spectra is shown in Figure 7.5 A. In the interesting amid I region where the alpha–helix (1650 - 1685 cm^{-1}), beta–sheet (1615 - 1635 cm^{-1}) and beta–sheet antiparallel (1670 - 1685 cm^{-1}) structures absorb nearly no differences were detected. This becomes clearer when the calculated areas for each region are compared to each other, see Figure 7.5 B. With these results, no influence of protein and salt concentration, stress type (FT or heat cycling), FT cycle number, and excipients could be determined in this study.
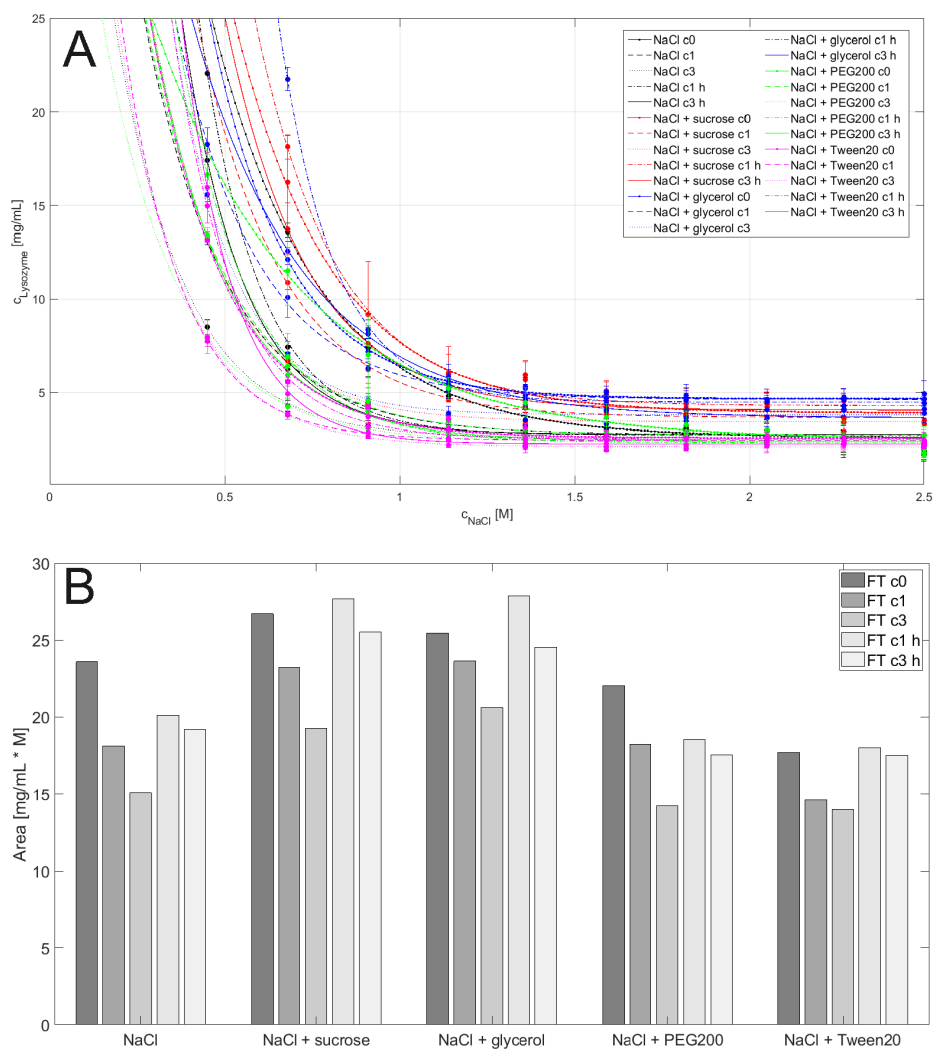
Figure 7.3.: In A the solubility lines of lysozyme in different formulations where different stress protocols were applied. The lysozyme concentration in mg/mL is plotted over a varying NaCl concentration in M. In B the calculated area of each phase diagram investigated is shown. The SL area is plotted over the different formulations tested, the different shades of gray represents FT c0 (darkest gray), FT c1, FT c3, FT c1 h, FT c3 h (lightest gray).
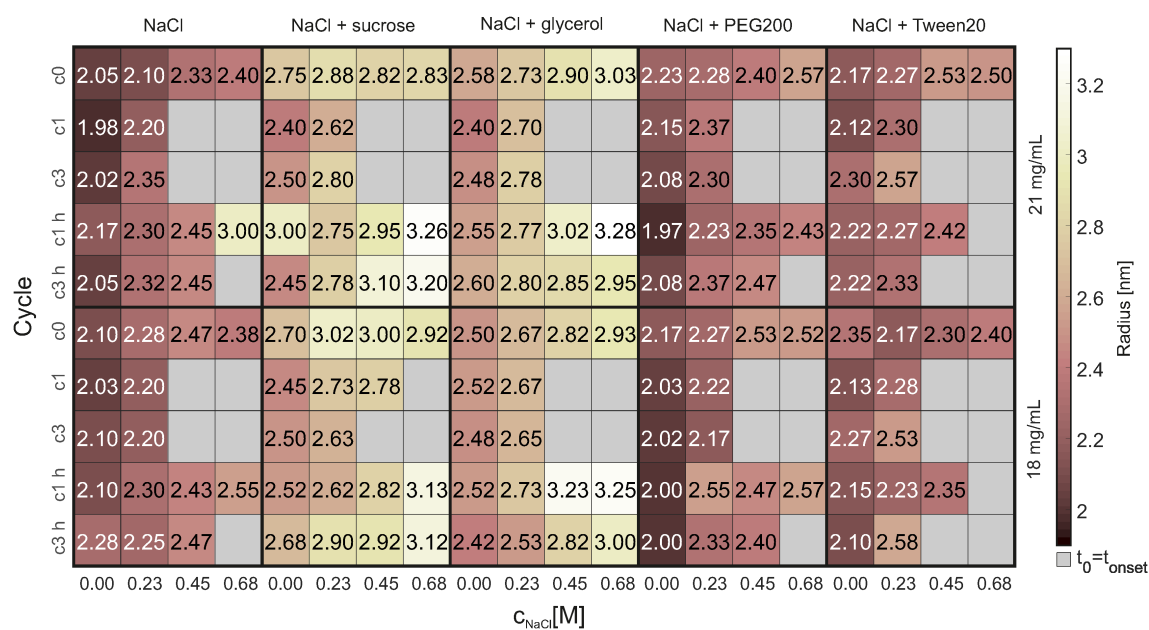
Figure 7.4.: The results of the 151 DLS measurements are shown. The NaCl concentration is plotted over the cycle number for the different formulations investigated. The upper row shows the results for 21 mg/mL lysozyme and the lower row for 18 mg/mL. The color bar represents the radius in nm. Measurements with the formulations where the box is marked gray were not possible due to aggregation appearance. The respective deviations from the triplicate measurements are shown in the Supplementary Material Figure B.16.
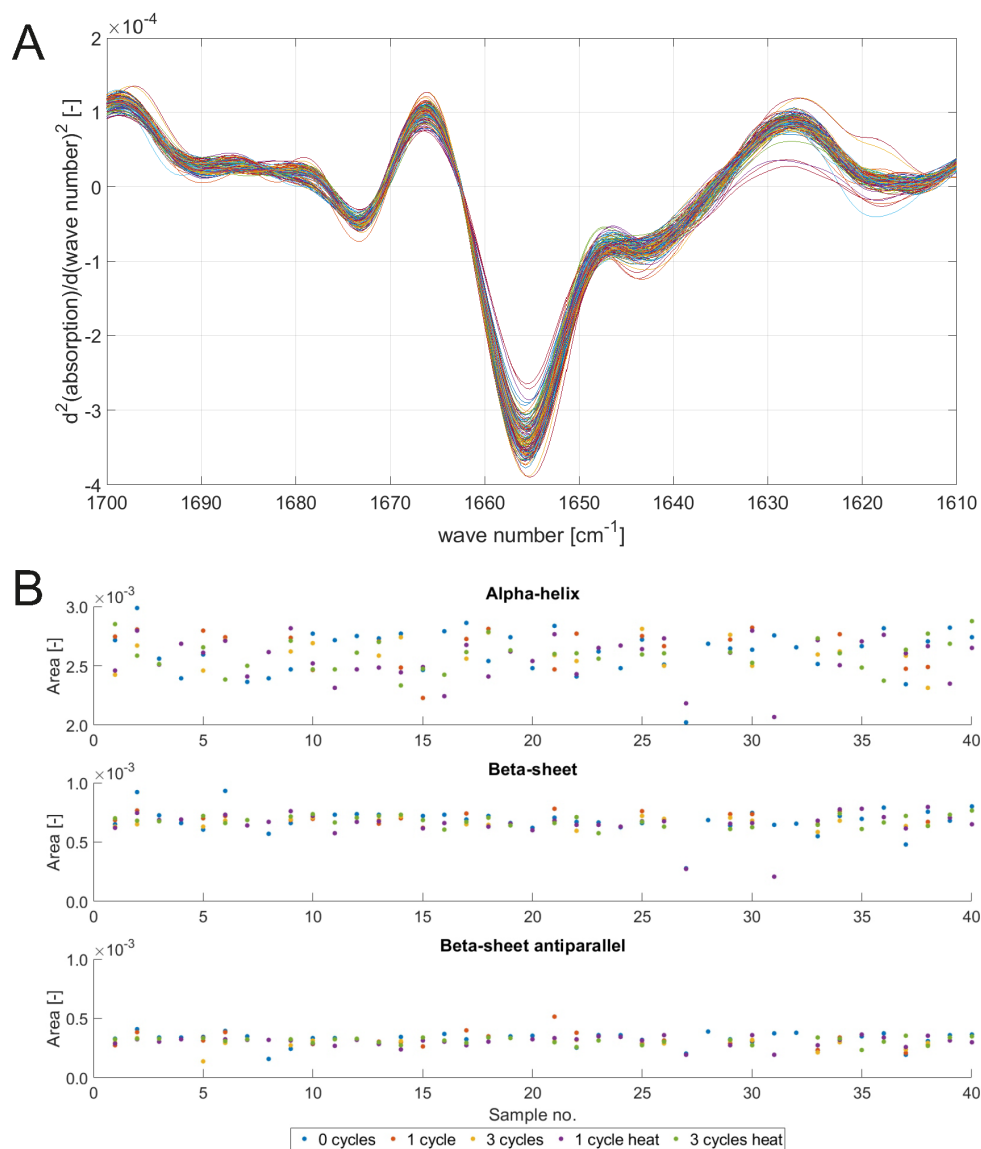
Figure 7.5.: In A the pre–processed FTIR spectra for all 151 samples, which performed also the DLS measurements, are plotted (see Figure 7.4). The range between a wave number of 1650 - 1685 cm^{-1} represents alpha–helix structure, 1615 - 1635 cm^{-1} beta–sheet structures, and 1670 - 1685 cm^{-1} beta–sheet antiparallel structures. In B the calculated areas of the interesting regions for alpha–helix (top), beta–sheet (middle) and beta–sheet antiparallel (bottom) are shown for all measured samples (Sample no. 1-8: NaCl; 9-16: NaCl + sucrose; 17-24: NaCl + glycerol; 25-32: NaCl + PEG200; 33:40: NaCl + Tween20). Blue dots represent 0 cycles, red points 1 cycle, yellow dots 3 cycles, purple dots 1 cycle heat, and green dots 3 cycles heat.

7.4. Discussion

In the following section, results are discussed concerning the influence of the tested excipients (300 mM sucrose, 1000 mM glycerol, 6.81 mM PEG200, 0.03 mM Tween20) on the long–term protein stability of FT–stressed formulations, as well as whether these changes are reversible by adding a heat cycle after the respective FT protocol was performed. The results are discussed separately for each formulation tested and the respective influence of the heat cycle. Finally, a comparison is made across the different formulations.

7.4.1. Multidimensional protein phase diagram (MPPD)

The creation of the MPPDs resulted in an information loss of only 10% due to data dimension reduction from nine to three dimensions. Consulting literature, this falls in an acceptable range [253].

The MPPD procedure allowed an automated evaluation and clustering providing a rapid overview over a huge data set of complex phase transitions taking place in the phase diagrams. As shown in Figure 7.2 it further provided insight into positioning (Figure 7.2 A) and occurrence (Figure 7.2 B) of different phase states. While clustering as such occurs in an automated fashion, the choice of suitable descriptors is of course subjective and great care needs to be taken when deciding on a certain set. Two examples underlining this are seen in the current study. The misclassifications seen for Cl I (meant to represent soluble formulations only) were due to accommodating the high variety of crystal sizes in a single data set. The data set included length and width values, which are very large (due to sea urchin crystals) and very small (due to micro crystals).

With the normalizing step during MPPD creation, the small size values close to zero let to an incorporation into Cl I. In addition, the formulations belonging to a cluster do show a distinct distribution and the transition from one to another cluster might lead to overlaps. This is visualized in Figure B.15 in the Supplementary Material, where all 2400 conditions are plotted.

A second issue going hand-in-hand with the above findings is the appearance of two different morphologies seen for Cl IV and Cl VI, as shown in Figure 7.1. Here, the reason lies clearly in the similarity of the image-based parameters taken into account, namely size and time. This shows the care and orthogonality needed when choosing descriptors for an automated classification scheme. In the present study, a distinction of different morphologies could be possibly reached by an addition of the crystal intensity, due to the higher intensity of sea urchin crystals and the dense micro crystal when compared to tetragonal crystals (independent of size).

Nevertheless, a MPPD creation allows an objective scoring and clustering of phase diagrams, based on crystal dimensions and other descriptors chosen. In a second step, however, the

raw data of the created clusters needs to be checked to ensure that choice of descriptors, overlap, and distribution of features does not lead to a false interpretation of data.

7.4.2. Formulations

In the following section the results obtained for each system tested using the MPPD approach are discussed. The evaluation of molecular starting conditions, namely the DLS and FTIR measurements of the soluble regions chosen (Figure 7.4 and Figure 7.5) for two different concentrations show no significant alteration in measured values as a function of stress applied. From this it can be concluded that the formation of different crystal morphologies and thus cluster distribution is not dependent on structural protein parameter. But it should keep in mind that a small fraction of protein might undergo partial unfolding and/or aggregation, which is not detectable using the described DLS or FTIR measurements. These small changes might cause undesirable particle formation and change in the crystallization kinetics.

The increase in apparent size seen for increasing salt concentrations, and respectively higher ionic strengths, within a certain formulation subgroup might be due to increasing hydrophobic protein–protein interactions [203]. The greater the protein–protein interactions, the lower the molecule diffusion in the solutions and the bigger the hydrodynamic radius estimated by DLS measurements [172]. The slightly bigger apparent radii of sucrose and glycerol formulations can be explained by an overall increased viscosity, due to the high excipient concentrations used, and the procedure of how the hydrodynamic radius is estimated (Stokes–Einstein equation) [171, 172].

The respective excipients were chosen due to their different protein interaction mechanism, which are explained in the following.

Salt: Using NaCl as an additive only, the salt concentration mainly modulates electrostatic interactions and suppressing these allows hydrophobic interactions to play a more dominant role. Lysozyme with a pI of 11.35 [23] is positively charged at the operating pH of pH 5. Given this, the distance to its pI seems wide enough so that a slight change in pH will not result in changes of surface charge and effects seen can be related to alteration in additive solely. The concentration range from 0-1.1 M NaCl was chosen due to the ability of stabilizing or destabilizing the protein stability depending on the protein surface charge and the salt concentration [74].

Osmolytes: Two different osmolytes were chosen in this study, due to their ability to stabilize the native structure of the protein upon environmental stress [141–143] and thus also act as cryoprotectants. The osmolytes used in this study are sucrose [88, 89], a sugar, and glycerol [142, 272], a polyol.

Sucrose: Sucrose is known to be an effective cryoprotectant, due to stabilizing the native structure of proteins by thermodynamic stabilization. Thereby, preferential exclusion of sucrose and subsequently hydration of the protein surface are taking place [67].

Glycerol: The mechanisms triggered by adding glycerol are not completely understood. The most significant contributions are twofold. There is preferential exclusion effect of glycerol,

comparable with sucrose, where the native protein structure is stabilized. Furthermore, stabilization of glycerol is assumed to be also due to preferential interaction of glycerol and the hydrophobic regions on the protein surface and following the inhibition of protein unfolding [272].

Polymers: Polymers are also known to generally stabilize protein solutions [75, 274], whereas the mode of action is strongly dependent on their molecular weight [84] and concentration applied [85]. Low molecular weight PEG present in low concentrations may induce protein stabilization due to the steric shielding of attractive protein-protein interactions [85, 143]. This effect is exploited in this study using 6.81 mM (6 w/w%) PEG200. Depending on the hydrophobicity of the protein surface, the mechanism of PEG is influenced. When the protein surface is hydrophobic, destabilizing preferential interaction of the hydrophilic PEG molecules and the hydrophobic patches on the protein surface is taking place. Otherwise, like in this study where the protein surface is positively charged, stabilizing preferential exclusion of the PEG molecules is taken place [274].

Surfactant: Finally surfactants, and in this group of excipients especially Tween20 and Tween80 are commonly used, due to their ability to stabilize protein stability against freeze stressinduced aggregation [90, 91]. In this study, 0.03 mM of Tween20 was chosen. The chosen concentration was distinctly below the critical micelle concentration (CMC) of 0.57 mM [275] to potentially prevent surface loss and aggregation [81]. Surfactants are known to interact with the hydrophobic regions on the protein surface [81, 82, 276]. In addition, surfactants are also known to prevent the unfolding of the protein on hydrophobic surfaces such as airwater [80].

Initial state – FT c0

Using NaCl as an additive, the salt concentration influenced the phase behavior, the aggregation kinetics, the crystal morphology, and the radius of lysozyme. Here we clearly see the interplay of electrostatic and hydrophobic interactions. In short, at lower salt concentrations, long-range repulsive electrostatic protein interactions are significant [158, 269]. These forces are reduced by the presence of salt ions and short-range attractive forces become dominant, which results in aggregation [18, 199, 202, 203]. Consequently, at low sNaCl concentrations (< 300 mM), a salting-in (stabilizing) effect and at high NaCl concentrations, a salting–out (destabilizing) effect was observed [74].

The salt concentration not only determined protein solubility but also influenced the crystal morphology. The aggregation zone occurs adjacent to Cl I, representing the soluble zone. This zone is often referred to as the labile or crystallization zone; here, the energy barrier to create nuclei is overcome and crystal growth can occur [41]. As the appearance of Cl II and Cl III corresponded to this zone, they showed similar crystal sizes but the growth time differs.

For Cl III the growth time (t_G) is smaller, however, this cluster was mainly seen for higher lysozyme concentrations, thus a higher supersaturation [258] and as a consequence enhanced creation of critical nuclei [47, 208]. Higher supersaturation is assumed to correlate to shorter growth time, which results of crystal growth to bigger sizes. Bigger crystals

were not reached in the phase diagram, here, it is assumed that the concentration steps of lysozyme and NaCl were too huge to reach this zone after Cl II and Cl III appeared. Instead, the supersaturation was too high for supporting crystal growth but with increasing salt concentrations and high protein concentrations, resulted in an increase in the amount of crystals and a decrease in crystal size [186, 258, 259], corresponding to Cl IV and Cl V, see Table 7.1. At very high lysozyme and NaCl concentrations, the supersaturation reaches a level where the growth of unstable polymorph crystals (sea urchin crystals) is promoted [35, 191]. This morphology is represented partly by Cl VI and mainly by Cl VII.

When adding sucrose – representing the group of osmolytes – to the salt containing systems at FT c0 a slightly higher lysozyme solubility was reached, whereas the size of the aggregation zone slightly decreased. Subsequently, a small stabilizing effect can be attributed, due to the mentioned preferential exclusion of sucrose [67].

Regarding cluster positioning and occurrence, the transition to the soluble zone seems unaltered, while the aggregation shape changed to smaller crystals (from Cl III to Cl IV) at higher protein and medium NaCl concentrations, when sucrose was added. The supersaturation level is high enough to create critical nuclei but due to preferential exclusion of sucrose, the growth time (t_G) is reduced, which results in a higher amount of small crystals. In addition, at higher NaCl concentrations, the zone of Cl VII is larger adding sucrose to the formulations when compared to pure NaCl formulations. This might be due to the higher viscosity of sucrose formulations in this region compared to pure NaCl formulations. The viscosity of a 300 mM sucrose solution ($\sim$10 w/w%) at 25 °C is 1.31 mPas which is higher than the viscosity of pure water at 25 °C of 0.89 mPas [271]. Due to the lower nucleation rate, high supersaturation in these formulations and the formation of temporary LLPS, sea urchin crystals grow preferably in this region [35, 191].

Comparable to the addition of sucrose, we see an increase of Cl I (soluble region) when adding glycerol. A higher viscosity of the formulation might also explain the increasing amount of small crystal sizes at intermediate salt concentrations. The viscosity at 25 °C of a 1000 mM glycerol ($\sim$9 w/w%) solution is slightly lower (1.15 mPas) compared to a 300 mM sucrose formulation (1.31 mPas) [271]. The cluster formation only differed in the high–salt region compared to sucrose formulations. No sea urchins (Cl VI or Cl VII) appeared with glycerol formulations, see Figure 7.2 A, C 3. Glycerol seems to influence the nucleation rate in this region. Nevertheless, due to the still very high nucleation rate micro crystals grow (Cl IV).

PEG200 – representing the group of polymers – is known to be preferentially excluded. However, according to the size of the aggregation zone, lysozyme solubility, and cluster formation, no significant changes were observed compared to the pure NaCl formulations. In the applied concentration (as compared to protein and salt concentration present) PEG200 is probably to low concentrated for non–stressed conditions to lead to a significant change. Due to NaCl attractive protein–protein interactions occur, which can be shielded by the PEG molecules. However, in this case it is assumed that the attractive protein–protein interactions are too present and/or the PEG concentration is too low to stabilize lysozyme. A higher PEG concentration or molecule weight is assumed to be more effective [84, 85].

Finally, the influence of surfactants was probed by adding Tween20. The protein phase behavior was not changed significantly by the addition of Tween20, but the morphology

and the protein solubility differ compared to pure NaCl formulations. The interaction of Tween20 probably resulted in lower protein solubility, and the SL area showed smaller values, see Figure 7.3 B, due to the shifted equilibrium between monomer and aggregated proteins towards aggregated proteins. The interaction of Tween20 with the hydrophobic patches on the protein surface [81, 82, 276] might have resulted in a significant cluster formation of Cl V, indicating micro crystals. It can be assumed that, due to the interaction of Tween20 on the protein surface, the formation of bigger tetragonal crystals is inhibited. Finally, unfolding on hydrophobic water-air interfaces seems to be not a problem for lysozyme in this study and subsequently, no stabilizing by Tween20 at FT c0 could be observed.

FT cycle – FT c1 and FT c3

The unmet ability of the MPPD approach to visualize positioning (Figure 7.2 A) and occurrence (Figure 7.2 B) of cluster transformation can also be seen in the development of cluster during FT cycling. In general, all tested excipients had an impact on the MPPD and the SL area compared to the pure NaCl formulations. In the following, the potential mechanistic processes occurring (shielding attractive proteinprotein interactions, preferential hydration, and the stabilization of the native state) and thus being the driver behind the cluster transformations during FT cycling are discussed. For all tested excipients, a reduction of Cl I is seen and can be linked to freeze concentration effects experienced during FT cycling. Freeze concentration results in an increase of supersaturation, leading to an increase in the concentration of all solutes, such as buffer components, excipient, and proteins, due to the formation of ice crystals [35, 268]. This results in protein aggregation [224, 249] and subsequently, the protein solubility is lowered due to the shifted aggregate/monomer equilibrium towards aggregates, which was observed with the solubility lines, see Figure 7.3 B. In addition to the effect of freeze concentration, the decrease in Cl I can also be attributed to the repetition of the FT stress effects as such. In combination, next to freeze concentration [35, 268], temperature–induced LLPS [35, 140, 150] and denaturation on the water–ice interface [90, 109] might take place. Among these effects, however, denaturation on the water–ice interface can be excluded, at least for the measured samples, due to the shown similarity of the FTIR spectra to those of FT c0 (Figure 7.5). A cluster transformation towards a higher portion of Cl IV and shift towards lower salt concentrations was shown for NaCl formulation (and all other systems discussed below), when FT stress was applied, see Figure 7.2. This indicates a change to more and smaller crystals, pointing towards a freeze concentration effect. The nucleation rate of crystals depends on the degree of supersaturation (Mullin, 1992). Due to freeze concentration, the supersaturation is increased and consequently, the nucleation rate is increased as well. For pure NaCl systems, above 1.82 M mainly Cl VI and Cl VII appeared, indicating a shift to sea urchin crystals. It can be assumed that the initial viscosity in these formulations (due to temperature [138] and protein concentration) was very high leading to a lower diffusion rate, which in return results in a lower nucleation rate [264]. Next to the lower nucleation rate, high supersaturation, as well as temporary LLPS, is another prerequisite for the growth of

sea urchin crystals [35, 191]. The application of FT stress to sucrose formulations resulted in an overall lower decrease in protein solubility. Thus, the known effectiveness of sucrose as a cryoprotectant could be confirmed with these observations [88, 89]. The dominating cluster formation of Cl V and Cl VI and spread towards lower excipient concentrations mimics the above stated line of argumentation, namely an increase in the nucleation rate due to freeze concentration [35, 191, 270]. For glycerol containing systems, FT stress application resulted in a smaller occurrence of Cl I and a decrease in solubility, but less significant than for NaCl formulations, see Figure 7.2 B and Figure 7.3 B. Subsequently, glycerol was - as expected - able to stabilize lysozyme regarding FT stress. The intermediate cluster transition from small (Cl IV) to bigger (Cl II) crystals seen for FT c1 took place at protein concentrations below 2 mg/mL lysozyme. This might be an indication for a situation where FT stress is no yet the dominating factor and the addition of glycerol resulted in slower aggregation kinetics and larger crystals [164]. When performing the FT cycles three times the observed cluster formation of Cl VI and its positioning resembled the above-described dominant situation. PEG200 showed no stabilizing effect, seen in the decrease of Cl I, compared to the NaCl formulations. Overall, as found for the other systems, the scheme of a dominant growth of Cl IV is seen and due to the above-described combination of FT stress. The systems containing Tween20 already started with a dominating Cl V. With an increase in FT stress, a clear decrease in Cl I was observed pointing towards the inability of the current formulation to act as stabilizing formulation under the given conditions. This is underlined by the most dominant appearance of Cl IV during FT cycling over the whole aggregation zone.

Overall, the highest values of the calculated SL area were reached with the osmolytes tested (sucrose and glycerol) due to preferential hydration of the surface and minimized protein–protein interactions. The smaller the proteinprotein interactions, the higher the solubility [164, 165]. Consequently, sucrose and glycerol are the excipients that were able to stabilize lysozyme the most regarding solubility and size of the solubility zone during FT cycling. PEG did not change stability significantly. For all systems investigated the addition of Tween20 led to destabilization when compared to pure NaCl containing systems, which is probably due to the applied concentration.newline

Heat cycle - FT c1 h and FT c3 h

When applying heat cycling after FT cycling a clear cluster transformation and thus reversibility of already formed aggregates resulting in a decrease of Cl IV and increase in Cl I as well as an increase in protein solubility (Figure 7.3) is seen. This clearly shows that heat cycling might be applied to exploit the reversibility of aggregates formed during FT cycling but also during general processing, i.e. other unit operations creating aggregates. In general, mainly Cl IV areas transformed back to Cl I, but also Cl II and Cl III. In common to these clusters is either no t_{onset} for Cl I (fully soluble area) or $t_{onset} > t_0$ for Cl II and Cl III, whereas the other clusters (Cl IV Cl VII) showed aggregates from the beginning when the plates were pictured the first time $t_{onset} = t_0$. The heat–induced reversibility is assumed to lead to a reset of the reversible systems and new arrangement of crystals independent of and undisturbed by stress resulting from FT or heat cycling.

A potential cause for a reset of systems in this study mainly systems lying in the metastable zone containing reversible aggregates by heat cycling might be that the applied heat/energy input was high enough to loosen proteinprotein interactions (only weak noncovalent protein interactions) [25], but also low enough not to induce heat aggregation and/or unfolding (Wang et al., 2010). In this context, it is assumed that aggregates in the lower supersaturated region (adjacent to Cl I) created weak proteinprotein interactions and therefore those are able to dissolve by heat [25], and consequently the same clusters are created than without FT stress or heat.

The good reversibility found for the osmolyte systems containing sucrose or glycerol is assumed to relate to weak proteinprotein interactions [25, 138] and thus potentially reversible, due to the preferential hydration of the protein surface supported by the excipients.

Also for the PEG200 systems, heat–induced reversibility was observed. However, the effect was found not as significant as for NaCl formulations. In contrary, PEG200 molecules seemed to stabilize the aggregates, which occurred due to the FT stress. The reason for this might be based on the overall higher polymer concentrations in solution due to freeze concentration, resulting in a displacement of the PEG molecules from between the protein molecules instead of steric stabilization [277]. Hence, the restructuring of the PEG molecules seems to be not completely reversible. For Tween20 formulations, the heat cycle only influences the occurrence of Cl I and the overall protein solubility. The protein solubility could be completely reversed by heat (Figure 7.2 B). The occurrence of Cl I, representing the soluble zone, was not completely reversed to the size observed at FT c0, but most of the FT stress–induced aggregates dissolved when heat was applied, see Figure 7.2 B.

In summary, the best performance (increase of Cl 1) in the heat–induced reversibility showed glycerol containing systems. The follow–up systems were sucrose, pure NaCl and the Tween20 systems (the latter showing a reduced reversibility for increasing FT cycling). The lowest effect on heat–induced reversibility was seen for the PEG200 containing systems.

7.5. Conclusion

In this study, the effects of instabilities induced by FT stress (up to three cycles) and the reversibility of those instabilities induced by heat on the long–term (MPPD,SL) and short–term protein stability (size and structure) were investigated using lysozyme as an exemplary protein. It was shown that a re-set of areas consisting of reversible aggregates could be reached by heat cycling. This led to a resolution of reversible aggregates. The influence of different well–known cryoprotectants (sucrose, glycerol, PEG200 and Tween20) showed, that the degree of instabilities and reversibility of aggregates was formulations dependent. The effects of FT induced instabilities and their reversibility by heat–cycling, depending on the different formulations can be summed up as follows: The addition of sucrose and glycerol resulted in the best performance as cryoprotectant. Regarding

aggregate reversibility (increase in ClI) glycerol performed best, followed by sucrose, NaCl and Tween. Finally, the use of MPPD to study the complexity and interplay of different formulations and processing situations showed to be excellent in terms of data visualization. In future work, the influence of heat cycling on reversible aggregation will be investigated. Furthermore, different formulation parameters like pH value, salts, cryoprotectants, and buffer systems need to be investigated. The transfer to other protein molecules and also to highly concentrated protein formulations is mandatory for applications in industry. Finally, the addition of a heat cycle might be an effective tool to minimize instabilities throughout general processing.

Acknowledgements

8. Conclusion and Outlook

A phase diagram–based method was developed which allows the investigation of FT stress–induced protein instabilities. For the developed method only a small sample volume (max. $30\,\mu$L) for each condition is needed, and HTS (96–well) is possible. Combined with the phase diagrams, the developed method is simple, cheap, and time–saving. The huge flexibility while creating phase diagrams allowed a screening of different formulation parameters, like different protein and salt concentrations, buffer systems, pH values, and additives (salts and cryoprotectants). The basic created phase diagram contained formulations with lysozyme from chicken egg white and sodium chloride. While varying their concentration a phase transition with different phase states, as soluble, crystal, and precipitate, appeared. Changes within these phase states, varying crystal morphologies and different protein solubilities, which were determined by supernatant concentration measurements, were identified to be sensitive parameters to rate FT stress–induced instabilities. All the named formulation parameters showed an influence on the phase behavior and result in a different degree of FT stress sensitivity. In addition, while handling the phase diagram the FT process parameters can be varied before the plates are placed in an incubation chamber for 40 days to investigate the long–term protein stability. Here, the influence of the number of FT cycles and different freezing/thawing ramps were investigated. The more FT cycles are applied to the formulations, the more instabilities were rated. Furthermore, the choice of the freezing rate was found to be more critical than the choice of the thawing rate for formulations with lysozyme. In addition, the faster the freezing/thawing rate was chosen, the less instabilities were induced due to the fact that probably not the water–ice interface but the overall process time was the destabilizing factor. After the method development and verification, the method was extended to be able to also detect system parameters and create even more knowledge about the freezing/thawing process. Therefore, images of the phase diagrams were recorded during freezing/thawing. The images were evaluated regarding their turbidity changes, which indicates T_{cloud}. A high sensitivity and robustness of this method extension was validated and a partial correlation of the short–term parameter T_{cloud} and long–term protein stability was determined. In addition, the reversibility of FT stress–induced protein instabilities as a function of different cryoprotectants was investigated. Dependent on the cryoprotectant, stabilization during freezing and thawing and reversibility by heat treatment was possible. For the degree of reversibility the type of the created aggregates might be critical. In addition, a correlation of short–term parameters (size and structure) of soluble formulations to long–term protein stability was strived. However, neither the size nor the protein structure were influenced

by the amount of FT stress, the addition of cryoprotectants, or the applied heat and a correlation to long–term stability was not possible.

In summary, the developed method enables a simple HT screening of small volumes of formulation and process parameters during freezing/thawing. Here, the crystal morphology is one of the main evaluation parameters. Subsequently, for proteins which do not crystallize, the method has to be developed further and another sensitive evaluation parameter has to be figured out. Then the transfer to biopharmaceutical proteins is easy and straight forward. Furthermore, the investigation of other process parameters like the storage temperature and its correlation to T_g, measured with e.g. DSC, might enable an even better understanding of the impact of freezing/thawing on proteins. Here, the sensitivity of T_g to formulation changes and/or process parameters might clarify and simplify the challenge regarding the choice of the storage temperature to be economically but still low enough to guarantee long–term protein stability. Within all the generation of the data and the influences of different parameters, the data handling, like visualization of effects, and the correlation of these parameters, has to be improved to identify all correlations. Here, the combination with protein characteristics to each other, e.g. protein structure, protein surface charge distribution, the pI of the protein, or the protein size, might be a successful step towards the prediction of protein long–term stability in combination with their stability during freezing and thawing. This would simplify the development of the freezing/thawing step and would save time, expenses, and would lower the loss of protein functionality. To also save product, needed for such developments, a correlation of small volumes (μL) to large volumes (L) is needed. The volume is known to be one of the critical parameters, due to the appearance of ice fronts within the bulk. This is strongly dependent on the geometry of the freezer. To investigate these effects and successfully scale–up/–down the process parameters, e.g. the FT ramp, and the degree of supercooling have to be the same due to their impact on the protein stability.

In general, freezing and thawing is applied within nearly all production processes of biopharmaceutical proteins. The detailed knowledge about this step is lacking and production loss was an increasing problem in the last years. This work developed a method to investigate the parameters affecting protein stability in a simple, cheap (low sample volume), and time–saving way (HT format). However, the method has to be further enhanced to be able to deepen the knowledge about freezing and thawing in general, but specifically about the correlation between the protein stability and the formulation, system, and process parameters even more. With this knowledge the research and development of a FT step for the production of biopharmaceutical proteins might be significantly enhanced, and the adaptation to changing formulation parameters would be simplified.

Bibliography

1. WALSH, G.: Biopharmaceutical benchmarks 2010. *Nature Biotechnology* (2010), vol. **28**(9): 917–924 (2010) (cit. on p. 1).

2. DEMAIN, A. L. & P. VAISHNAV: Production of recombinant proteins by microbes and higher organisms. *Biotechnology Advances* (2009), vol. **27**(3): 297–306 (2009) (cit. on p. 1).

3. NAYAR, R. & M. MOSHARRAF. *Formulation and Process Development Strategies for Manufacturing Biopharmaceuticals* 309–328 (2010) (cit. on pp. 1, 21).

4. INTERNATIONAL COUNCIL FOR HARMONIZATION: Stability testing of biotechnological/biological products Q5C. *ICH Harmonised Tripartite Guideline* (1995), vol. (November): 1–8 (1995) (cit. on pp. 1, 21, 75).

5. WANG, W. & C. J. ROBERTS: Protein aggregation - Mechanisms, detection, and control. *International Journal of Pharmaceutics* (2018), vol. **550**(1-2): 251–268 (2018) (cit. on pp. 1, 11).

6. CROMWELL, M. E. M., E. HILARIO & F. JACOBSON: Protein aggregation and bioprocessing. *The AAPS journal* (2006), vol. **8**(3): E572–E579 (2006) (cit. on pp. 1, 6, 21, 46, 75).

7. TUOMI, T., N. SANTORO, S. CAPRIO, M. CAI, J. WENG & L. GROOP: The many faces of diabetes: A disease with increasing heterogeneity. *The Lancet* (2014), vol. **383**(9922): 1084–1094 (2014) (cit. on p. 1).

8. FORLONI, G., L. TERRENI, I. BERTANI, S. FOGLIARINO, R. INVERNIZZI, A. ASSINI, G. RIBIZZI, A. NEGRO, E. CALABRESE, M. A. VOLONTÉ, C. MARIANI, M. FRANCESCHI, M. TABATON & A. BERTOLI: Protein misfolding in Alzheimer's and Parkinson's disease: Genetics and molecular mechanisms. *Neurobiology of Aging* (2002), vol. **23**(5): 957–976 (2002) (cit. on p. 1).

9. FROKJAER, S. & D. E. OTZEN: Protein drug stability: A formulation challenge. *Nature reviews. Drug discovery* (2005), vol. **4**(4): 298–306 (2005) (cit. on p. 1).

10. BRANDEN, C. I. & J. TOOZE: *Introduction to protein structure* (Garland Science, Taylor & Francis Group, New York, USA and Abingdon, UK, 1999) (cit. on p. 1).

11. SCHOLTZ, J. M. & R. L. BALDWIN: The mechanism of alpha-helix formation by peptides. *Annual Review of Biophysics and Biomolecular Structure* (1992), vol. **21**: 95–118 (1992) (cit. on p. 2).

12. Berg, J. M., J. L. Tymoczko & L. Stryer: *Biochemie* 7. (Springer Verlag, Berlin Heidelberg, 2012) (cit. on p. 2).

13. Wang, W.: *Instability, stabilization, and formulation of liquid protein pharmaceuticals* **2**: 129–188 (1999) (cit. on pp. 2, 18, 22, 100).

14. Chi, E. Y., S. Krishnan, T. W. Randolph & J. F. Carpenter: Physical stability of proteins in aqueous solution: Mechanism and driving forces in nonnative protein aggregation. *Pharmaceutical Research* (2003), vol. **20**(9): 1325–1336 (2003) (cit. on pp. 2, 6–8, 18, 68, 75).

15. Pace, C. N. & B. A. Shirley: Forces contributing proteins of proteins. *FASEB Journal* (1996), vol. **10**(1): 75–83 (1996) (cit. on p. 2).

16. Pace, C. N., S. Treviño, E. Prabhakaran, J. M. Scholtz, F. Franks, K. Wilson, R. M. Daniel, P. J. Halling, D. S. Clark & A. Purkiss: Protein structure, stability and solubility in water and other solvents. *Philosophical Transactions of the Royal Society B: Biological Sciences* (2004), vol. **359**(1448): 1225–1235 (2004) (cit. on p. 2).

17. Myers, J. K. & C. N. Pace: Hydrogen bonding stabilizes globular proteins. *Biophysical Journal* (1996), vol. **71**(4): 2033–2039 (1996) (cit. on p. 2).

18. Leckband, D. & J. Israelachvili: Intermolecular forces in biology. *Quarterly reviews of biophysics* (2001), vol. **34**(2): 105–267 (2001) (cit. on pp. 2, 46, 100, 119).

19. Van Oss, C. J.: Long-range and short-range mechanisms of hydrophobic attraction and hydrophilic repulsion in specific and aspecific interactions. *Journal of Molecular Recognition* (2003), vol. **16**(4): 177–190 (2003) (cit. on p. 2).

20. Piazza, R.: Interactions and phase transitions in protein solutions. *Current Opinion in Colloid & Interface Science* (2000), vol. **5**(1-2): 38–43 (2000) (cit. on pp. 2, 46).

21. Research, H.: *Lysozyme User Guid* tech. rep. (2014): 1–2 (cit. on p. 3).

22. Palmer, K. J., M. Ballantyne & J. A. Galvin: The molecular weight of lysozyme determined by the X-ray diffraction method. *Journal of the American Chemical Society* (1948), vol. **70**(3): 906–908 (1948) (cit. on p. 3).

23. Wetter, L. R. & H. F. Deutsch: Immunological studies on egg white proteins IV. Immunochemical and physical studies of lysozyme. *Journal of Biological Chemistry* (1951), vol. **192**: 237–242 (1951) (cit. on pp. 3, 91, 118).

24. Mahler, H.-C., W. Friess, U. Grauschopf & S. Kiese: Protein aggregation: Pathways, induction factors and analysis. *Journal of Pharmaceutical Sciences* (2009), vol. **98**(9): 2909–2934 (2009) (cit. on pp. 3, 6, 7, 32, 75).

25. Narhi, L. O., J. C. Smith, K. Bechtold-Peters & D. Sharma: Classification of protein aggregates. *Journal of Pharmaceutical Sciences* (2012), vol. **101**(2): 493–498 (2012) (cit. on pp. 3, 11, 22, 100, 101, 123).

26. Philo, J. S. & T Arakawa: Mechanisms of protein aggregation. *Curr Pharm Biotechnol* (2009), vol. **10**(4): 348–351 (2009) (cit. on pp. 3, 4, 6, 22, 75, 100, 101).

27. Faber, C. & T. J. Hobley: *Measurement and prediction of protein phase behaviour and protein-protein-interactions* PhD thesis (Technical Univerity of Denmark, 2006): 197 (cit. on pp. 4, 5, 19).

28. Garca-Ruiz, J. M.: Nucleation of protein crystals. *Journal of Structural Biology* (2003), vol. **142**: 22–31 (2003) (cit. on pp. 4, 5, 47, 69, 93).

29. Volmer, M. & A. Weber: Keimbildung in ubersattigten Gebilden. *Zeitschrift fur Physikalische Chemie* (1926), vol. **119**: 207–301 (1926) (cit. on p. 4).

30. Feher, G & Z Kam. *Methods in Enzymology* 77–112 (1985) (cit. on pp. 4, 6).

31. Vekilov, P. G. & F. Rosenberger: Dependence of lysozyme growth kinetics on step sources and impurities. *Journal of Crystal Growth* (1996), vol. **158**(4): 540–551 (1996) (cit. on p. 5).

32. Veesler, S. & R. Boistelle. *Crystalliztion of Nucleic Acids and Proteins* (eds Ducruix, A. & R. Giege) 313–340 (Oxford University Press, Oxford, UK, 1999) (cit. on p. 6).

33. Wang, W., S. Nema & D. Teagarden: Protein aggregation-pathways and influencing factors. *International Journal of Pharmaceutics* (2010), vol. **390**(2): 89–99 (2010) (cit. on pp. 6, 7, 9–11, 13, 14, 22, 31, 54, 75, 100).

34. Lewus, R. A., P. A. Darcy, A. M. Lenhoff & S. I. Sandler: Interactions and phase behavior of a monoclonal antibody. *Biotechnology Progress* (2011), vol. **27**(1): 280–289 (2011) (cit. on p. 6).

35. Muschol, M. & F. Rosenberger: Liquid liquid phase separation in supersaturated lysozyme solutions and associated precipitate formation / crystallization. *The Journal of Chemical Physics* (1997), vol. **107**(6) (1997) (cit. on pp. 6, 13, 22, 31, 32, 47–49, 51, 67, 68, 76, 86, 93, 94, 100, 120–122).

36. Fink, A. L.: Protein aggregation: Folding aggregates, inclusion bodies and amyloid. *Folding and Design* (1998), vol. **3**(1): 9–23 (1998) (cit. on p. 6).

37. Liu, J., M. D. Nguyen, J. D. Andya & S. J. Shire: Reversible self-association increases the viscosity of a concentrated monoclonal antibody in aqueous solution. *Journal of Pharmaceutical Sciences* (2005), vol. **94**(9): 1928–1940 (2005) (cit. on p. 6).

38. Veerman, C., K. Rajagopal, C. S. Palla, D. J. Pochan, J. P. Schneider & E. M. Furst: Gelation kinetics of β-hairpin peptide hydrogel networks. *Macromolecules* (2006), vol. **39**(19): 6608–6614 (2006) (cit. on p. 6).

39. Dumetz, A. C., A. M. Chockla, E. W. Kaler & A. M. Lenhoff: Protein phase behavior in aqueous solutions: Crystallization, liquid-liquid phase separation, gels, and aggregates. *Biophysical Journal* (2008), vol. **94**(2): 570–583 (2008) (cit. on pp. 6, 17, 47, 49).

40. Matheus, S., W. Friess, D. Schwartz & H.-C. Mahler: Liquid high concentration IgG1 antibody formulations by precipitation. *Journal of Pharmaceutical Sciences* (2009), vol. **98**(9): 3043–3057 (2009) (cit. on p. 6).

41. ASHERIE, N.: Protein crystallization and phase diagrams. *Methods* (2004), vol. **34**(3): 266–272 (2004) (cit. on pp. 6, 13, 18, 19, 22, 31, 32, 35, 48, 68, 75, 76, 92, 100, 119).

42. MCPHERSON, A.: Introduction to protein crystallization. *Methods* (2004), vol. **34**: 254–265 (2004) (cit. on pp. 6, 69).

43. WANG, W.: Protein aggregation and its inhibition in biopharmaceutics. *International Journal of Pharmaceutics* (2005), vol. **289**(1-2): 1–30 (2005) (cit. on pp. 6, 9, 22, 31, 32, 54, 75, 100).

44. SHEN, C. L., G. L. SCOTT, F. MERCHANT & R. M. MURPHY: Light scattering analysis of fibril growth from the amino-terminal fragment beta(128) of beta-amyloid peptide. *Biophysical Journal* (1993), vol. **65**(6): 2383–2395 (1993) (cit. on pp. 6, 31, 32).

45. CHAYEN, N. E.: Turning protein crystallisation from an art into a science. *Current Option in Structural Biology* (2004), vol. **14**: 577–583 (2004) (cit. on pp. 6, 31, 32, 69).

46. ATAKA, M.: Protein crystal growth: An approach based on phase diagram determination. *Phase Transitions: A Multinational Journal* (1993), vol. **45**(2-3): 205–219 (1993) (cit. on pp. 6, 31, 69).

47. LIN, C., Y. ZHANG, J. J. LIU & X. Z. WANG: Study on nucleation kinetics of lysozyme crystallization. *Journal of Crystal Growth* (2017), vol. **469**: 59–64 (2017) (cit. on pp. 6, 31, 47, 48, 51, 69, 119).

48. SOMERO, G. N.: Proteins and temperature. *Annual Review of Physiology* (2011), vol. **57**: 43–68 (2011) (cit. on pp. 6, 11, 31, 54).

49. MANNING, M. C., K. PATEL & R. T. BORCHARDT: Stability of protein pharmaceuticals. *Pharmaceutical Research* (1989), vol. **06**(11): 903–918 (1989) (cit. on pp. 6, 31).

50. MANNING, M. C., D. K. CHOU, B. M. MURPHY, R. W. PAYNE & D. S. KATAYAMA: Stability of protein pharmaceuticals: An update. *Pharmaceutical Research* (2010), vol. **27**(4): 544–575 (2010) (cit. on pp. 6, 31, 100).

51. SCOPES, R. K. *Protein Purificcation* 71–72 (1994) (cit. on pp. 7, 47, 49, 50).

52. SHAW, K. L., G. R. GRIMSLEY, G. I. YAKOVLEV, A. A. MAKAROV & C. N. PACE: The effect of net charge on the solubility , activity , and stability of ribonuclease Sa. *The Protein Society* (2001), vol. **10**(6): 1206–1215 (2001) (cit. on pp. 7, 46).

53. KUMAR, V., N. DIXIT, L. ZHOU & W. FRAUNHOFER: Impact of short range hydrophobic interactions and long range electrostatic forces on the aggregation kinetics of a monoclonal antibody and a dual-variable domain immunoglobulin at low and high concentrations. *International Journal of Pharmaceutics* (2011), vol. **421**(1): 82–93 (2011) (cit. on pp. 7, 75).

54. SAITO, S., J. HASEGAWA, N. KOBAYASHI, N. KISHI, S. UCHIYAMA & K. FUKUI: Behavior of monoclonal antibodies: Relation between the second virial coefficient (B22) at low concentrations and aggregation propensity and viscosity at high concentrations. *Pharmaceutical Research* (2012), vol. **29**(2): 397–410 (2012) (cit. on p. 7).

55. FENG, Y. W., A. OOISHI & S. HONDA: Aggregation factor analysis for protein formulation by a systematic approach using FTIR, SEC and design of experiments techniques. *Journal of Pharmaceutical and Biomedical Analysis* (2012), vol. **57**(1): 143–152 (2012) (cit. on p. 7).

56. JEZEK, J., M. RIDES, B. DERHAM, J. MOORE, E. CERASOLI, R. SIMLER & B. PEREZ-RAMIREZ: Viscosity of concentrated therapeutic protein compositions. *Advanced Drug Delivery Reviews* (2011), vol. **63**(13): 1107–1117 (2011) (cit. on p. 7).

57. SALUJA, A. & D. S. KALONIA: Nature and consequences of protein-protein interactions in high protein concentration solutions. *International Journal of Pharmaceutics* (2008), vol. **358**(1-2): 1–15 (2008) (cit. on p. 7).

58. CHARI, R., K. JERATH, A. V. BADKAR & D. S. KALONIA: Long- and short-range electrostatic interactions affect the rheology of highly concentrated antibody solutions. *Pharmaceutical Research* (2009), vol. **26**(12): 2607–2618 (2009) (cit. on p. 7).

59. JIAO, M., H. T. LI, J. CHEN, A. P. MINTON & Y. LIANG: Attractive protein-polymer interactions markedly alter the effect of macromolecular crowding on protein association equilibria. *Biophysical Journal* (2010), vol. **99**(3): 914–923 (2010) (cit. on p. 7).

60. STOLL, V. S. & J. S. BLANCHARD. *Methods in Enzymology* 1966: 24–38 (1990) (cit. on p. 8).

61. THIEL, T., L. LICZKOWSKI & S. T. BISSEN: New zwitterionic butanesulfonic acids that extend the alkaline range of four families of good buffers: Evaluation for use in biological systems. *Journal of Biochemical and Biophysical methods* (1998), vol. **37**: 117–129 (1998) (cit. on pp. 8, 49, 50).

62. HAMADA, H., T. ARAKAWA & K. SHIRAKI: Effect of additives on protein aggregation. *Current pharmaceutical biotechnology* (2009), vol. **10**(4): 400–407 (2009) (cit. on pp. 8, 9).

63. OHTAKE, S., Y. KITA & T. ARAKAWA: Interactions of formulation excipients with proteins in solution and in the dried state. *Advanced Drug Delivery Reviews* (2011), vol. **63**(13): 1053–1073 (2011) (cit. on pp. 8, 100).

64. GOLOVANOV, A. P., G. M. HAUTBERGUE, S. A. WILSON, L.-Y. LIAN, W. BANK & S SHEFFIELD: A simple method for improving protein solubility and long-term stability. *Journal of American Chenmcal Society* (2004), vol. **126**(29): 8933–8939 (2004) (cit. on p. 8).

65. KAMERZELL, T. J., R. ESFANDIARY, S. B. JOSHI, C. R. MIDDAUGH & D. B. VOLKIN: Protein-excipient interactions: Mechanisms and biophysical characterization applied to protein formulation development. *Advanced Drug Delivery Reviews* (2011), vol. **63**(13): 1118–1159 (2011) (cit. on pp. 8, 9).

66. TSUMOTO, K., M. UMETSU, I. KUMAGAI, D. EJIMA, J. S. PHILO & T. ARAKAWA: Role of Arginine in protein refolding, solubilization, and purification. *Biotechnology Process* (2004), vol. **20**: 1301–1308 (2004) (cit. on p. 8).

67. LEE, J. C. & S. TIMASHEFF: The stabilization of proteins by sucrose. *The journal of Biological Chemestry* (1981), vol. **256**(14): 7193–7201 (1981) (cit. on pp. 8, 118, 120).

68. GEKKO, K. & S. N. TIMASHEFF: Mechanism of protein stabilization by glycerol: Preferential hydration in glycerol-water mixtures. *Biochemistry* (1981), vol. **20**(16): 4667–4676 (1981) (cit. on p. 8).

69. ARAKAWA, T. & S. N. TIMASHEFF: Stabilization of protein structure by sugars. *Biochemistry* (1982), vol. **21**(25): 6536–6544 (1982) (cit. on pp. 8, 9).

70. ARAKAWA, T & S. N. TIMASHEFF: Mechanism of protein salting in and salting out by divalent cation salts: Balance between hydration and salt binding. *Biochemistry* (1984), vol. **23**(25): 5912–5923 (1984) (cit. on p. 8).

71. DE YOUNG, L. R., A. L. FINK & K. A. DILL: Aggregation of globular proteins. *Accounts of Chemical Research* (1993), vol. **26**(12): 614–620 (1993) (cit. on p. 8).

72. HOFMEISTER, F.: Zur Lehre von der Wirkung der Salze. *Archiv für experimentelle Pathologie und Pharmakologie* (1888), vol. **25** (1888) (cit. on pp. 8, 9, 50, 91).

73. BOSTRÖM, M, F. W. TAVARES, S FINET, F SKOURI-PANET, A TARDIEU & B. W. NINHAM: Why forces between proteins follow different Hofmeister series for pH above and below pI. *Biophysical Chemistry* (2005), vol. **117**(3): 217–224 (2005) (cit. on pp. 9, 91).

74. ZHANG, Y. & P. S. CREMER: The inverse and direct Hofmeister series for lysozyme. *Proceedings of the National Academy of Sciences* (2009), vol. **106**(36): 15249–15253 (2009) (cit. on pp. 9, 91, 118, 119).

75. TIMASHEFF, S. N.: Protein-solvent preferential interactions, protein hydration, and the modulation of biochemical reactions by solvent components. *Proceedings of the National Academy of Sciences of the United States of America* (2002), vol. **99**(15): 9721–9726 (2002) (cit. on pp. 9, 100, 119).

76. YANCEY, P. H.: Water stress, osmolytes and proteins. *American Zoologist* (2001), vol. **41**(4): 699–709 (2001) (cit. on p. 9).

77. MANNING, M. C., J. LIU, T. LI & R. E. HOLCOMB. *Advances in Protein Chemistry and Structural Biology* 1–59 (Elsevier Inc., 2018) (cit. on p. 9).

78. ARAKAWA, T., K. TSUMOTO, Y. KITA, B. CHANG & D. EJIMA: Biotechnology applications of amino acids in protein purification and formulations. *Amino Acids* (2007), vol. **33**(4): 587–605 (2007) (cit. on p. 9).

79. ARAKAWA, T., D. EJIMA, K. TSUMOTO, N. OBEYAMA, Y. TANAKA, Y. KITA & S. N. TIMASHEFF: Suppression of protein interactions by arginine: A proposed mechanism of the arginine effects. *Biophysical Chemistry* (2007), vol. **127**(1-2): 1–8 (2007) (cit. on p. 9).

80. MOLLMANN, S. H., U. ELOFSSON, J. T. BUKRINSKY & S. FROKJAER: Displacement of adsorbed insulin by tween 80 monitored using total internal reflection fluorescence and ellipsometry. *Pharmaceutical Research* (2005), vol. **22**(11): 1931–1941 (2005) (cit. on pp. 9, 14, 119).

81. DEECHONGKIT, S., J. WEN, L. O. NARHI, Y. JIANG, S. S. PARK, J. KIM & B. A. KERWIN: Physical and biophysical effects of polysorbate 20 and 80 on Darbepoetin alfa. *Journal of pharmaceutical sciences* (2009), vol. **98**(9): 3200–3217 (2009) (cit. on pp. 9, 119, 121).

82. RANDOLPH, T. W. & L. S. JONES. *Rational Design of Stable Protein Formulations* (eds CARPENTER, J. F. & M. C. MANNING) 159–175 (Springer, Boston, MA, 2002) (cit. on pp. 9, 119, 121).

83. KERWIN, B. A.: Polysorbates 20 and 80 used in the formulation of protein biotherapeutics: Structure and degradation pathways. *Journal of Pharmaceutical Science* (2007), vol. **97**(8): 2924–2935 (2007) (cit. on p. 9).

84. POLSON, A., G. POTGIETER, J. LARGIER, G. MEARS & F. JOUBERT: The fractionation of protein mixtures by linear polymers of high molecular weight. *Biochimica et Biophysica Acta (BBA)-General Subjects* (1964), vol. **82**: 463–475 (1964) (cit. on pp. 9, 119, 120).

85. ATHA, D. H. & K. C. INGHAM: Mechanism of precipitation of proteins by polyethylene glycols. Analysis in terms of excluded volume. *Journal of Biological Chemistry* (1981), vol. **256**(23): 12108–12117 (1981) (cit. on pp. 9, 14, 119, 120).

86. MINTON, A. P.: The effect of volume occupancy upon the thermodynamic activity of proteins: Some biochemical consequences. *Mol. Cell. Biochem* (1983), vol. **55**: 119–140 (1983) (cit. on p. 9).

87. KUMAR, V., V. K. SHARMA & D. S. KALONIA: Effect of polyols on polyethylene glycol (PEG)-induced precipitation of proteins: Impact on solubility, stability and conformation. *International Journal of Pharmaceutics* (2009), vol. **366**(1-2): 38–43 (2009) (cit. on pp. 9, 14).

88. ARSICCIO, A. & R. PISANO: Stability of proteins in carbohydrates and other additives during freezing: The human growth hormone as a case study. *Journal of Physical Chemistry B* (2017), vol. **121**(37): 8652–8660 (2017) (cit. on pp. 9, 118, 122).

89. ARSICCIO, A. & R. PISANO: Surfactants as stabilizers for biopharmaceuticals: An insight into the molecular mechanisms for inhibition of protein aggregation. *European Journal of Pharmaceutics and Biopharmaceutics* (2018), vol. **128**: 98–106 (2018) (cit. on pp. 9, 118, 122).

90. CHANG, B. S., B. S. KENDRICK & J. F. CARPENTER: Surface-induced denaturation of proteins during freezing and its inhibition by surfactants. *Journal of Pharmaceutical Sciences* (1996), vol. **85**(12): 1325–1330 (1996) (cit. on pp. 9, 11, 12, 14–16, 31, 47, 48, 54, 100, 119, 121).

91. WEBB, S. D., J. L. CLELAND, J. F. CARPENTER & T. W. RANDOLPH: A new mechanism for decreasing aggregation of recombinant human interferon-gamma by a surfactant: Slowed dissolution of lyophilized formulations in a solution containing 0.03% polysorbate 20. *Journal of pharmaceutical sciences* (2002), vol. **91**(2): 543–58 (2002) (cit. on pp. 9, 14, 119).

92. MAA, Y.-F. & C. C. HSU: Effect of high shear on proteins. *Biotechnology and Bioengineering* (1996), vol. **51**(4): 458–465 (1996) (cit. on p. 9).

93. ASHTON, L., J. DUSTING, E. IMOMOH, S. BALABANI & E. W. BLANCH: Shear-induced unfolding of lysozyme monitored in situ. *Biophysical Journal* (2009), vol. **96**(10): 4231–4236 (2009) (cit. on p. 9).

94. BEKARD, I. B., P. ASIMAKIS, J. BERTOLINI & D. E. DUNSTAN: The effects of shear flow on protein structure and function. *Biopolymers* (2011), vol. **95**(11): 733–745 (2011) (cit. on p. 9).

95. ANFINSEN, C. B.: Principles that govern the folding of protein chains. *Science* (1973), vol. **181**(4096): 223–230 (1973) (cit. on p. 10).

96. JAMEEL, F. & S. HERSHENSON: *Formulation and process development strategies for manufacturing biopharameuticals* (Hobolem. New Jersey, 2010) (cit. on pp. 10, 67).

97. BRADY, G. P. & K. A. SHARP: Entropy in protein folding and in protein-protein interactions. *Current Opinion in Structural Biology* (1997), vol. **7**(2): 215–221 (1997) (cit. on p. 10).

98. HILSER, V. J., J. GÓMEZ & E. FREIRE: The enthalpy change in protein folding and binding: Refinement of parameters for structure-based calculations. *Proteins: Structure, Function and Genetics* (1996), vol. **26**(2): 123–133 (1996) (cit. on p. 10).

99. REES, D. C. & A. D. ROBERTSON: Some thermodynamic implications for the thermostability of proteins. *Protein Science* (2001), vol. **10**(6): 1187–1194 (2001) (cit. on p. 10).

100. MORRA, G.: *Role of electrostatics explored with molecular dynamics simulations for protein stability and folding* PhD thesis (2006): 5–17 (cit. on p. 11).

101. BECKERTEL, W. J. & J. A. SCHELLMAN: Protein stability curves. *Biopolymers* (1987), vol. **26**(1): 1859–1877 (1987) (cit. on p. 11).

102. GRIKO, Y. V., P. L. PRIVALOV, J. M. STURTEVANT & S. Y. VENYAMINOV: Cold denaturation of staphylococcal nuclease. *Proceedings.of.the.National.Academy.of.Scie.* (1988), vol. **85**(10): 3343–3347 (1988) (cit. on p. 11).

103. Bhatnagar, B. S., R. H. Bogner & M. J. Pikal: Protein stability during freezing: Separation of stresses and mechanisms of protein stabilization. *Pharmaceutical Development and Technology* (2007), vol. **12**(5): 505–523 (2007) (cit. on pp. 11–14, 17, 21, 22, 32, 49, 54, 67, 100).

104. Privalov, P. L.: Cold denaturation of proteins. *Critical Reviews in Biochemistry and Molecular Biology* (1990), vol. **25**(5): 281–306 (1990) (cit. on pp. 11, 12, 15, 31, 48, 54, 100).

105. Heller, M. C., J. F. Carpenter & T. W. Randolph: Protein formulation and lyophilization cycle design: Prevention of damage due to freeze-concentration induced phase separation. *Biotechnology and Bioengineering* (1999), vol. **63**(2): 166–174 (1999) (cit. on pp. 11, 13, 31, 47, 48, 54).

106. Her, L.-M., M. Deras & S. L. Nail: Electrolyte-induced changes in glass transition temperatures of freeze-concentrated solutes. *Pharmaceutical Research* (1995), vol. **12**(5): 768–772 (1995) (cit. on pp. 11, 31, 47, 48, 54).

107. Heller, M. C., J. F. Carpenter & T. W. Randolph: Effects of phase separating systems on lyophilized hemoglobin. *Journal of Pharmaceutical Sciences* (1996), vol. **85**(12): 1358–1362 (1996) (cit. on pp. 11, 13, 31, 47, 48, 54).

108. Heller, M. C., J. F. Carpenter & T. W. Randolph: Manipulation of lyophilization-induced phase separation: Implications for pharmaceutical proteins. *Biotechnology Progress* (1997), vol. **13**(5): 590–596 (1997) (cit. on pp. 11, 13, 31, 47, 48, 54).

109. Strambini, G. B. & E Gabellieri: Proteins in frozen solutions: evidence of ice-induced partial unfolding. *Biophysical Journal* (1996), vol. **70**(2): 971–976 (1996) (cit. on pp. 11–13, 15, 16, 31, 47, 48, 54, 68, 69, 100, 121).

110. Kitahara, R., A. Okuno, M. Kato, Y. Taniguchi, S. Yokoyama & K. Akasaka: Cold denaturation of ubiquitin at high pressure. *Magnetic Resonance in Chemistry* (2006), vol. **44**(7 SPEC. ISS.): 108–113 (2006) (cit. on p. 11).

111. Pastore, A., S. R. Martin, A. Politou, K. C. Kondapalli, T. Stemmler & P. A. Temussi: Unbiased cold denaturation: Low- and high-temperature unfolding of yeast frataxin under physiological conditions. *Journal of the American Chemical Society* (2007), vol. **129**(17): 5374–5375 (2007) (cit. on p. 11).

112. Dias, C. L., T. Ala-Nissila, M. Karttunen, I. Vattulainen & M. Grant: Microscopic mechanism for cold denaturation. *Physical Review Letters* (2008), vol. **100**(11): 1–4 (2008) (cit. on pp. 11, 12).

113. Jaenicke, R.: Protein structure and function at low temperatures. *Philosophical transactions of the Royal Society of London. Series B: Biological sciences* (1990), vol. **326**(1237): 535–551; discussion 551 (1990) (cit. on p. 11).

114. Lindenmeyer, C. S., G. T. Orrok, K. A. Jackson & B. Chalmers: Rate of growth of ice crystals in supercooled water. *The Journal of Chemical Physics* (1957), vol. **27**(3): 822 (1957) (cit. on p. 12).

115. Hsu, C. C., H. M. Nguyen, D. A. Yeung, D. A. Brooks, G. S. Koe, T. A. Bewley & R. Pearlman: Surface denaturation at solid-void interface - A possible pathway by which opalescent particulates from during the storage of lypholized tissue-type plasminogen activator at high temperatures. *Pharmaceutical Research* (1995), vol. **12**(1): 69 –77 (1995) (cit. on pp. 12, 15, 16, 54, 69).

116. Webb, S. D., J. L. Cleland, J. F. Carpenter & T. W. Randolph: Effects of annealing lyophilized and spray-lyophilized formulations of recombinant human interferon-gamma. *Journal of Pharmaceutical Sciences* (2003), vol. **92**(4): 715–729 (2003) (cit. on pp. 12, 15, 16, 54).

117. Rodrigues, M. A., M. A. Miller, M. A. Glass, S. K. Singh & K. P. Johnston: Effect of freezing rate and dendritic ice formation on concentration profiles of proteins frozen in cylindrical vessels. *Journal of pharmaceutical sciences* (2011), vol. **100** (2011) (cit. on pp. 12, 13, 16, 68, 69, 100).

118. Cao, E., Y. Chen, Z. Cui & P. R. Foster: Effect of freezing and thawing rates on denaturation of proteins in aqueous solutions. *Biotechnology and Bioengineering* (2003), vol. **82**(6): 684–690 (2003) (cit. on pp. 12–14, 16, 48, 54, 69, 70).

119. Morris, G. J. & E. Acton: Cryobiology Controlled ice nucleation in cryopreservation A review q. *Cryobiology* (2013), vol. **66**(2): 85–92 (2013) (cit. on p. 12).

120. Mazur, P., J. Farrant, S. P. Leibo & E. H. Y. Chu: Survival of hamster tissue culture cells after freezing and thawing. *Cryobiology* (1969), vol. **6**(1): 1969 (1969) (cit. on p. 12).

121. Leibo, S. P., J. Farrant, P. Mazur, M. G. Hanna & L. H. Smith: Effects of freezing on marrow stem cell suspensions: Interactions of cooling and warming rates in the presence of PVP, sucrose, or glycerol. *Cryobiology* (1970), vol. **6**(4): 315–332 (1970) (cit. on p. 12).

122. Massie, I., C. Selden, H. Hodgson & B. Fuller: Cryopreservation of encapsulated liver spheroids for a bioartificial liver: Reducing latent cryoinjury using an ice nucleating agent. *Tissue Engineering - Part C: Methods* (2011), vol. **17**(7): 765–774 (2011) (cit. on p. 12).

123. Han, X., H. B. Ma, C. Wilson & J. K. Critser: Effects of nanoparticles on the nucleation and devitrification temperatures of polyol cryoprotectant solutions. *Microfluidics and Nanofluidics* (2008), vol. **4**(4): 357–361 (2008) (cit. on p. 12).

124. Kojima, T., T. Soma & N. Oguri: Effect of ice nucleation by droplet of immobilized silver iodide on freezing of rabbit and bovine embryos. *Theriogenology* (1988), vol. **30**(6): 1199–1207 (1988) (cit. on p. 12).

125. Rau, W.: Eiskeimbildung durch dielektrische Polarisation. *Zeitschrift fur Naturforschung - Section A Journal of Physical Sciences* (1951), vol. **6**(11): 649–657 (1951) (cit. on p. 12).

126. Hobbs, P.: *Ice Physics* (Clarendon Press, Oxford, UK, 1974) (cit. on p. 12).

127. GARCIA-LOPEZ, J. & R. AYATS: Criopreservacion de precursors hematopoyeticos. *Biol. Clin. Hematol.* (1985), vol.: 177–185 (1985) (cit. on p. 12).

128. PEREZ-OTEYZA, J., R. BORNSTEIN, M. CORRAL, V. HERMOSA, A. ALEGRE, M. TORRABADELLA, P. RAMOS, J. GARCIA, J. ODRIOZOLA & J. L. NAVARRO: Controlled-rate versus uncontrolled-rate cryopreservation of peripheral blood progenitor cells: a prospective multicenter study. *Heamatologica* (1998), vol. **83**: 1001–1005 (1998) (cit. on p. 12).

129. KONSTANTINIDIS, A. K., W. KUU, L. OTTEN, S. L. NAIL & R. R. SEVER: Controlled nucleation in freeze-drying: Effects on pore size in the dried product layer, mass transfer resistance, and primary drying rate. *Journal of Pharmaceutical Sciences* (2011), vol. **100**(8): 3453–3470 (2011) (cit. on p. 12).

130. SHALAEV, E. & F. FRANKS. *Amorphous Food and Pharmaceutical Systems* (ed LEVINE, H.) 200–215 (Royal Society of Chemistry, Cambridge, 2002) (cit. on pp. 13, 14, 17, 48).

131. GÓMEZ, G., M. J. PIKAL & N. RODRÍGUEZ-HORNEDO: Effect of initial buffer composition on pH changes during far-from-equilibrium freezing of sodium phosphate buffer solutions. *Pharmaceutical Research* (2001), vol. **18**(1): 90–97 (2001) (cit. on pp. 13, 14, 17).

132. MURASE, N. & F. FRANKS: Salt precipitation during the freeze-concentration of phosphate buffer solutions. *Biophysical Chemistry* (1989), vol. **34**: 293–300 (1989) (cit. on p. 13).

133. SINGH, S. K. & S. NEMA. *Formulation and Process Development Strategies for Manufacturing Biopharmaceuticals* 625–675 (2010) (cit. on pp. 13–15, 17, 21, 22, 31, 67, 68, 93, 100).

134. HELLER, M. C., J. F. CARPENTER & T. W. RANDOLPH: Application of a thermodynamic model to the prediction of phase separations in freeze-concentrated formulations for protein lyophilization. *Archives of biochemistry and biophysics* (1999), vol. **363**(2): 191–201 (1999) (cit. on p. 13).

135. IZUTSU, K. I, S YOSHIOKA, S KOJIMA, T. W. RANDOLPH & J. F. CARPENTER: Effects of sugars and polymers on crystallization of poly(ethylene glycol) in frozen solutions: Phase separation between incompatible polymers. *Pharmaceutical Research* (1996), vol. **13** (1996) (cit. on p. 13).

136. IZUTSU, K & S KOJIMA: Freeze-concentration separates proteins and polymer excipients into different amorphous phases. *Pharmaceutical research* (2000), vol. **17**(10): 1316–22 (2000) (cit. on p. 13).

137. IZUTSU, K & K SHIGEO: Phase separation of polyelectrolytes and non-ionic polymers in frozen solutions. *Physical Chemistry Chemical Physics* (2000), vol. **2**(1): 123–127 (2000) (cit. on p. 13).

138. KESTIN, J., M. SOKOLOV & W. A. WAKEHAM: Viscosity of liquid water in the range -8℃to 150℃. *Journal of Physical and Chemical Reference Data* (1978), vol. **7**(3): 941–948 (1978) (cit. on pp. 13, 94, 121, 123).

139. PIKAL, M. J. *Freeze Drying / Lyophilization of Pharmaceutical and Biological Products* 198–232 (2004) (cit. on pp. 13, 54, 100).

140. LIU, C., N. ASHERIE, A. LOMAKIN, J. PANDE, O. OGUN & G. B. BENEDEK: Phase separation in aqueous solutions of lens gamma-crystallins: Special role of gamma s. *Proceedings of the National Academy of Sciences of the United States of America* (1996), vol. **93**(1): 377–382 (1996) (cit. on pp. 13, 16, 47, 49, 75, 76, 86, 100, 121).

141. ARAKAWA, T. & S. N. TIMASHEFF: The stabilization of proteins by osmolytes. *Biophysical Journal* (1985), vol. **47**(3): 411–414 (1985) (cit. on pp. 14, 118).

142. BOLEN, D. W.: Effects of naturally occurring osmolytes on protein stability and solubility: Issues important in protein crystallization. *Methods* (2004), vol. **34**(3): 312–322 (2004) (cit. on pp. 14, 118).

143. KUMAR, R.: Role of naturally occurring osmolytes in protein folding and stability. *Archives of Biochemistry and Biophysics* (2009), vol. **491**(1-2): 1–6 (2009) (cit. on pp. 14, 118, 119).

144. CARPENTER, J. F. & J. H. CROWE: The mechanism of cryoprotection of proteins by solutes. *Cryobiology* (1988), vol. **25**(3): 244–255 (1988) (cit. on p. 14).

145. PIKAL-CLELAND, K. A., N RODRÍGUEZ-HORNEDO, G. L. AMIDON & J. F. CARPENTER: Protein denaturation during freezing and thawing in phosphate buffer systems: monomeric and tetrameric beta-galactosidase. *Archives of biochemistry and biophysics* (2000), vol. **384**(2): 398–406 (2000) (cit. on pp. 14, 16, 17, 54, 68–70).

146. VITKUP, D., D. RINGE, G. A. PETSKO & M. KARPLUS: Solvent mobility and the protein 'glass' transition. *Nature Structural Biology* (2000), vol. **7**(1): 34–38 (2000) (cit. on pp. 15, 67, 68, 70).

147. *Eutektikum* 2012 (cit. on p. 15).

148. CHAPLIN, M.: *Water Structure and Science* tech. rep. (2017) (cit. on p. 15).

149. BROIDE, M. L., T. M. TOMINC & M. D. SAXOWSKY: Using phase transitions to investigate the effect of salts on protein interactions. *Physical Review E* (1996), vol. **53**(6): 6325–6335 (1996) (cit. on pp. 16, 75).

150. GRIGSBY, J. J., H. W. BLANCH & J. M. PRAUSNITZ: Cloud-point temperatures for lysozyme in electrolyte solutions: Effect of salt type, salt concentration and pH. *Biophysical Chemistry* (2001), vol. **91**(3): 231–243 (2001) (cit. on pp. 16, 47–49, 75, 76, 88, 94, 100, 121).

151. TARATUTA, V. G., A. HOLSCHBACH, G. M. THURSTON, D. BLANKSCHTEIN & G. B. BENEDEK: Liquid-liquid phase separation of aqueous lysozyme solutions: Effects of pH and salt identity. *The Journal of Physical Chemistry* (1990), vol. **94**(5): 2140–2144 (1990) (cit. on pp. 16, 32, 47, 49, 75, 80, 87, 165, 166).

152. HAUPTMANN, A., K. PODGORŠEK, D. KUZMAN, S. SRČIČ, G. HOELZL & T. LOERTING: Impact of buffer, protein concentration and sucrose addition on the aggregation and particle formation during freezing and thawing. *Pharmaceutical Research* (2018), vol. **35**(5) (2018) (cit. on pp. 16, 21, 54).

153. ANCHORDOQUY, T. J. & J. F. CARPENTER: Polymers protect lactate dehydrogenase during freeze-drying by inhibiting dissociation in the frozen state. *Archives of biochemistry and biophysics* (1996), vol. **332**(2): 231–238 (1996) (cit. on pp. 16, 17, 54, 68–70).

154. FRANSEN, G., P. SALEMINK & D. CROMMELIN: Critical parameters in freezing of liposomes. *International Journal of Pharmaceutics* (1986), vol. **33**(1-3): 27–35 (1986) (cit. on pp. 16, 54).

155. AHAMED, T., B. N. ESTEBAN, M. OTTENS, G. W. VAN DEDEM, L. A. VAN DER WIELEN, M. A. BISSCHOPS, A. LEE, C. PHAM & J. THÖMMESY: Phase behavior of an intact monoclonal antibody. *Biophysical Journal* (2007), vol. **93**(2): 610–619 (2007) (cit. on p. 17).

156. ASHERIE, N., A. LOMAKIN & G. B. BENEDEK: Phase diagram of colloidal solutions. *Physical Review Letters* (1996), vol. **77**(23): 21–24 (1996) (cit. on p. 17).

157. HAAS, C. & J. DRENTH: The protein-water phase diagram and the growth of protein crystals from aqueous solution. *Journal of Physical Chemistry B* (1998), vol. **102**(21): 4226–4232 (1998) (cit. on p. 17).

158. BAUMGARTNER, K., L. GALM, J. NÖTZOLD, H. SIGLOCH, J. MORGENSTERN, K. SCHLEINING, S. SUHM, S. A. OELMEIER & J. HUBBUCH: Determination of protein phase diagrams by microbatch experiments: Exploring the influence of precipitants and pH. *International Journal of Pharmaceutics* (2015), vol. **479**(1): 28–40 (2015) (cit. on pp. 18, 21, 22, 25, 34, 46, 48, 56, 75, 81, 102, 119).

159. TALREJA, S., S. L. PERRY, S. GUHA, V. BHAMIDI, C. F. ZUKOSKI & P. J. KENIS: Determination of the phase diagram for soluble and membrane proteins. *Journal of Physical Chemistry B* (2010), vol. **114**(13): 4432–4441 (2010) (cit. on p. 18).

160. BOISTELLE, R. & J. P. ASTIER: Crystallization mechanisms in solution. *Journal of Crystal Growth* (1988), vol. **90**(1-3): 14–30 (1988) (cit. on p. 18).

161. LUFT, J. R. & G. T. DETITTA. *Protein Crystalization* (ed TERESE M. BERGFORS) 2nd Editio: 11–46 (International Univerity Line, 2009) (cit. on p. 18).

162. HOWARD, S. B., P. J. TWIGG, J. K. BAIRD & E. J. MEEHAN: The solubility of hen egg-white lysozyme. *Journal of Crystal Growth* (1988), vol. **90**: 94–104 (1988) (cit. on pp. 18, 19, 32).

163. RETAILLEAU, P., M. RIÈS-KAUTT & A. DUCRUIX: No salting-in of lysozyme chloride observed at low ionic strength over a large range of pH. *Biophysical Journal* (1997), vol. **73**(4): 2156–2163 (1997) (cit. on pp. 18, 19, 91).

164. GALM, L., J. MORGENSTERN & J. HUBBUCH: Manipulation of lysozyme phase behavior by additives as function of conformational stability. *International Journal of Pharmaceutics* (2015), vol. **494**(1): 370–380 (2015) (cit. on pp. 18, 19, 21, 22, 32, 35, 37, 58, 75, 105, 122, 167).

165. Curtis, R. A., J. M. Prausnitz & H. W. Blanch: Protein-protein and protein-salt interactions in aqueous protein solutions containing concentrated electrolytes. *Biotechnology and Bioengineering* (1998), vol. **57**(1): 11–21 (1998) (cit. on pp. 19, 46, 76, 100, 122).

166. Guo, B., S. Kao, H. McDonald, A. Asanov, L. L. Combs & W. W. Wilson: Correlation of second virial coefficients and solubilities useful in protein crystal growth. *Journal of Crystal Growth* (1999), vol. **196**(2-4): 424–433 (1999) (cit. on p. 19).

167. Haas, C & J Drenth: Understanding protein crystallization on the phase diagram. *J. Cryst.Growth* (1999), vol. **196**: 388–394 (1999) (cit. on p. 19).

168. Ruppert, S., S. I. Sandler & A. M. Lenhoff: Correlation between the osmotic second virial coefficient and the solubility of proteins. *Biotechnology Progress* (2001), vol. **17**(1): 182–187 (2001) (cit. on p. 19).

169. Lorber, B. *International Conference on Pattern Recognition Applications and Methods* 663–668 (SCITEPRESS, 2018) (cit. on pp. 19, 20).

170. Instruments, M.: *Zetasizer Nano Series* tech. rep. (2004) (cit. on p. 20).

171. Technology, W.: *DynaPro Plate Reader II User ' s Guide* tech. rep. (2014): 77 (cit. on pp. 20, 118).

172. Lorber, B., F. Fischer, M. Bailly, H. Roy & D. Kern: Protein analysis by dynamic light scattering: Methods and techniques for students. *Biochemistry and Molecular Biology Education* (2012), vol. **40**(6): 372–382 (2012) (cit. on pp. 20, 118).

173. Bhattacharjee, S.: DLS and zeta potential What they are and what they are not? *Journal of Controlled Release* (2016), vol. **235**: 337–351 (2016) (cit. on p. 20).

174. Chang, B. S. & B. Yeung. *Formulation and Process Development Strategies for Manufacturing Biopharmaceuticals* 69 –104 (2010) (cit. on p. 20).

175. Miyazawa, T. & E. R. Blout: The infrared spectra of polypeptides in various conformations: Amide I and II Bands. *Journal of the American Chemical Society* (1961), vol. **83**(3): 712–719 (1961) (cit. on p. 20).

176. Krimm, S. & J. Bandekar. *Advances in Protein Chemistry* C: 181–364 (1986) (cit. on p. 20).

177. Dong, A., P. Huang & W. S. Caughey: Protein secondary structures in water from second-derivative Amide I infrared spectra. *Biochemistry* (1990), vol. **29**(13): 3303–3308 (1990) (cit. on p. 20).

178. Kueltzo, L. A., W. Wang, T. W. Randoplph & J. F. Carpenter: Effects of solution conditions, processing parameters, and container materials on aggregation of a monoclonal antibody during freeze-thawing. *Journal of Pharmaceutical Sciences* (2008), vol. **99**(10): 4215–4227 (2008) (cit. on pp. 21, 31, 32, 54, 67, 100).

179. Her, L.-M. & S. L. Nail: Measurement of glass transition temperatures of freeze-concentrated solutes by differential scanning calorimetry. *Pharmaceutical Research* (1994), vol. **11** (1994) (cit. on p. 21).

180. PANSARE, S. K. & S. M. PATEL: Practical considerations for determination of glass transition temperature of a maximally freeze concentrated solution. *AAPS PharmSciTech* (2016), vol. **17**(4): 805–819 (2016) (cit. on p. 21).

181. MOHSEN-NIA, M., H. RASA & H. MODARRESS: Cloud-point measurements for (water + poly(ethylene glycol) + salt) ternary mixtures by refractometry method. *Journal of Chemical and Engineering Data* (2006), vol. **51**(4): 1316–1320 (2006) (cit. on p. 21).

182. BAUER, K. C., M. GÖBEL, M.-L. SCHWAB, M.-T. SCHERMEYER & J. HUBBUCH: Concentration-dependent changes in apparent diffusion coefficients as indicator for colloidal stability of protein solutions. *International Journal of Pharmaceutics* (2016), vol. **511**(1): 276–287 (2016) (cit. on pp. 21, 22, 75).

183. KLIJN, M. E. & J. HUBBUCH: Correlating multidimensional short-term empirical protein properties to long-term protein physical stability data via empirical phase diagrams. *International Journal of Pharmaceutics* (2019), vol. **560**: 166–174 (2019) (cit. on pp. 21, 22, 75).

184. SCHERMEYER, M. T., A. K. WÖLL, B. KOKKE, M. EPPINK & J. HUBBUCH: Characterization of highly concentrated antibody solution - A toolbox for the description of protein long-term solution stability. *mAbs* (2017), vol. **9**(7): 1169–1185 (2017) (cit. on pp. 21, 22, 75).

185. BAUER, K., S. SUHM, A. WÖLL & J. HUBBUCH: Impact of additives on the formation of protein aggregates and viscosity in concentrated protein solutions. *International Journal of Pharmaceutics* (2017), vol. **516**(1-2) (2017) (cit. on pp. 21, 22).

186. SARIDAKIS, E. & N. E. CHAYEN: Towards a universal ' nucleant for protein crystallization. *Cell Press* (2008), vol. **27**(2) (2008) (cit. on pp. 31, 47, 48, 68, 120).

187. SUNDARAMURTHI, P. & R. SURYANARAYANAN: The effect of crystallizing and non-crystallizing cosolutes on succinate buffer crystallization and the consequent pH shift in frozen solutions. *Pharmaceutical Research* (2011), vol. **28**(2): 374–385 (2011) (cit. on p. 31).

188. BHATNAGAR, B. S., M. J. PIKAL & R. H. BOGNER: Study of the individual contributions of ice formation and freeze-concentration on isothermal stability of lactate dehydrogenase during freezing. *Journal of Pharmaceutical Sciences* (2008), vol. **97**(2) (2008) (cit. on p. 31).

189. FIDDIS, R. W., R. A. LONGMAN & P. D. CALVERT: Crystal growth kinetics of globular proteins. *Journal of Chemical Society, Faraday Trans. 1* (1978), vol. **75** (1978) (cit. on p. 31).

190. BHAMIDI, V, E SKRZYPCZAK-JANKUN & C. A. SCHALL: Dependence of nucleation kinetics and crystal morphology of a model protein system on ionic strength. *Journal of Crystal Growth* (2001), vol. **232**: 77–85 (2001) (cit. on pp. 32, 47, 48).

191. Georgalis, Y., P. Umbach, D. M. Soumpasis & W. Saenger: Dynamics and microstructure formation during nucleation of lysozyme solutions. *Journal of the American Chemical Society* (1998), vol. **120**(22): 5539–5548 (1998) (cit. on pp. 32, 47, 48, 51, 120, 122).

192. Ishimoto, C. & T. Tanaka: Critical Behavior of a binary mixture of protein and salt water. *Physical review letters* (1977), vol. **39**(8): 8–11 (1977) (cit. on p. 32).

193. Judge, R. A., R. S. Jacobs, T. Frazier, E. H. Snell & M. L. Pusey: The effect of temperature and solution pH on the nucleation of tetragonal lysozyme crystals. *Biophysical Journal* (1999), vol. **77**: 1585–1593 (1999) (cit. on p. 32).

194. Ataka, M. & S. Tanaka: The growth of large single crystals. *Biopolymers* (1986), vol. **67**(5): 337–350 (1986) (cit. on pp. 32, 68, 92).

195. Benjakul, S. & F. Bauer: Physicochemical and enzymatic changes of cod muscle proteins subjected to different freeze-thaw cycles. *Journal of the Science of Food and Agriculture* (2000), vol. **80**(8): 1143–1150 (2000) (cit. on p. 32).

196. Radmanovic, N., T. Serno, S. Joerg & O. Germershaus: Understanding the freezing of biopharmaceuticals: First-principle modeling of the process and evaluation of its effect on product quality. *Journal of pharmaceutical sciences* (2013), vol. **102**(8): 2495–2507 (2013) (cit. on pp. 32, 54).

197. Kröner, F. & J. Hubbuch: Systematic generation of buffer systems for pH gradient ion exchange chromatography and their application. *Journal of Chromatography A* (2013), vol. **1285**: 78–87 (2013) (cit. on pp. 33, 55, 77, 101).

198. Column, P.-. D.: *PD-10 desalting column* 2007 (cit. on pp. 34, 55, 102).

199. Stradner, A., H. Sedgwick, F. Cardinaux, W. C. K. Poon, S. U. Egelhaaf & P. Schurtenberger: Equilibrium cluster formation in concentrated protein solutions and colloids. *Nature* (2004), vol. **432**: 492–495 (2004) (cit. on pp. 35, 119).

200. Scopes, R. K.: *Protein Purification: Principles and practice* (Springer Science & Business Media, 2013) (cit. on p. 46).

201. *Food chemestry research developments* (ed Papadopoulos, K.) (Nova Science Publishers, Inc., New York, USA, 2008) (cit. on p. 46).

202. Tardieu, A., F. Bonneté, S. Finet & D. Vivarès: Understanding salt or PEG induced attractive interactions to crystallize biological macromolecules. *Acta Crystallographica Section D Biological Crystallography* (2002), vol. **58**: 1549–1553 (2002) (cit. on pp. 46, 119).

203. Curtis, R. A., J. Ulrich, A. Montaser, H. W. Blanch & M. Prausnitz: Protein-protein interactions in concentrated electrolyte solutions: Hofmeister-series effects. *Biotechnology and Bioengineering* (2002), vol. **79**(4): 367–380 (2002) (cit. on pp. 46, 118, 119).

204. KUEHNER, D. E., J. ENGMANN, F. FERGG, M. WERNICK, H. W. BLANCH & J. M. PRAUSNITZ: Lysozyme net charge and ion binding in concentrated aqueous electrolyte solutions. *The Journal of Physical Chemistry B* (1999), vol. **103**(8): 1368–1374 (1999) (cit. on p. 46).

205. WANG, W., N. LI & S. SPEAKER. *Aggregation of Therapeutic Proteins* (eds WANG, W. & C. J. ROBERTS) (John Wiley & Sons, Inc., 2010) (cit. on pp. 47, 48).

206. GUO, D., C. T. MANT, A. K. TANEJA, J. R. PARKER & R. S. RODGES: Prediction of peptide retention times in reversed-phase high-performance liquid chromatography I. Determination of retention coefficients of amino acid residues of model synthetic peptides. *Journal of Chromatography A* (1986), vol. **359**: 499–518 (1986) (cit. on p. 47).

207. AMRHEIN, S., K. C. BAUER & L. GALM: Non-invasive high throughput approach for protein hydrophobicity determination based on surface tension. *Biotechnology and Bioengineering* (2015), vol. **112**(12): 2485–2494 (2015) (cit. on p. 47).

208. CHERNOV, A. A.: Protein crystals and their growth. *Journal of Structural Biology* (2003), vol. **142**: 3–21 (2003) (cit. on pp. 47, 48, 69, 93, 119).

209. ZEELEN, J. P. *Protein Crystallization* (ed BERGFORS, T. M.) 2nd (2009) (cit. on pp. 47, 49, 70).

210. ZIEGLER, G. R. & E. A. FOEGEDING: The gelation of proteins. *Advances in Food and Nutrition Research* (1990), vol. **34**: 203–298 (1990) (cit. on p. 47).

211. BELITZ, H., W. GROSCH & S. P.: *Lebensmittelchemie* 6th ed. (Springer Berlin Heidelberg, Berlin, Heidelberg, 2008) (cit. on p. 48).

212. CHANG, B. S. & C. S. RANDALL: Use of subambient thermal analysis to optimize protein lyophilization. *Cryobiology* (1992), vol. **29**(5): 632–656 (1992) (cit. on p. 48).

213. ZHANG, Y. & P. S. CREMER: Interactions between macromolecules and ions: the Hofmeister series. *Current Opinion in Chemical Biology* (2006), vol. **10**(6): 658–663 (2006) (cit. on pp. 49, 50).

214. FORSYTHE, E. L. & M. L. PUSEY: The effects of acetate buffer concentration on lysozyme solubility. *Journal of Crystal Growth* (1996), vol. **168**(1-4): 112–117 (1996) (cit. on pp. 49, 50).

215. SHAMLOU, P. a., L. H. BREEN, W. V. BELL, M. POLLO & B. A. THOMAS: A new scaleable freeze-thaw technology for bulk protein solutions. *Biotechnology and applied biochemistry* (2007), vol. **46**: 13–26 (2007) (cit. on pp. 54, 100).

216. HO, K., S. TCHESSALOV, A. KANTOR & N. WARNE: Development of freeze and thaw processes for bulk biologics in disposable bags. *American Pharmaceutical Review* (2008), vol. **11**(4): 1–6 (2008) (cit. on pp. 54, 100).

217. SINGH, S. K., P. KOLHE, A. P. MEHTA, S. C. CHICO, A. L. LARY & M. HUANG: Frozen state storage instability of a monoclonal antibody: Aggregation as a consequence of trehalose crystallization and protein unfolding. *Pharmaceutical Research* (2011), vol. **28**(4): 873–885 (2011) (cit. on pp. 54, 100).

218. Liu, L., L. J. Braun, W. Wang, T. W. Randolph & J. F. Carpenter: Freezing-induced perturbation of tertiary structure of a monoclonal antibody. *Journal of Pharmaceutical Sciences* (2014), vol. **103**(7): 1979–1986 (2014) (cit. on pp. 54, 100).

219. Miller, M. A., M. A. Rodrigues, M. A. Glass, S. K. Singh, K. P. Johnston & J. A. Maynard: Frozen-state storage stability of a monoclonal antibody: Aggregation is impacted by freezing rate and solute distribution. *Journal of Pharmaceutical Science* (2013), vol. **102**(4): 1194–1208 (2013) (cit. on pp. 54, 67–69).

220. Maity, H., C. Karkaria & J. Davagnino: Mapping of solution components, pH changes, protein stability and the elimination of protein precipitation during freeze-thawing of fibroblast growth factor 20. *International Journal of Pharmaceutics* (2009), vol. **378**(1-2): 122–135 (2009) (cit. on p. 54).

221. Kolhe, P., E. Amend & S. K. Singh: Impact of freezing on pH of buffered solutions and consequences for monoclonal antibody aggregation. *Biotechnology Progress* (2010), vol. **26**(3): 727–733 (2010) (cit. on p. 54).

222. Hernández-Jiménez, J., A. Martínez-Ortega, A. Salmerón-García, J. Cabeza, J. C. Prados, R. Ortíz & N. Navas: *Study of aggregation in therapeutic monoclonal antibodies subjected to stress and long-term stability tests by analyzing size exclusion liquid chromatographic profiles* 511–524 (Elsevier B.V, 2018) (cit. on p. 54).

223. Rašković, B., M. Popović, S. Ostojić, B. Ancrossed D Signelković, V. Tešević & N. Polović: Fourier transform infrared spectroscopy provides an evidence of papain denaturation and aggregation during cold storage. *Spectrochimica Acta - Part A: Molecular and Biomolecular Spectroscopy* (2015), vol. **150**: 238–246 (2015) (cit. on p. 54).

224. Wöll, A. K., J. Schütz, J. Zabel & J. Hubbuch: Analysis of phase behavior and morphology during freeze-thaw applications of lysozyme. *International Journal of Pharmaceutics* (2019), vol. **555**(C): 153–164 (2019) (cit. on pp. 54, 56, 60, 67, 76, 79, 93, 100, 121).

225. Kumar, P., Z. Yan, L. Xu, M. G. Mazza, S. V. Buldyrev, S. H. Chen, S. Sastry & H. E. Stanley: Glass transition in biomolecules and the liquid-liquid critical point of water. *Physical Review Letters* (2006), vol. **97**(17): 1–4 (2006) (cit. on pp. 67, 70).

226. Cocks, F. H. & W. E. Brower: Phase diagram relationships in cryobiology. *Cryobiology* (1974), vol. **11**: 340–358 (1974) (cit. on p. 67).

227. Kerwin, B. A., M. C. Heller, S. H. Levin & T. W. Randolph: Effects of Tween 80 and sucrose on acute short-term stability and long-Term storage at 20 C of a recombinant hemoglobin. *Journal of Pharmaceutical Sciences* (1998), vol. **87**(9): 1062 –1068 (1998) (cit. on p. 67).

228. Desai, K. G., W. A. Pruett, P. J. Martin, J. D. Colandene & D. P. Nesta: Impact of manufacturing scale freeze-thaw conditions on a mab solution. *BioPharm International* (2017), vol.: 30–36 (2017) (cit. on pp. 67, 70).

229. BRODY, H. D.: Solute redistribution in dendritic solidification. *Transactions of the Metallurgical Society of AIME* (1966), vol. **236**(5): 615–624 (1966) (cit. on p. 69).

230. BUTLER, M. F.: Freeze concentration of solutes at the ice / solution interface studied by optical interferometry. *Crystal Growth & Design* (2002), vol. **2**(6): 541–548 (2002) (cit. on p. 69).

231. BUTLER, M. F.: Instability formation and directional dendritic growth of ice studied by optical interferometry. *Crystal Growth and Design* (2001), vol. **1**(3): 213–223 (2001) (cit. on p. 69).

232. KÖRBER, C.: Phenomena at the advancing iceliquid interface: Solutes particles and biological cells. *Quarterly Reviews of Biophysics* (1988), vol. **21**(2): 229–298 (1988) (cit. on p. 69).

233. WEISS IV, W., T. M. YOUNG & C. J. ROBERTS: Principles, approaches, and challenges for predicting protein aggregation rates and shelf life. *International Journal of Drug Development and Research* (2009), vol. **98**(4): 1246 –1277 (2009) (cit. on pp. 69, 75).

234. ROSENBERG, A. S.: Effects of protein aggregates: An immunologic perspective. *The AAPS Journal* (2006), vol. **8**(3): E501–E507 (2006) (cit. on p. 75).

235. GOLDBERG, D. S., S. M. BISCHOP, A. U. SHAH & H. A. SATHISH: Formulation development of therapeutic monoclonal antibodies using high-throughput fluorescence and static light scattering Techniques: Role of conformational and colloidal stability. *Journal of Pharmaceutical Science* (2011), vol. **100**(4): 1306–1215 (2011) (cit. on p. 75).

236. GEORGE, A. & W. W. WILSON: Predicting protein crystallization from a dilute solution property. *Acta Crystallographica Section D Biological Crystallography* (1994), vol. **50**(4): 361–365 (1994) (cit. on p. 75).

237. HIRANO, A., H. HAMADA, T. OKUBO, T. NOGUCHI, H. HIGASHIBATA & K. SHIRAKI: Correlation between thermal aggregation and stability of lysozyme with salts described by molar surface tension increment: An exceptional propensity of ammonium salts as aggregation suppressor. *The Protein Journal* (2007), vol. **26**(6): 423–433 (2007) (cit. on p. 75).

238. MADDUX, N. R., V. IYER, W. CHENG, A. M. YOUSSEF, S. B. JOSHI, D. B. VOLKIN, J. P. RALSTON, G. WINTER & C. RUSSELL MIDDAUGH: High throughput prediction of the long-term stability of pharmaceutical macromolecules from short-term multi-instrument spectroscopic data. *Journal of Pharmaceutical Sciences* (2014), vol. **103**(3): 828–839 (2014) (cit. on p. 75).

239. GALM, L., S. AMRHEIN & J. HUBBUCH: Predictive approach for protein aggregation: Correlation of protein surface characteristics and conformational flexibility to protein aggregation propensity. *Biotechnology and Bioengineering* (2017), vol. **114**(6): 1170–1183 (2017) (cit. on p. 75).

240. Thiagarajan, G., A. Semple, J. K. James, J. K. Cheung & M. Shameem: A comparison of biophysical characterization techniques in predicting monoclonal antibody stability. *mAbs* (2016), vol. **8**(6): 1088–1097 (2016) (cit. on p. 75).

241. Heijna, M. C. R., W. J. P. V. Enckevort & E Vlieg: Crystal growth in a three-phase system: Diffusion and liquid-liquid phase separation in lysozyme crystal growth. *Physical Review* (2007), vol. **76**: 1–7 (2007) (cit. on p. 75).

242. Park, E. J. & Y. C. Bae: Cloud-point temperatures of lysozyme in electrolyte solutions by thermooptical analysis technique. *Biophysical Chemistry* (2004), vol. **109**(1): 169–188 (2004) (cit. on pp. 75, 76, 88).

243. Raut, A. S. & D. S. Kalonia: Effect of excipients on liquid-liquid phase separation and aggregation in dual variable domain immunoglobulin protein solutions. *Molecular Pharmaceutics* (2016), vol. **13**(3): 774–783 (2016) (cit. on pp. 75, 76).

244. Boire, A., P. Menut, M. H. Morel & C. Sanchez: Phase behaviour of a wheat protein isolate. *Soft Matter* (2013), vol. **9**(47): 11417–11426 (2013) (cit. on p. 76).

245. Bloustine, J, T Virmani, G. M. Thurston & S Fraden: Light scattering and phase behavior of lysozyme-poly (ethylene glycol) mixtures. *Physical Review Letters* (2006), vol. **96**(3): 1–4 (2006) (cit. on p. 76).

246. Galkin, O. & P. G. Vekilov: Are nucleation kinetics of protein crystals similar to those of liquid droplets? *Jornal of American Society* (2000), vol. **122**(1): 156–163 (2000) (cit. on p. 76).

247. Pincemaille, J., A. Banc, E. Chauveau, J. M. Fromental, L. Ramos, M. H. Morel & P. Menut: Methods for screening cloud point temperatures. *Food Biophysics* (2018), vol. **13**(4): 422–431 (2018) (cit. on pp. 76, 85, 86).

248. Williamson, A. P. & J. Kiefer: Automatic low-cost method to determine the solubility of liquid-liquid mixtures by continuous-flow cloud point titration. *Chemical Engineering and Technology* (2014), vol. **37**(10): 1736–1740 (2014) (cit. on p. 76).

249. Wöll, A. K., M. Desombre, L. Enghauser & J. Hubbuch: A phase diagram based toolbox to assess the impact of freeze/thaw ramps on the phase behavior of proteins. *Bioprocess and Biosystems Engineering* (2019), vol. (2019) (cit. on pp. 76, 79, 80, 93, 100, 103, 121).

250. GE Healthcare: *PD-10 desalting column* tech. rep. (2007): 1–4 (cit. on p. 78).

251. Klijn, M. E. & J. Hubbuch: Application of empirical phase diagrams for multidimensional data visualization of high-throughput microbatch crystallization experiments. *Journal of Pharmaceutical Sciences* (2018), vol. **107**(8): 2063–2069 (2018) (cit. on pp. 83, 84, 90, 103).

252. Rodgers, J. L. & W. A. Nicewander: Thirteen ways to look at the correlation coefficient. *The American Statistician* (1988), vol. **42**(1): 59–66 (1988) (cit. on p. 87).

253. Leskovec, J., A. Rajaraman & J. D. Ullman: *Mining of massive datasets* 1–458 (2014) (cit. on pp. 90, 117).

254. Lewis, G. N. & M. Randall: The activity coefficient of strong electrolytes. *Journal of the American Chemical Society* (1921), vol. **43**(5): 1112–1154 (1921) (cit. on p. 91).

255. Schwierz, N., D. Horinek, U. Sivan & R. R. Netz: Reversed Hofmeister series - The rule rather than the exception. *Current Opinion in Colloid and Interface Science* (2016), vol. **23**: 10–18 (2016) (cit. on p. 91).

256. Ries-Kautt, M. M. & A. F. Ducruix: Relative effectiveness of various ions on the solubility and crystal growth of lysozyme. *The Journal of Biological Chemistry* (1989), vol. **264**(2): 745–748 (1989) (cit. on pp. 91, 92).

257. Collins, K. D.: Ions from the Hofmeister series and osmolytes: Effects on proteins in solution and in the crystallization process. *Methods* (2004), vol. **34**(3): 300–311 (2004) (cit. on p. 91).

258. Ries-Kautt, M. & A. Ducruix. *Methods in Enzymology* 1988: 23–59 (1997) (cit. on pp. 92, 119, 120).

259. Burke, M. W., R. Leardi, R. A. Judge & M. L. Pusey: Quantifying main trends in lysozyme nucleation: The effect of precipitant concentration, supersaturation, and impurities. *Crystal Growth and Design* (2001), vol. **1**(4): 333–337 (2001) (cit. on pp. 92, 94, 120).

260. Mullin, J. W.: *Crystallization* 3rd: 182 (Butterworth Heinemann, Oxford, UK, 1992) (cit. on p. 93).

261. Aleksandrov, A. A., E. V. Dzhuraeva & V. F. Utenkov: Viscosity of aqueous solutions of sodium chloride. *High Temperature* (2012), vol. **50**(3): 354–358 (2012) (cit. on p. 94).

262. Goldsack, D. E. & R. C. Franchetto: The viscosity of concentrated electrolyte solutions. II. Temperature dependence. *Canadian Journal of Chemistry* (1978), vol. **56**(10): 1442–1450 (1978) (cit. on p. 94).

263. Pusey, M. L.: Continuing adventures in lysozyme crystal growth. *Journal of Crystal Growth* (1992), vol. **122**(1-4): 1–7 (1992) (cit. on p. 94).

264. Vekilov, P. G.: Nucleation. *Crystal Growth and Design* (2010), vol. **10**(12): 5007–5019 (2010) (cit. on pp. 94, 121).

265. Lu, J., K. Carpenter, R. J. Li, X. J. Wang & C. B. Ching: Cloud-point temperature and liquid-liquid phase separation of supersaturated lysozyme solution. *Biophysical Chemistry* (2004), vol. **109**(1): 105–112 (2004) (cit. on p. 95).

266. Wang, W.: Lyophilization and development of solid protein pharmaceuticals. *International Journal of Pharmaceutics* (2000), vol. **203**(1-2): 1–60 (2000) (cit. on p. 95).

267. Klijn, M. E., A. K. Wöll & J. Hubbuch: Apparent protein cloud point temperature determination using a low volume high - throughput cryogenic device in combination with automated imaging. (2019), vol.: 1–45 (2019) (cit. on p. 100).

268. Singh, S. K. & S. Nema. *Formulation and Process Development Strategies for Manufacturing Biopharmaceuticals* 625–675 (2010) (cit. on pp. 100, 121).

269. VELEV, O. D., E. W. KALER & A. M. LENHOFF: Protein interactions in solution characterized by light and neutron scattering: Comparison of lysozyme and chymotrypsinogen. *Biophysical Journal* (1998), vol. **75**(6): 2682–2697 (1998) (cit. on p. 119).

270. MULLIN, J. W.: *Crystallization* 3rd: 182 (Butterworth Heinemann, Oxford, UK, 1992) (cit. on p. 122).

271. AHMED, N., D. F. NINO & V. T. MOY: Measurement of solution viscosity by atomic force microscopy. *Review of Scientific Instruments* (2001), vol. **72**(6): 2731–2734 (2001) (cit. on p. 120).

272. VAGENENDE, V., M. G. S. YAP & B. L. TROUT: Mechanisms of protein stabilization and prevention of protein aggregation by glycerol. *Biochemistry* (2009), vol. **48**(46): 11084–11096 (2009) (cit. on pp. 118, 119).

273. GALM, L., J. MORGENSTERN & J. HUBBUCH: Manipulation of lysozyme phase behavior by additives as function of conformational stability. *International Journal of Pharmaceutics* (2015), vol. **494**(1): 370–380 (2015).

274. BHAT, R. & S. N. TIMASHEFF: Steric exclusion is the principal source of the preferential hydration of proteins in the presence of polyethylene glycols. *Protein Science* (1992), vol. **1**(9): 1133–1143 (1992) (cit. on p. 119).

275. WAN, L. S. & P. F. LEE: CMC of polysorbates. *Journal of Pharmaceutical Sciences* (1974), vol. **63**(1): 136–137 (1974) (cit. on p. 119).

276. KENDRICK, B. S., T. LI & B. S. CHANG. *Rational Design of Stable Protein Formulations* (eds CARPENTER, J. F. & M. C. MANNING) 61–84 (Springer New York, 2002) (cit. on pp. 119, 121).

277. KOZER, N., Y. Y. KUTTNER, G. HARAN & G. SCHREIBER: Protein-protein association in polymer solutions: From dilute to semidilute to concentrated. *Biophysical Journal* (2007), vol. **92**(6): 2139–2149 (2007) (cit. on p. 123).

List of Figures

List of Tables

A. Abbreviations and Symbols

Abbreviations

CMC	critical micelle concentration
DLS	dynamic light scattering
DSC	differential scanning calorimetry
DSP	downstream process
FT	freeze/thaw
FTIR	Fourier transform infrared spectroscopy
HT	high–throughput
HTS	high–throughput screening
IQR	interquartile range
IS	ionic strength
LLPS	liquid–liquid phase separation
MAD	median absolute deviation
MCB	multi–component buffer
MPPD	multidimensional protein phase diagram
MSE	mean squared error
PCC	Pearson correlation coefficient
PEG	polyethylen glycol
PES	polyethersulfone
pI	isoelectric point
SEC	size exclusion chromatography
SI	stability index
SL	solubility lines
TOA	thermo–optical analysis
USP	upstream process
UV	ultraviolet

Symbols

A	variable parameter
$c_{protein}$	protein concentration
c_{salt}	salt concentration
cx	cycle number (x = 0, 1, 3, 5)
D_t	diffusion coefficient
η	viscosity
G	gibbs free energy
G^*	critical gibbs free energy
Γ	decay rate
γ	interfacial free energy
k_b	Boltzmann constant
L_C	crystal length
n	total number of data points
n_{Agg}	percentage of aggregation well coverage
ν	molar volume
q	wave vector
r	radius
r^*	critical nucleus radius
R_0	variable parameter
R_H	hydrodynamic radius
Ry	ramp(y = 1-15)
S	enthropy
S_0	theoretical protein solubility
S_{sat}	supersaturation
S_{sol}	protein solubility
T	temperature
t_0 start point	
t_{onset}	aggregation growth onset time
t_E	aggregation cessation time
t_G	growth time
T_{CE}	clouding end temperature

T_{cloud}	cloud point
T_{CO}	clouding onset temperature
T_{DE}	declouding end temperature
T_{DO}	declouding onset temperature
T_{eu}	eutectic point
T_g	glass transition temperature
W_C	crystal width
y	raw value
$\hat{y}_i$	literature data
y_{max}	maximum value
y_{min}	minimum value
y	scaled value

B. Supplementary Material

B.1. Analysis of phase behavior and morphology during freeze-thaw applications of lysozyme

Table B.1.: Parameters and coefficients used for correlation of experimental data to Eq. (1) in the manuscript for creating the solubility lines.

pH	buffer systems	cycle	S^0	A	R^0	R_2
3	Citrate	0	0.7203	55.9489	3.2210	0.9958
		1	0.7436	59.5678	3.3186	0.9989
		3	0.8653	87.9429	4.5668	0,9934
		5	0.8726	90.7610	4.4721	0.9922
	MCB	0	0.8122	92.394	3.6183	0.9977
		1	0.8045	50.7459	3.5686	0.9954
		3	0.7362	33.0881	3.1105	0.9977
		5	0.7585	53.7530	3.5621	0.9977
	MCB_{IS}	0	0.6125	35.3575	2.9458	0.9975
		1	-	-	-	-
		3	-	-	-	-
		5	-	-	-	-
5	Acetate	0	1.5391	42.3201	2.4778	0.9338
		1	0.9208	13.0441	1.3040	0.9685
		3	1.1361	18.1945	1.7710	0.9728
		5	1.7836	59.3601	3.0552	0.9701
	MCB	0	2.3471	58.1755	3.2288	0.9637
		1	2.1266	29.9694	2.5820	0.9800
		3	2.2411	77.4003	4.0093	0.9964
		5	2.0560	49.9577	3.3660	0.9976
	MCB_{IS}	0	2.5607	56.1989	2.7339	0.9790
		1	2.9398	62.0308	4.3738	0.9900
		3	2.6542	52.8444	4.4027	0.9957
		5	2.5168	42.6943	4.0984	0.9948

B.2. A phase diagram based toolbox to assess the impact of freeze/thaw ramps on the phase behavior of proteins
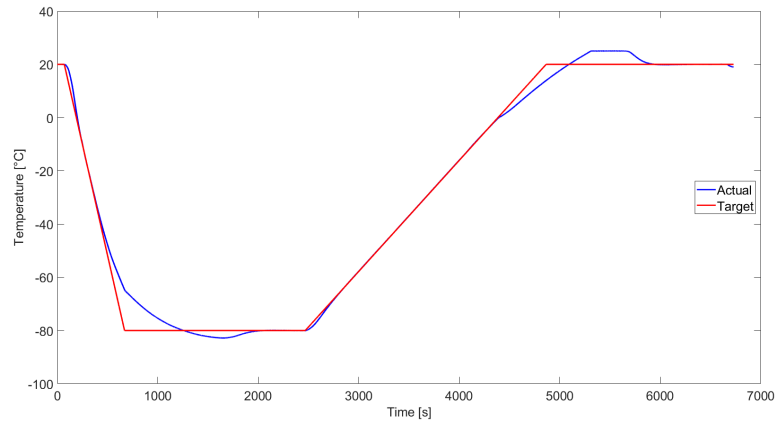
Figure B.1.: Exemplary Temperature-Time-Profile of Ramp 3. The blue line represents the actual temperature at the sample and the red line represents the temperature profile which is adjusted.
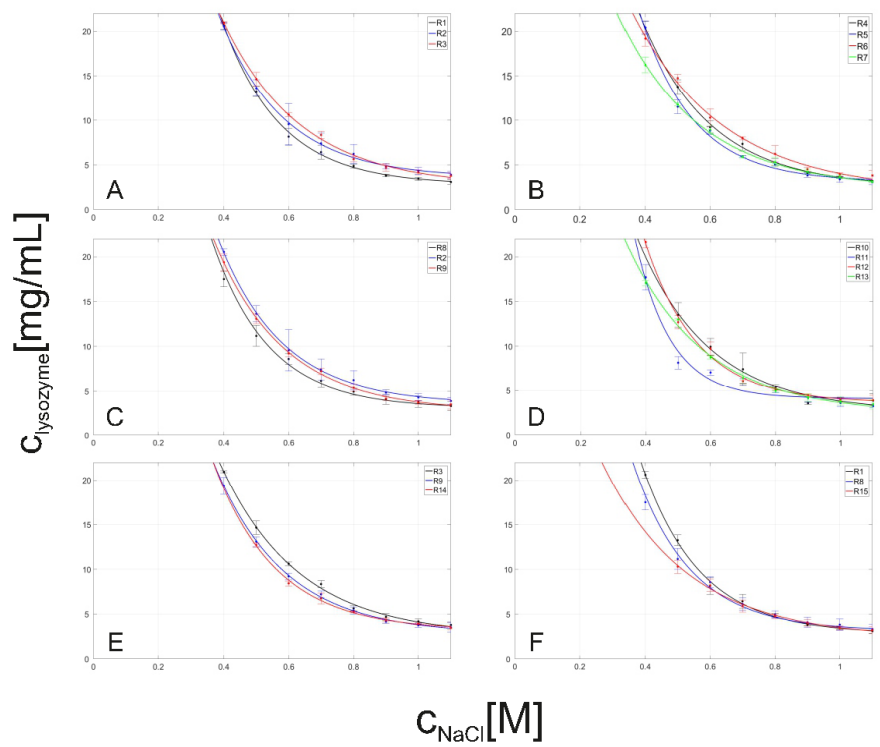
Figure B.2.: An overview of the solubility lines at FT c1 is shown. A Freezing speed; B Changing speed at different temperature while freezing; C Thawing speed; D Changing speed at different temperature while thawing; E Combinations fast; F Combinations slow
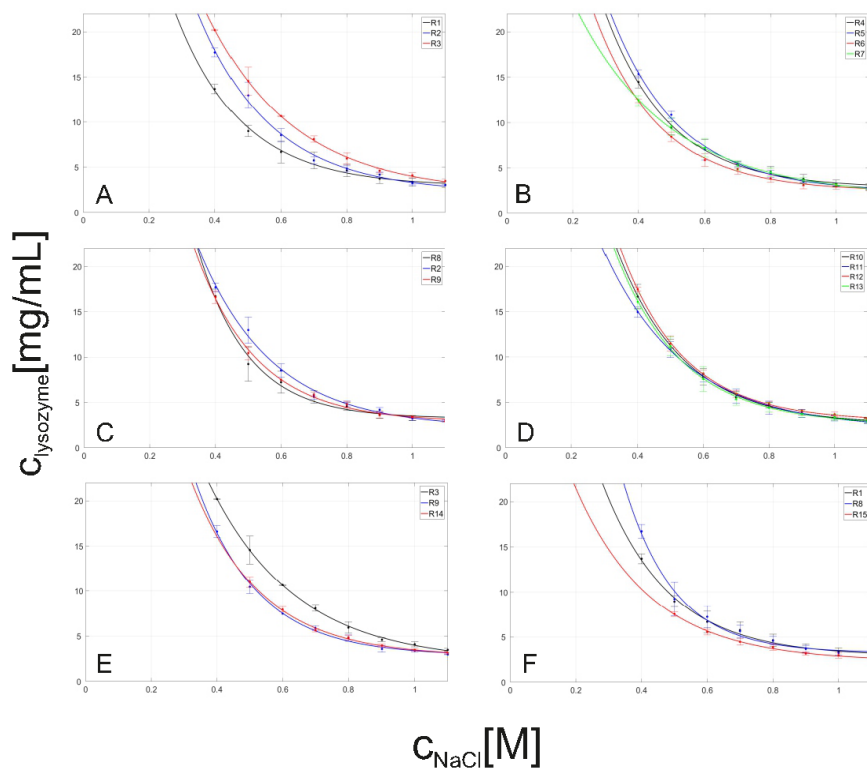
Figure B.3.: An overview of the solubility lines at FT c3 is shown. A Freezing speed; B Changing speed at different temperature while freezing; C Thawing speed; D Changing speed at different temperature while thawing; E Combinations fast; F Combinations slow

B.3. Apparent cloud point temperature determination using a low volume high-throughput cryogenic device in combination with automated imaging

B.3.1. Data evaluation

This section of the Supplementary Material shows more information on the image processing steps as well as the extraction of temperatures of interest, which was used for all studies presented in this work.

Image processing

An image processing workflow was designed to extract the total intensity difference between the first image and all images captured over time. This image processing workflow is shown in Figure B.4.
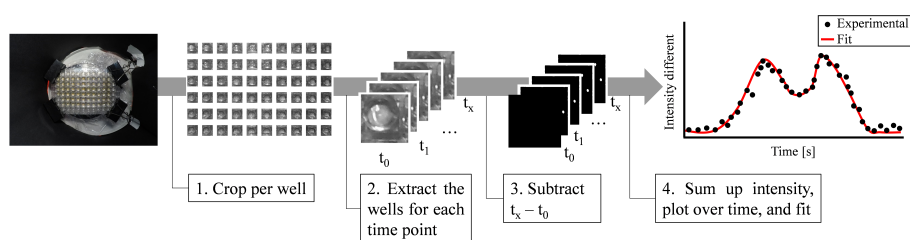
Figure B.4.: Overview of image processing steps. (1) The raw GoPro Hero4 image is cropped into separate wells, (2) cropping is repeated for each time point, (3) the t_0 image is subtracted from each time point image, for each well, and (4) the intensity per image resulting from the subtraction is summed up and plotted over time. The experimental data (black dot) is then fitted (red line).

B.3.2. Robustness study

Temperature rates

Three different temperature rate combinations were employed in the robustness study. The set temperature values, the measured temperature values, and the absolute difference between these two temperatures, is plotted in Figure B.5. Figure B.5 shows an increasing deviation of the set temperature compared to the measured temperature for increasing freezing rates and thawing rates, represented by an increase of the MSE from 0.01 to
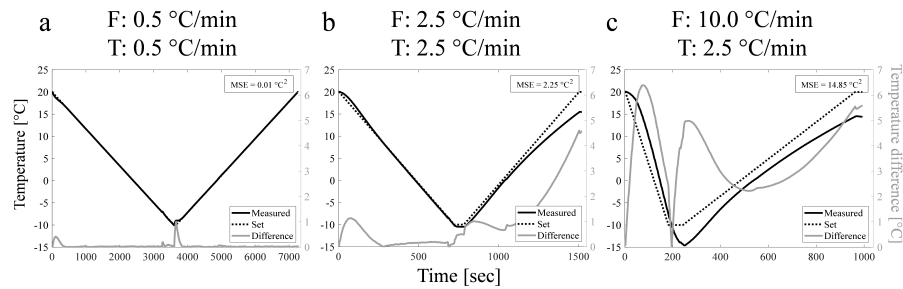
Figure B.5.: Overview of the set (black dotted line) and measured (black solid line) temperatures during the cloud point measurement at three different temperature rate combinations. (a) Freezing rate of 0.5 °C/min in combination with a thawing rate of 0.5 °C/min, (b) freezing rate of 2.5 °C/min in combination with a thawing rate of 2.5 °C/min, and (c) freezing rate of 10.0 °C/min in combination with a thawing rate of 2.5 °C/min. The difference between the set and measured temperature is shown as a grey solid line. The mean squared error (MSE; °C²) between the set and measured temperature is given in the text box.

14.85 when comparing the slowest freezing and thawing rate (Figure B.5 a; 0.5 °C/min for each) and the fastest freezing and thawing rate (Figure B.5 c; 10.0 °C/min and 2.5 °C/min, respectively). The high MSE value for the fastest freezing and thawing is a result of a higher measured temperature during freezing and a lower temperature during thawing. Figure S3b shows an MSE of 2.25 for a freezing and thawing rate of 2.5 °C/min, where the set temperature deviates most during thawing. In Figure B.5 b it is observed that the measured temperature is lower than the set temperature. A similar effect during thawing at 2.5 °C/min is observed for Figure B.5 c.

Position sensitivity

Intensity

The influence of the well position was also evaluated for the intensity that could be detected for T_{CE} and T_{DO} This was also extracted from the data obtained with the robustness study. This was evaluated as location specific trends could indicate uneven lighting or issues due to the fisheye lens of the GoPro Hero4 camera. The results are shown in Figure B.6. Figure B.6 shows a difference in intensity between the upper half of the plate (row B to D) and the bottom half of the plate (row E to G), where a lower intensity is seen for the upper half of the plate. This is consistent for all three freezing and thawing rate combinations. As mentioned before, this may be due to the primitive lighting setup or the use of a GoPro Hero4 fish eye lens. In order to determine whether the intensity difference influences the results, the cloud end temperature was assessed as a function of the well position too.
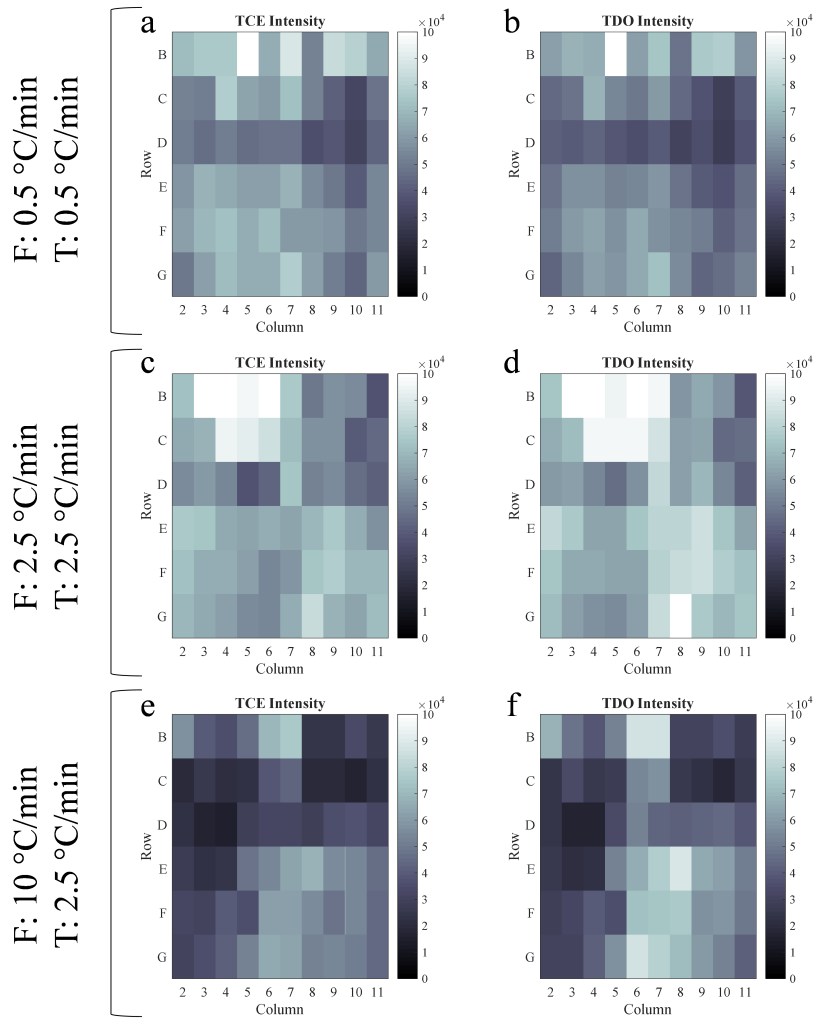
Figure B.6.: Total intensity obtained at the clouding end temperature (T_{CE}; a, c, and e) and declouding onset temperature (T_{DO}; b, d, and f) for three different freezing and thawing rate combinations. (1) freezing rate of $0.5\,°C/min$ in combination with a thawing rate of $0.5\,°C/min$ (a and b), (2) freezing rate of $2.5\,°C/min$ in combination with a thawing rate of $2.5\,°C/min$ (c and d), and (3) freezing rate of $10.0\,°C/min$ in combination with a thawing rate of $2.5\,°C/min$ (e and f). Intensity values are shown per plate row (y-axis) and plate column (x-axis).

Cloud end temperature

The influence of the well position on the multi–well plate on the extraction of T_{CE} for each well was evaluated with the data generated for the robustness study. Figure B.7 shows T_{CE} heat maps for each of the employed freezing and thawing rate combinations, using the standard 96–well plate orientation. Figure B.7 shows no influence of the well position regarding the measurement of T_{CE}. Figure B.7 b shows two deviating T_{CE} values at position D5 and D6, compared to the rest of the data in Figure B.7 b. Figure B.7 c
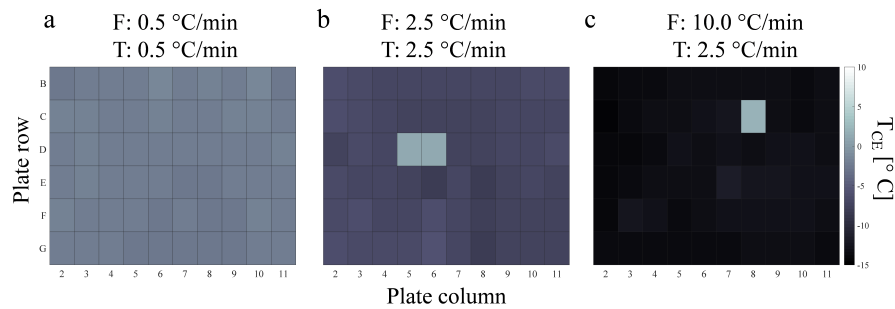
Figure B.7.: T_{CE}; ℃) for 60 replicate samples obtained with three freezing and thawing rate combinations, shown per plate row (y-axis) and plate column (x-axis). (a) Freezing rate of 0.5 ℃/min in combination with a thawing rate of 0.5 ℃/min, (b) freezing rate of 2.5 ℃/min in combination with a thawing rate of 2.5 ℃/min, and (c) freezing rate of 10.0 ℃/min in combination with a thawing rate of 2.5 ℃/min.

shows one deviating T_{CE} value for well C8, compared to the rest of the T_{CE} values in Figure B.7 c. These three deviations were considered outliers and not a result of measurement bias towards the position of the well, as the outlier position is not similar for each plate.

B.3.3. Validation study

Freezing and thawing rate

The difference between the set and measured temperature during the validation study is shown in Figure B.8.
 Figure B.8 shows a MSE of 0.004, which indicates a low difference between the set and measured temperature during the validation study.

Position sensitivity

To determine whether there was an influence of the well positions during the validation study, the T_{CE} per replicate sample is shown in Figure B.9.
 Figure B.9 shows an increase in T_{CE} for increasing pH values. This is a reproducible trend as it is observed for each of the replicates of the samples. Two outliers can be identified at pH 5.8 and pH 6.5 for replicate number 6. These outliers were not removed during the calculations as descriptive statistics such as the median and MAD are less sensitive to outliers than the mean value and the standard deviation. Figure B.9 shows no influence of the well position on the extraction of T_{CE}.
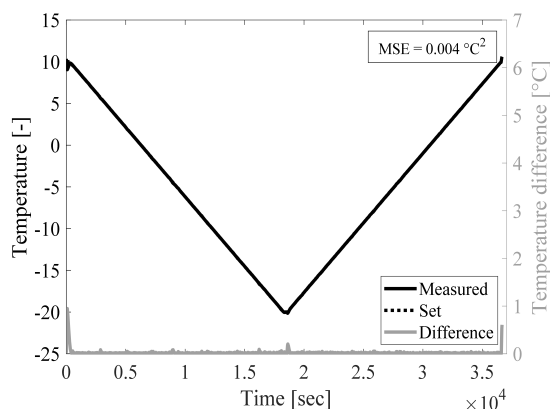
Figure B.8.: Overview of the set (black dotted line) and measured (black solid line) temperatures during the cloud point measurement, employing a freezing and thawing rate of 0.1 °C/min during the validation study. The difference between the set and measured temperature is shown as a grey solid line. The mean squared error (MSE; °C^2) between the set and measured temperature is given in the text box.
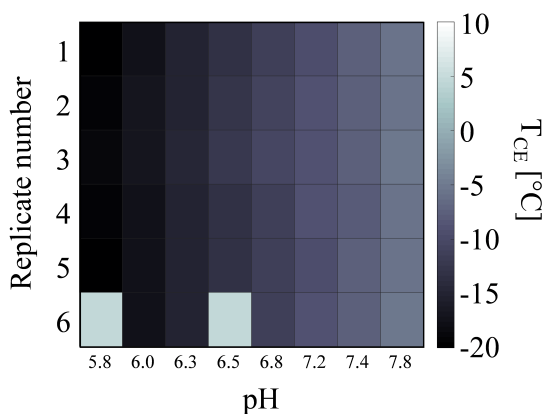
Figure B.9.: Clouding end temperature (T_{CE}; °C) for all validation samples, shown per replicate (y–axis) and pH (x–axis). T_{CE} values were extracted from raw data obtained during the validation study.

Absolute literature comparison

The exact absolute temperature values estimated from literature graphs [151] and obtained with the proposed experimental setup are listed in Table B.2.

Table B.2 is solely added to present the absolute values, interpretation of the results is discussed in the main text and therefore considered redundant in this section.

Table B.2.: List of temperature values per pH, where literature values were obtained from [151] and experimental data is given as median ± median absolute deviation based on six replicate measurements.

pH	Literature [℃]	Experimental [℃]
5.8	-6.5	-19.4 ± 0.3
6.0	-5.9	-17.4 ± 0.2
6.3	-4.9	-14.9 ± 0.0
6.5	-4.2	-13.0 ± 0.2
6.8	-2.9	-11.3 ± 0.0
7.2	-2.1	-9.0 ± 0.2
7.4	-1.4	-7.8 ± 0.1
7.8	-0.6	-5.6 ± 0.1

Moving mean

Figure B.10 shows an example of the validation data smoothing by means of a moving mean window of 100.
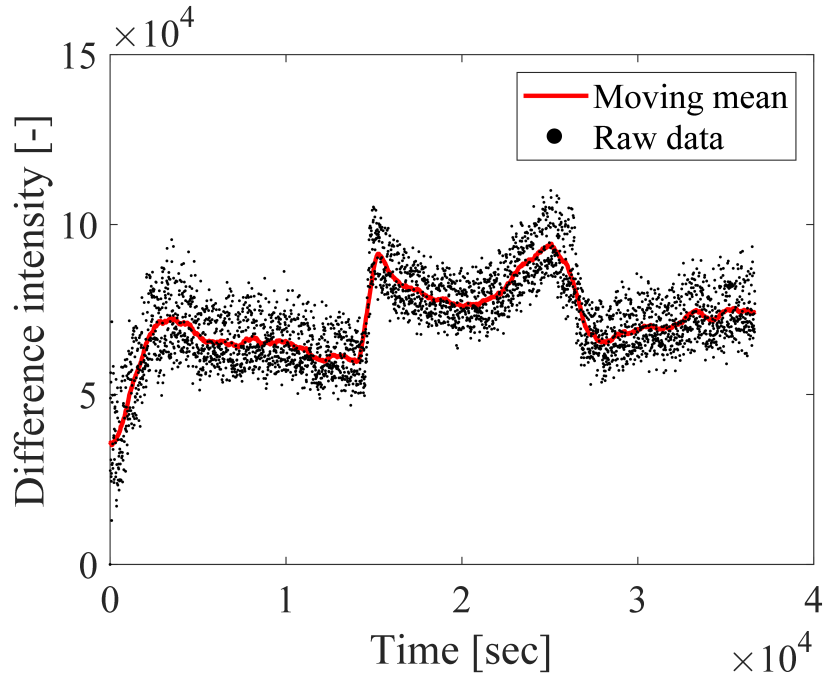

Figure B.10.: Exemplary plot of raw data (black dot) and the data smoothed with a moving mean window of 100 (red line) during the validation study, where the intensity difference (y–axis) is plotted over time (x–axis; seconds).

B.3.4. Case study

Solubility Line

Supernatant lysozyme concentration measurements were performed to determine the solubility line of different formulations. In order to do so, the supernatant lysozyme concentration of all formulations that showed a phase transition in the respective phase diagrams was measured. It was performed like described by Galm *et.al* [164]. The resulting solubility lines are shown in Figure B.11.
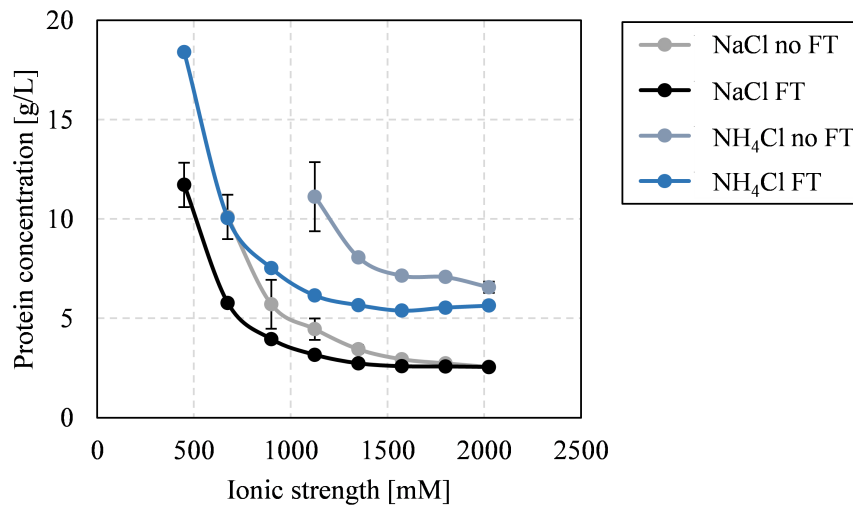
Figure B.11.: Lysozyme solubility for varying concentration (y-axisl g/L) and ionic strength (x-axis; mM). Solubility lines are shown for sodium chloride (NaCl) and ammonium chloride (NH$_4$Cl), without being subjected to a freeze and thaw run (no FT) and after a freeze and thaw run (FT).

Average MPPD cluster values

Table B.3 lists the absolute image-based feature values for each of the clusters (I-VI) found for the average MPPD.

Table B.3 shows the absolute vales for the crystal length (L_C), variation in crystal width ($\triangle W_C$), variation in crystal length ($\triangle L_C$), aggregation abundancy (n_{Agg}), aggregation growth time (t_G), aggregation onset time (t_0), and crystal width (W_C). These values correspond to the MPPDs in Figure 6.4, presented and discussed in Section 6.3.3 (Long–term protein stability).

Table B.3.: Overview of median $\pm$ MAD image-based feature values. The values are listed per cluster identified in the average MPPD.

	I	II	III	IV	V	VI
L_C [μm]	0 ± 0	271 ± 67	424 ± 138	340 ± 124	44 ± 53	35 ± 25
W_C [μm]	0 ± 0	157 ± 67	295 ± 99	219 ± 84	36 ± 32	26 ± 18
t_0 [hours]	0 ± 0	301 ± 61	273 ± 135	0 ± 0	424 ± 104	0 ± 0
t_G [hours]	0 ± 0	553 ± 173	660 ± 116	534 ± 341	536 ± 104	296 ± 101
n_{Agg} [%]	0 ± 0	5 ± 4	8 ± 4	23 ± 15	79 ± 19	95 ± 4
$\triangle L_C$ [μm]	0 ± 0	185 ± 61	371 ± 86	98 ± 84	16 ± 20	6 ± 6
$\triangle W_C$ [μm]	0 ± 0	130 ± 73	253 ± 58	84 ± 81	8 ± 9	4 ± 3

Example cluster images

Each of the clusters found for the construction of the MPPD using the average long-term stability data, represents a group of formulations that have similar morphologic and kinetic features. An example visible light, cross polarized light, and UV light for each of the clusters is shown in Figure B.12.
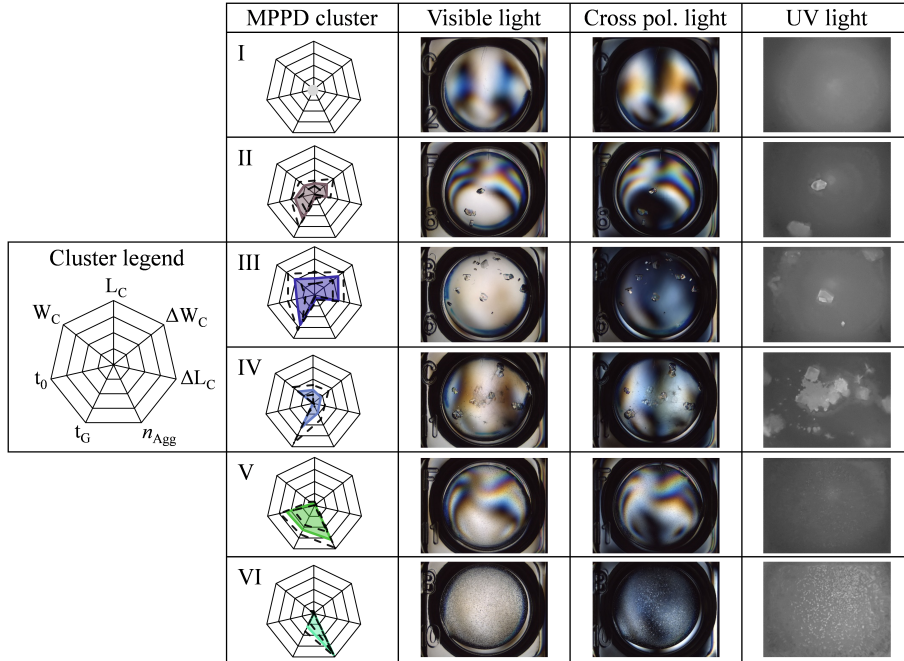

Figure B.12.: Exemplary images for the six MPPD clusters (first column) obtained with the average image-based data (legend). Three different light sources are shown: (1) visible light (second column), (2) cross polarized (pol.) light (third column), and (3) UV light (fourth column).

Cloud end temperature per plate

Figure B.13 shows the T_{CE} for each salt and each plate per well, in order to represent the reproducibility of the T_{CE} obtained during the case study.
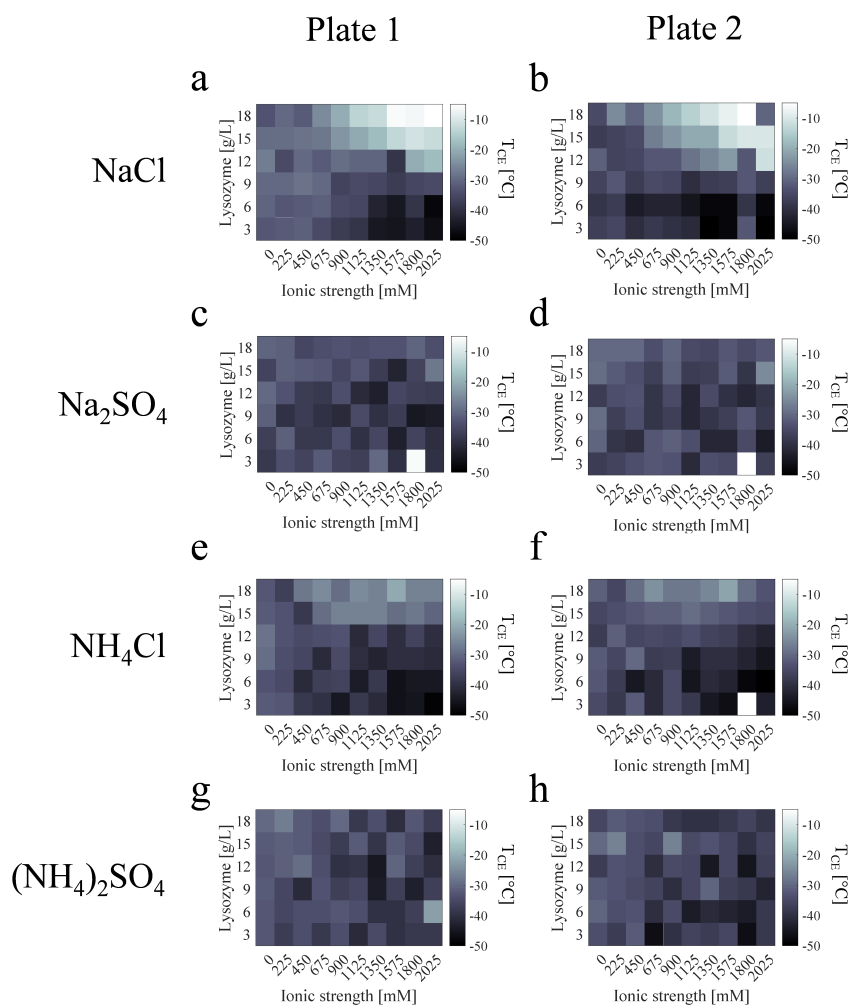
Figure B.13.: Cloud end temperature (T_{CE}; °C) for sodium chloride (NaCl; a and b), sodium sulfate (Na$_2$SO$_4$; c and d), ammonium chloride (NH$_4$Cl; e and f), and ammonium sulfate ((NH$_4$)$_2$SO$_4$; g and h), under varying lysozyme concentrations (y–axis; g/L) and ionic strength (x–axis; mM). Duplicate plates are shown (major grid columns).

Multidimensional protein phase diagrams per plate

To determine the reproducibility of the long–term stability storage results, all plates were stored in duplicate. The resulting MPPD is shown in Figure B.14. Figure B.14 indicates the reproducibility of the long-term storage in terms of observed aggregation morphology and

aggregation kinetics. This is shown by the identification of similar MPPD Clusters for the duplicate plates, thus similar morphology and kinetics for duplicate conditions. A difference is observed for Plate 1 and Plate 2 for ammonium chloride, where cluster IV is identified for Plate 1 and cluster I for Plate 2. This was attributed to dried-up wells in Plate 1 for ammonium chloride conditions, which significantly affected the extracted morphology and kinetic data. Therefore, only Plate 2 data was used during the construction of the averages MPPD, which is presented in the main text.

Table B.4 lists the absolute image-based feature values for each of the clusters (I-V) found for the MPPD constructed for all plates separately, presented in Figure B.14.

Table B.4 shows the absolute vales for the crystal length (L_C), variation in crystal width

Table B.4.: Overview of median $\pm$ MAD image-based feature values. The values are listed per cluster identified in the separate MPPD.

		I	II	III	IV	V
L_C	[μm]	0 ± 0	696 ± 202	315 ± 100	$496 \pm$ś 250	38 ± 26
W_C	[μm]	0 ± 0	433 ± 128	184 ± 112	200 ± 101	28 ± 19
t_0	[hours]	0 ± 0	252 ± 374	0 ± 0	0 ± 0	0 ± 0
t_G	[hours]	0 ± 0	628 ± 137	582 ± 201	262 ± 726	301 ± 137
n_{Agg}	[%]	0 ± 0	5 ± 0	15 ± 7	90 ± 7	95 ± 5
$\triangle L_C$	[μm]	0 ± 0	471 ± 141	99 ± 92	635 ± 112	9 ± 9
$\triangle W_C$	[μm]	0 ± 0	306 ± 127	78 ± 73	334 ± 147	8 ± 7

($\triangle W_C$), variation in crystal length ($\triangle L_C$), aggregation abundancy (n_{Agg}), aggregation growth time (t_G), aggregation onset time (t_0), and crystal width (W_C).
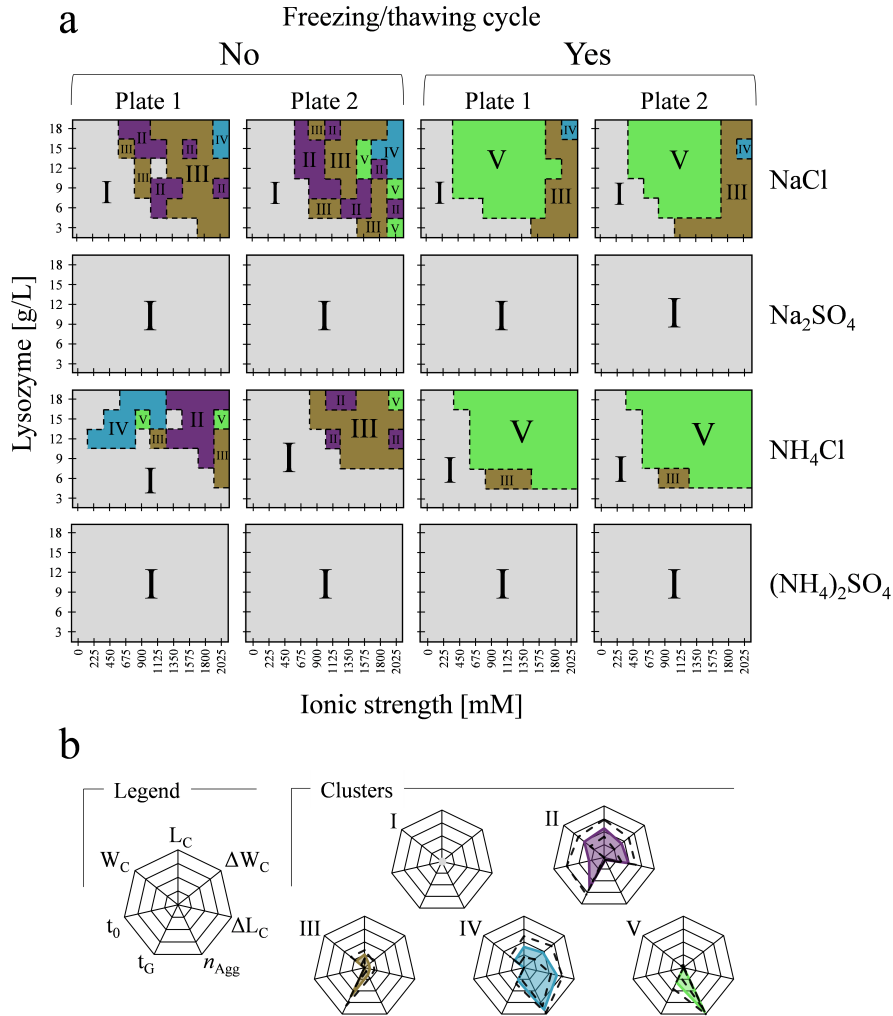
Figure B.14.: (a) MPPD for four different salts (grid rows) and with or without freezing and thawing (major grid columns) for duplicate plates (grid columns), as well as varying lysozyme concentrations (y–axis; g/L) and ionic strength (x-axis; mM). Applied salts are sodium chloride (NaCl), sodium sulfate (NaSO$_4$), ammonium chloride (NH$_4$Cl), and ammonium sulfate ((NH$_4$)$_2$SO$_4$). Five clusters were identified and visualized in the MPPD using the mean cluster color and cluster number similar to the radar charts shown in (b). The cluster regions are highlighted in the MPPD with a dashed line to guide the eye. (b) Radar charts representing the normalized median values of each image feature with a color surface. The dotted line in the radar chart represents the median absolute deviation within each cluster for each image feature. The following image-based features are displayed per cluster: median crystal length (L_C), IQR of the crystal width ($\triangle W_C$), IQR of the crystal length ($\triangle L_C$), aggregation well coverage (n_{Agg}), aggregation growth time (t_G), aggregation onset time (t_0), and median crystal width (W_C). Absolute cluster values can be found in Supplementary Table B.4.

B.4. Investigation of the reversibility of freeze/thaw stress-induced instability using heat cycling as a function of different cryoprotectants

B.4.1. MPPD construction

Scatterplot

Figure B.15 shows the position of all 2400 conditions regarding the RGB color code.
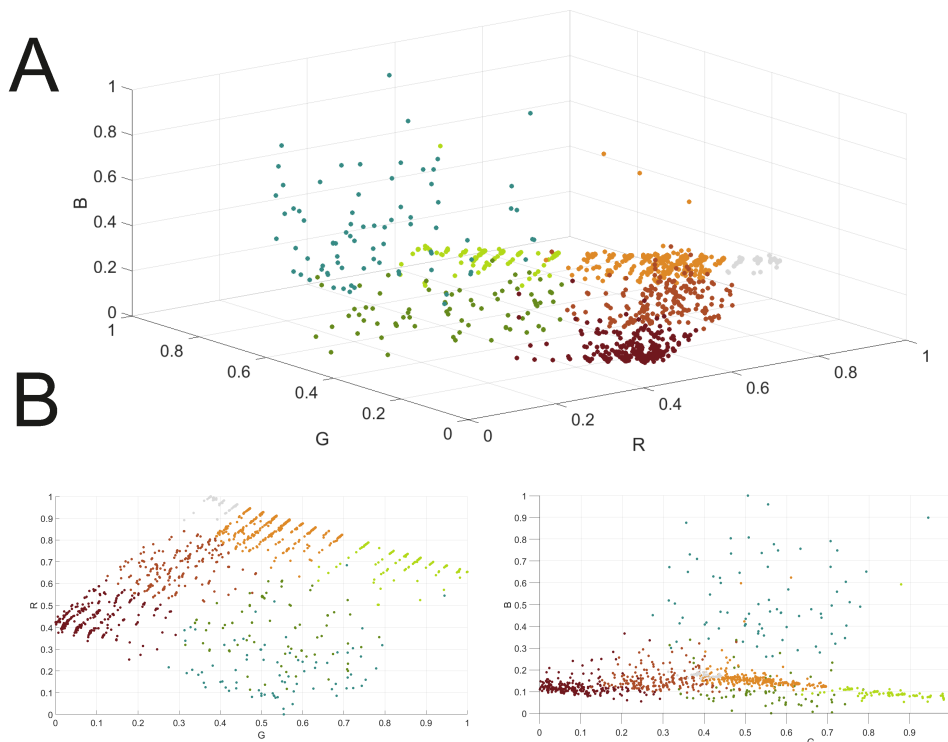
Figure B.15.: The position of all 2400 tested conditions regarding the RGB color code after clustering, in 3D (A) and 2D (B). Grey represents Cluster I, dark brown Cluster II, brown Cluster III, orange Cluster IV, green Cluster V, dark green Cluster VI, and blue Cluster VIII.

B.4.2. Analytic

DLS data

The DLS data shown in Figure 7.4 in the manuscript are shown with the respective deviation from the triplicate measurements in Figure B.16.
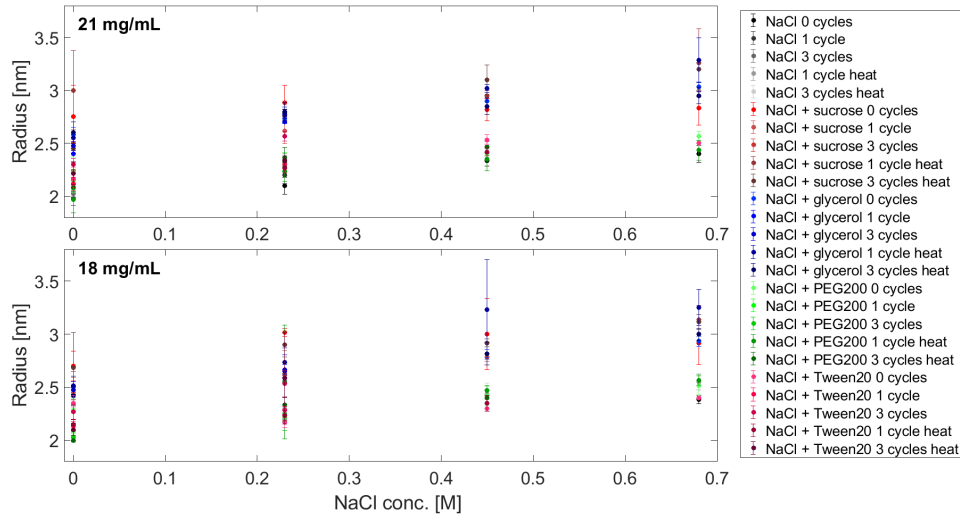
Figure B.16.: The DLS data plotted with the respective deviations for $21\,\text{mg/mL}$ (top) and $18\,\text{mg/mL}$ (bottom) lysozyme. The radius in nm is plotted over the NaCl concentration in M. All 153 conditions are plotted which performed different stress protocols.